III-Nitride Nanowire Based Near-Infrared Optoelectronic Devices on (001) Silicon

by

Arnab Shashi Hazari

A dissertation submitted in partial fulfillment
of the requirements for the degree of
Doctor of Philosophy
(Electrical Engineering)
in The University of Michigan
2017

Doctoral Committee:

Professor Pallab K. Bhattacharya, Chair
Professor Wei Lu
Professor Joanna Mirecki-Millunchick
Professor Jamie D. Phillips

Arnab S. Hazari

harnab@umich.edu

ORCID iD: 0000-0001-8025-7284

To my parents,

KRISHNA HAZARI

and

ASHOK K. HAZARI

for their unconditional love and unwavering support

ACKNOWLEDGEMENT

I would like to thank my advisor Professor Pallab Bhattacharya for his constant support throughout my work. I have the utmost respect and deepest appreciation towards Professor Bhattacharya. He has always encouraged me with my research and ensured I never lost sight or focus even at times of failure. Professor Bhattacharya's hard work inspired all of us, and I thank him for all the support and mentorship he has provided. Throughout my life, I will use the lessons that I learned from his excellent teaching. His constant help to numerous problems in research allowed me to reach my goals. I express my sincere gratitude for the many hours he spent making sure my research is a success. Even outside research, I had the pleasure of taking two courses with Professor Bhattacharya as the instructor. He is by far one of the best teachers I had the honor of knowing directly. His teaching has inspired not just me but many of my classmates.

I would like to thank my committee members, Professor Wei Lu, Professor Joanna Mirecki-Millunchick and Professor Jamie Phillips. Without their careful review of this work and valuable suggestions, this thesis would have been incomplete. I would like to acknowledge my mentors, Dr. Thomas Frost, and Dr. Shafat Jahangir for teaching me epitaxial growth, semiconductor fabrication, and optoelectronic device characterization. I am grateful for the lessons I have learned from them. I thank my fellow group members and collaborators, Aniruddha Bhattacharya, Dr. Thomas Frost, Dr. M. Zuanid Baten, and Anthony Aiello. Their contributions have greatly helped in my work. I would also like to

thank my fellow group members, Dr. Sishir Bhowmick, Dr. Animesh Banerjee, Dr. Shafat Jahangir, Dr. Saniya Deshpande, Dr. Thomas Frost, Dr. Zunaid Baten, Aniruddha Bhattacharya, Anthony Aiello, Yuanpeng Wu and Ayush Pandey. Their cooperation, help, and friendship have made this work successful, and my graduate school experiences a memorable experience.

I would also like to thank my collaborators, Dr. Songrui Zhao from McGill University, Montreal, Canada, Dr. Lifan Yan, Professor Zetian Mi and Professor Joanna Mirecki-Millunchick from the University of Michigan, Michigan, USA, Tien-Khee Ng and Professor Boon S. Ooi from King Abdullah University of Science & Technology (KAUST), Saudi Arabia, Professor Junseok Heo from Ajou University, Suwon, South Korea, Fu-Chen Hsiao and Professor John Dallesasse from the University of Illinois, Urbana-Champaign, Illinois, USA, Dr. Alexander Soibel and Dr. Sarath D. Gunapala from the National Aeronautics and Space Administration (NASA) Jet Propulsion Laboratory (JPL), California, USA. The research work and the resulting research papers published throughout this thesis are results of an efficient and productive collaboration that was only possible because of such a positive collaborative space that all of us created together.

I would like to thank all staff of the Lurie Nanofabrication Facility (LNF) and Michigan Center for Materials Characterization (MC2) laboratories at the University of Michigan for their support in and out of the cleanroom. I am grateful for all the help provided by Dennis Schweiger, Robert Hower, Brian Armstrong, Nadine Wang, Pilar Herrera-Fierro, Gregory Allion, David Sebastian, Anthony Sebastian, Matthew Oonk, Terre Briggs, Steven Sostrom, James Kulman, Katharine Beach, Sandrine Martin, Kevin

Owen and Shawn Wright from Lurie Nanofabrication Facility (LNF). I am also grateful to Bobby Kerns, John Mansfield, Haiping Sun, Allen Hunter, Kai Sun, Beverly Clampit, and Professor Emmanuelle Marquis from Michigan Center for Materials Characterization (MC2). Their mentorship and support with many of the lab processes have helped me successfully fabricate and characterize different devices mentioned in this work.

I thank Lisa Vogel, Melanie Caughey, Deb Swartz, Karen Liska, Anne Rhodes, Beth Stalnaker, Steven Pejuan, and Jose-Antonio Rubio. Their administrative support has helped me throughout my graduate school career. I thank the Materials Research Science and Engineering Centers (MRSEC) program of National Science Foundation (NSF), Strategic University Research Partnership (SURP) program of the Jet Propulsion Laboratory (JPL), Horace H. Rackham School of Graduate Studies at the University of Michigan, and Electrical Engineering and Computer Science (EECS) department of the University of Michigan for funding my research and my studies. This work would have been impossible to achieve without the necessary funding.

Finally, I thank my family, friends and loved ones. I thank my close friends Niket Prakash, Aniket Deshmukh, Abhishek Bafna, Harshita Rathi-Bafna, and Sneha Agarwal. I will always cherish all the fun times we had together. I also thank my elder brother, Arkashree Hazari, for always supporting and loving his little brother. I thank Amberlyn Britt and her family for their unconditional love and support through thick and thin. None of this would have been possible without my mother, Krishna Hazari, and my father, Ashok Kumar Hazari. Their love and encouragement have been one of my biggest strengths throughout my graduate school career.

TABLE OF CONTENTS

LIST OF FIGURES

Figure

LIST OF TABLES

Table

LIST OF APPENDICES

Appendix

ABSTRACT

III-nitride-based optoelectronics research has seen rapid progress since the demonstration of the first blue-emitting diode laser by Nakamura *et. al*. The research has so far focused mainly on devices emitting in the visible spectrum, and significant work can still be done in the near-infrared (near-IR) to infrared (IR) spectrum. Photonic devices based on the III-nitrides and operating at near-IR can have several advantages over other material systems. Such devices emitting in the near-IR can also be used in various applications including silicon-photonics, fiber optic communications, and various biomedical applications. A photonic integrated circuit consisting of a coherent light source such as a laser and detector directly on (001) silicon will be of great importance for the progress of silicon photonics. This work focuses on the III-nitride-based alloys which have operating wavelengths in the near-IR. The present work successfully demonstrates lasers, detectors, and a complete monolithic photonic integrated circuit all directly grown on (001)Si. The presented work includes some preliminary results on III-nitride-based devices operating in the infrared instead of the near-infrared.

To accomplish the above-mentioned objective, self-assembled III-nitride nanowire arrays have been epitaxially grown on (001)Si instead of using planar III-nitride layers, which cannot be directly grown on Si with good optical quality. The density and diameter of these nanowires have been varied over a wide range by tuning the growth conditions. The nanowires grow strain relaxed and are relatively free of extended defects.

Due to the strain relaxation, nanowires exhibit superior properties compared to their planar counterparts such as higher radiative efficiency, and reduction of the polarization field. Strain relaxation has also enabled the In composition in the disks to be increased to 100% forming binary InN disks used as the active region. Formation of quantum dots has also been observed in similar disks which further enhance quantum confinement of the carriers. A nanowire array has been used to demonstrate the first monolithic nanowire laser on (001) silicon emitting at 1.3μm. The nanowire arrays have also been used to demonstrate near-IR detectors on (001)Si. Both the optoelectronic devices have been fabricated on the same chip to demonstrate the operation of a photonic integrated circuit directly grown on (001)Si. Both the laser and the detector have the same nanowire heterostructure simplifying the fabrication of the photonic integrated circuits.

The active region of the disks-in-nanowire heterostructure arrays, grown using molecular beam epitaxy, is essentially InGaN with the In composition varying from ~85% to ~100%. These InN disk based half-laser heterostructures demonstrate excellent optical and structural characteristics. Lasers have been characterized which demonstrate high optical output power levels (~7mW above threshold), a differential slope efficiency of ~12%, an ideal emission wavelength of ~1.2-1.3μm, excellent temperature stability (T_0 > 200K) and a differential gain of ~$3\times10^{-16}cm^2$. The detectors show good responsivity of 0.11A/W at near-IR. The photonic integrated circuits show about a 10-fold increase in the detector photocurrent as a function of laser injection current. All photonic integrated circuit related measurements have been made at room temperature. The disks-in-nanowire heterostructures grown on (001)Si also demonstrate absorption in the mid-IR (MIR) as well as in the long wavelength IR (LWIR) wavelength regimes. Absorption

peaks in the wavelength range of ~1.6 to ~20μm have been measured at room temperature paving the path for future demonstration of long wavelength detectors using the III-nitrides.

Chapter I

Introduction

1.1 A Brief Overview of III-Nitride-based Research with Emphasis on Solid-state Lighting

Artificial lighting has significant importance in human productivity and day-to-day activities. The electric lighting industry is about 140 years old, since Thomas Alva Edison's invention of the incandescent light bulb [1]. In this period this industry has seen a significant evolution. Groundbreaking discoveries have been made to change the way we perceive the source of artificial light. Edison's invention was based on the principle that some metals (e.g., Tungsten) are incandescent if they are heated to extremely high temperatures (e.g., ~2100°C). These light sources suffer from a significant energy loss and low lifetime. The next prominent invention was the fluorescent light bulb. Even though there is a considerable amount of debate about which of the visible fluorescent bulbs should be considered the first of its kind, a mercury vapor lamp invented by Peter Cooper Hewitt in 1903 is credited as the first fluorescent bulb [2]. The lamp did not have the fluorescent coating but was similar to the modern fluorescent bulbs. These bulbs had significantly higher efficiencies and lifetimes compared to that of the incandescent bulbs. The next major milestone in lighting research is credited to Professor Nick Holonyak Jr. for the demonstration of the first visible light emitting diode (LED) in 1963 [3].

Interestingly, one of the first semiconductor diode laser was invented before this by Dr. Robert N. Hall in 1962 which only emitted near-infrared (near-IR) light [4]. Concurrently, other independent groups were also developing a GaAs-based homojunction semiconductor laser diode that can operate at cryogenic temperatures. Near-IR light is also of significant interest in the industry and will be discussed later in this chapter. The first Nitride based blue LED that opened the door to white lamps only consisting of semiconductor materials was not invented till 1993 by Shuji Nakamura [5].

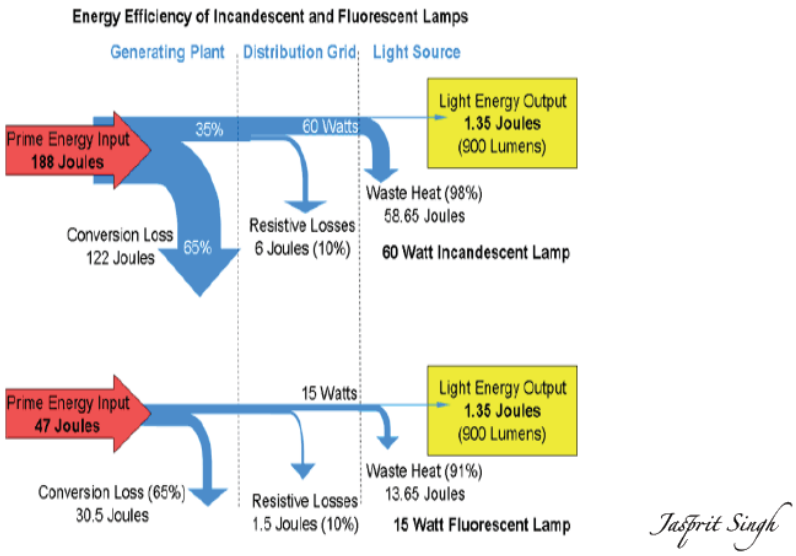

Figure 1.1 Energy Loss in an Incandescent Lamp versus a Fluorescent Lamp (Courtesy of Professor Jasprit Singh, University of Michigan).

Even in the 21st century, almost 90% of the supplied electric power is dissipated to non-radiative channels such as heat in a typical incandescent light bulb resulting in low conversion efficiencies. Fluorescent and LEDs have much higher conversion efficiencies compared to incandescent light bulbs [6]. There are other losses associated with the power distribution line. Figure 1.1 (Courtesy of Professor Jasprit Singh, University of Michigan) is an average estimate of how energy is dissipated to heat for a fluorescent light compared to an incandescent light. Even though the fluorescent lighting is almost

five times more efficient (in this case) than incandescent light, there is still a substantial dissipation of energy. A significant amount of energy dissipation occurs as electricity is converted into light. Such energy dissipation can be significantly reduced with solid state lighting which has promising luminous efficiency [7]. The high luminous efficiency can dramatically reduce the overall energy dissipation in such power grids which is one of the main reasons such light based emitters are being heavily researched.

The other important aspect of solid state lighting is the lifetime. The incandescent light bulbs suffer from a low lifetime due to the high temperature used in these bulbs. Modern incandescent bulbs only have ~1,000 hours of lifetime. The fluorescent bulbs have almost ten times more lifetime (~10,000 hours) which is still small compared to the high lifetimes of modern semiconductor based LEDs. An average LED from CREE can have lifetimes of ~25,000-50,000 hours. Such high lifetimes can also have significant economic advantages over low lifetime products [8]. Figure 1.2 shows typical examples of such light bulbs.

Figure 1.2 Typical (a) Incandescent light bulb (courtesy of http://www.industrytap.com/), (b) Fluorescent light bulb (courtesy of http://www.amazon.com/), and (c) Semiconductor LED (courtesy of http://www.cree.com/).

1.2 Near-Infrared Light and Its Applications

Our day-to-day experiences directly show us the significance of artificial visible source. Light bulbs, television screens, computer screens are all part of this day-to-day experience of human and visible light source interactions. Artificial infrared light sources have equal significance as artificial visible light sources. In this regard, semiconductor based light sources are not only superior in the visible spectrum but also in the infrared spectrum. Such light sources and light detectors are being used in various areas including, terrestrial, extra-terrestrial imaging, chemical spectroscopy, short and long-range communication, global weather monitoring systems (e.g., NASA's earth observing systems) [9], [10]. Infrared light has a vast range starting from 0.75μm and reaching all the way to 1mm. While different sections of the infrared light spectrum have various applications, this work will focus in the range of 0.75μm to 1.4μm known as near-infrared (Near-IR) light. Among many advantageous applications of near-IR, the four most important applications of near-IR Semiconductor based light sources are in silicon photonics [11], on-chip communication [12], optical fiber communication [13] and medical applications [14].

1.2.1 Silicon photonics

The electronics industry has been following "Moore's law" for the last 40 years which suggests that the speed and capability of electronic devices will double about every two years [15]. A visual depiction of this law can be seen in Fig. 1.3 (Courtesy of Professor Jasprit Singh, University of Michigan). In the 21st century, transistors have reached a length of only 14nm [16]. These transistors are all based on silicon, the second most abundant material on our planet [17]. Silicon has an atomic size of about 0.2nm.

The direct conclusion is that the current electronic industry is reaching the lowest limit rapidly. Ground breaking inventions have to be made to continue Moore's law. One such revolutionary field is photonics and particularly, in this case, silicon photonics. The idea is to use photons (light) instead of electrons (electricity). Typically in a chip, light is about 20 times faster than electricity. This advantage can make future light based chips far more enhanced than the current standards. To emphasize, a 20 times increase in speed happens in about 15 years in the electronics industry [18].

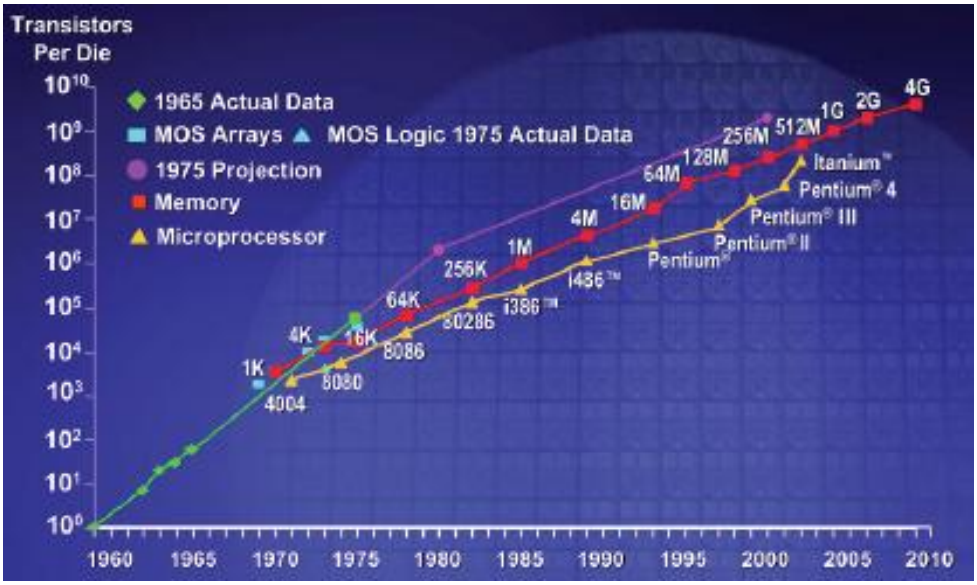

Figure 1.3 Moore's law for transistors used in different technology (Courtesy of Professor Jasprit Singh, University of Michigan).

The name "silicon photonics" stems from the fact that the technology is based on silicon but driven with light (photons) instead of electricity (electrons). Silicon absorbs light with wavelengths below 1.1μm [19]–[21], and it does not emit any light. Hence light sources and detectors used in silicon photonics based technology must be able to operate at near-IR wavelengths making near-IR essential for silicon photonics. Following this method, many companies are trying to integrate light with traditional electronics [22] resulting in numerous devices seen in Fig. 1.4 (Courtesy of Intel). Such devices include

light sources (lasers), detectors, data encoders, light routing devices, multiplexers, and demultiplexers. Such devices can pave the path to a complete photonic computer system in the near-future, and near-IR light will be the key to the successful operation of such photonic computer systems.

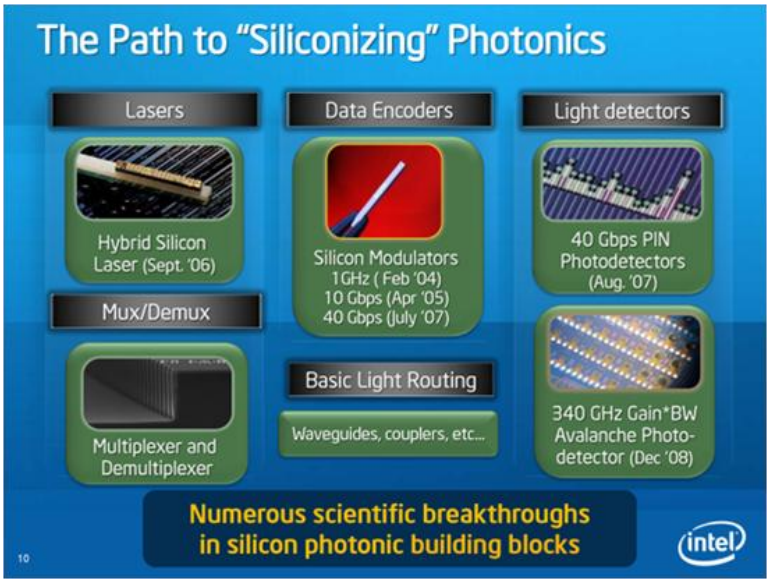

Figure 1.4 Different kinds of Photonic devices (Courtesy of Intel).

1.2.2 On-chip communication

Following the extensive research on photonic devices, various photonic circuits have been suggested over the last few decades. A typical photonic circuit is shown in Fig. 1.5 [23]. Such a circuit typically has two or more of the following optoelectronic components: a laser, a detector and a waveguide. Additionally, various other optoelectronic components, to be used in photonic circuits, are continuously being researched and designed. A simple but complete photonic circuit should have a laser (generates the light), a waveguide (controls the light path) and a detector (detects the light). As silicon does not emit light, many other materials and nanostructures have been used as integrated light sources with silicon. This section discusses four reported

approaches to integrate a laser with silicon among many suggested ones. None of the approaches have been able to demonstrate a complete monolithic photonic integrated circuit directly on (001) silicon.

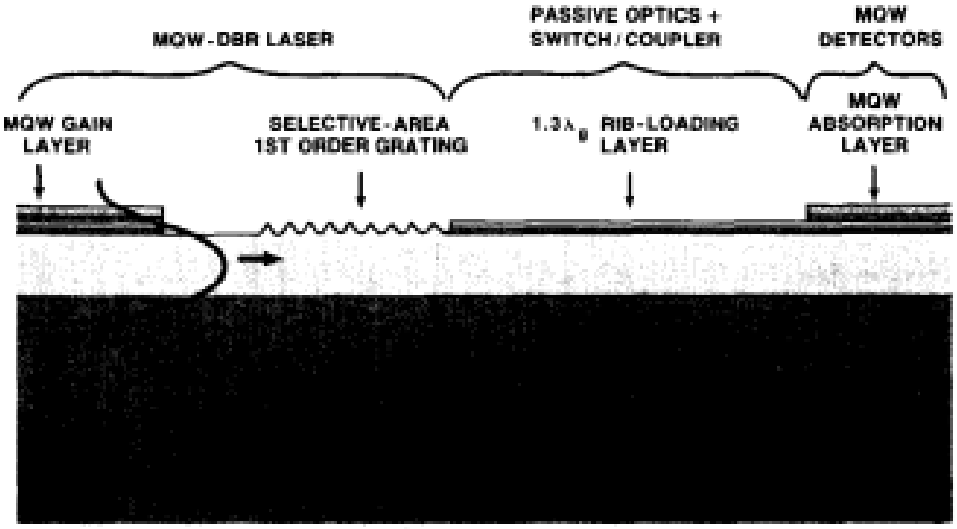

Figure 1.5 A photonic integrated circuit (Koch *et. al.*, "Semiconductor photonic integrated circuits," IEEE J. Quantum Electron., vol. 27, no. 3, pp. 641–653, Mar. 1991.).

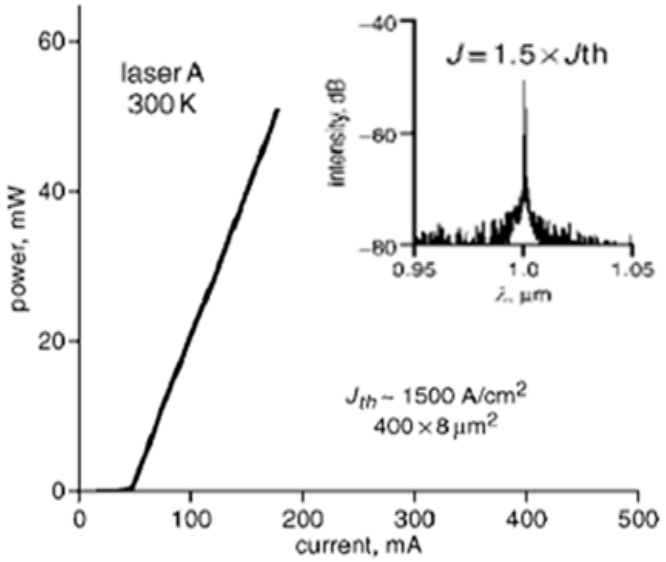

Figure 1.6 Light-current characteristics of a GaAs-based laser on offcut Si. Inset shows the above-threshold electroluminescence spectrum (Mi et al., Elec. Lett. 41, 13 (2005)).

In the first approach, GaAs-based lasers have been demonstrated on offcut (001)Si [24]–[26] by various research groups around the world. The characteristics of such a

GaAs-based laser characteristics can be seen in the Fig. 1.6 [25]. The offcut silicon is used to circumvent problems due to the formation of anti-phase domains and the ~4.1% lattice mismatch between Si and GaAs. The lasers demonstrated with this approach are promising and have excellent steady-state and dynamic characteristics. The major disadvantage of this approach is the use of offcut Si which makes these devices incompatible with the traditional Complementary metal–oxide–semiconductor (CMOS) technology.

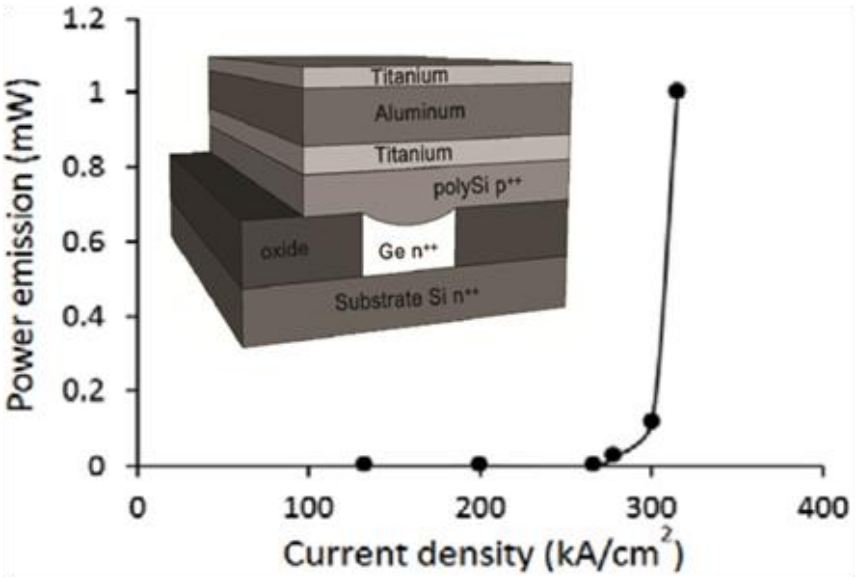

Figure 1.7 Light-current characteristics of a Ge based laser on Si. The inset shows the corresponding laser heterostructure. (Aguilera *et al.*, Opt. Exp. **20**, 11316 (2012)).

The second approach focuses on the use of strained and heavily doped germanium (Ge) on silicon (Si) [27]. Unlike the previous approach, here there is no need to use offcut Si. This laser does emit light at ~1.54μm although the main problem stems from the fact that unstrained Ge is also an indirect semiconductor. Even after the significant strain and doping, it is challenging to make Ge to electroluminescent. As can be seen in Fig. 1.7, lasing action is accomplished at an injected current density of ~300kA/cm^2. The previously discussed GaAs based lasers have a threshold current density of about

~2kA/cm^2. Even at such high injection currents, these Ge based lasers emit only about ~1mW of output power. Hence, this type of lasers will have a significant heating problem and will suffer from low wall-plug efficiency.

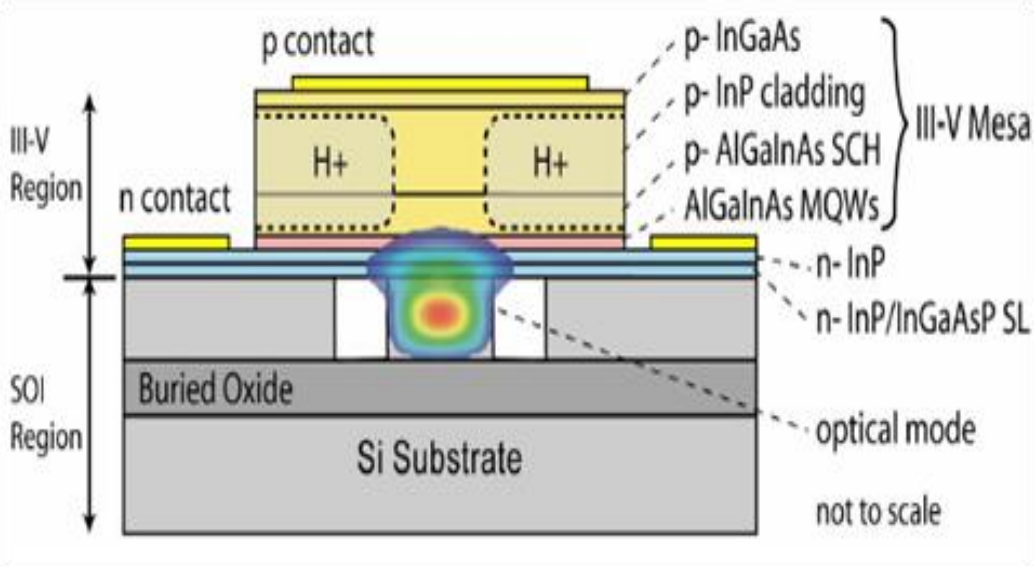

Figure 1.8 Laser heterostructure and mode confinement of a wafer bonded III-V laser (Fang et al., Opt. Exp. 14, 9203 (2006)).

In the third approach, wafer bonding is used to bond a III-V laser heterostructure on to a (001)Si wafer [28]. One such wafer bonded laser is shown in Fig. 1.8. So far this approach has gained significant popularity and success in the silicon photonics community, due to the favorable laser output characteristics. The lasers have demonstrated an ideal emission wavelength of 1.55μm and high differential quantum efficiency of 12.7%. The lasers have a relatively low output power of ~2mW, which is sufficient for on-chip applications.

However, these hybrid lasers have a low characteristic temperature of 39K thus demonstrating poor temperature stability. There can also be significant power loss if the mode is inefficiently coupled to the Si substrate. Additionally, the bonding area is limited by the available size of InP or GaAs wafers. Since Si wafers used in CMOS have higher

area compared to the III-V wafers, this can result in loss of valuable on-chip area. Moreover, the wafer bonding process itself can cause stability problems. To ensure good quality wafer bonding, the technology being used can also increase the price of these type of lasers significantly.

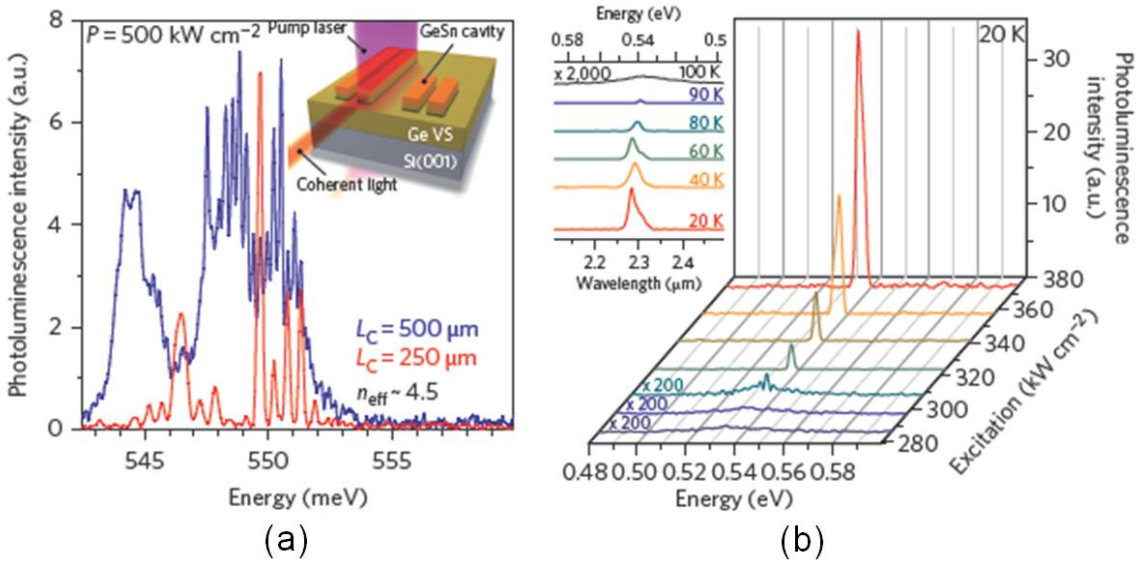

Figure 1.9 (a) Output spectrum of a GeSn laser. Inset shows a schematic of the laser. (b) Output spectrum of the laser as a function of excitation power. Inset shows the output spectrum as a function of temperature (S. Wirths *et. al.*, Nat. Photonics 9, 88–92 (2015)).

The fourth approach uses a novel material system GeSn [29]. These lasers are also directly epitaxially grown on (001)Si. The emission wavelength, being at ~2μm, does not take advantage of the lowest dispersion point (1.3μm) or lowest attenuation point (1.55μm) of SiO_2. Due to the use of new materials, contact metals have yet not been determined. Thus an electrical device is yet to be demonstrated. The lasers demonstrated with this material system are optically excited. Figure 1.9 shows few characteristics of such a laser.

All these approaches have significantly contributed to the progress of silicon photonics, and near-IR is extremely important while discussing these devices. The work

here will also present a laser on silicon which tries to circumvent the disadvantages of various approaches as stated above.

1.2.3 Optical fiber communication

One of the most important applications of near-IR lasers is optical fiber communication. Such communication can be long distance (e.g., transatlantic fiber networks) and short distance (e.g., Google Fiber network).

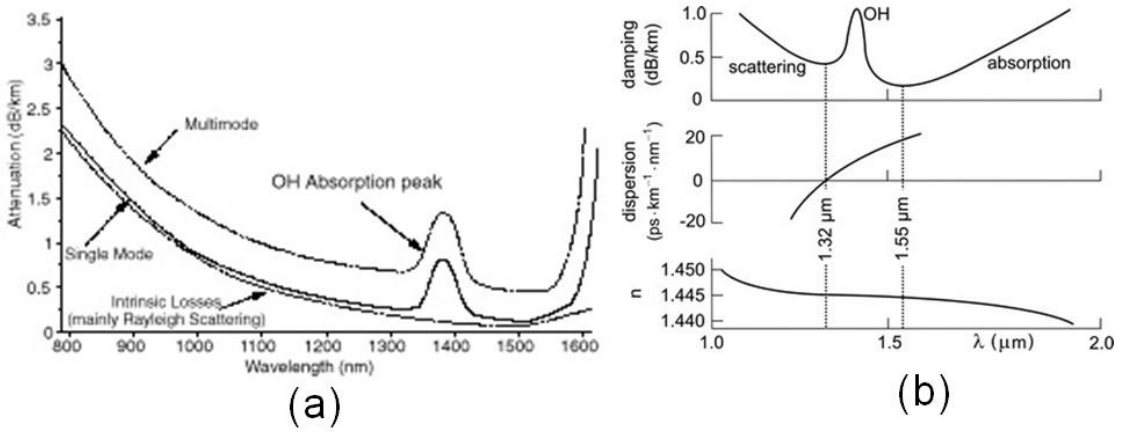

Figure 1.10 (a) Absorption spectra of different glass fibers (Courtesy of www.imedea.uib-csic.es), (b) Refractive index, damping and dispersion of glass fibers (Courtesy of www.researchgate.net).

Most fiber optic communication uses glass (SiO_2) fibers and glass has the lowest absorption at 1.55µm, and zero dispersion at 1.3µm [30] as seen from Fig. 1.10. Both of these wavelength ranges are in the infrared region, and the lowest dispersion point is in the near-IR regime. For on-chip communication, it is more important to transmit more channels in short distances. Hence the zero dispersion point is crucial for fiber optic communication again showing the importance of near-IR based light sources.

1.2.4 Medical applications

Near-IR light is invisible to the human eye making lasers emitting light in this wavelength range ideal for eye surgeries. High power near-IR lasers can still cause

damage to the human eye, but controlled lasers can be utilized for a variety of medical applications. In general, lasers are being used in a variety of medical applications [14].

1.3 Scope of III-Nitrides in Near-Infrared

The previous section shows that there are significant applications of near-IR based sources and detectors. A substantial amount of work has already been done on such optoelectronic devices. The work presented in this section focuses on such optoelectronic devices using III-nitride nanowire arrays. Since the first successful demonstration of the III-nitrides by Nakamura in 1993 [31], III-nitride research has increased exponentially and affected many types of industries. One such industry is the lighting industry, which has annual revenue of $200 billion per year. Such an increase in nitride research has significantly affected the global lighting market as seen in Fig. 1.11 (Courtesy of Professor Jasprit Singh, University of Michigan). Every day better, brighter and more efficient light sources are being designed by companies around the world.

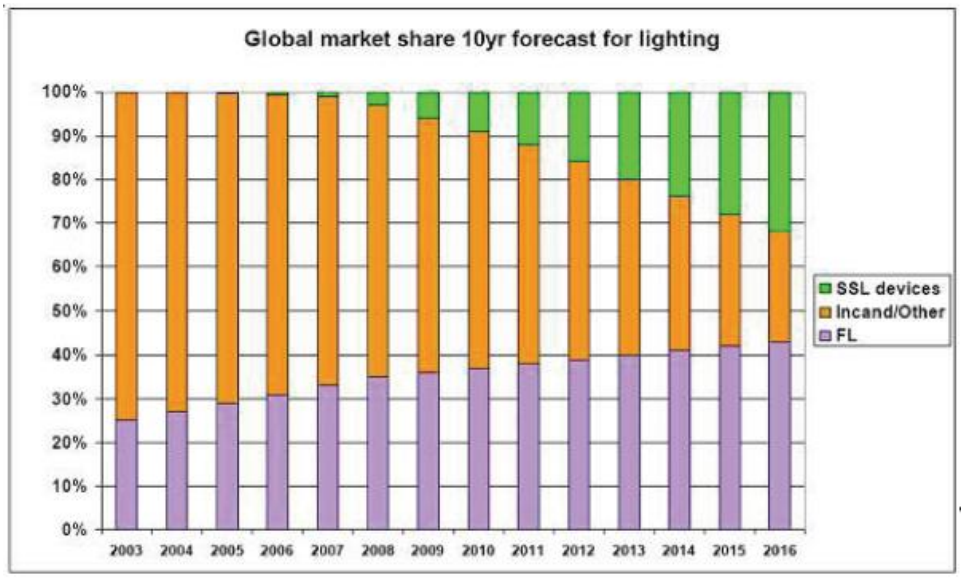

Figure 1.11 Global market share for lighting (Courtesy of Professor Jasprit Singh, University of Michigan).

Since nitride based light sources are more energy efficient [8] and nitrides hold a significant portion of the solid state lighting market, such lighting can pave the way towards a greener future and energy efficient technologies. Such a bright future would not have been possible without the continuous efforts of Professor Shuji Nakamura, Professor Isamu Akasaki, and Professor Hiroshi Amano. For their outstanding contribution to the development of nitrides, they were awarded the Nobel Prize in Physics in 2014.

Nitrides have proven to be excellent in the visible spectrum. From the bandgap energy values, it can be seen that nitrides not only can encompass the entire visible spectrum but also can be operated in the deep ultraviolet (AlN-205nm) [32] to infrared (InN-1800nm) [33] as shown in Fig. 1.12 [34]. The work presented here will focus on the InN side of the III-nitrides as InN is ideal for near-IR applications. The nitride alloys discussed in this work mainly will be either InN or InGaN with high indium (In) composition.

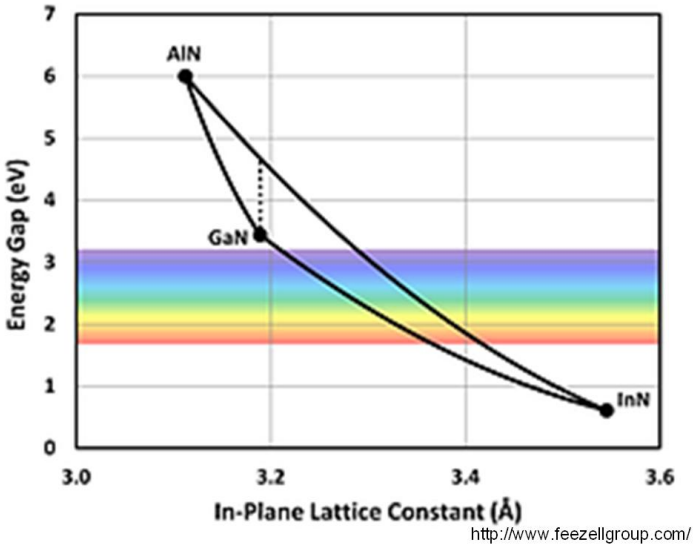

Figure 1.12 Variation of the fundamental bandgap as a function of lattice constant for the III-nitrides (Courtesy of www.feezellgroup.com).

1.4 Advantages of Nanowires over Traditional Planar Layers

All the different approaches in realizing near-IR light-emitting sources described above use planar layers. Traditionally planar layers are used for most fabrication processes. In the case for nitrides, there is a significant polarization field inherent to the materials [35]. With higher In composition the polarization field increases which reduce the electron-hole wavefunction overlap. For this reason, emission wavelengths beyond green have not been achieved by planar nitride-based heterostructures as depicted in Fig. 1.13. There has been significant research on the growth of III-nitrides on non-polar and semi-polar surfaces as well [36], but these methods have numerous drawbacks including low In incorporation and high defect densities.

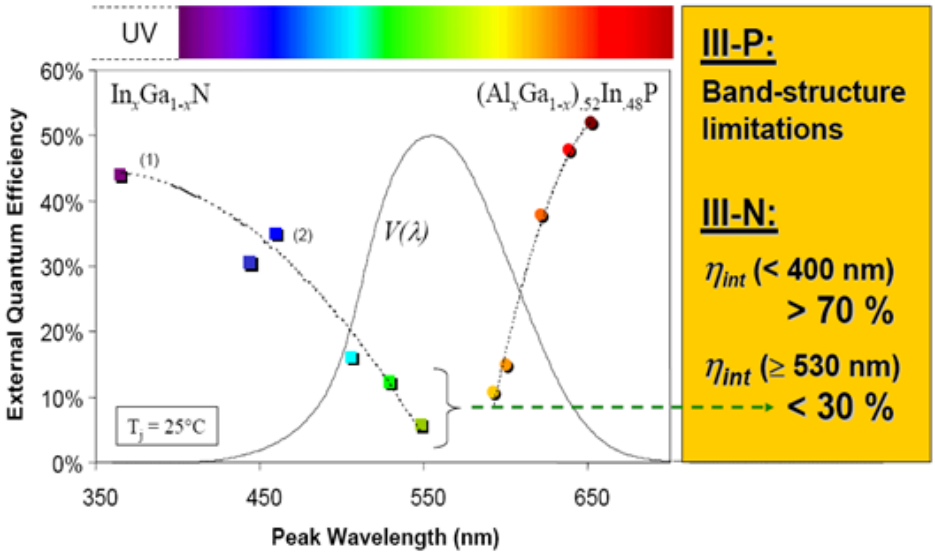

Figure 1.13 Variation of the external quantum efficiency of various material systems as a function of peak emission wavelength. (Courtesy of www.faculty.engineering.asu.edu/zhao/research/)

The appreciable built-in polarization field is not the only drawback of the III-nitride planar layers. Epitaxial Growth of free standing GaN is extremely challenging and thus commercially rather expensive. For example, a single 1″ free standing GaN substrate can cost $3,000 whereas a 4″ Si substrate costs ~$20. From this estimated prices, it can be

roughly estimated that free standing GaN substrates are ~2,400 times more expensive than Si. Hence, many GaN samples use lattice mismatched substrates, e.g., silicon carbide, sapphire, silicon. Such lattice mismatched samples generate a significant number of defects which considerably degrades the crystalline quality [37], [38].

The use of nanowires instead of planar layers can circumvent the above-mentioned disadvantages [39]. The nanowires can grow fairly independent of the substrate lattice constants and this aspect will be discussed in the next chapter in somewhat greater detail. Such substrate isolation [40] of the epitaxial nanowires results in significant improvement in optical quality as compared to their planar counterparts grown on lattice mismatched templates. Figure 1.14 shows the large surface-to-volume ratio of nanowires which reduces the number of extended defects [41] resulting in overall better crystalline quality.

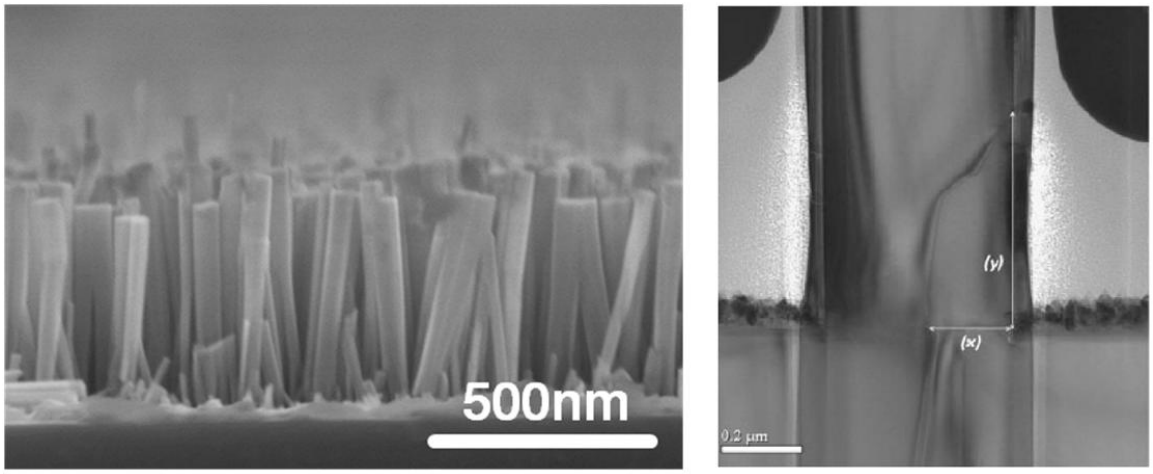

Figure 1.14 (a) Scanning electron microscope (SEM) image of a nanowire array, and (b) bending of the threading dislocations seen using cross-sectional transmission electron micrograph (XTEM) (Hersee *et. al.*, J. Mater. Res., 26, 2293, (2011)).

The next major advantage of nanowires is strain relaxation. As the nanowires grow, radial relaxation of strain during epitaxy significantly reduces the polarization field in the nanowires. For example, a green disk-in-nanowire has a polarization field of 618kV/cm

[42] compared to a blue quantum well with polarization field of 2MV/cm [35]. Such low polarization fields in the nanowires enable InGaN disks with high In composition to be inserted in the GaN or InGaN nanowires. Such a disks-in-nanowire has been shown in Fig. 1.15 [43].

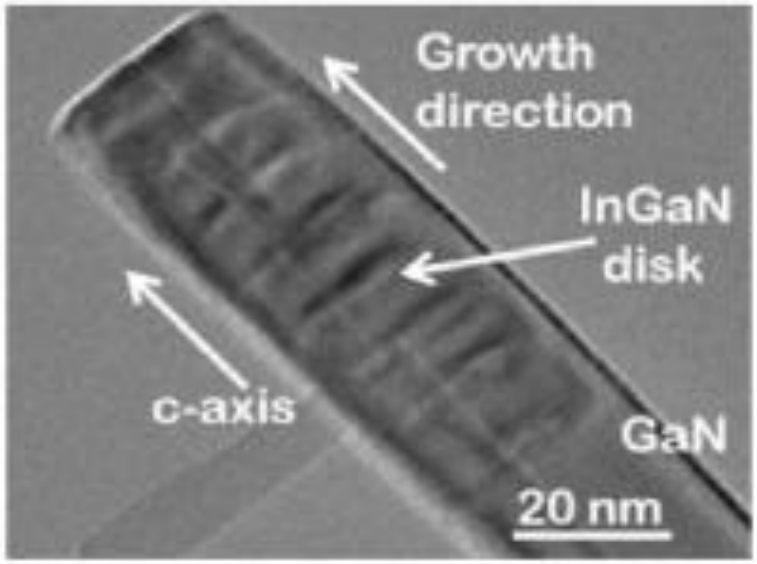

Figure 1.15 Transmission electron microscope (TEM) image of a disks-in-nanowire (Jahangir *et. al.*, J. of Quant. Elec., 50, 530 (2014)).

The emission wavelengths of the nanowires can be varied by controlling the In composition in the disks [44]. Due to the low polarization fields of the nanowires, the composition of In can be as high as 100%. Such essentially binary InN disks have been demonstrated to achieve a high radiative efficiency of ~67% [45]. The ability to incorporate disks with varying In compositions also enabled the emission wavelengths of the nanowires to be successfully tuned from blue to infrared as can be seen from the photoluminescence spectra shown in Fig. 1.16. In Fig. 1.16a, the full width half maximum (FWHM) of the GaN sample is lower than that of the InGaN samples measured under identical conditions. This may be attributed to various effects such as alloy scattering and poor crystal quality due to defect generation.

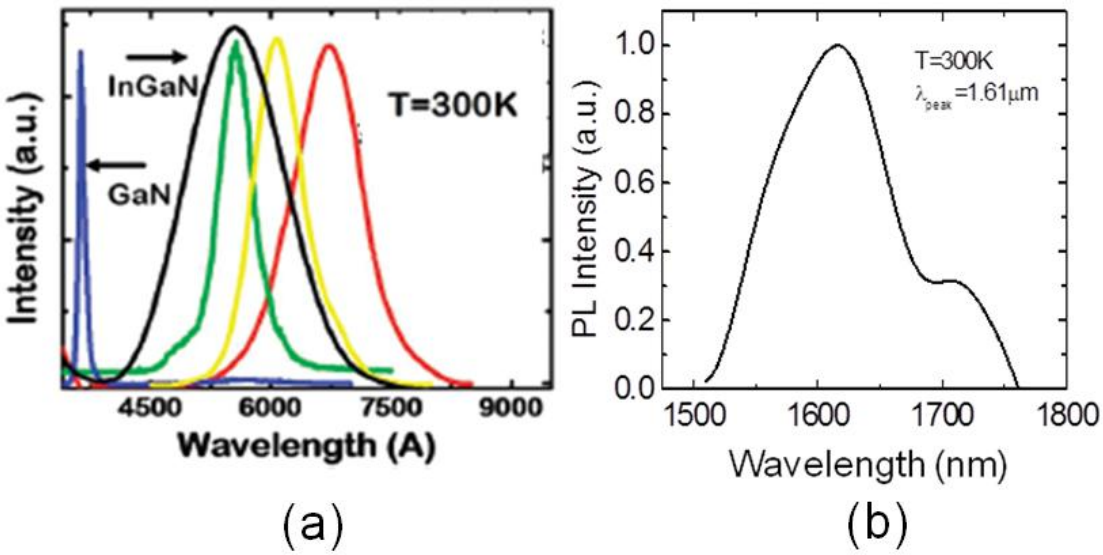

Figure 1.16 Photoluminescence spectra of the disk-in-nanowires in the (a) visible and the (b) infrared regime (Guo *et. al.*, Nano Lett., 2010, 10 (9), pp 3355–3359 (2010)).

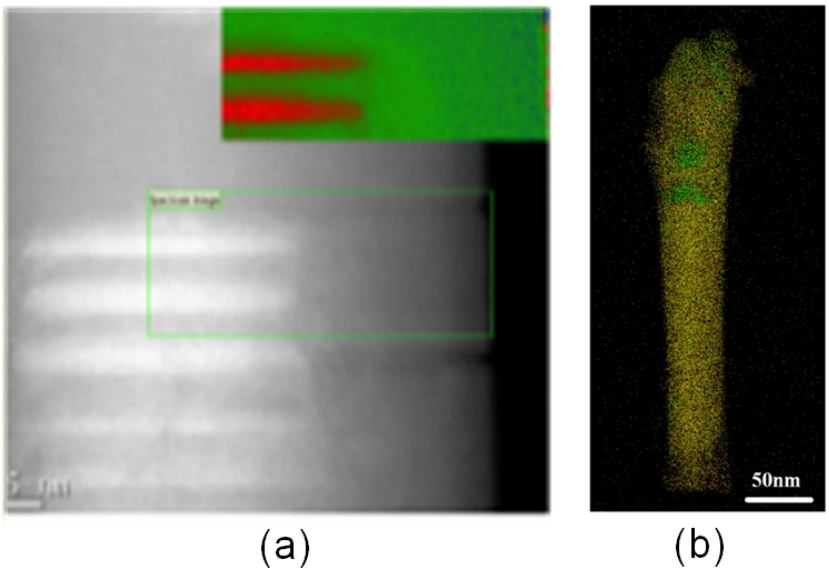

Figure 1.17 Transmission electron microscope (TEM) images of quantum dot formation in (a) $In_{0.34}Ga_{0.66}N/GaN$ (Deshpande *et. al.*, Nano Lett., 15, 3, 1647-1653 (2015)), and (b) $InN/In_{0.4}Ga_{0.6}N$ disks-in-nanowires (Hazari *et. al.*, J. Quantum Electron., 53, 4, 1-9 (2017)).

The disks-in-nanowire arrays also add a unique advantage to the nanowires as quantum dots are formed inside the disk regions, further enhancing the carrier confinement. Figure 1.17 shows TEM images that provide clear evidence of quantum dot

formation in the disk regions for both types of disks with low In composition [46], and with high In composition [45].

1.5 Photon Field Distribution and Light Propagation in a Nanowire Array

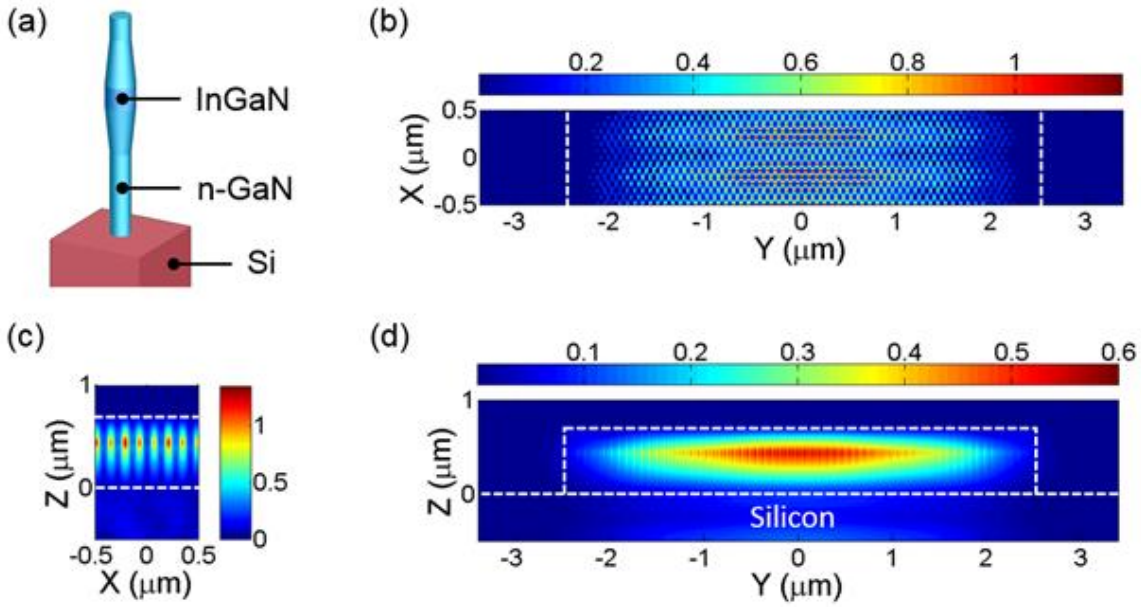

Figure 1.18 (a) Schematic diagram of the representative heterostructure nanowire considered in the 3D-FDTD simulation. (b)-(d) Calculated electric field intensity distribution in x-y, x-z and y-z planes. (Courtesy of Professor Junseok Heo, Ajou University, South Korea)

The field distribution and light propagation in the nanowire-parylene waveguide were characterized using a three-dimensional (3D) finite difference time domain (FDTD) simulation. The simulation was performed by Professor Junseok Heo at the Ajou University, South Korea and reported in [45]. The simulation was done on a nanowire heterostructure consisting of InN to closely approximate the near-IR light emitting nanowire arrays used extensively throughout this work. The nanowire waveguide was modeled as a 700 nm thick nanowire heterostructure which was embedded in a 5 μm wide parylene-on-silicon ridge with a metal contact atop. It has been reported that parylene is transparent at 1.3 μm [47]. The bulging InN active region in the individual nanowires, seen from TEM imaging, due to a change of growth temperature was

considered in the simulation as shown in Fig. 1.18(a). Such bulging will be described in detail later in this chapter. For simplicity, the diameters of GaN and InN active regions are taken to be 40 and 60 nm, respectively. The tapering of the nanowires also seen from TEM imaging has not been incorporated in the simulation, and the nanowire heterostructure is assumed to be identical throughout the array in the simulations for ease of calculation. The nanowires are positioned in a hexagonal close packed array, and the lattice constant of the array was taken to be 80nm which corresponds to a nanowire density of $\sim 2.4\times10^{10}$ cm^{-2}. Distributed feedback from the periodically positioned nanowires is not relevant because the nanowire radii are much smaller compared to the emission wavelength of 1.3μm. A periodic boundary condition was applied along the light-propagating direction (x-direction), and perfectly matched layers were chosen at the other boundaries (y- and z-directions). The calculated electric field distributions in the x-y, x-z, and y-z planes are depicted in Figs. 1.18(b)-(d) shows. The waveguide region is represented as the dotted white line.

From these simulations, it has been found that the light is localized between the nanowires in the y-z plane, because the waveguide supports a TE-like mode in which E_y and H_z are dominant. The simulation also shows a good confinement of the light in the nanowire-parylene composite waveguide which is surrounded by the top electrode and the bottom silicon substrate. The bulging InN gain region causes the nanowires to come to closer proximity, effectively enhancing the refractive index. The enhancement of the refractive index causes most of the light to be confined near the bulging InN gain region, further improving the mode confinement and reduction of the optical loss to the silicon substrate. The mode confinement is found to be 0.0134 from the simulations. The

simulation shows that light propagation in the nanowire arrays is comparable to that in planar layers. Thus nanowire arrays can be used similarly to planar layers to demonstrate optoelectronic devices. Such devices have been discussed later in this thesis.

1.6 Basic Challenges with III-Nitrides Operating in Near-IR

From the above discussion, it is quite clear that III-nitride-based nanowires have significant advantages over traditional planar layers. Additionally, nanowires are so far the best low-dimensional heterostructures for achieving near-IR operation using the III-nitrides. However, a few challenges have to be overcome to achieve nanowires operating in near-IR. The next chapter details the challenges encountered in the growth of these nanowires. In this section, only two basic challenges with near-IR III-nitride nanowires are discussed briefly. The first challenge is the low desorption temperature of InGaN alloys with high In composition, and the second challenge is the high radial growth rate of these In rich alloys.

1.6.1 Low desorption temperature

InN has a low bandgap (~0.7eV) and consequently a low desorption temperature [48], a fact that applies to any In-rich III-nitride alloys. Hence a high growth temperature will cause all adatoms to desorb, and consequently the crystal will not form. All the crystal growths in this work have employed a plasma-assisted molecular beam epitaxy (PA-MBE) system [49]. Sufficient growth temperature is required for such surface kinetics driven growth to get high quality crystal. Thus, a rather low substrate temperature will generate defects and poor crystal quality. Such opposing growth requirements cause the epitaxy of near-IR emitting III-nitride InGaN nanowires with high

In composition to be extremely challenging. To overcome the growth challenges, the growth parameters have to be carefully determined. Effectively, the growth window becomes smaller than the corresponding growth windows for growth of visible light-emitting nanowires. Further the metal fluxes along with the nitrogen flow rate have to be accurately calibrated. Figure 1.19 shows a visual representation of the growth surface kinetics (Courtesy of www.archive.cnx.org). The optimized growth parameters for successful growth of III-nitrides with In rich alloys will be described in detail in the next chapter.

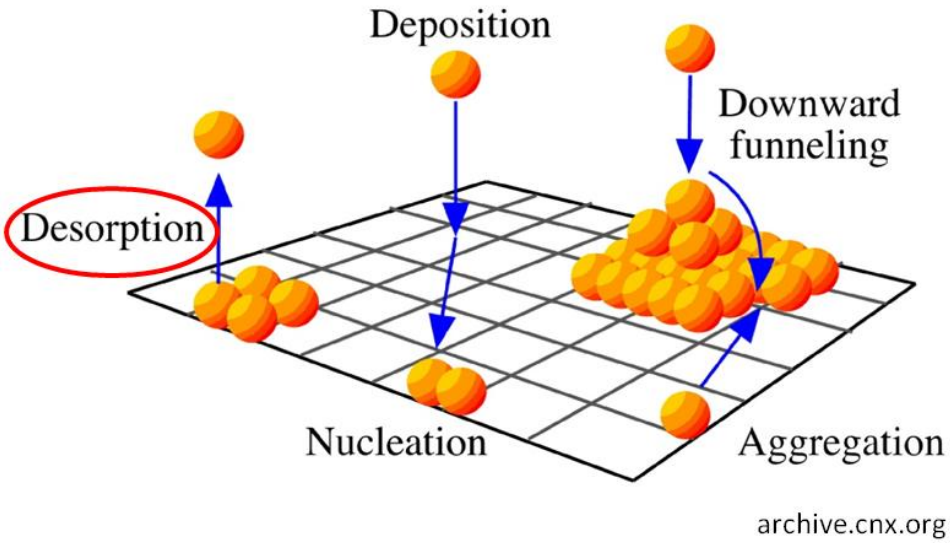

Figure 1.19 Surface kinetics in molecular beam epitaxy growth (Courtesy of www.archive.cnx.org).

1.6.2 High radial growth rate

The use of low desorption temperature and high In to group III ratio significantly enhances the radial growth rate [50]. A high radial growth rate can cause severe coalescence of the nanowires which can degrade crystal quality. To circumvent this problem, In rich alloys are grown with much lower group III fluxes as compared to gallium (Ga) rich alloys. The group III fluxes used in near-IR emitting nanowires are

almost one order of magnitude lower than that of visible wavelength emitting nanowires. The use of such different growth parameters does prevent the coalescence of nanowires but result in unique nanowire shapes. Coalesced nanowire arrays along with nanowire arrays devoid of any coalescence are shown in Fig. 1.20 (SEM image of Fig. 1.20(b) is courtesy of Lifan Yan, Millunchick Group, University of Michigan). The exact growth parameters for near-IR emitting nanowires along with their structural and optical characteristics are discussed in detail in the next chapter.

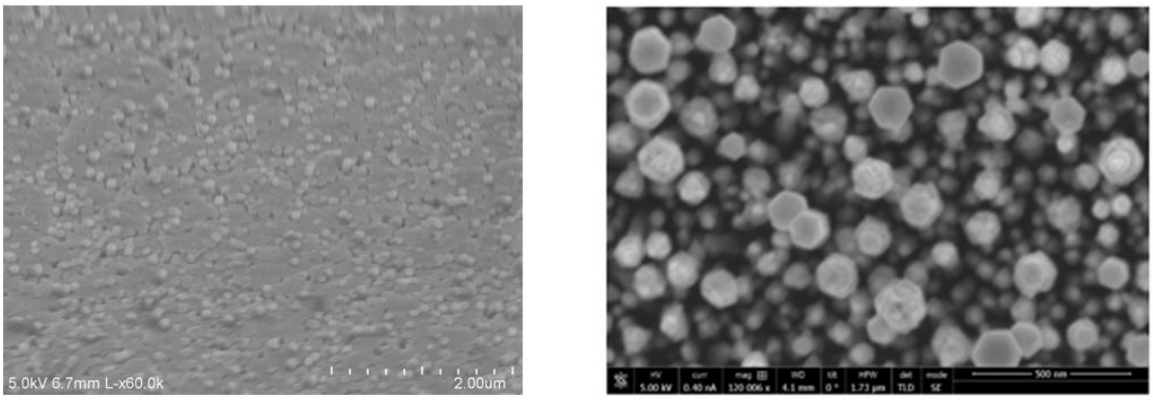

Figure 1.20 Scanning electron microscope (SEM) image of (a) coalesced and (b) coalescence free In-rich nanowires (SEM image of (b) is courtesy of Lifan Yan, Millunchick Group, University of Michigan).

Even with these unique growth parameters, the In-rich disks do show higher radial growth-rate compared to that of the low In-based barrier regions [45] which have already been predicted theoretically [51]. Both the theoretical [51] and experimental results [45] are shown in Fig. 1.21 (TEM image is courtesy of Lifan Yan, Millunchick Group, University of Michigan). The bulging of the disks region adds an additional advantage to the heterostructure array by increasing the transverse optical mode confinement [45].

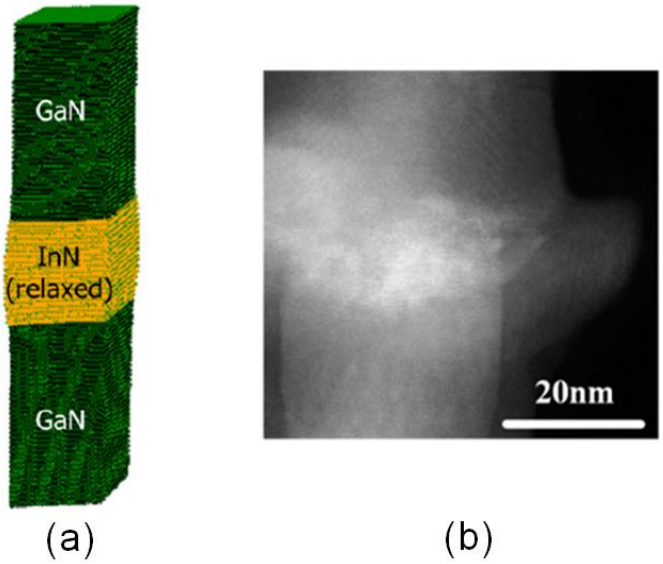

Figure 1.21 Bulging of the In-rich disk region as deduced from (a) theoretical calculations (Merrill et al., Superlattice Microst., 52, 946-961, 2012.) and (b) experimental studies based on transmission electron microscopy (TEM). (Hazari et. al., IEEE J. Quantum Electron., 53, 4, May 2017) (TEM image is courtesy of Lifan Yan, Millunchick Group, University of Michigan).

1.7 Overview of Dissertation

The focus of this dissertation research is molecular beam epitaxy of III-nitride-based nanowires and their application toward diode lasers emitting at near-IR wavelengths. These nanowires are grown by PA-MBE directly on (001)Si and processed in a clean room environment. The nanowires are characterized in detail to understand both their optical and structural characteristics. Different optoelectronic devices, like lasers, LEDs, detectors, photonic integrated circuits, have been fabricated using these nanowires. These devices are characterized in detail using state-of-the-art measurement set-ups.

Chapter II focuses on the growth, optical and structural characteristics of the self-organized InGaN/GaN, InGaN/InGaN and InN/InGaN disks-in-nanowire arrays directly grown on (001) silicon. Detailed growth parameters of the near-IR based nanowires have been discussed. The variation of the growth parameters used for nanowires operating in the visible wavelength regimes compared to that of the near-IR wavelength regimes have

also been examined in detail. The nanowires are optically characterized by a combination of temperature-dependent, excitation-dependent and time resolved photoluminescence (PL) measurements. The radiative efficiencies, radiative and non-radiative lifetimes have been determined and the multi-peak PL spectra are analyzed in detail to understand the possible sources of various peaks and shoulders. The nanowires are also characterized in great detail using scanning electron microscopy (SEM) and transmission electron microscopy (TEM) which has enabled a detailed understanding of how growth parameters can potentially affect nanowire shapes and the consequent effects on device performance. The densities and diameters of the nanowires are optimized to accomplish successful parylene passivation which can substantially enhance the fabrication process and improve the optical quality of the nanowires.

Due to the different lattice constants, nanowires operating at near-IR have considerably different optical constants in contrast to the visible emitting nanowires. Such optical constants have not been studied in detail in previous publications and presented a challenge in designing a nanowire laser heterostructure with good optical confinement. Detailed optical constant measurements using spectroscopic ellipsometry was performed, and the results are briefly discussed in chapter III to solve the challenge. Planar $In_xGa_{1-x}N$ ($0 \leq x \leq 0.73$) layers were grown on (001)Si to reduce error in the measurements from light scattering from the nanowire array. The planar layers are characterized using a combination of photoluminescence (PL), x-ray diffraction (XRD), scanning electron microscopy (SEM), and atomic force microscopy (AFM). The results of the spectroscopic ellipsometry have been used to design optimal device

heterostructures. More advanced heterostructures have also been studied using GaN lattice matched $In_{0.18}Al_{0.82}N$ and graded $In_xGa_{1-x}N$ alloys.

Fabrication and characteristics of optoelectronic devices based on disks-in-nanowire arrays operating at near-IR have been discussed in chapter IV. LEDs and lasers were fabricated using $InN/In_{0.4}Ga_{0.6}N$ and $In_{0.85}Ga_{0.15}N/In_{0.4}Ga_{0.6}N$ disks-in-nanowires. Lasers emitting at both ~1.2μm and ~1.3μm lasers have been fabricated and characterized. Steady-state characteristics of the lasers such as light-current (L-I) output, spectral characteristics, temperature dependence of the threshold current density, cavity-length dependence of the threshold current density were measured. Small-signal modulation measurements were also performed to determine the -3dB modulation bandwidths, resonance frequencies, differential gain and gain compression factors of the lasers. The lifetimes of the lasers were also measured. A control sample was used to measure the waveguide loss in these heterostructures.

Chapter V demonstrates a complete photonic integrated circuit with both the laser and the detector fabricated on the same chip. Each component of the photonic circuit has been fabricated and characterized separately to ensure greater detail. The nanowire arrays and individual nanowires used in this device have been optically and structurally characterized. The laser, waveguide and detector characteristics have also been described. The photonic circuit shows excellent characteristics as the detector photocurrent accurately follows the laser injection current. This chapter also discusses intersubband absorption in the disks-in-nanowires. $In_{0.34}Ga_{0.66}N/GaN$ disks-in-nanowires were grown for this purpose. Transmission and reflectance measurements have provided evidence of

intersubband absorption in these nanowires which can be used in the future to make mid-IR (MIR) or long wavelength-IR (LWIR) based detectors.

Chapter VI discusses preliminary results on growth and material characterization of dilute-antimonide III-nitride (III-N-Sb) based nanowires. Addition of antimony can lead to a red shift of the nanowire peak emission which can potentially solve the problems related to III-nitride nanowires operating in the near-IR. Possible methods to incorporate Sb in the nitrides have been explored and discussed. The grown materials have been characterized in detail using photoluminescence (PL), scanning electron microscopy (SEM) and x-ray diffraction (XRD) to understand the effects of Sb incorporation. Initial drawbacks and possible solutions have been described in detail. Preliminary data showing the possible red-shift from the addition of Sb has also been discussed.

Finally, chapter VII briefly summarizes and discusses possible future work that can follow from the research reported in this dissertation.

Chapter II

Molecular Beam Epitaxial Growth of $In_{0.85}Ga_{0.15}N/In_{0.4}Ga_{0.6}N/GaN$ and $InN/In_{0.4}Ga_{0.6}N/GaN$ Disk-in-Nanowire Arrays on (001)Silicon

2.1 Introduction

Near-IR lasers emitting beyond 1.1 μm (bandgap of Si) can be useful for silicon photonics applications as the loss due to silicon waveguides will be negligible [19]–[21]. If these lasers can be directly grown on (001) silicon, they will also be CMOS compatible making the lasers ideal for on-chip communication applications. The lasers are also eye-safe making them ideal for biomedical applications [52], [53] as well as being used in critical applications such as optical information processing [54], and plastic fiber communication systems [55], [56]. Nitride quantum well-based devices cannot be used to design such near-IR emitting lasers due to material inhomogeneity [57] and considerable strain induced polarization fields [58] present in the quantum wells. Therefore, in this study, such near-IR light emitting lasers have been demonstrated using nanowire arrays.

The nanowire laser heterostructures are epitaxially grown using a plasma-assisted molecular beam epitaxy (PA-MBE) machine [49]. The MBE machine is equipped with two gallium (Ga), one indium (In), one aluminum (Al) effusion cells. The machine also has one antimony (Sb) cracker cell and a nitrogen plasma source connected to a high purity gaseous nitrogen supply. The tool also has two dopant cells equipped with silicon

(n-dopant) and magnesium (p-dopant). The optical and structural properties of the nanowire heterostructures epitaxially grown using the MBE system and the effect of growth parameters on these properties have been detailed in this chapter.

2.2 Overview of Plasma-Assisted Molecular Beam Epitaxy (PAMBE) System

This section briefly discusses a typical molecular beam epitaxy system [49]. The term "molecular beam epitaxy" was first used in the 1970s, but the concept of MBE originates even before that. MBE distinctly differ from other evaporation systems due to their precise flux control. For example, modern MBE systems can grow with layer thickness control of the order of a half monolayer. MBE growth provides significant diversity as they are utilized in various materials system, including, III-nitride, InGaAsP system, and group II-VI materials. The system discussed and used in this work is a nitrogen plasma assisted epitaxy system shown in Fig. 2.1.

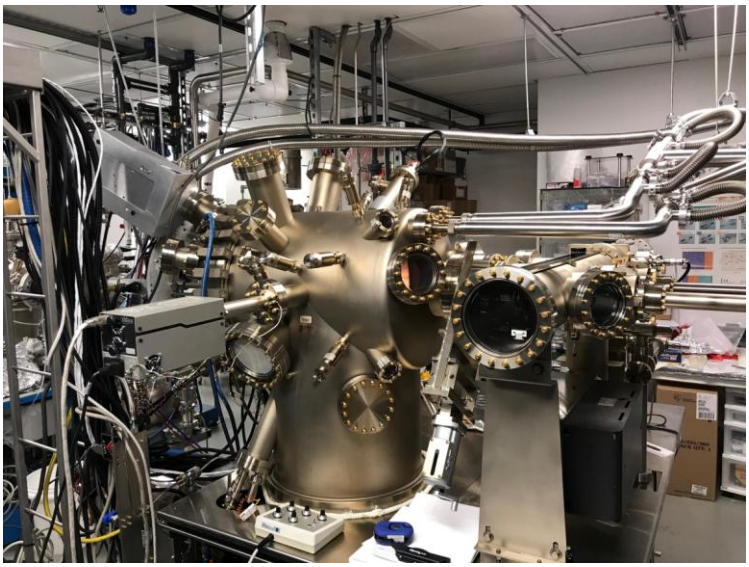

Figure 2.1 Veeco Gen II plasma assisted molecular beam epitaxy (PA-MBE) system.

MBEs have much more precise control of beam fluxes and deposition conditions. With the development of double filament metal sources (cells), the control over beam

flux has further improved. MBEs also use ultra-high vacuum conditions with lowest vacuum levels of the order of 10^{-10} Torr. These qualities ensure MBE grown material layers to have far superior optical and electrical properties than previously used vacuum evaporation techniques.

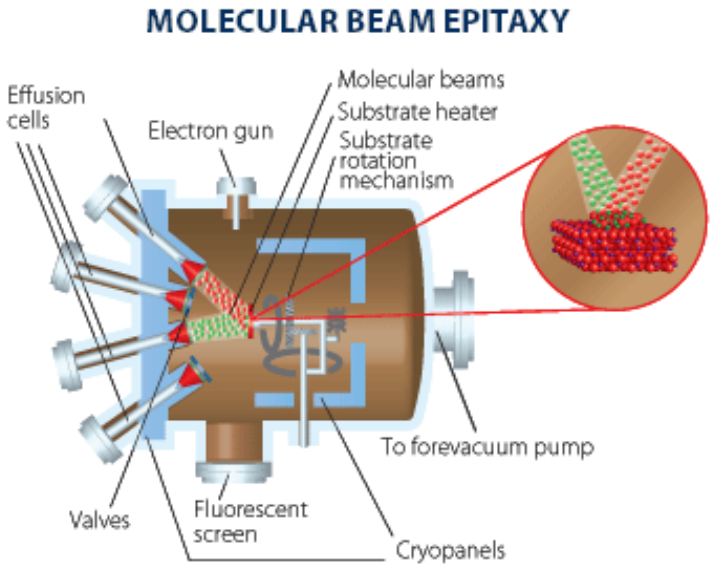

Figure 2.2 Inside of a typical MBE system (Courtesy of http://en.rusnano.com/).

Internal schematic of an average MBE is shown in Fig. 2.2. Unlike many vacuum evaporation techniques, the substrate heater can be heated to high temperatures (~1000°C) which is ideal for the epitaxy of high bandgap (e.g., AlN) materials. Typically, liquid nitrogen is used to ensure the heat is dissipated efficiently. Some parts of the MBE are also cooled with chilled water supplied from a chiller which maintains the water temperature at pre-determined values (e.g., ~20°C). The MBE, used in this work, was equipped with four double filament effusion cells with two of them containing gallium (Ga), one for indium (In), the other one for aluminum (Al), and one cracker cell containing antimony (Sb). The tool also used nitrogen plasma derived from an ultra

purity (6N) nitrogen source. The tool was also equipped with two dopant cells, silicon (Si) for n-doping and magnesium (Mg) for p-doping.

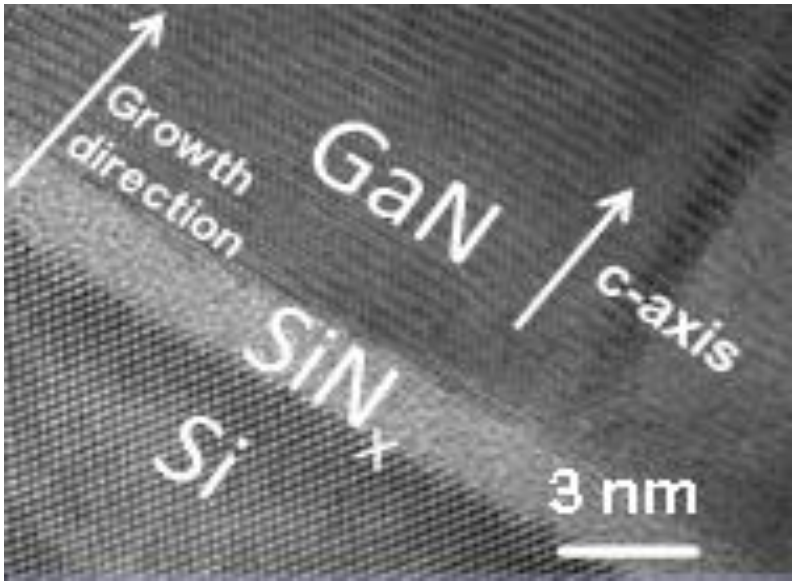

Figure 2.3 Transmission electron microscopy – high angle annular dark field (TEM-HAADF) imaging of the interface between a GaN nanowire and Si substrate (Courtesy of Professor Wei Guo, former post doctoral researcher, Bhattacharya Research Group, University of Michigan, Currently Professor of Physics and Applied Physics at the University of Massachusetts, Lowell).

Different MBE systems are capable of growing various types of materials, and even within the same material system, there is a considerable amount of diversity regarding structural characteristics. As an example, MBEs can be used to epitaxially grow different quantum structures like quantum wells, nanowires or quantum dots. Each such nanostructure has unique structural characteristics even if all of them are III-nitride-based. The presented thesis mainly focuses on nanowires though some bulk planar epitaxial layers have also been epitaxially grown and discussed. The MBE system described here is also capable of epitaxially growing on a variety of substrates, including (001) and (111) silicon, free-standing GaN, GaN-on-sapphire templates, GaN-on-Si templates, sapphire, and SiC. The work here focuses on epitaxial growth directly on

(001)Si although (111)Si substrates have also been used to calibrate the growth temperatures. The optimized growth parameters will be discussed in more detail later in this chapter. Growths related to wet oxidation work, discussed in the next chapter, were done on GaN-on-sapphire templates.

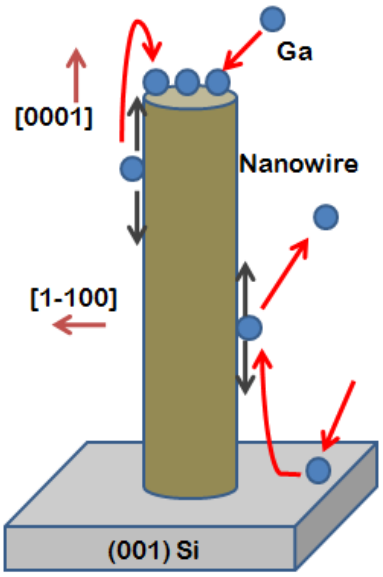

Figure 2.4 Nanowire growth mechanisms (S. Jahangir, "III-Nitride self-assembled nanowire light emitting diodes and lasers on (001) silicon," Dr. Diss. Univ. Mich., 2015).

The nanowire growths are performed at a nitrogen plasma rich environment. The metals (Ga, In, Al) impinge on the surface while keeping high substrate temperatures. For a typical GaN nanowire growth, substrate temperatures are maintained as high as 820°C. The temperature is calibrated from (1×1) to (7×7) transition seen from the heated surface of (111)Si [59], [60]. These transitions are observed using reflection high-energy electron diffraction (RHEED) pattern. The RHEED is also built-into the MBE system. At the beginning of the growth a thin (2-3nm), non-uniform, amorphous layer of SiN_x grows on the Silicon substrate shown in Fig. 2.3 [40], [61]. The SiN_x layer forms as the Si-N bonding is more favorable than Ga-N bonding. The SiN_x layer is crucial for nanowire growth as it removes the epitaxial requirement of Si from the III-nitride nanowires and

also generates a stress field which helps in the formation of the initial Ga clusters. The nanowires start growing from these initial Ga clusters.

The nanowires grow due to material adatoms impinging from three directions shown in the Fig. 2.4. The adatoms impinge on the top surface of the nanowires, nanowire sidewalls and on the Si substrate. The adatoms impinging on the Si substrate later diffuses to the nanowires. Fastest growth occurs on the lowest energy (0001) GaN facet which helps in the formation of the shape resulting into nanowires.

2.3 Epitaxial Growth of Near-IR Light Emitting Laser Heterostructures

Two different laser heterostructures were grown to achieve emission wavelength beyond 1 μm. The first structure consisted of $In_{0.85}Ga_{0.15}N$ disks as the active region and the second structure involved InN disks. Both the heterostructures are shown in Fig. 2.5(a) and (b). The cladding and barrier layers are kept same for both layers in contrast to the active region. These monolithic InGaN/InGaN disks-in-nanowire array p-i-n heterostructures (Fig. 2.5(a)) were grown on n-type (001)Si by plasma-assisted molecular beam epitaxy (PA-MBE). The resistivity of the Si wafers ranges from 0.001-0.005 Ohm-cm. The average thickness of the silicon wafers is 585 μm. The Si substrate was cleaned with a hydrofluoric acid solution and then cleaned using standard solvents (Acetone and IPA) to remove any surface oxide and surface impurities. Inside the MBE, the substrates were thermally degassed in two steps of 200°C for 60 minutes followed by 450°C for 60 minutes to reduce surface contamination. Finally, in the MBE growth chamber, the substrate was heated at 900°C for 60 minutes which again removes any native oxide on the surface of the substrate.

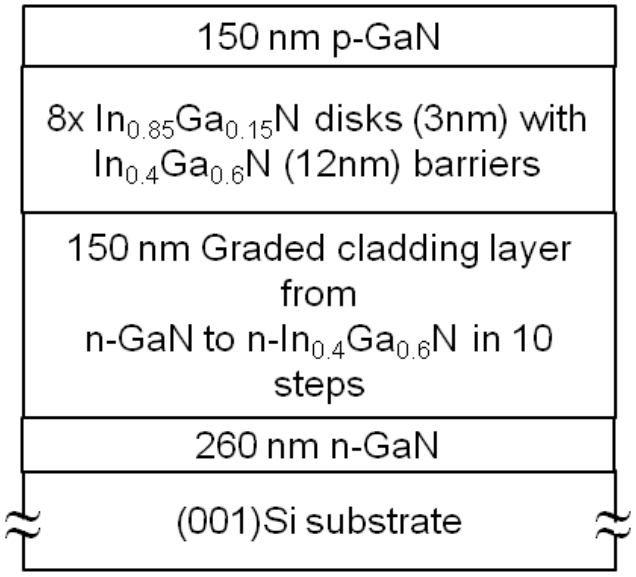

(a)

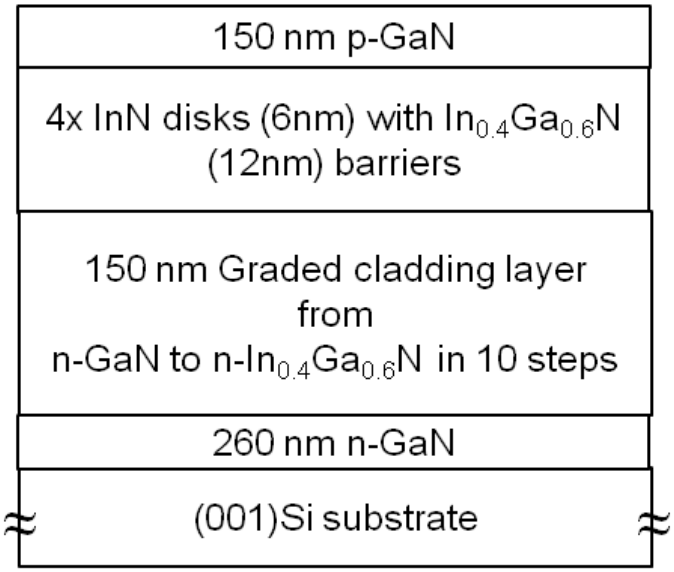

(b)

Figure 2.5 Full laser heterostructure incorporating (a) $In_{0.85}Ga_{0.15}N$ and (b) InN disks-in-nanowires emitting at near-infra red.

The growth was carried out in a nitrogen plasma rich environment with a fixed nitrogen plasma flow rate of 1 sccm. Firstly, 260 nm of Si-doped n-type GaN nanowire was grown followed by the growth of a n-type 150 nm graded cladding layer. The graded layer was started from GaN and ended to $In_{0.4}Ga_{0.6}N$ in 10 equal 15nm steps. The steps

uniformly increased with thickness, e.g., GaN to $In_{0.04}Ga_{0.96}N$ and then $In_{0.04}Ga_{0.96}N$ to $In_{0.08}Ga_{0.92}N$. Then eight pairs of undoped $In_{0.85}Ga_{0.15}N$ (3nm) disks/ $In_{0.4}Ga_{0.6}N$ (12 nm) barriers were grown which is the active region. After that, a 150 nm Mg-doped p-type GaN layer was grown. A substrate temperature of 819°C was used to grow the n-doped GaN region under nitrogen rich conditions with a Ga flux of $1.17x10^{-7}$ Torr. The substrate temperature was then varied from 819°C to 631°C to grow the n-doped graded layer. Throughout the graded layer, the Ga and In fluxes were fixed at $1.1x10^{-7}$ Torr and $4.03x10^{-8}$ Torr, respectively. The substrate temperature was lowered to 442°C for the growth of the InGaN disks. The disks were grown at a In flux of $6.04x10^{-8}$ Torr and a Ga flux of $2x10^{-8}$ Torr. The substrate temperature was kept constant at 442°C for the InGaN barriers, but the In and Ga fluxes were changed to of $3.01x10^{-8}$ Torr and $1.1x10^{-7}$ Torr, respectively. Then the substrate temperature was increased to 800°C for the growth of the p-GaN region. The p-GaN was grown with a Ga flux of $9.63x10^{-8}$ Torr. A higher Mg flux was used to increase the p-doping level at the final 20nm of the p^{+}-GaN layer.

For the heterostructure shown in Fig. 2.5(b) the active region consists of InN disks which were epitaxially grown at a substrate temperature of 433°C. The InN disks were grown at a In flux of 4.01x10-8 Torr and barriers were grown at a In flux of $1.35x10^{-8}$ Torr and a Ga flux of $4.01x10^{-8}$ Torr. All other layers were grown similarly as the previous heterostructure which consisted of $In_{0.85}Ga_{0.15}N$ disks. The average growth rate was determined to be 400 nm/hour from scanning electron microscopy measurements. As InN is a binary material, the growth of InN can be performed at varying substrate temperatures and the In flux can be varied in a wide range. InN materials are grown with high In flux and high substrate temperature behave quite

differently compared to InN grown at low In flux and low substrate temperature. The difference in the photoluminescence (PL) will be described in the later sections of this chapter.

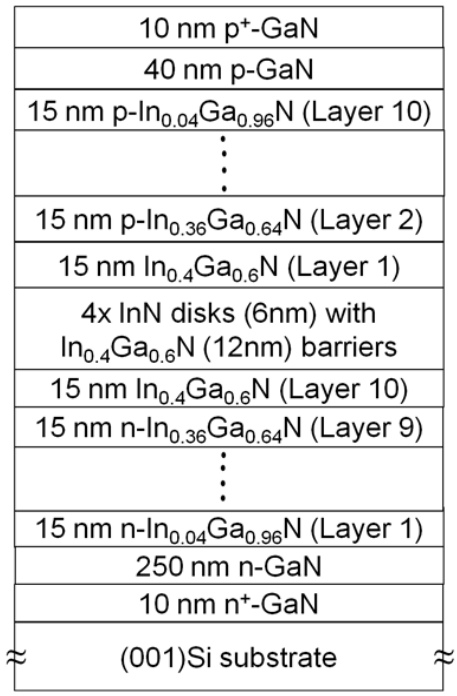

Figure 2.6 InN disks-in-nanowire based Full laser heterostructure incorporating graded cladding layer on both sides.

To further enhance mode confinement a graded cladding layer on the p-side was also included. Figure 2.6 shows this type of heterostructures. This p-doped graded layer was grown at different substrate temperature than the n-doped one but the thickness was kept same at 150nm. The change of grading is also kept uniform as the n-doped graded layer. The substrate temperature was varied from 778°C to 600°C. Here also the Ga and In fluxes were fixed at 9×10^{-8} Torr and 3.51×10^{-8} Torr, respectively.

The growth temperatures are quite low which reduces desorption significantly thus the metal fluxes have to be calibrated carefully. Such low-temperature growths have

also resulted in fascinating heterostructures which will be discussed in detail in the following sections.

2.4 Photoluminescence measurements

Temperature dependent, excitation dependent and time resolved photoluminescence (TRPL) were carried out on the disk-in-nanowire half-laser heterostructures, which were only grown from the n-GaN till the end of the active region. Such half heterostructures ensured absence of unwanted absorption of the excitation light in the p-GaN and p-doped graded layer. The excitation light was mainly absorbed in the active region resulting in accurate optical characterization.

The samples were mounted in a closed loop He cryostat and excited non-resonantly by a frequency tripled Ti:Sapphire laser (hν = 4.66eV). Temperature dependent (from 20K to 300K) photoluminescence (PL) spectra of the $In_{0.85}Ga_{0.15}N/In_{0.4}Ga_{0.6}N$ disk-in-nanowires are shown in Fig. 2.7.

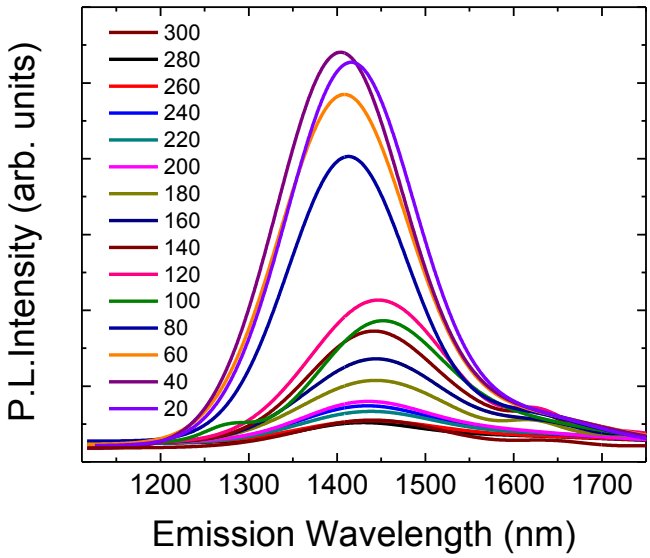

Figure 2.7 Temperature-dependent photoluminescence spectra from $In_{0.85}Ga_{0.15}N/In_{0.4}Ga_{0.6}N$ disks-in-nanowire arrays.

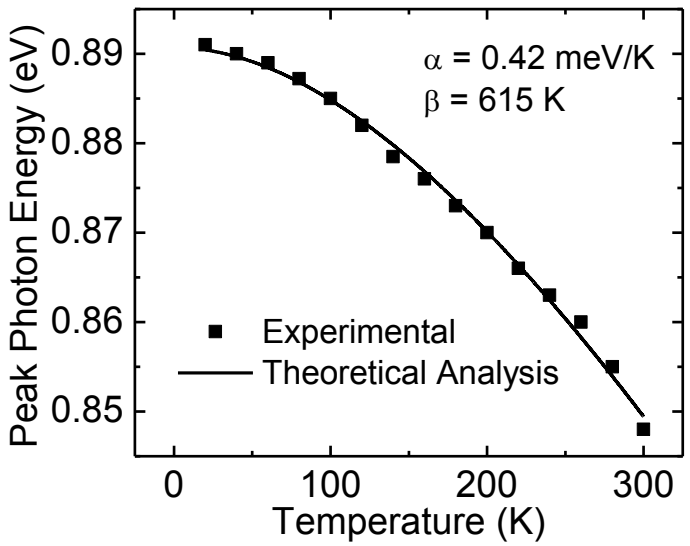

Figure 2.8 Variation of the emission peak of the $In_{0.85}Ga_{0.15}N/In_{0.4}Ga_{0.6}N$ disk-in-nanowire half laser heterostructure with temperature.

The peak energies in the PL spectra, shown in Fig. 2.7, are analyzed with the Varshni equation [62] with increasing temperature, shown in Fig. 2.8. The Varshni's equation is given below,

$$E_g(T) = E_g(0) - \frac{\alpha T^2}{\beta + T} \qquad (2.1)$$

where $E_g(T)$ is the bandgap which is a function of temperature (T) and α and β are analysis parameters. Further information has been extracted by analyzing the photoluminescence spectra peaks from which a value of α and β can be derived. The Varshni plot in Fig. 2.8 can be analyzed with the parameters α = 0.42 meV/K and β = 615 K. These values match well with the theoretically calculated values [63]. The curve does not show any significant S-shape behavior [64], [65]. Typically, such S-shape behavior is attributed to multiple phases and clusters present in the material. Similar plots to that of Fig. 2.8 for quantum well based materials show strong S-shape behavior [64], [65] exhibiting strong material drawbacks.

Figure 2.9 shows the Arrhenius plot [66] of the measured variation of the integrated PL intensity with temperature. Activation energy values of E_1 = 23.6 meV and E_2 = 173.0 meV were determined from the overall temperature dependence. These values were obtained by analyzing the plot using the following equation,

$$I(T) = \frac{I_0}{1+\alpha_1 \exp\left(-\frac{E_1}{kT}\right)+\alpha_2 \exp\left(-\frac{E_2}{kT}\right)} \qquad (2.2)$$

where E_1 and E_2 are activation energies, k is the Boltzmann constant, T is the temperature in Kelvin, α_1 and α_2 are analysis parameters, I(T) is the PL intensity at temperature T and I_0 is the PL intensity at 0K.

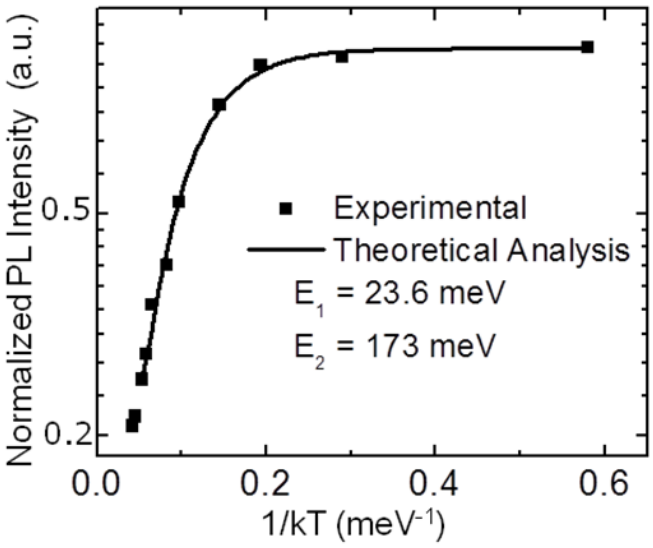

Figure 2.9 Variation of the integrated photoluminescence intensity with the inverse of electron volt equivalent of temperature.

The value of X_A exciton binding energy matches well with the value of E_1. The quenching of luminescence can be explained from the de-activation of the free exciton [67]. E_2 is explained using band offset values. The determined E_2 value is much smaller than the band offset values under flat-band conditions. Such deviation is explained by the presence of the polarization field in the material which can significantly reduce the

effective barrier from the ground state for electron escape by field-assisted emission or tunneling. The effective barrier can be much smaller than the band offset value and is comparable to 173 meV. Non-radiative recombination centers in the barriers or other regions of the nanowire heterostructure then cause these electrons to recombine non-radiatively. There are existing reports of deep level traps that have been identified in GaN nanowires [43]. An approximate value of the internal quantum efficiency (η_i) of 17% is derived from the ratio of the PL intensity at room and cryogenic temperatures at an excitation level of 150 kW/cm^2.

The temperature-dependent measurements were also characterized as a function of the incident excitation power. The variations of integrated PL intensity with excitation power for two temperatures are shown in Fig. 2.10.

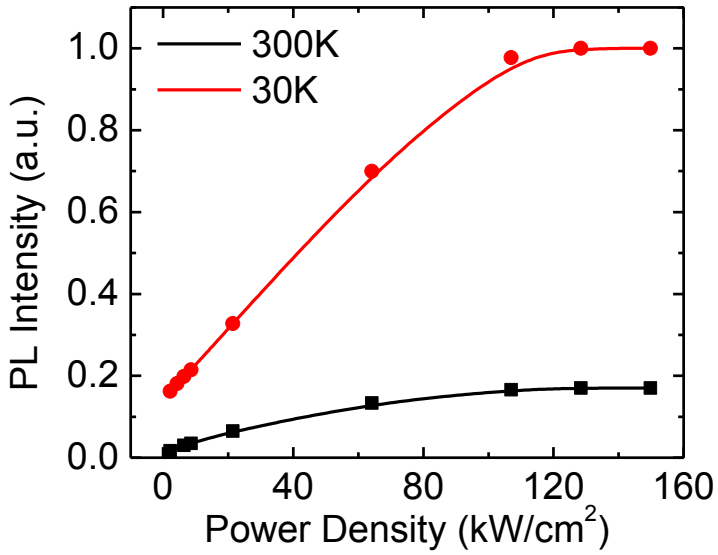

Figure 2.10 Excitation dependent PL intensity of the $In_{0.85}Ga_{0.15}N/In_{0.4}Ga_{0.6}N$ disk-in-nanowire half laser heterostructure.

In the nitride material system, due to the large polarization field for c-plane growth [58], it becomes essential to measure η_i at high injection for which the disks (or wells) reach flat band condition. At such high injection levels the polarization field is

screened. The screening of polarization field results in a blue shift with increasing excitation which is shown for room temperature in Fig. 2.11. The polarization field also causes band bending. Effects of such band bending will be discussed in the later chapters.

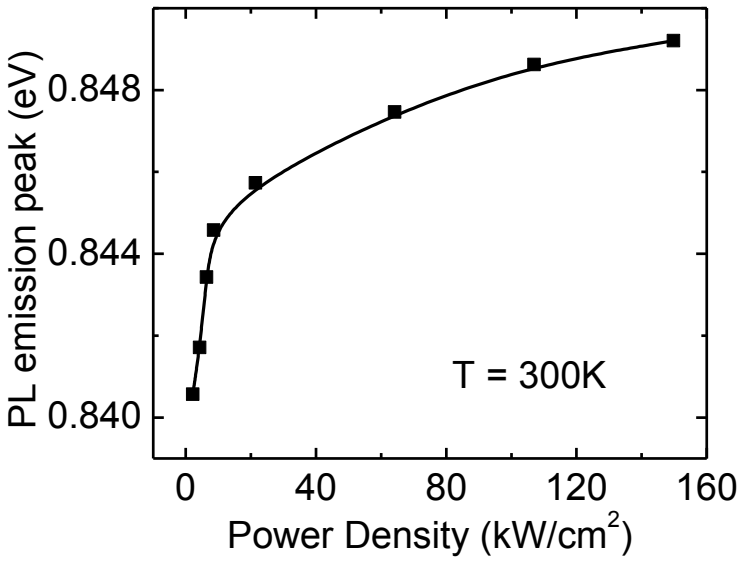

Figure 2.11 PL emission peak as a function of incident excitation power density of the disk-in-nanowire.

At low temperatures, injected carriers are confined in the localization potential of the quantum dots or in the potentials due to compositional fluctuations [68]–[70]. With increasing temperature, the carriers acquire sufficient energy to overcome the potential barriers and recombine at non-radiative recombination centers in the barrier and wetting layer regions. Hence, the ratio of the saturated peak PL intensity at 30K and 300K at high excitation powers is an approximate measure of the internal quantum efficiency (η_i). The thermionic emission of carriers and recombination in other layers at elevated temperatures may result in an underestimation of η_i. However, this effect can be minimized by measuring the dots at high excitation where the dots are saturated with carriers.

The low value of η_i was further investigated by temperature dependent time-resolved PL (TRPL) measurements performed with a 267 nm excitation provided by a mode-locked Ti-sapphire laser. A high-speed ID Quantique id220 detector was used to detect transient luminescence signal. The data were analyzed with the stretched exponential model:

$$I = I_0 \exp\left(-\left(\frac{t}{\tau}\right)^{\beta}\right) \tag{2.3}$$

where τ is the carrier lifetime, β is the stretching parameter or the clustering coefficient, I_0 is the transient luminescence signal strength at t=0 time instant, and I is the transient luminescence signal strength at time instant t.

The measured recombination lifetime τ and radiative efficiency (η_i) were used to determine the radiative and non-radiative lifetimes, τ_r and τ_{nr}, as a function of temperature shown in Fig. 2.12. It is assumed that at low temperature (20K) the value of τ_{nr} is ∞. As the temperature of the measurement increases, the ratio between the integrated intensity of the photoluminescence spectra measured at that temperature compared to 20K is taken to be η (equation 2.4). This η and τ values are used to determine τ_r and τ_{nr} (equation 2.5). The equations required to solve this is shown below,

$$\eta(T) = \frac{I(T)}{I(0)} = \frac{1}{1+\frac{\tau_r}{\tau_{nr}}} \tag{2.4}$$

$$\frac{1}{\tau} = \frac{1}{\tau_r} + \frac{1}{\tau_{nr}} \tag{2.5}$$

where τ, τ_r and τ_{nr} at room temperature are calculated to be 0.3 ns, 1.84 ns, and 0.36 ns, respectively, using this process. The inset of Fig. 2.12 shows the measured transient PL at

room temperature. The inset shows the collected data along with the multi-exponential analyzed data.

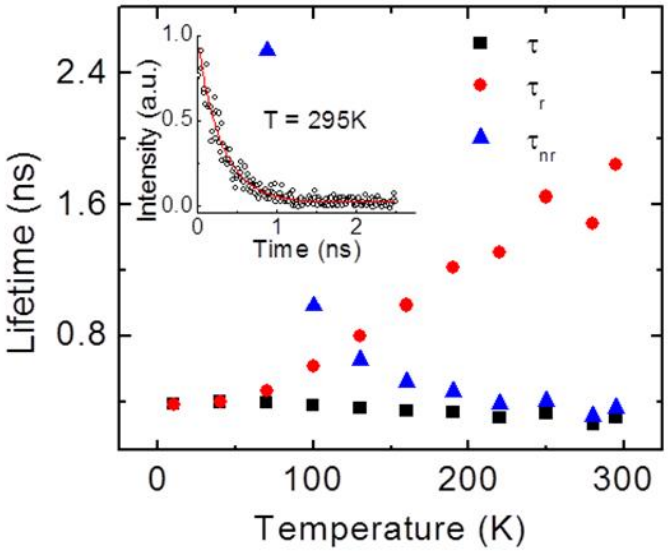

Figure 2.12 Total carrier lifetimes and the corresponding radiative and non-radiative components for an $In_{0.85}Ga_{0.15}N/In_{0.4}Ga_{0.6}N$ disk-in-nanowire sample. The inset shows room temperature transient photoluminescence and analysis with the stretched exponential model. (TRPL data is courtesy of Anthony Aiello, Bhattacharya Research Group, University of Michigan) (The data is published in Hazari *et. al.*, *Appl. Phys. Lett.*, vol. 107, no. 19, p. 191107, Nov. 2015)

The value of β at room temperature is calculated to be 0.94. The close to 1.0 β value suggests low material inhomogeneity. The defects in the nanowire and disk regions result in the low values of η_i and non-radiative lifetime. Coalescing of nanowires during epitaxy [71] can cause extended defects. Coalescing can occur due to nanowire growth misorientation or due to the increase of nanowire diameter at the low temperature of epitaxy. Such extended defects are the primary source for non-radiative deep levels [43]. There is a ~5% lattice mismatch between the disk and barrier regions which can result in additional defects. The other source of defect originate from alloy clustering [72], [73] in the disk regions due to the use of high In flux.

Photoluminescence (PL) measurements have also been carried out for the $InN/In_{0.4}Ga_{0.6}N$ disks-in-nanowire array laser heterostructures. In most cases, PL has been measured on half-laser heterostructures where the p-region is absent which removes unwanted absorption of the excitation light at the p-region. First, a low temperature PL has been shown in Fig. 2.13.

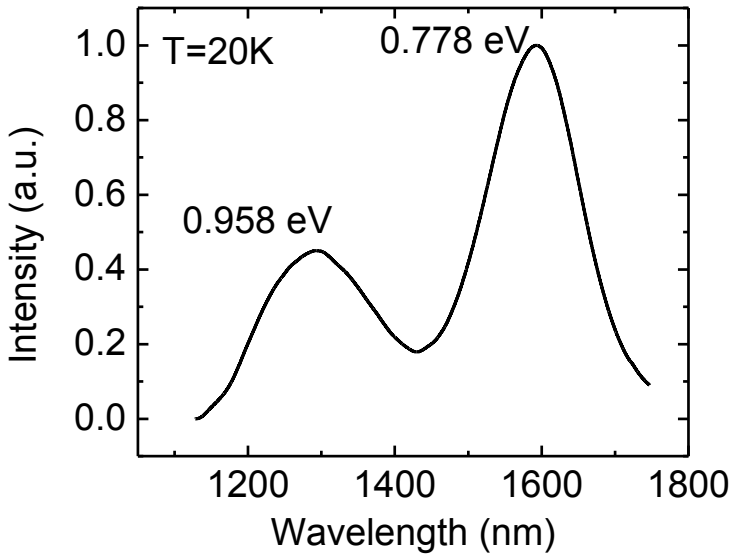

Figure 2.13 Low temperature photoluminescence spectrum of the $InN/In_{0.4}Ga_{0.6}N$ disks-in-nanowire half laser heterostructure.

The primary phase has been shown to emit at 0.78 eV (~1.6 μm), and there is also a strong second phase emitting at 0.96 eV (~1.3 μm). The second phase is probably a result of In clustering which is more dominant in such low temperature growth windows. Such multiple phases can also occur at the transition areas between the barrier and the disk. In diffusion can cause such changes of composition in between the Ga-rich barrier and the In-rich disks. The secondary phase can also be from In segregation inside the disks. The multiphase effect needs to be explored even further to determine the exact reason for the occurrence. Further optimizations have significantly reduced such multiple phase related effects and increased η_i as seen in Fig. 2.14. Here even at room temperature

photoluminescence can be observed and the multi-phase effects have also been reduced. The temperature dependent photoluminescence data has also been analyzed with Varshni's equation [62] and Arrhenius plot of the integrated intensity [66]. Such analyses have also shed light to various relevant parameters of the material as will be described in the next sections.

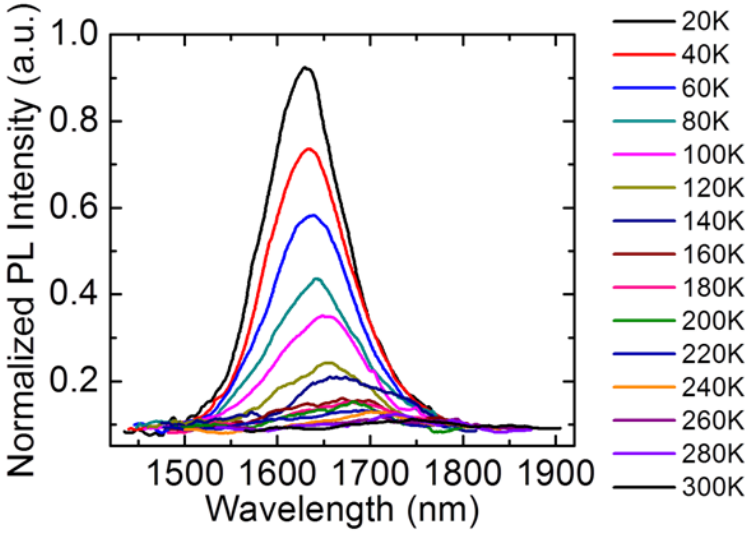

Figure 2.14 Temperature-dependent photoluminescence spectra from $InN/In_{0.4}Ga_{0.6}N/GaN$ disk-in-nanowires.

There is a blueshift observed in Fig. 2.14. The blueshift is measured by measuring the peaks at 300K which is at 1744nm (0.71eV) and at 20K which is at 1630nm (0.76eV). From these measurements, the blueshift is calculated to be 114nm as the temperature is reduced to 20K from 300K. The photoluminescence spectra do show some shoulders which can be explained similarly to the multiple phase effects observed in previous measurements (Fig. 2.13). In this case, the multiple phase effect is less severe. A Varshni plot, similar to that shown in Fig. 2.8, is shown in Fig. 2.15. From Fig. 2.15, α and β values of 0.37meV/K and 418K have been derived, respectively. The values again match other reported values for InN [63] proving the growth was successful. For comparison, in

bulk InN α and β are calculated to be 0.41meV/K, and 454K, respectively [63]. The blueshift of 50meV also agrees reasonably with the published data [63]. It can again be observed that there is no significant S-shape behavior demonstrating that the material does not have any serious inhomogeneity related problems. The material IQE or radiative efficiency can still be improved, and this has been further discussed in the following sections. The highest IQE achieved is 67% much higher than samples grown before the optimization of the growth parameters.

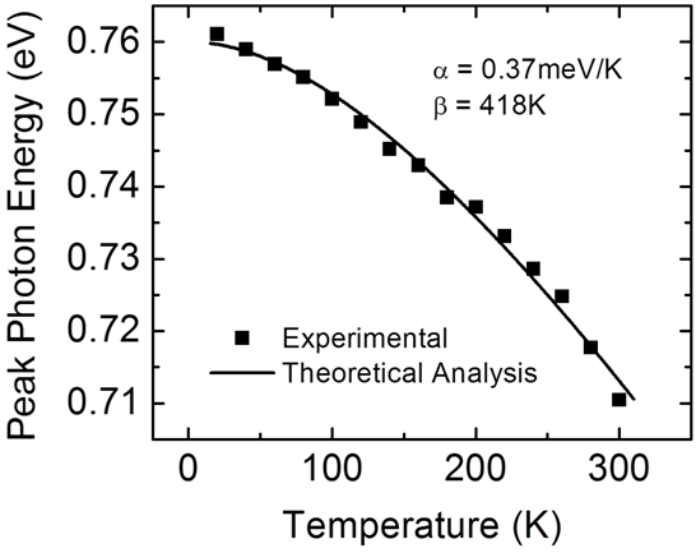

Figure 2.15 Variation of the emission peak of the InN/$In_{0.4}Ga_{0.6}N$ disk-in-nanowire half laser heterostructure with temperature.

Similar to $In_xGa_{1-x}N$ disks-in-nanowire arrays, this temperature dependent photoluminescence data can also be analyzed using equation 2.2. An analyzed Arrhenius plot of the integrated intensity has been plotted in Fig. 2.16.

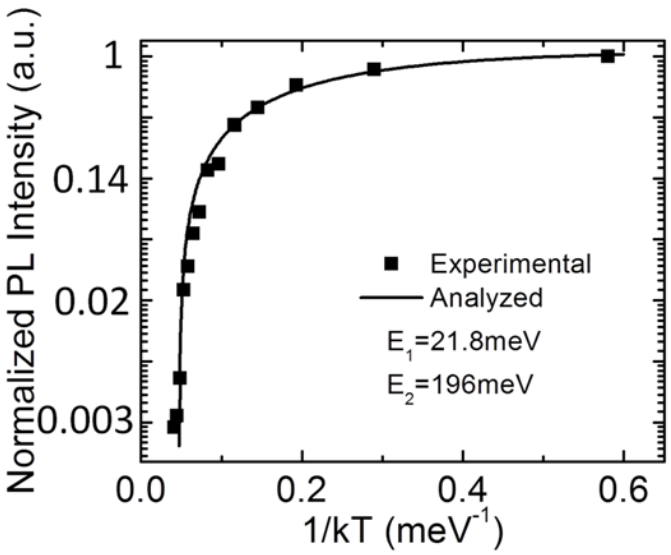

Figure 2.16 Variation of the integrated photoluminescence intensity from the $InN/In_{0.4}Ga_{0.6}N/GaN$ disk-in-nanowire with the inverse of electron volt equivalent of temperature.

E_1 and E_2 are calculated from the analysis to be 21.8meV and 196meV, respectively from analyzing the data in Fig. 2.16 using equation 2.2. Similar to the $In_{0.85}Ga_{0.15}N/In_{0.4}Ga_{0.6}N/GaN$ disk-in-nanowire heterostructure, E_1 matches well with the X_A exciton binding energy. Here also E_2 is believed to be a modified band-offset value. The low band offset value is possibly due to band-bending which is highly likely with materials that have strong polarization field, like InN. The presence of such polarization fields has also been observed from temperature dependent photoluminescence measurements. Initial time resolved photoluminescence measurements have been performed to understand the carrier lifetimes in these materials. One such measured data is shown in Fig. 2.17 which has been analyzed with equations 2.3 to 2.5. Average carrier lifetime at room temperature is determined to be ~400ps. The analysis also shows multi-exponential decay suggesting some amount of inhomogeneity. Since the clustering coefficient (β in equation 2.3) is close to 1, such inhomogeneity is not dominant in these materials.

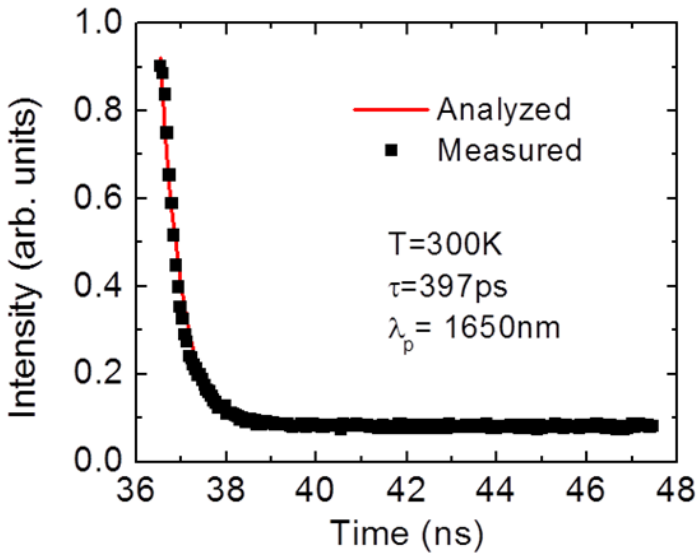

Figure 2.17 Room temperature transient photoluminescence and analysis with the stretched exponential model. (TRPL data is courtesy of Anthony Aiello, Bhattacharya Research Group, University of Michigan)

In all the samples, the InN based active regions were grown at low substrate temperature and low In flux, which reduces the possibility of coalescence and improves the nanowire uniformity. However, the low substrate temperature does reduce the material quality as MBE growth is kinetic driven. Low substrate temperature does mean low kinetic energy of the III, V adatoms on the substrate surface. Thus the adatoms have lower chances of forming good quality crystals. At such low growth temperatures, most optimized InN disk based samples have low internal quantum efficiency (IQE) of ~30%. The IQE or radiative efficiency of the disks-in-nanowire arrays had to be improved even further to achieve superior devices. Several methods were employed to achieve higher IQE. The most promising method was to grow the disks at higher substrate temperature. Higher substrate temperature would allow more surface kinetic energy to the In molecules thus forming better crystals and reducing chances of forming defects. Such results are consistent with the growth attributes of MBE systems. The high temperature growths of nanowires and their optical characteristics are described next.

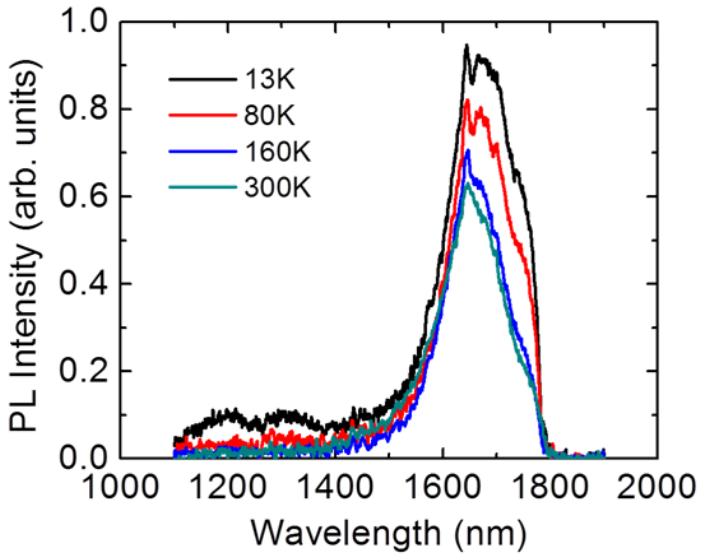

Figure 2.18 Temperature-dependent photoluminescence spectra from $InN/In_{0.4}Ga_{0.6}N/GaN$ disk-in-nanowires grown at a high In flux and high substrate temperature.

Due to the low desorption temperature of InN, the In flux was increased as well as the substrate temperature to achieve InN nanowires. As a comparison, the substrate temperature of the previous samples was an average of 433°C. For the growth of these new samples, a substrate temperature of 489°C was used. In flux was increased 2-fold, from 4×10^{-8} Torr to 8×10^{-8} Torr. As seen from the measured PL data in Fig. 2.18, the IQE has improved significantly. An IQE value of ~67% can be observed from the measured PL data. This value is more than twice the value of earlier samples. Unlike previous PL, the spectra do not show any significant blueshift as the temperature of measurement is reduced. Such pinning of the PL peak has already been reported [74] for InN. Nitrogen vacancies are thought to be the reason for such characteristics. It is possible that at such high growth temperature and high In flux, there is an increase of nitrogen vacancy, which increases background doping. The high background doping possibly pins the Fermi level thus the peak of the PL spectra remain constant with the change of measurement temperature.

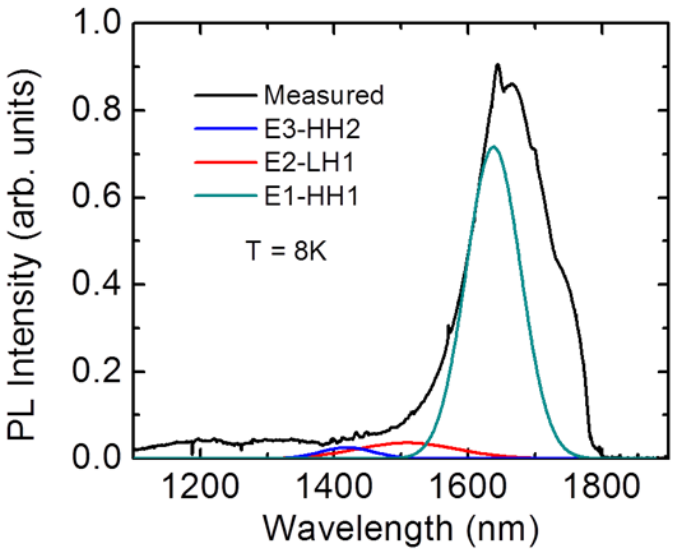

Figure 2.19 Measured low temperature photoluminescence spectrum from InN/$In_{0.4}Ga_{0.6}N$/GaN disk-in-nanowires and theoretically predicted electron-hole transitions.

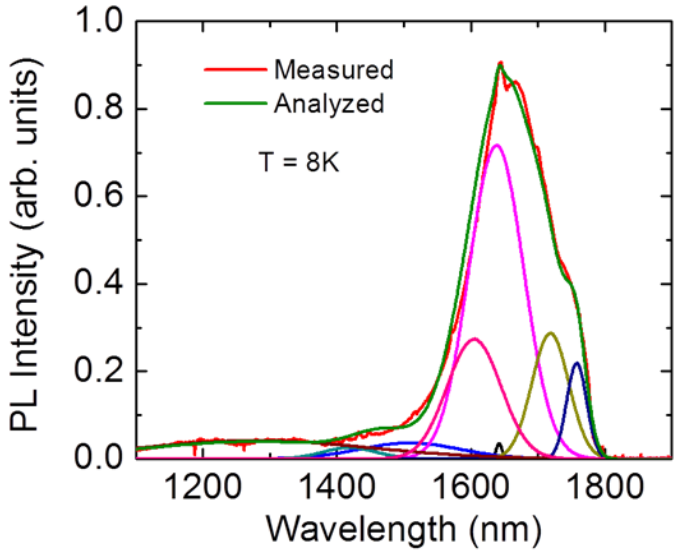

Figure 2.20 Measured and analyzed low temperature photoluminescence spectra from InN/$In_{0.4}Ga_{0.6}N$/GaN disk-in-nanowires. Five more transitions have been shown which are used to model the analyzed transition along with the main three electron-hole transitions.

The PL of this type of sample is further looked at 8K. The measured data is shown in black color in Fig. 2.19. Such low temperature high-resolution PL data exhibits multiple resonance peaks. It is expected that these resonance peaks are from various transitions due to multiple effects. It is seen from TEM images that different In

composition based quantum dots are formed in the active region of these nanowires. Such TEM images will be shown later in this work. The inhomogeneity in the quantum dot composition causes multiple transitions to take place. The PL shown in Fig. 2.19 is an ensemble of all these transitions.

A theoretical analysis of the PL data was carried out by Fu Chen Hsiao under the guidance of Professor John Dallesasse at the University of Illinois, Urbana-Champaign [45]. The analysis theoretically estimated the three main transition energies (E_1-HH_1, E_2-LH_1, and E_3-HH_2) for InN based quantum dots to be at 0.757eV (1638nm – E_1-HH_1), 0.823eV (1507nm – E_2-LH_1) and 0.874eV (1419nm – E_3-HH_2).

To further understand the different transitions observed in the low temperature (8K) PL data, another theoretical analysis was carried out in the present study. In the present study, it is assumed that in the measured data, the transitions occur at exactly in the same place as the already reported [45] calculated data. Such assumption is supported by consistent theoretical and measured results seen in previously reported data [45]. According to these three transitions, three Gaussian functions were generated, and the overlap of these three Gaussian functions was calculated. The difference between the measured PL and the convolution of the three Gaussian functions was minimized by changing the peak value, and standard deviations of the Gaussian functions. Even with the best optimized values, there was a considerable difference between the measured PL and the calculated convolution of the three Gaussian functions. To reduce this difference, five more Gaussian functions were further introduced. The total eight functions construct the analyzed PL revealing a complete picture. The entire system of eight Gaussian functions was optimized to obtain the best match between the measured and analyzed PL.

In the optimization algorithm, the peak positions of the first three Gaussian functions, corresponding to the main three interband transitions, were unchanged. The final optimized system of Gaussian functions constructed a satisfactory analyzed PL as compared to the measured PL. The measured and analyzed PL spectra along with all the eight calculated spectra can be seen in Fig. 2.20.

As can be seen, the integrated intensity of the main three peaks in 0.757eV (1638nm – E_1-HH_1), 0.823eV (1507nm – E_2-LH_1), and 0.874eV (1419nm – E_3-HH_2) reduces with increasing energy. This is expected as higher order transitions are less likely due to lower carrier population in excited states compared to ground state. The other four strong peaks (1320nm, 1606nm, 1719nm and 1759nm), which were calculated from theoretical data [63], correspond to $In_{0.82}Ga_{0.18}N$, $In_{0.91}Ga_{0.09}N$, $In_{0.95}Ga_{0.05}N$ and $In_{0.96}Ga_{0.04}N$ alloys, respectively. The alloy formation possibly originates from different quantum dots formed in the active region with different In compositions. Such dot formation is seen in TEM images shown in section 2.5.2 of this work and in previously reported data [33], [45]. A combination of In segregation, clustering and diffusion may be the reasons behind the In variation in the quantum dots. The exact origin of this variation of dot In composition cannot be fully ascertained in the present study. The fifth weak peak at 1641nm (0.76eV - $In_{0.92}Ga_{0.08}N$) may be from a disallowed transition. Different transitions, similar to the ones calculated here, have also been seen in photocurrent spectra [33], [45], [75] of nanowire based detectors, which will be discussed in chapter V. Overall these first of a kind InN based disk-in-nanowires show promising optical characteristics which will be further utilized to demonstrate optoelectronic devices. The characteristics of the demonstrated devices will be discussed in chapters IV, and V.

2.5 Structural Characteristics of the Disk-In-Nanowires

2.5.1 Characterization using SEM and XRD

Understanding the structural characteristics of these disk-in-nanowires is vital to using them to demonstrate state-of-the-art optoelectronic devices. To study the structural characteristics of the disk-in-nanowires, scanning electron microscopy (SEM), and x-ray diffraction (XRD) have been performed. XRD has also helped in determining the composition of the different layers. The nanowires were grown on (001) silicon substrate. The growth temperature was calibrated using the (1x1) to (7x7) transition [76], [77] in (111) silicon observed by reflection high-energy electron diffraction (RHEED) built into the MBE system. As-grown nanowire samples were placed on a 0° and a 45° angle mount which were then introduced into a Hitachi SU8000 to capture the SEM image of the heterostructure at an accelerated voltage of 5kV and emission current of 7μA.

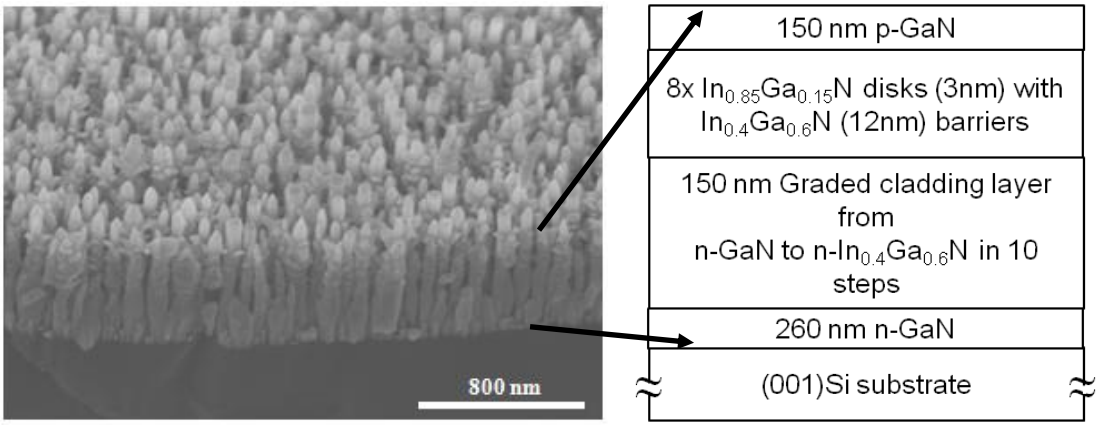

Figure 2.21 Scanning electron microscopy image (SEM) of the $In_{0.85}Ga_{0.15}N/In_{0.4}Ga_{0.6}N$ laser heterostructure with a schematic of the heterostructure shown in the inset.

Such a SEM image of the array of $In_{0.85}Ga_{0.15}N/In_{0.4}Ga_{0.6}N$ disks-in-nanowire heterostructure is shown in Fig. 2.21. The height of the nanowires was measured to be ~700nm which matches quite well with the expected values from the growth. The area density was determined from top view images using a 0° angle mount which can also

clearly show nanowire coalescence. Coalescence is harder to observe by using a 45° angle mount but the nanowire array is easier to image with this mount. It is important to note that for the isometric view (45° angle), a 1.414 multiplication factor needs to be included while measuring nanowire heights from the measurement scales. Multiple SEM images were recorded to determine the area density. Since the nanowire array is grown without any patterns, such statistical measurement is crucial to determine the correct area density of the array. The diameter and area density of the nanowires were measured to be ~60 nm and ~$3x10^{10}$ cm^{-2}, respectively from these measurements.

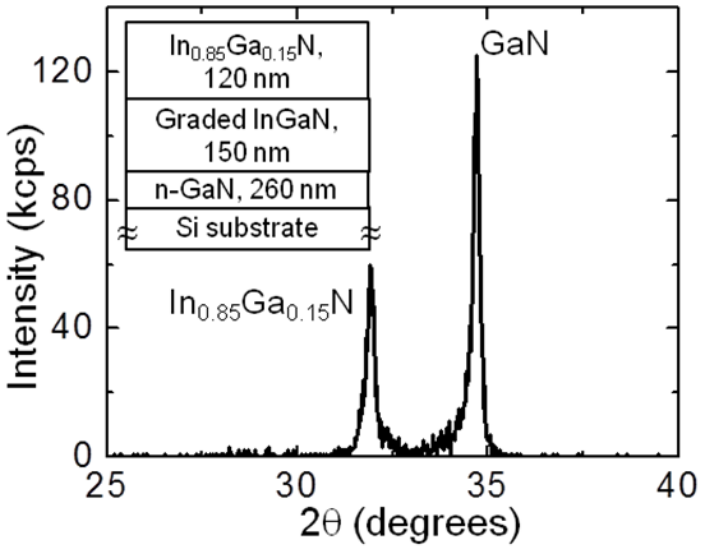

Figure 2.22 X-ray diffraction profile of 120nm $In_{0.85}Ga_{0.15}N$ layer grown on GaN and graded $In_xGa_{1-x}N$ layers (x = 0-0.4) on (001)Si substrate. Inset shows the control sample grown for the XRD measurements.

As the disk regions are very thin (3-6nm), x-ray diffraction (XRD) cannot be performed on such disk-in-nanowire sample. Hence, a separate control nanowire array sample was grown on (001)Si to confirm the alloy composition in the InGaN disk regions using XRD. This sample consisted of 260 nm Si-doped GaN. The GaN region was followed by 150 nm graded $In_xGa_{1-x}N$ (x=0 to 0.4 in 10 equal steps) layer. Then 120 nm $In_xGa_{1-x}N$ layer was grown. The $In_xGa_{1-x}N$ layer had the same composition (x~0.85) as

the disk regions of the laser heterostructures. The sufficient thickness of this region ensures strong XRD signal that can be accurately measured. Figure 2.22 shows the XRD data from this sample. The alloy peak position confirms the composition of the disk material of the laser heterostructures. Mismatch-induced defects [72], [73] are reflected from the relatively broad peak of the XRD which is due to the presence of the thick 120 nm disk material. The XRD also shows tails between the GaN and $In_{0.85}Ga_{0.15}N$ peaks which are believed to be from the graded InGaN region in the sample. The other possible source of the tails can also be alloying effects. Such alloying can happen at the interface between the $In_{0.85}Ga_{0.15}N$ and the $In_{0.4}Ga_{0.6}N$ region.

Detailed structural characterizations have also been performed on the $InN/In_{0.4}Ga_{0.6}N$ disks-in-nanowire samples. One such SEM image of a sample is shown in Fig. 2.23 along with the intended nanowire heterostructure. The growth has been calibrated to keep the nanowire area density and diameter to ~$3x10^{10}$ cm^{-2} and ~60 nm, respectively. The SEM image along with the heterostructure is shown below.

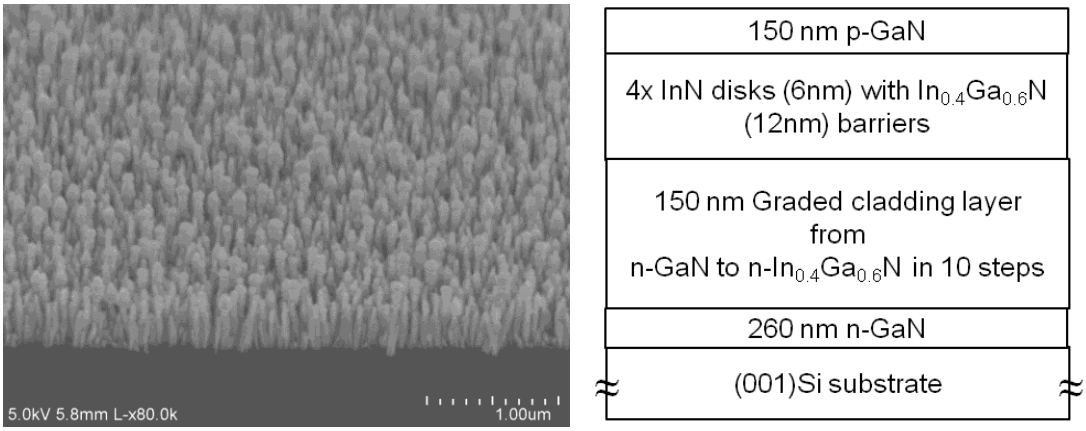

Figure 2.23 Scanning electron microscopy image (SEM) of the $InN/In_{0.4}Ga_{0.6}N$ laser heterostructure with a schematic (Right) of the heterostructure.

From the SEM images, the height of the nanowires was determined to be on an average of 640nm which again matches closely to the expected values from the growth.

For the high temperature, high flux growth the morphology has changed by some amount though the major difference is seen from the optical characterization as discussed in the previous chapter. Further investigation of these nanowires using transmission electron microscopy (TEM) has been described in the later sections of this chapter.

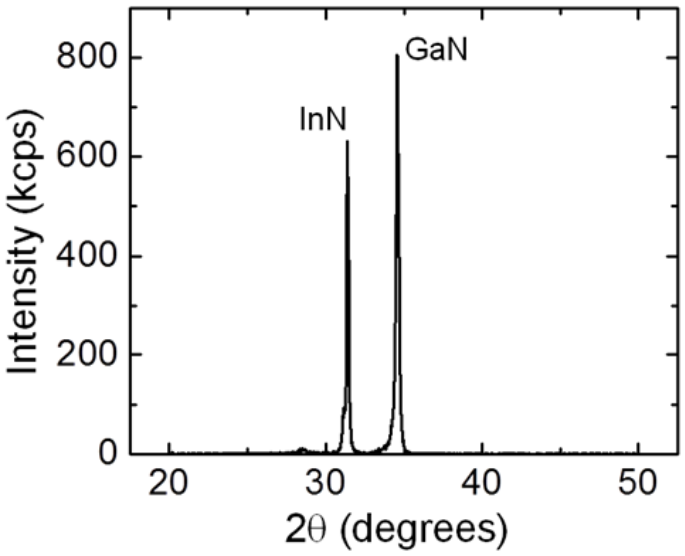

Figure 2.24 X-ray diffraction profile of 120nm InN layer grown on GaN and graded $In_xGa_{1-x}N$ layers (x = 0-0.4) on (001)Si substrate.

Following the previous method, to confirm that there is InN disk forming in the disk regions using XRD, a separate control nanowire sample was grown on (001)Si. The control sample consists of 260 nm Si-doped GaN followed by 150 nm graded $In_xGa_{1-x}N$ (x=0 to 0.4 in 10 equal steps). Finally, 120 nm thick InN was grown on top of the graded region instead of the disk regions of the laser heterostructures. The growth temperatures were kept same as the temperatures used in the nanowire laser heterostructure. This ensured fairness of the experiment as the data is compared to the disks-in-nanowire array laser heterostructures. The XRD data from this sample is shown in Fig. 2.24. The alloy peak position confirms the formation of InN [78] as the disk material of the laser heterostructures. Like in the case of the $In_{0.85}Ga_{0.15}N$ alloy, mismatch-induced defects

because of the 120 nm thickness cause the relatively broad peak. The tails observed in between the GaN and InN peaks are again believed to result from the graded InGaN region in the sample. The tails can also be due to alloying effects at the transition area of the end of the graded layer ($In_{0.4}Ga_{0.6}N$) and the InN possibly due to In diffusion. Additionally, the (001) silicon substrate peak can also be observed on the left side of the InN peak from the XRD though the peak is quite weak as the measurement was done at relatively low voltage and current. The use of low current and voltage ensured the safety of the x-ray detector. High counts on the detector translate to larger detector driving currents which can substantially and irreversibly damage the detectors. At such low voltage and current, the x-ray cannot penetrate the grown epitaxial layers and reach the substrate considerably. Hence the signal from the substrate is relatively weak.

2.5.2 Transmission electron microscopy

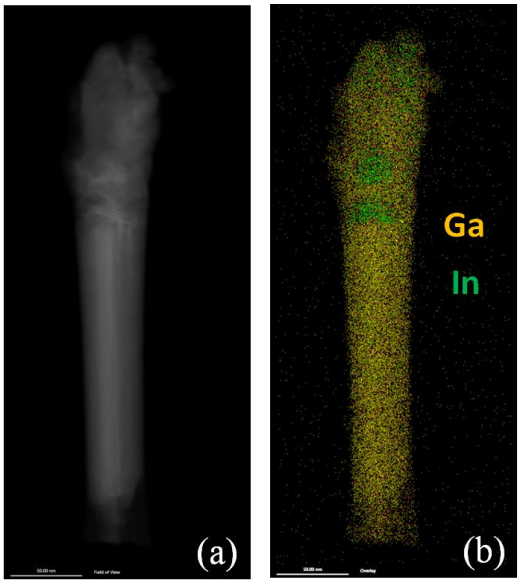

Figure 2.25 (a) HAADF and (b) EDS images of a single InN disk-in-nanowire full heterostructure. The structure does not have the graded cladding layer. The EDS images show the formation of quantum dots (Image Courtesy: Lifan Yan, Millunchick Group, University of Michigan).

To further understand the structural characteristics of the nanowires, transmission electron microscopy (TEM) imaging has been employed. The methods used in TEM are high angle annular dark field (HAADF), and energy dispersive spectroscopy (EDS) based imaging. The TEM based characterization has been carried out by Lifan Yan, under the guidance of Professor Joanna Millunchick at the University of Michigan. The first few samples on which TEM has been performed did not have the graded cladding layer. HAADF and EDS images from one such sample are shown in Fig. 2.25. Clear quantum dot formation can be observed in the EDS image (Fig. 2.26(b)). The sample was targeted for four quantum dots, but only two can be visible in the EDS image. The top of the EDS image shows some residual In. It is possible that the absence of the graded layer caused a significant stress to build up. Due to this stress field, only two disk layers could have been grown. The third and fourth disk layers disassociated and could not form due to the high stress. The residual In is possibly from these two InN disks.

2.6 Determination of the Origin of Defects from Structural Characterization

This section highlights two important origins of defects in such nanowire arrays and how these defects affect the optical quality of the nanowires. The first defect generation mechanism is the coalescence of neighboring nanowires [43], and the second one is the six-fold symmetric lateral branching, termed as “nanocrowns”, from the active regions [79]. Such mechanisms of defect generation have been carefully studied using transmission electron microscopy, near-field imaging, and cathodoluminescence. The transmission electron microscopy was performed by members of the Millunchick research group at the University of Michigan.

2.6.1 Defects from nanowire coalescence

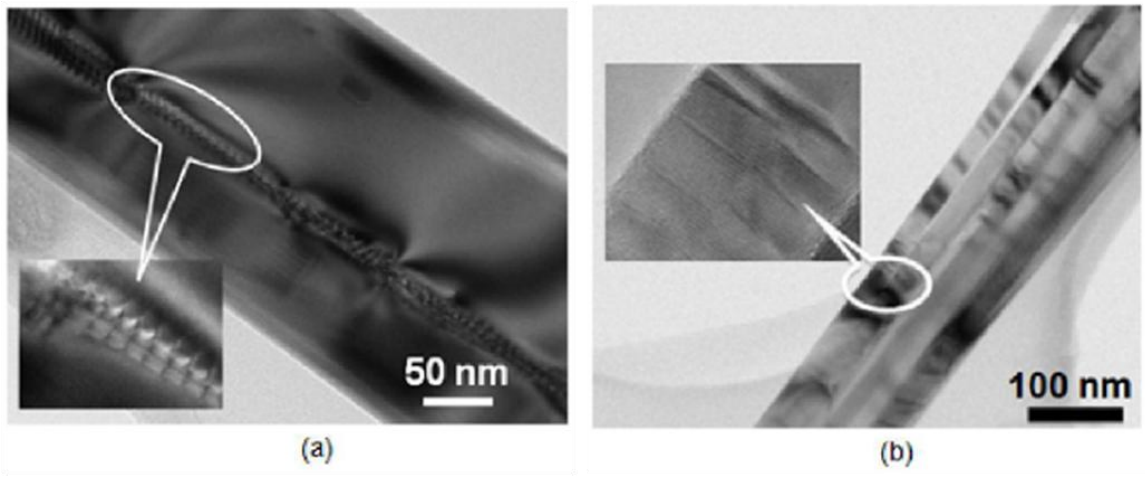

Figure 2.26 Transmission electron microscopy (TEM) images of coalesced GaN nanowires with area density of ~3×10^{11}cm^{-2}: (a) an example of chain of stacking fault defects near the boundary of coalescing nanowires at low and high magnification (inset); (b) a pair of nanowires that coalesced and a high resolution image of the defects (inset) in the vicinity of the juncture. (Jahangir *et. al.*, IEEE J. Quantum Electron., **50**, 7, 530–537 (2014)). (Image Courtesy: Millunchick Group, University of Michigan).

Earlier work has already reported coalescing of neighboring nanowires and formation of defects in high density nanowire arrays [43]. Figure 2.26 shows such coalesced nanowire arrays with area density of ~3×10^{11}cm^{-2}. The TEM images are courtesy of Millunchick group at the University of Michigan. Such coalescence can occur between nanowires due to slight misalignment or due to increase in nanowire diameters during the epitaxial growth. The coalescence becomes more enhanced if the nanowire area density is large. Nanowire coalescence causes crystallographic misorientation, which leads to formation of arrays of dislocation and stacking faults as seen in Fig. 2.26. These defects can act as non-radiative recombination centers. The defect density increases with increase in the coalescence of the nanowires, which degrades the optical quality of the nanowires. Detailed near-field imaging of visible (red) LEDs directly demonstrates such degradation of light emission, as shown in Fig. 2.27.

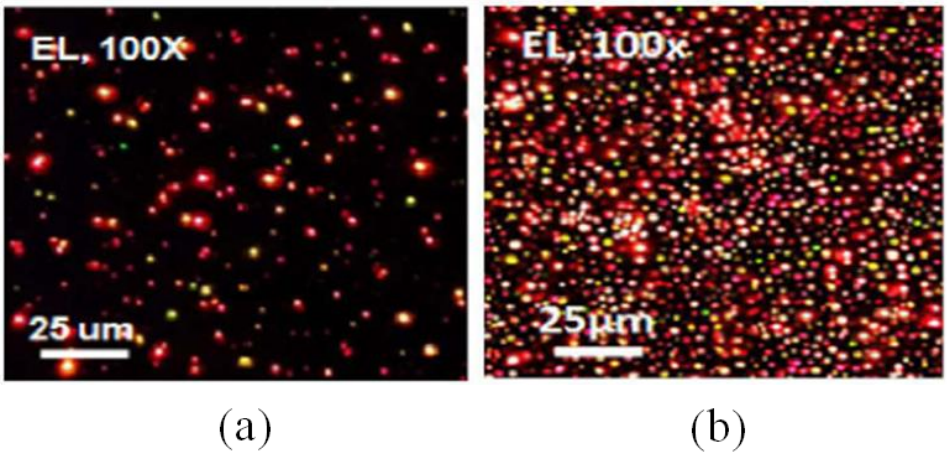

Figure 2.27 Near field image of emission from the LEDs with 100× magnification and 5V bias for LEDs having nanowire area density of (a) 2×10^{11}, and (b) 2×10^{10} cm^{-2}. (Jahangir *et. al.*, IEEE J. Quantum Electron., **50**, 7, 530–537 (2014)).

It is evident from Fig. 2.27 that as nanowire area density increases, more defects are formed due to nanowire coalescence. The increase in defects results in a reduction in the number of nanowires which actually emit light. The degradation of optical quality can also be ascertained from IQE measurements. The increase in nanowire diameter can happen due to higher metal fluxes, or low growth temperatures. Near-IR light emitting nanowires are grown at low growth temperatures which can result in large nanowire diameter, increasing nanowire coalescence. The growth parameters and IQE values of such disks are shown in Table 2.I with visible disk growth parameters and IQE values reproduced from Ref. [61].

Table 2.I. Comparison of Growth Parameters and IQE values of Different Disk-in-Nanowires

Growth parameters	Blue disks (430nm)	Green disks (540nm)	Red disks (650nm)	$In_{0.85}Ga_{0.15}N$ disks (1460nm)	InN disks (1648nm)
Substrate T (^oC)	630	590	545	442	489
In flux (BEP)	$3.4x10^{-8}$	$6.5x10^{-8}$	$1.2x10^{-7}$	$6x10^{-8}$	$8x10^{-8}$
Ga flux (BEP)	1.57x10-7	1.48x10-7	1.45x10-7	2x10-8	-
IQE (%)	48	43	41	17	67

Higher degree of nanowire coalescence due to larger nanowire diameter further increases defects and reduces the optical quality of the near-IR light emitting nanowire arrays. Such degradation in crystalline quality is directly observed from the low IQE value of 17% of the $In_{0.85}Ga_{0.15}N$ disks compared to the visible light emitting disks, tabulated in Table 2.I. In contrast, binary InN disks can be grown at relatively high temperatures and the binary nature of these disks ensures lower alloying effects. The favorable growth conditions ensure lower nanowire coalescence in the InN disk-in-nanowires. As a result, the IQE value of the InN disks is maximized to a high value of 67% with the disk emission wavelength at near-IR (1.6μm).

2.6.2 Effect of nanocrowns on optical quality

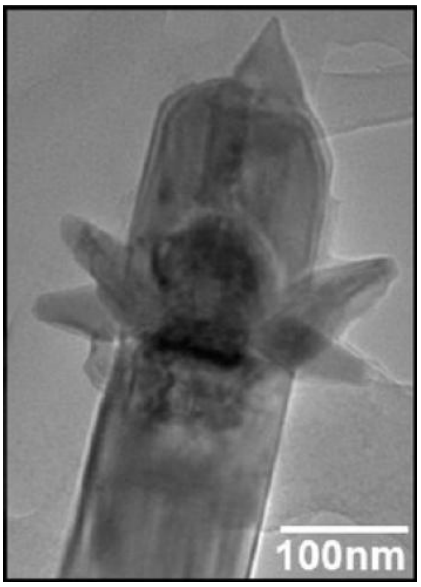

Figure 2.28 Low-magnification bright-field image of a nanocrown. (Yan *et. al.*, Nano Lett., **15**, 1535–1539 (2015)) (Courtesy of Millunchick Group, University of Michigan)

This section details effects of six-fold symmetric lateral branching, termed "nanocrowns", formed in the active region of the $In_xGa_{1-x}N/In_yGa_{1-y}N$ disk-in-nanowires and reported in [79]. A TEM image of one such nanocrown formed from a $In_{0.53}Ga_{0.47}N$ disk is shown in Fig. 2.28 (courtesy of Millunchick Group, University of Michigan). The nanocrowns are not single crystal and they nucleate as separate grains on the nanowire sidewalls. As the nanocrowns are optically inactive at room temperature, the grain boundaries of such nanocrowns can act as deep electron and hole traps, further degrading nanowire optical quality.

The formation of nanocrowns is further enhanced with higher In compositions and lower epitaxial growth temperatures. Such effect is evident from the growth parameters and variation of IQE values of the different $In_xGa_{1-x}N$ based disk-in-

nanowires shown in Table 2.I. As the In composition increases, and the growth temperature is reduced, the possibility of the formation of nanocrowns is enhanced. The IQE values reduce from 48% to a low value of 17% as higher In composition disks require lower growth temperature and higher In flux. As discussed already, unlike $In_{0.85}Ga_{0.15}N$ disks binary InN disks can be grown at relatively high temperatures. Additionally, the binary nature of the disks ensures smaller clustering effects. As a direct consequence, formation of nanocrowns in the InN disks is minimized, and such disks can be seen in Ref. [33]. In addition to the lower degree of coalescence as described in the previous section, the relative absence of nanocrowns also contributes to the high IQE value of 67% of the InN disks.

2.7 Calibration of Nanowire Density for Efficient Parylene Planarization

It is imperative to planarize the nanowires with parylene or some dielectric (e.g., Si_3N_4). Such planarization has shown to improve the optical quality of the nanowires through passivation of the surface states [43]. The parylene planarization is also useful as the nanowire-parylene composite can be treated similar to planar layers making the optoelectronic device fabrication rather straight-forward. Nanowire density needs to be within certain limits to achieve both of these merits of parylene. If the nanowire density is too high, then the parylene cannot reach the active region of the nanowires. In such a scenario, the optical quality will not improve.

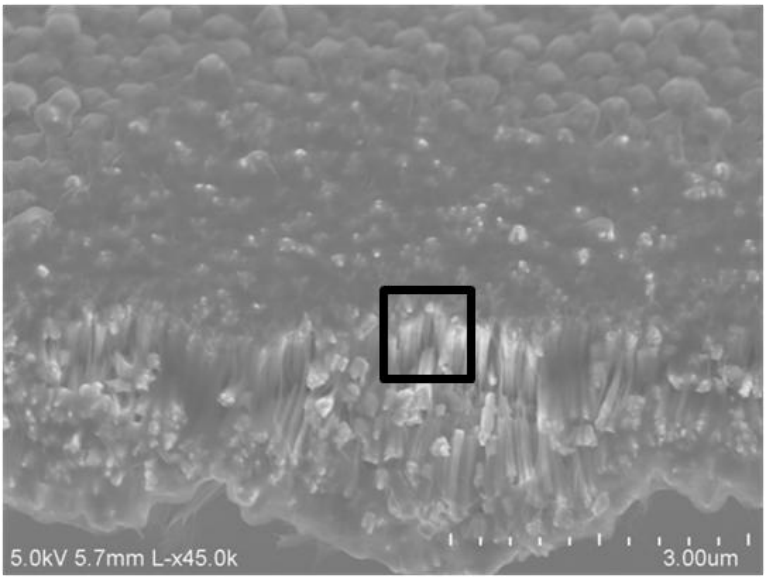

Figure 2.29 SEM image of a parylene passivated nanowire array. The parylene cannot reach the bottom of the nanowires due to the high density of the nanowires as seen in the black square.

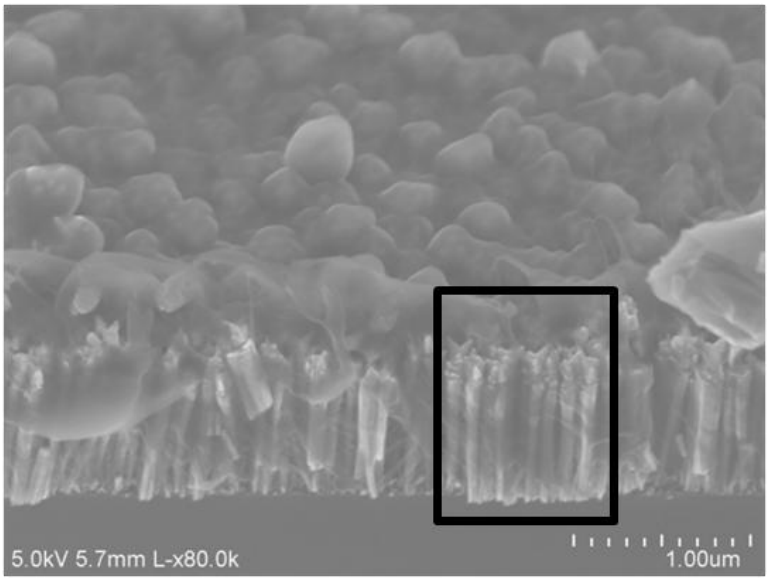

Figure 2.30 SEM image of a parylene passivated nanowire array. The parylene can be seen to cover all the nanowires.

Figure 2.29 shows a situation where the parylene cannot reach till the Si substrate. In contrast, if the nanowire density is below 3.5×10^{10} cm^{-2}, the parylene can reach all the way to the silicon substrate which is seen in Fig. 2.30. Multiple nanowire array samples were grown to measure the optimum density below which the parylene can reach all the

way to the substrates. The area densities of the nanowire arrays were varied by changing the growth temperatures. The metal fluxes were also varied to keep the nanowire diameter fairly constant throughout the entire study.

The calibration data yields a density value of 3.5×10^{10} cm^{-2} below which parylene passivation works quite well. In all the growths, the nanowire growth conditions were controlled such that the nanowire array area density is below 3.5×10^{10} cm^{-2}.

2.8 Summary

This chapter discusses in detail the molecular beam epitaxial growth and optical and structural characteristics of nanowires emitting light in the near-infrared. To summarize, disks-in-nanowire arrays (DINW) emitting light at near-infrared have been epitaxially grown and characterized. These DINWs are the first of its kind and can have far reaching potential. DINWs with $In_{0.85}Ga_{0.15}N$ as the disk material emits light at ~1.4μm and InN as the disk material emits light at ~1.64μm. Half laser heterostructures were grown to measure photoluminescence (PL). An IQE of 17% was calculated for the $In_{0.85}Ga_{0.15}N$ DINWs from the PL measurements. Two different types of InN DINWs were grown. One demonstrated an IQE of 28%, and the other showed a high IQE of 67%. Full laser heterostructures were grown using these novel materials. Temperature dependent PL, excitation dependent PL and time resolved PL were also performed to determine various characteristics of these materials, including X_A exciton binding energy, Varshni's parameters, blueshift, and different carrier lifetimes. Full laser heterostructures were also grown to perform structural characterization. SEM, TEM, HAADF, EDS, and XRD were carried out to understand various structural attributes of these heterostructures. Clear formation of quantum dots in the disks has been observed [45] which was

previously only seen in disks with low In composition [46]. The nanowire array density was optimized to ensure accessibility of parylene throughout the array, which further improved the optical quality of the nanowires. The full laser heterostructures were used to make optoelectronic devices. The nanowire-based device characteristics will be detailed in the following chapters.

Chapter III

Measurement of Optical Constants of III-Nitride Materials at Near-IR and Design of Efficient Cladding Layers for Nanowire Laser Heterostructure

3.1 Introduction

To design a laser heterostructure with emission wavelength at near-infrared (near-IR), an accurate knowledge of the optical constants, especially the refractive index of the InGaN alloys, is required. The reported values of optical constants for InGaN in near-IR wavelength range has variations [80], [81]. Additionally, there is a minimal amount of available data for the refractive indices of wurtzite InGaN alloys with high In composition emitting at longer wavelengths due to multiple reasons. The most important reason stems from the growth of the materials as the In-rich nitride alloy growth is very challenging. Most metal-organic chemical vapor deposition (MOCVD) processes cannot grow InGaN with high In composition with good optical quality. Other methods (e.g., plasma-enhanced chemical vapor deposition (PECVD), physical vapor deposition (PVD)) have also been explored for InGaN growth, but these methods cannot generate monocrystalline material. Therefore, this study uses plasma assisted molecular beam epitaxy (PA-MBE) to epitaxially grow the InGaN samples. The growth will be discussed in more detail later in this section.

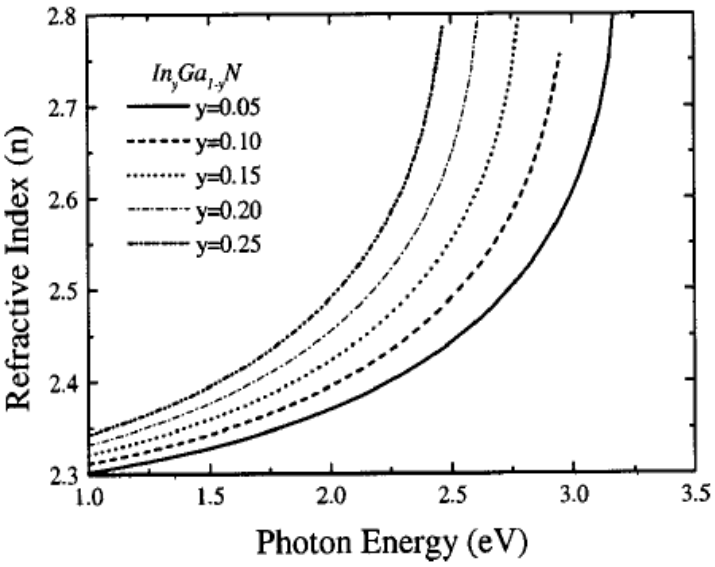

(a)

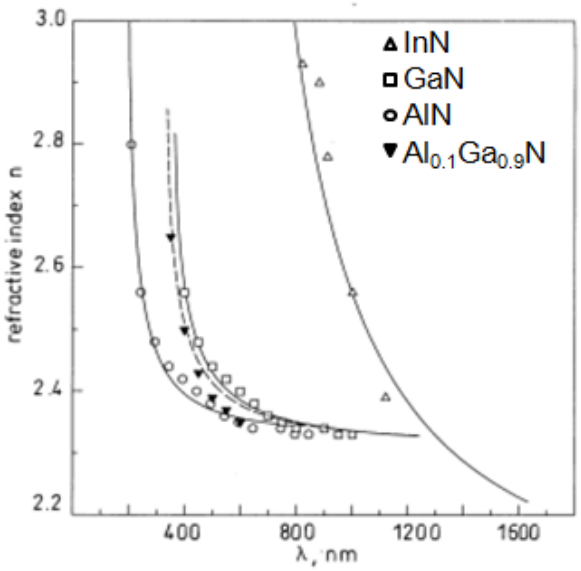

(b)

Figure 3.1 (a) Refractive index as a function of photon energy, G. M. Laws et al., *Appl. Phys. Lett.*, **89**, 1108 (2001). (b) Refractive index as a function of wavelength, Peng, T. *et. al. Elec. Lett.* **32** 2285 (1996).

The reported data in Fig. 3.1(a) extends only up to an indium composition of 25%. The indium composition needs to be beyond 80% to achieve emission wavelengths in the range of 1.3μm. The refractive indices of GaN and InGaN are depicted to converge at wavelengths of ~1.2 μm in other reports such as the one shown in the Fig. 3.1(b). If

this was the case then designing such a laser heterostructure would be impossible. Hence spectroscopic ellipsometry has been performed to determine the correct optical constants, ensuring the optimum design of the laser heterostructure.

The knowledge of optical constants of such InGaN layers has been applied to design the graded cladding layer as discussed in the previous chapter. The mode confinement properties of such graded layers will be discussed in chapter IV. This chapter also discusses epitaxial growth and characterization of $In_{0.18}Al_{0.82}N$ layers, which is lattice matched to GaN.

3.2 Epitaxy of Planar InGaN Layers on (001) Silicon for Spectroscopic Ellipsometry

It is not convenient to do ellipsometry on nanowire samples because the surface scattering can add considerable error in the data. Therefore epitaxial planar layers were grown directly on n-type (001) silicon substrates with varying composition of $In_xGa_{1-x}N$ (x = 0, 0.26, 0.43, 0.60, and 0.73) by plasma-assisted molecular beam epitaxy (PA-MBE). The background (unintentional) doping in the samples was determined from capacitance-voltage (C-V) measurements made on Schottky diodes fabricated on such planar layers. Palladium (Pd), and Aluminum (Al) were used for the Schottky diode metal contacts. The background doping measured on all the samples were n-type, and the doping concentrations are listed in Table 3.I. The doping concentrations have increased with increasing In composition which is consistent with available works on background doping in InGaN materials [82]. The average thickness of the grown layers was ~600 nm. A critical thickness of 80 nm has been determined from the lowest lattice mismatch between the (001) silicon substrate and InGaN epitaxial layer grown in this study. The average thickness of the InGaN layers is ~600 nm with the minimum being 558 nm. Thus

from the critical thickness calculations, it can be ascertained that the epitaxial layers are relaxed and relatively strain-free.

Table 3.I. Parameters of $In_xGa_{1-x}N$ Epitaxial Layers Grown on (001)Si

Sample	Substrate temperature (°C)	Unintentional doping (n-type) (cm^{-3})	Thickness (nm)	Surface roughness (nm)
GaN	747	$5.0x10^{16}$	657.5 ± 0.2	13.1 ± 0.1
$In_{0.26}Ga_{0.74}N$	518	$1.5x10^{17}$	558.2 ± 0.3	56.1 ± 0.3
$In_{0.43}Ga_{0.57}N$	470	$2.3x10^{17}$	588.9 ± 0.6	17.6 ± 0.2
$In_{0.60}Ga_{0.40}N$	438	$5.2x10^{17}$	580.1 ± 0.5	25.5 ± 0.2
$In_{0.73}Ga_{0.27}N$	415	$7.3x10^{17}$	681.4 ± 3.4	37.1 ± 0.3

Table 3.II. Metal Fluxes for InGaN Epitaxial Layer Growths on (001)Si

Sample	Ga flux (Torr)	In flux (Torr)
GaN	$2.2x10^{-7}$	-
$In_{0.26}Ga_{0.74}N$	$1.09x10^{-7}$	$7.3x10^{-8}$
$In_{0.43}Ga_{0.57}N$	$9.04x10^{-8}$	$1.21x10^{-7}$
$In_{0.60}Ga_{0.40}N$	$7.1x10^{-8}$	$1.86x10^{-7}$
$In_{0.73}Ga_{0.27}N$	$5.15x10^{-8}$	$2.51x10^{-7}$

To keep the average thickness constant among different samples which help in the ellipsometry and to maintain acceptable material quality, the growth substrate

temperature was decreased with increasing In composition. The surface roughness is negligible compared to incident wavelength for spectroscopic ellipsometry. Hence the error due to surface roughness is also negligible. The metal fluxes for the epitaxial layer growths are given in the following table 3.II. All layers were grown with a nitrogen plasma flow rate of 0.5 sccm.

These layers were characterized by scanning electron microscopy (SEM), atomic force microscopy (AFM), X-ray diffraction (XRD), room temperature and low temperature photoluminescence (PL) measurements. Such SEM and AFM images are shown in Fig. 3.2. A Hitachi SU8000 in-line cold field emission scanning electron microscope (SEM) was used for the SEMs, a Bruker Dimension Icon atomic force microscopy system was utilized for the AFMs, and a Rigaku rotating anode x-ray diffraction tool was employed for the XRD. The SEM tool has a resolution of about 1nm at a working distance of 4mm. The tool also can produce a magnification of 10^6 times. Other SEM tools have also been used. Some of these tools use tungsten filament or LaB_6 as the electron source. These sources have lower lifetimes compared to the field emission based sources. The tungsten sources have a lifetime of about ~100 hours, and the LaB_6 sources have a lifetime of about ~500 hours. The cold field emission electron microscopes' electron sources can have more than 1000 hours of lifetime. Such advanced electron sources also have a low energy spread further increasing the resolution of the microscopes.

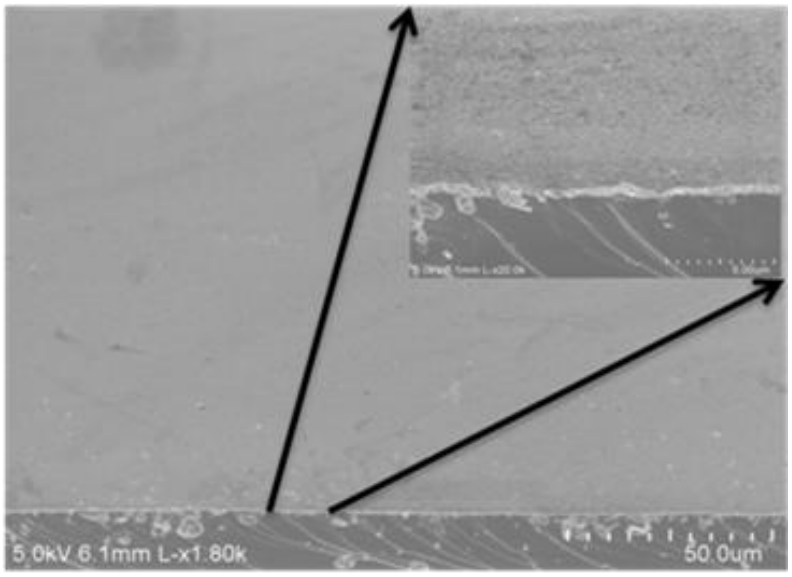

(a)

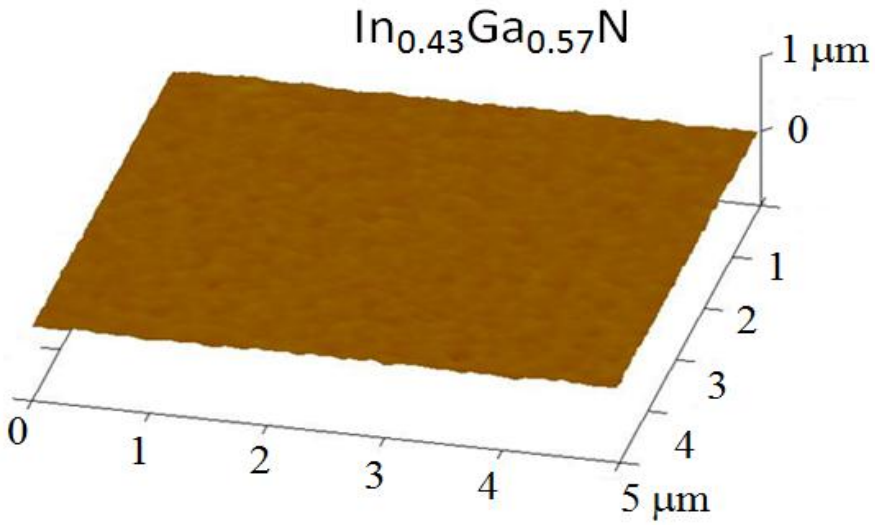

(b)

Figure 3.2 (a) Scanning electron microscopy (SEM) image of GaN epitaxial layer. Inset shows magnified area on the top layer. (b) Atomic force microscopy (AFM) image of the $In_{0.43}Ga_{0.57}N$ epitaxial layer.

The scanning electron microscopy and atomic force microscopy images show fairly flat surfaces, ideal for performing spectroscopic ellipsometry. Without the flat surfaces, incident wavelengths used for ellipsometry can suffer significant scattering which will incorporate a substantial error in the spectroscopic ellipsometry measurements.

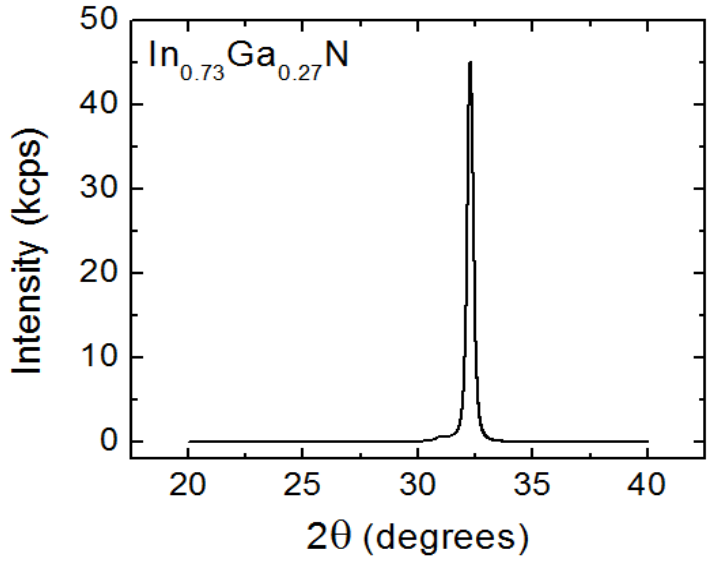

(a)

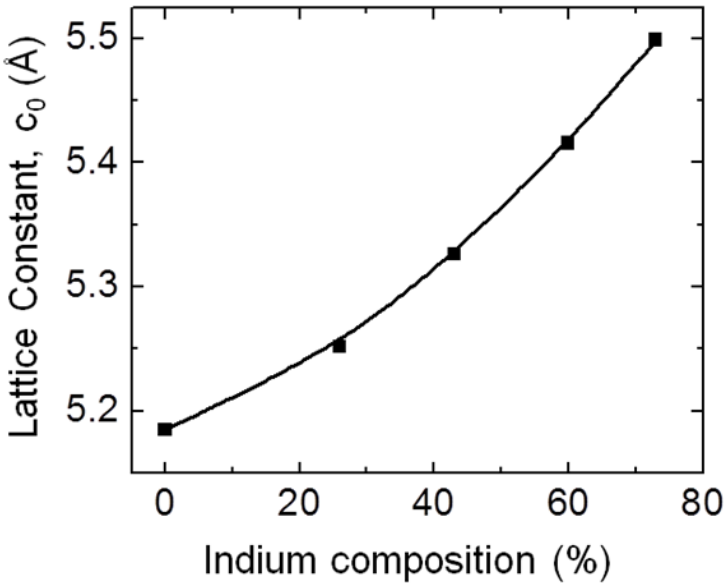

(b)

Figure 3.3 (a) X-ray diffraction profile of $In_{0.73}Ga_{0.27}N$ epitaxial layer, (b) the lattice constant as a function of indium composition.

The crystal structure type of the planar layers has also been verified to be wurtzite type, which is same as the nanowire crystal structure that grows on (001)silicon. Such verifications further highlight that the comparison between the planar layers and the nanowire arrays is fair. The crystal structure of the gallium nitride planar layer on silicon was determined by X-ray diffraction (XRD). The (002) peak of the gallium nitride layer

was observed at 17.26^{o} which closely matches to what would be expected for wurtzite gallium nitride. One such XRD profile of the $In_{0.73}Ga_{0.27}N$ alloy is shown in Fig. 3.3(a). The comparable peak in cubic gallium nitride would be at around 19^{o} [83].

Energy dispersive spectroscopy was employed to determine the alloy compositions. The dependence of the lattice constant determined by XRD on these indium compositions is shown in Fig. 3.3(b). The lattice constant variation with indium composition shows a small bowing factor described by the given equation (3.1).

$$c(x) = xc_{InN}+(1-x)c_{GaN}-0.35x(1-x) \qquad (3.1)$$

where c_{InN} is the lattice constant of InN, c_{GaN} is the lattice constant of GaN in the c-axis, and x is the In composition in the InGaN alloy.

Photoluminescence (PL) measurements were made with a He-Cd (λ = 325nm) or semiconductor diode (λ = 635nm) laser excitation and a high-resolution scanning spectrometer. Room-temperature and low-temperature PL spectra of a GaN and $In_{0.26}Ga_{0.74}N$ layer are shown in figure 3.4(a). Room-temperature PL spectra of $In_{0.73}Ga_{0.27}N$ and $In_{0.43}Ga_{0.57}N$ layers are depicted in figure 3.4(b). The PL data of the $In_{0.73}Ga_{0.27}N$ layer is courtesy of Dr. Songrui Zhao in Professor Zetian Mi's group at the McGill University, Montreal, Canada.

A blue shift of 82 meV and 90 meV are observed for GaN and $In_{0.26}Ga_{0.74}N$, respectively between room temperature and low temperature emission peaks. Such blue shift is consistent with Varshni's equation [62] and is the result of bandgap variation with temperature. The consistencies of the PL data with Varshni's equation have also been observed in InN disk-in-nanowires as described in the previous chapter. The PL peak

wavelength again confirms the composition and the wurtzite nature of the epitaxial planar layers which is consistent with X-ray diffraction data. As an example, in this work, the measured peak emission energy in the PL spectra of GaN at room temperature is measured to be at 3.38 eV matching reasonably well with the wurtzite GaN peak. The same peak for cubic GaN is identified at 3.27 eV [84].

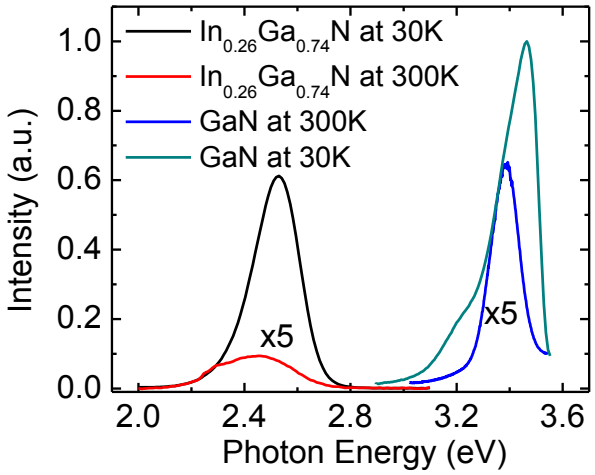

(a)

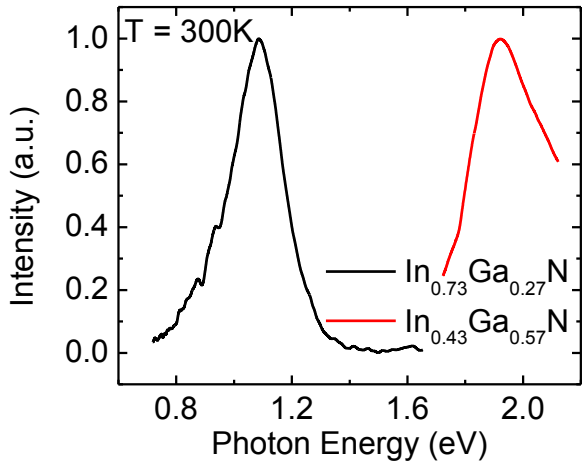

(b)

Figure 3.4 (a) Room-temperature and low-temperature PL spectra of GaN and $In_{0.26}Ga_{0.74}N$ layers. (b) Room-temperature PL spectra of $In_{0.73}Ga_{0.27}N$ and $In_{0.43}Ga_{0.57}N$ layers (The PL data of the $In_{0.73}Ga_{0.27}N$ layer is courtesy of Dr. Songrui Zhao in Professor Zetian Mi's group at the McGill University, Montreal, Canada).

The PL peak wavelengths and corresponding energies give a direct relation between the emission peaks and the In composition. Such a relation can again be

correlated with lattice constant using the data shown in Fig. 3.3(b). The figure derived from the PL and XRD measurements is shown in Fig. 3.5, which shows variation of the PL peak energy with lattice constant. The bowing seen in the results again is expected for these materials and confirm the accuracy of the measurements.

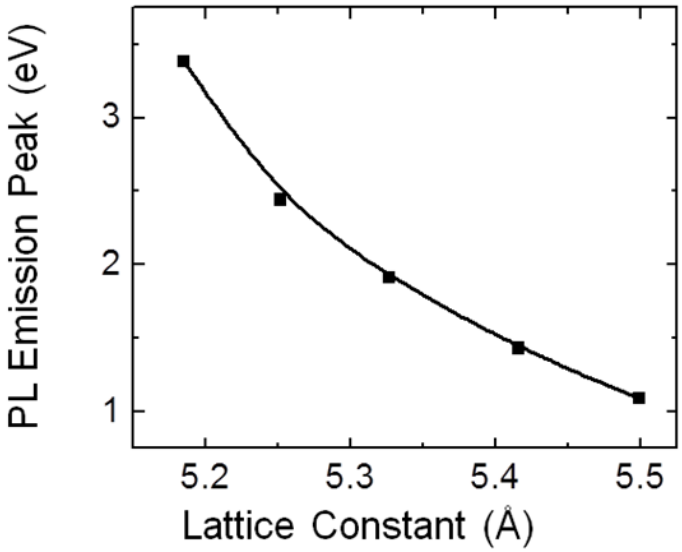

Figure 3.5 Variation of photoluminescence emission peak with lattice constant.

3.3. Spectroscopic Ellipsometry

A Woollam M-2000DI variable-angle spectroscopic ellipsometer was used to measure the optical constants of the samples. The tool uses incidence and detection angles of 55°, 65° and 75° to measure the changes in p- and s-polarizations. The three different angles of incidence help in the better analysis of the data. The variation of the optical constants as a function of incidence wavelengths can also be determined from such measurements. Figures 3.6(a) and (b) show the measured values of Ψ and Δ for a GaN epitaxial layer grown on (001)Si. Ψ is the angle derived from the ratio of amplitude reductions of the p- and s-polarizations upon reflection and Δ is the phase difference between the reflected p- and s-polarizations, respectively. The relation between Ψ,Δ and

the complex reflectance ratio (**ρ**) is given by the relation: $\rho = \tan\Psi \exp(i\Delta) = r_p/r_s$, where r_p and r_s are, the Fresnel amplitude reflection coefficient for p- and s-polarized light [85], respectively.

The ellipsometry was performed in a wavelength range 800-1683 nm. In this wavelength range, the InGaN samples do not absorb any of the light thus they can be assumed to be optically transparent. Cauchy-Urbach model [85] was employed to analyze the data along with the measured epitaxial layer thickness, surface roughness and bandedge energy as input parameters. The epitaxial planar layer thicknesses, and surface roughness were measured from SEM and AFM, respectively and the bandedge energy was measured from PL measurements. The (001)Si substrate was assumed to be semi-infinite as it was 585μm thick. The substrates were single-side polished. The Urbach absorption tail was described by the relation:

$$k(E) = k\_Amplitude.\, e^{Exponent(E-Bandedge)} \tag{3.2}$$

where k(E) is the extinction coefficient, E is the photon energy, and k-Amplitude and Exponent are empirical analysis parameters. These empirical analysis parameters control the overall shape and decay of the absorption tail. Both the calculated values and the measured values of Ψ and Δ are plotted together in Figs. 3.6(a) and 3.6(b). It can be observed that the two sets of values have an excellent agreement. The measurements were performed carefully to ensure similar excellent agreement between measured and analyzed data for all the different In-based alloys that were used in this study. Further analyses has been performed based on these calculated Ψ and Δ values using Gaussian Oscillator model. Generally, a model is selected depending upon the wavelength of interest and the material behavior in that wavelength range. For example, the previously

used Cauchy-Urbach model is efficient at long wavelengths where the InGaN material is transparent with respect to the incident wavelengths. If the material has substantial absorption, the Cauchy-Urbach model will not be ideal to use. The Gaussian Oscillator model does not suffer from the drawbacks of the Cauchy-Urbach model but it is harder to set-up. Results derived using Gaussian Oscillator model and Cauchy-Urbach model will be discussed in detail.

Using the Cauchy-Urbach model, mean squared error (MSE) values were determined for data sets like the one shown in Fig. 3.6. The MSE values ranged from 6.9 for GaN to 28.27 for $In_{0.73}Ga_{0.27}N$. The low MSE has been achieved by standard error minimization algorithms. The increase of MSE values with decreasing bandgap is attributed to the absorption of light by the material. The appreciable absorption of the incident light by the low bandgap material somewhat invalidates the optical transparency condition of the material. The absorption also increases at longer wavelengths. For this reason, the agreement between measured and analyzed data also reduces at the longer wavelengths.

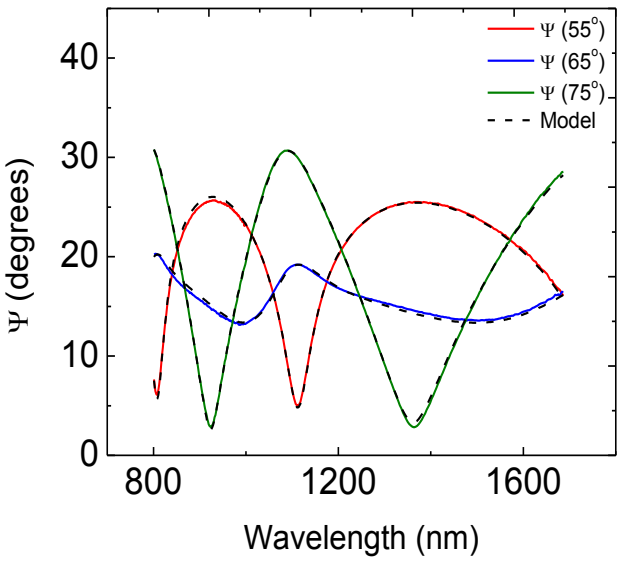

(a)

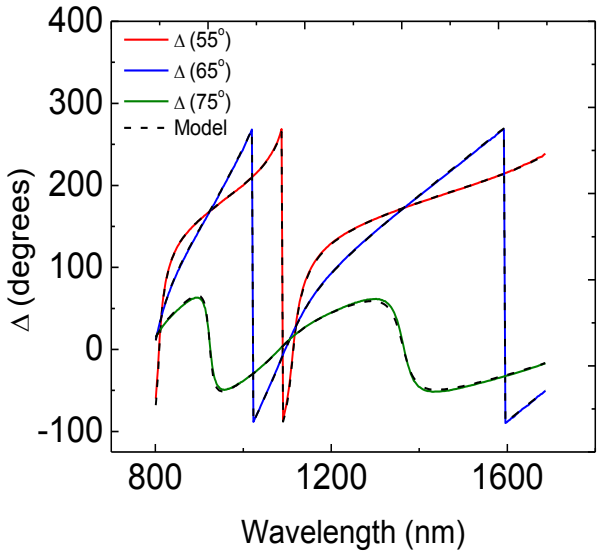

(b)

Figure 3.6 Empirical modeling of ellipsometric parameters (a) Ψ and (b) Δ using Cauchy-Urbach model for the GaN layer. (Courtesy of Aniruddha Bhattacharya, Bhattacharya Research Group, University of Michigan)

Figure 3.7 depicts the variation of refractive index with wavelength for all the measured samples obtained from both Cauchy-Urbach and Gaussian Oscillator model. Similar optical constant values for photon energies of 1.0 to 1.5eV have already been reported G. M. Laws et. al. [86]. The data in this work and the Laws et. al. data are within ±5% in the before said energy difference. The differences in the optical constants values

significantly increase at higher photon energies because the InGaN layers start absorbing the incident light at such high photon energies making the transparency condition invalid. Thus both refractive index (n) and extinction coefficient (k) need to be analyzed carefully to accurately determine the optical constants. At such complex situations, the Gaussian Oscillator model outperforms the Cauchy-Urbach model. Hence this study has used both models. The addition of parameters makes Gaussian Oscillator model accurate but at the same time makes it more computationally intensive compared to the Cauchy-Urbach model.

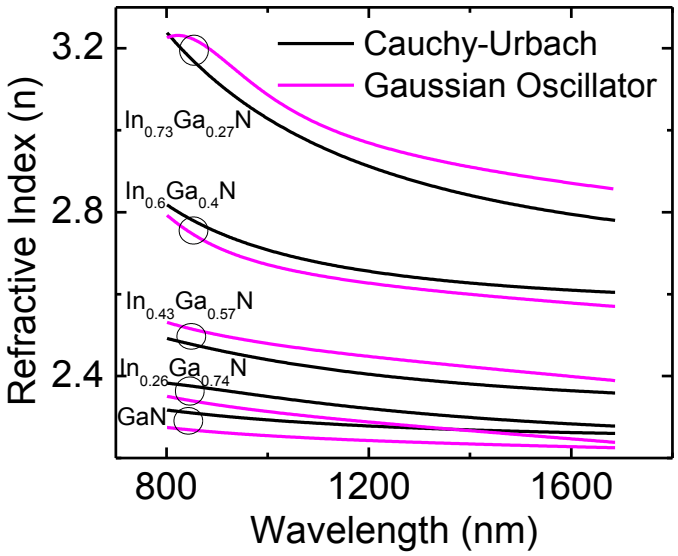

Figure 3.7 Refractive index as a function of wavelength for different compositions of $In_xGa_{1-x}N$ layers obtained by using Cauchy-Urbach and Gaussian Oscillator model. (Courtesy of Aniruddha Bhattacharya, Bhattacharya Research Group, University of Michigan)

Here the refractive indices of $In_xGa_{1-x}N$ ($0 \leq x \leq 0.73$) epitaxial planar layers have been identified by spectroscopic ellipsometry in the wavelength range of $800 \leq \lambda \leq 1687$nm. Further study has been carried out and reported in [87], where the wavelengths of investigation has been extended to $400 \leq \lambda \leq 1687$nm using the Gaussian Oscillator model. The planar layers used in this study were grown directly on (001) silicon substrates by

plasma assisted molecular beam epitaxy. This study [87] of refractive indices of III-nitrides significantly helps to understand their behavior in long wavelengths. III-nitrides are generally used in visible (specifically blue and green) and hence this adds valuable data that are otherwise not available. Additionally, the data presented in this section has also helped in designing high-performance laser heterostructures as discussed in the previous chapters.

3.4. Characterization of $In_{0.18}Al_{0.82}N$ and $In_xGa_{1-x}N$ Graded Cladding Layers

This section discusses possible future cladding layers that can be used for optoelectronic device design. The cladding layers discussed here will provide better mode confinement. This section first discusses $In_{0.18}Al_{0.82}N$ lattice matched to GaN followed by graded cladding layers using $In_xGa_{1-x}N$.

3.4.1 $In_xAl_{1-x}N$ layer lattice matched to GaN

The alloy $In_{0.18}Al_{0.82}N$ is lattice matched to GaN in $\vec{a}$ lattice direction. With its larger bandgap and lower refractive index, the material is useful as a waveguide cladding layer [88]. As the material is also lattice matched to GaN, the epitaxial growth does not generate appreciable amount of defects. The growth of $In_{0.18}Al_{0.82}N$ is fairly challenging as In and Al have significantly different sticking coefficients. The lattice matched condition has been verified using X-ray diffraction (XRD) as shown in Fig. 3.8 on a epitaxially grown planar $In_{0.18}Al_{0.82}N$ layer. Due to the different $\vec{c}$ to $\vec{a}$ ratio of GaN and $In_{0.18}Al_{0.82}N$ lattice, the peaks for the two materials measured from XRD are generally within 850 to 1000 arcseconds [89], [90]. Figure 3.8 shows the two peaks to be around 936 arcseconds highlighting the matched condition of the GaN and $In_{0.18}Al_{0.82}N$ lattices.

The $In_{0.18}Al_{0.82}N$ layer was grown under metal rich environment on GaN on sapphire templates in a nitrogen plasma assisted molecular beam epitaxy system (PA-MBE). To improve the crystal quality a thin 100nm MBE grown GaN planar layer was grown first on the template at nitrogen flow rate of 0.66sccm before growing the 200nm $In_{0.18}Al_{0.82}N$ layer at a nitrogen flow rate of 0.8sccm. The GaN and the $In_{0.18}Al_{0.82}N$ layers were grown at growth temperatures of 758°C, and 550°C, respectively. The Ga flux was kept at 2.35×10^{-7} Torr for the GaN layer and In and Al flux were maintained at 2.86×10^{-8} Torr and 2.42×10^{-8} Torr, respectively for the $In_{0.18}Al_{0.82}N$ layer. The high bandgap of $In_{0.18}Al_{0.82}N$ makes it difficult to dope, especially p-type. Therefore alternate solutions to a better cladding layer have been explored and discussed in the next sections.

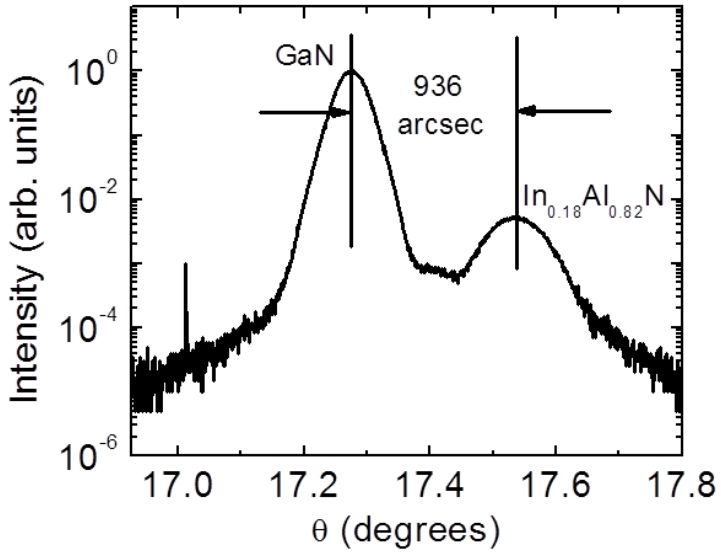

Figure 3.8 X-ray diffraction (XRD) of $In_{0.18}Al_{0.82}N$ lattice matched to GaN.

The $In_{0.18}Al_{0.82}N$ peak seen in the XRD of Fig. 3.8 has a full width half maximum (FWHM) of ~320 arcseconds demonstrating the high quality of the $In_{0.18}Al_{0.82}N$ crystal. The additional peak at lower bandgap seen in the XRD is from the underneath GaN layer grown using MBE on top of the GaN-on-sapphire substrate. The GaN already existing on the substrate is grown using HVPE. The underneath GaN layer has an FWHM of ~160

arcseconds, nearly half of that of $In_{0.18}Al_{0.82}N$, demonstrating even superior material quality. Such advanced cladding layers can be epitaxially grown on (001)Si as well.

3.4.2 Characterization of graded cladding layers

The different $In_xGa_{1-x}N$ planar layers have not only been characterized by photoluminescence (PL) but also by X-ray diffraction (XRD). From the XRD seen in Fig. 3.9, the change in the bandgap can be observed by the change in the peak position of the different XRD peaks corresponding to alloys of different In compositions. Such InGaN layers have been employed as graded cladding layer of the graded refractive index – separate confinement heterostructures (GRIN-SCH). The design of such nanowire-based GRIN-SCH structures has been discussed in the previous section. The modal confinement does significantly improve using these layers and will be detailed in the later chapters.

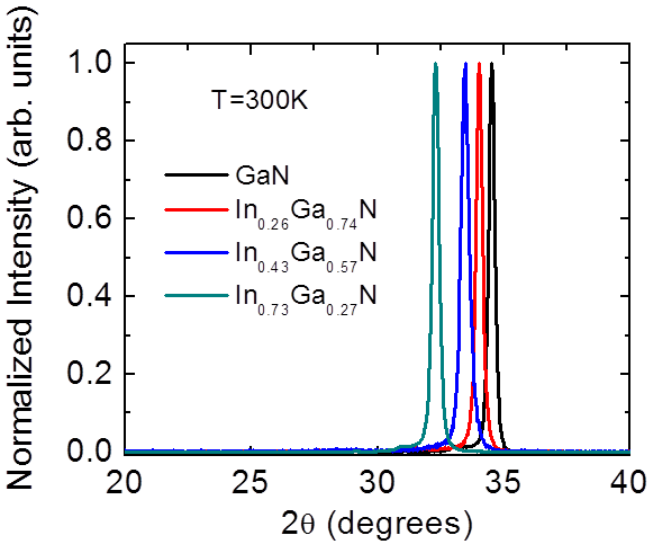

Figure 3.9 X-ray diffraction (XRD) of $In_xGa_{1-x}N$ planar layers.

The full width half maxima (FWHM) of the different peaks have increased as more In is incorporated which is expected as larger FWHM denote higher alloying

effects. Such alloying effects are caused as the higher In composition causes enhanced In segregation, and clustering effects.

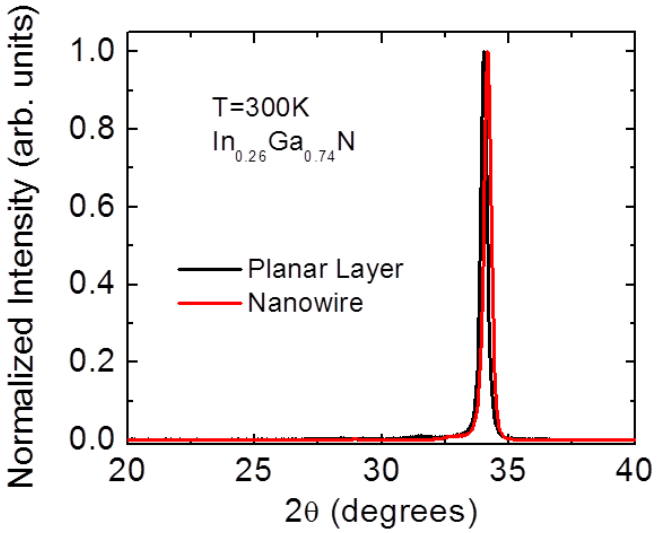

Figure 3.10 X-ray diffraction (XRD) of $In_{0.26}Ga_{0.74}N$ planar layer compared to nanowire with same In and Ga composition.

So far in this section, XRDs of only planar layers have been shown although the focus of this thesis is nanowires. The lattice constants of a planar layer and a nanowire do have a measurable difference even if they have the identical alloy composition. Such minimal difference can be observed in Fig. 3.10 where the XRDs of a planar layer and nanowire have been compared. Both types of nanostructures have approximately same alloy composition of $In_{0.26}Ga_{0.74}N$ ensuring the fairness of the comparison. The bandgap of the nanowire seems to have slightly increased possibly due to compressive strain which can cause the shift towards larger θ values. Overall the nanowire XRD does show that similar planar layer and nanowire can be grown without a significant difference in lattice constants. Thus the comparison between a planar layer and nanowires in terms of XRD is reasonably fair.

3.5 Summary

To summarize, optical constants of III-nitride materials were measured at a wide range of wavelengths (800 to 1687nm) using spectroscopic ellipsometry. Efficient cladding layers were also designed and characterized using the optical constant data. Planar layers of various $In_xGa_{1-x}N$ alloys were grown directly on (001) silicon and characterized to determine their optical constants as a function of wavelength. The surface roughness of the samples was minimized to reduce error in the ellipsometry data. Schottky diodes were fabricated, and measured to determine the background carrier concentration in these alloys. XRD was performed to determine possible bowing in the lattice constants with variation of the bandgap. The data from spectroscopic ellipsometry was analyzed using two models (Cauchy-Urbach and Gaussian Oscillator model) to determine the optical constants of the InGaN alloys. $In_{0.18}Al_{0.82}N$ epitaxial layers lattice matched to GaN layers were grown and characterized. $In_xGa_{1-x}N$ cladding layers were also characterized and explored as a possible cladding layer since p-doping the InAlN layers can be difficult. Such graded cladding layers using InGaN were characterized by XRD, and PL.

Chapter IV

Near-Infrared Disk-in-Nanowire LEDs, and Lasers on (001) Silicon

4.1 Introduction

Near-IR optoelectronic devices are extremely useful in a variety of applications including silicon photonics, optical communication, optical information processing, on-chip communication, and a host of biomedical applications. These devices have to be (001) silicon based to be useful and accesible in silicon photonics. So far there have been different approaches to achieve such optoelectronic devices, especially lasers. Each approach has several drawbacks as discussed in the introduction chapter.

III-nitride nanowire arrays can be grown relatively free of extended defects on (001)Si substrates creating the possibility of monolithic displays and sensors on a silicon platform [91], [92]. To be useful for silicon photonics or for fiber optic communication networks, the operating wavelength of optoelectronic devices made with nanowire heterostructure arrays should be within the 1.3 - 1.55μm range. Light emitting diodes (LEDs) and diode lasers emitting in the ultraviolet (UV) to near infrared range of the spectrum [93]–[97], [42], [98] using In(Ga)N/GaN disk-in-nanowire heterostructure arrays grown on silicon substrates have been already reported. Additionally, detection of UV light with single nanowires [99]–[101], nanowire ensemble p-i-n diodes [102], [103]

and nanowire transistors [104], [105] have also been reported. In this chapter, the epitaxy, fabrication, and characterization of $In_xGa_{1-x}N/In_yGa_{1-y}N$ disk-in-nanowire array based LEDs, and lasers on (001)Si substrates, with emission wavelengths of 1.2 to 1.3 μm have been discussed.

Catalyst-free III-nitride [(Al, Ga, In)N] nanowire arrays and nanowire heterostructure arrays can be directly grown on (001)Si substrates. These nanowires grow in the wurtzite crystalline form with the c-axis parallel to the growth direction [93], [95], [106]–[109], [44]. In the simplest form, the nanowires grow on substrates that do not have any patterns. The nanowires grow upon an initial randomly spaced array of seed crystals. These crystals are nucleated upon a thin 2-4nm non-uniform amorphous Si_xN_y layer formed on the Si substrate. By changing the growth parameters, the area density of the nanowires can be varied in the range of 10^9-$10^{11}cm^{-2}$. The large surface-to-volume ratio further adds advantages to the nanowires by limiting the propagation of defects. These defects are mostly confined in the Si - SiN - GaN nanowire interfaces. The nanowires also have reduced polarization fields compared to planar layers with similar InGaN compositions due to radial relaxation of strain during epitaxy leading to smaller radiative lifetimes [46], [110]. Single or multiple $In_xGa_{1-x}N$ disks can be inserted in GaN or AlGaN nanowires to vary the emission wavelength of the disk-in-nanowires (DINWs). The fractional composition (x) of the $In_xGa_{1-x}N$ disks can be varied in the range 0.0 to 1.0 enabling the photoluminescence intensity peak to be tuned from violet to near infrared (near IR). In this chapter, InN and $In_{0.85}Ga_{0.15}N$ disks will constitute the light emitting region in the nanowire arrays which were used to fabricate the optoelectronic devices.

Several nanowire heterostructures were grown to fabricate the optoelectronic devices. The growth of the heterostructures has been detailed in chapter II. In this chapter, the fabrication process and optical characteristics of the LEDs, and lasers have been detailed. First, the LEDs have been discussed which are designed using $In_{0.85}Ga_{0.15}N/In_{0.4}Ga_{0.6}N$ DINW heterostructures. They emit light at ~1.3μm exhibiting a significant blueshift from the PL peak of the before mentioned heterostructure. Then lasers using the same heterostructure have been discussed. The lasers demonstrate more blueshift than the LEDs possibly due to higher injection levels. Due to the higher blueshift, the lasers emit light at ~1.2μm. Next lasers with $InN/In_{0.4}Ga_{0.6}N$ DINW heterostructures have been described. These lasers also show a strong blueshift from the PL peak of the nanowire heterostructure. The laser emission peak occurs at 1.3μm whereas the PL peak was at 1.6μm as discussed in chapter II. Optoelectronic properties of the lasers have been discussed in detail, including light-current characteristics, characteristics temperature, differential gain, and modulation bandwidth.

4.2 Light Emitting Diodes using $In_{0.85}Ga_{0.15}N/In_{0.4}Ga_{0.6}N$ DINW Heterostructures

4.2.1 Fabrication of light emitting diodes using $In_{0.85}Ga_{0.15}N/In_{0.4}Ga_{0.6}N$ DINW heterostructures

The optoelectronic devices discussed here are fabricated using nanowire arrays. The nanowire arrays were directly grown on (001)Si ensuring compatibility with existing CMOS technology. The top emitting LEDs were fabricated to demonstrate near-infrared light emission from these nanowire heterostructures under electrical injection.

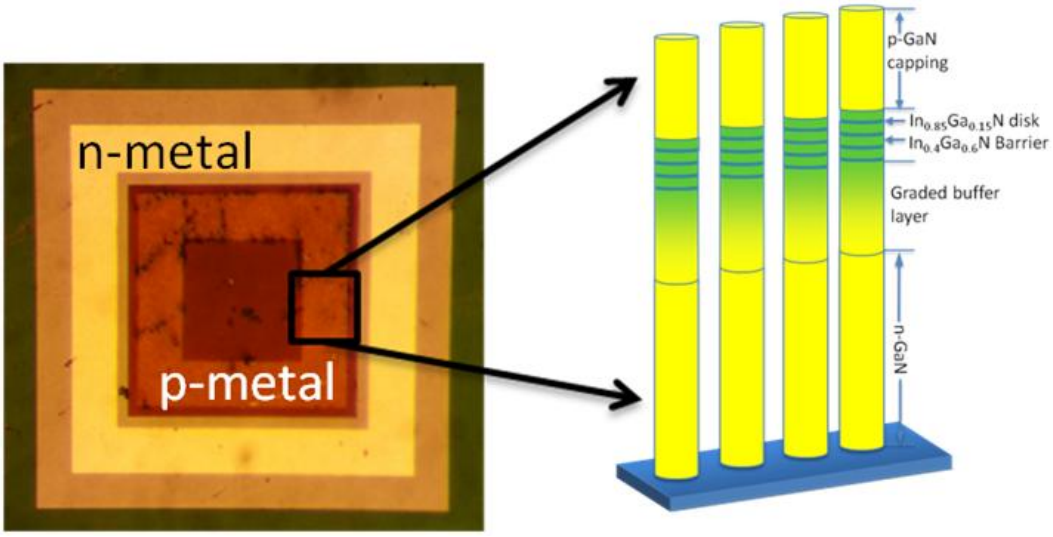

Figure 4.1 Optical image of the top emitting LED showing the p- and n-metals. Inset shows the nanowire heterostructure used to fabricate the LEDs.

The LEDs are shown in Fig. 4.1 along with the nanowire heterostructure (the inset of Fig. 4.1). LEDs have been fabricated by employing a series of photolithography, plasma etch and metallization processes. The nanowires were first parylene passivated and planarized. After that p-contact metals (Ni/Au) and ITO were deposited of pre-defined thicknesses in areas selected using optical projection photolithography. Ni, Au and ITO of 5nm, 5nm, and 200nm, respectively, were deposited on top of the nanowire array as the current spreading layer. Next mesas were patterned using photolithography and etched to the n-type (001)Si substrate using a plasma-assisted reactive ion etch process. The etch process was performed under the presence Cl_2 and BCl_3 gases. Ar plasma was used to accelerate the etch process. Finally, Al of 800nm thickness was deposited on the etched mesa regions as the n-contact metal. The sample is annealed to achieve low contact resistance.

4.2.2 LED characteristics

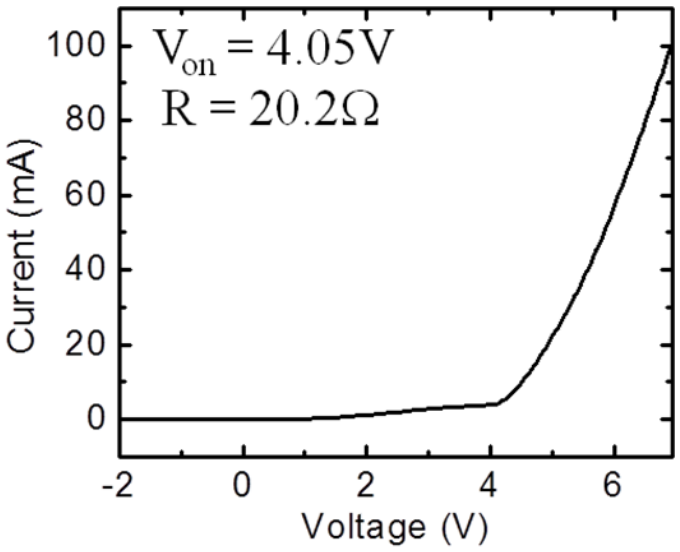

Figure 4.2 Current-voltage (I-V) characteristics of the near-IR emitting LED.

A series resistance of ~20Ω and a turn on voltage (V_{ON}) of ~4V were measured from current-voltage (I-V) measurements performed on the diodes. One such set of measured I-V characteristics can be seen in Fig. 4.2. The electroluminescence output of the diodes was measured using a Newport IR detector (818-IG) and is shown in Fig. 4.3.

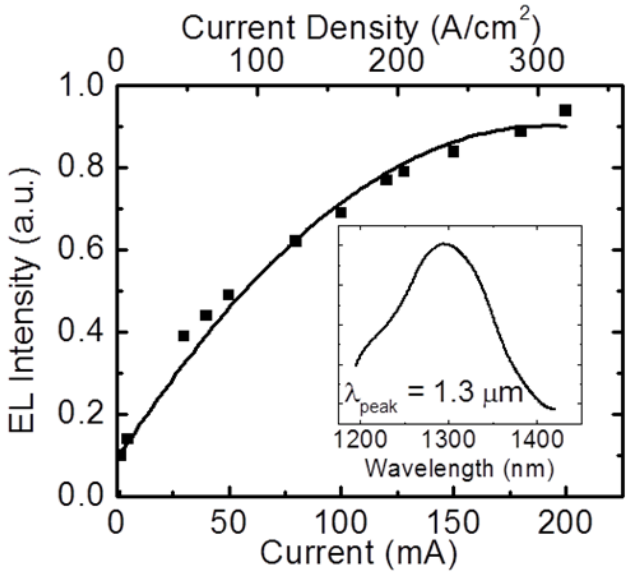

Figure 4.3 Electroluminescence characteristics of $In_{0.85}Ga_{0.15}N$/GaN disk-in-nanowire LED. Inset shows output spectrum at low injection level.

The output spectrum of the LEDs was measured using a liquid nitrogen cooled germanium detector. The detector is manufactured by Edinburgh Instruments Ltd. and is of EI-L type. It has a reasonable response time of 1ms and a low noise equivalent power of 1×10^{-15}WHz$^{-1/2}$. The detector has a high responsivity of 5×10^{9} V/W. The peak of the output spectrum is measured at 1.3μm wavelength at low injections. The output spectra were further measured at high injections. A blueshift was observed from these measurements which suggest the presence of high polarization fields in the materials. The blueshift was measured between injection current density of 5 to 320 A/cm^2. The measured blueshift can be seen in Fig. 4.4. A blueshift of ~26meV was calculated which corresponds to a polarization field of ~860kV/cm from this data. Simulations based on existing data [63] were used to determine that about ~77% of the polarization field is from piezoelectric polarization and ~23% is from spontaneous polarization. Much higher values of polarization fields have been calculated in the case of lasers as will be discussed later in this chapter.

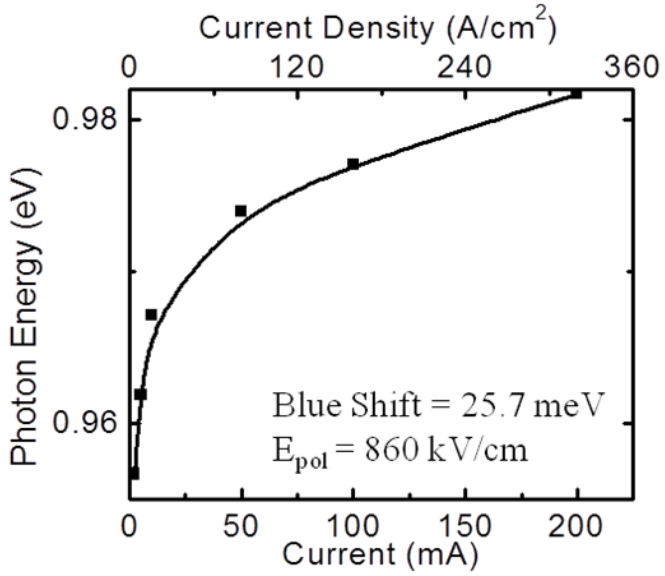

Figure 4.4 Measured blueshift of the near-IR LEDs.

4.3 InN/$In_{0.4}Ga_{0.6}N$ and $In_{0.85}Ga_{0.15}N/In_{0.4}Ga_{0.6}N$ Disk-in-Nanowire Lasers

4.3.1 Fabrication of nanowire lasers

Identical heterostructures to the above-mentioned LEDs have been used to fabricate lasers as well. Before the laser was fabricated, transfer matrix method (TMM) was applied to determine the mode confinement provided by these laser heterostructures at 1.3μm. The TMM data is courtesy of Tien-Khee Ng under the supervision of Professor Boon S. Ooi at the King Abdullah University of Science and Technology (KAUST), Saudi Arabia. The simulated TMM data is shown in Fig. 4.5. The simulation was performed considering the continuous epitaxial structure and without taking into account scattering losses. Figure 4.5 shows the composition dependent refractive index profile which was calculated from [87] or interpolated from measured values in [87]. The Fig. exhibits leakage of the optical mode into the graded InGaN layer, as well as leakage into the p-GaN and n-GaN layers. Such mode leakage is consistent with the experimental near-field optical mode measurement which will be discussed later.

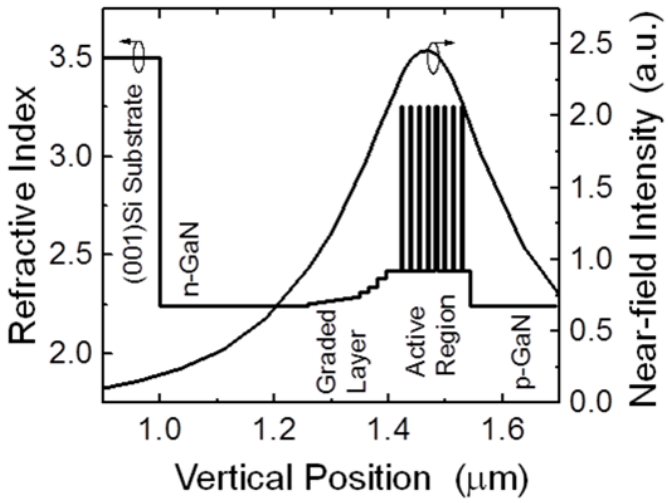

Figure 4.5 Mode intensity distribution as calculated for the full laser heterostructure shown in the inset of Fig. 4.1. (Courtesy of Tien-Khee Ng, Professor Boon S. Ooi research group, King Abdullah University of Science and Technology (KAUST), Saudi Arabia)

A combination of planarization with parylene, photolithography, and reactive ion etching have been used to fabricate edge-emitting nanowire lasers. Parylene planarization was performed by iteratively performing dry etch and measurement using a scanning electron microscope (SEM) system. The parylene etch was stopped after nanowire tips were exposed. The photolithography and the etch tool has been described in more detail in chapter III. Parylene also acts as a passivation material to the nanowire and disk regions which increases the relative IQE by ~ 10-12% [111]. An example will be a relative IQE of 40% can increase to a value of 50-52% after parylene passivation on an as-grown sample. The laser width was defined to be 50 μm in a ridge geometry by using two-step mesa etching. The n-contacts were formed using Al/Au (50nm/200nm) on the Si substrate surface. Ni/Au (5nm/200nm) was used to form the p-contact. This step was followed by deposition of indium tin oxide (ITO) (250nm) and annealing of the devices.

Dicing was used to define lasers of cavity lengths varying from 0.5 to 2 mm. Dicing was followed by focused ion beam (FIB) etching of both sides of the laser facets, and the deposition of 2 pairs of MgF_2/ZnSe (235nm/130nm) distributed Bragg reflectors (DBRs) on those facets. Such FIB and DBR deposition steps enable a facet reflectivity of 0.68 at both ends. A series resistance of 25Ω was derived from the laser diode from current-voltage measurements. SEM and micrograph images of such lasers are shown in Fig. 4.6(a) and (b) respectively.

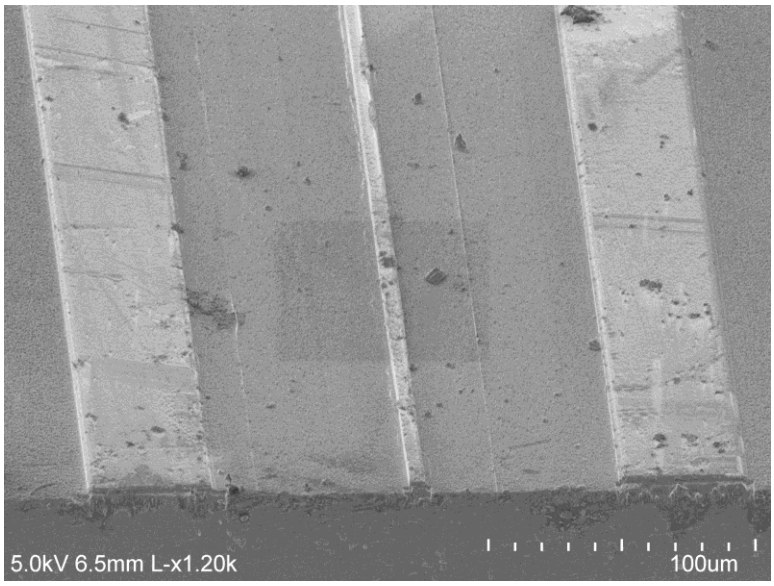

(a)

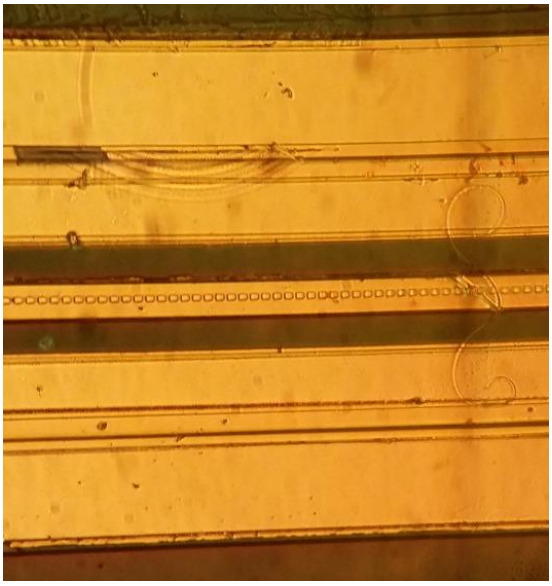

(b)

Figure 4.6 (a) SEM image and (b) Micrograph image of fabricated nanowire lasers with $In_{0.85}Ga_{0.15}N$ as the disk material.

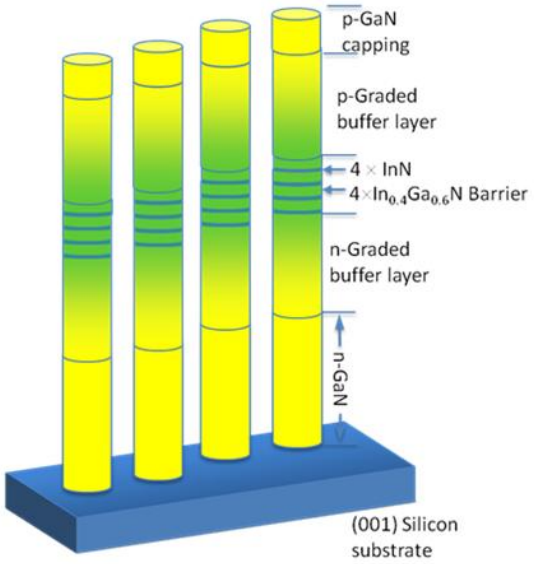

Figure 4.7 Full laser heterostructure with InN as the active disk region. The top p-graded cladding layer further improves the mode confinement factor.

Most of the steps for fabricating the InN disk based nanowire laser were identical to the above-mentioned laser fabrication process. The main difference was that ITO was not deposited in this fabrication process to ensure lower series resistance. Regarding the nanowire heterostructure, the top cladding layer was further improved by adding a p-graded layer similar to the one on the n-side. The modified heterostructure can be seen in Fig. 4.7. As before, a detailed mode intensity distribution simulation has been performed on this heterostructure from which a mode confinement factor of 0.0137 has been determined. The mode intensity distribution calculated from TMM has been shown in Fig. 4.8.

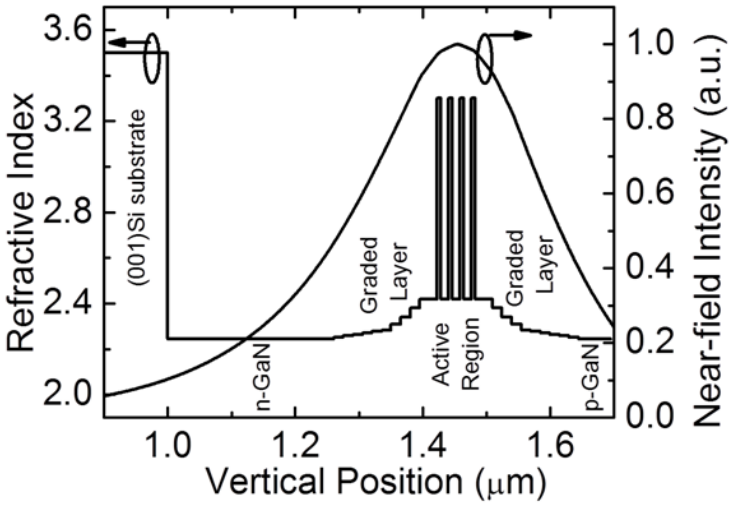

Figure 4.8 Mode intensity distribution as computed for the full laser heterostructure shown in Fig. 4.7.

The thicknesses of the distributed Bragg reflector (DBR) layers were modified to enhance laser facet reflectivity at 1.3μm instead at 1.2μm as done in the previous fabrication process. DBR layers of magnesium fluoride (MgF_2) and zinc selenide (ZnSe) of 237nm and 132nm were deposited, respectively. Three pairs of such DBR layers were deposited on both facets of the laser. The DBR layers were also deposited on control Si samples to ease the DBR reflectivity measurement performed using ellipsometry. It is estimated that the reflectivity from the three pairs of DBR mirror is about 88%. Before the DBR deposition, the laser facets were FIB polished also. Such a laser with its one FIB polished facet can be seen in Fig. 4.9(a) and (b).

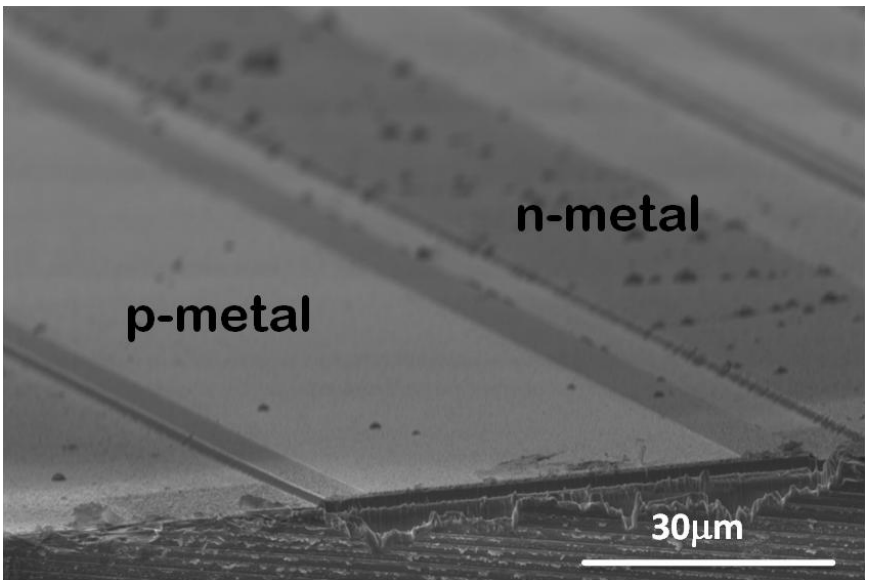

(a)

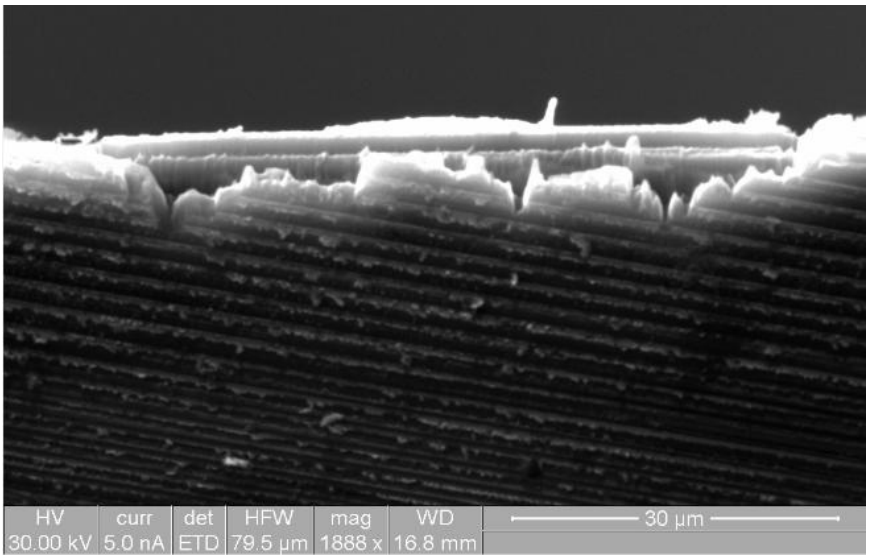

(b)

Figure 4.9 SEM image of (a) a fabricated nanowire laser with InN as the disk material and (b) one FIB polished facet on which DBRs will be deposited.

4.3.2 Waveguide loss measurement

A control nanowire array sample was grown to measure the waveguide loss. The control sample consisted of a nanowire heterostructure which is almost identical to that grown for laser fabrication (Fig. 4.1). The only major difference is that the waveguide region consisted of 120 nm of $In_{0.4}Ga_{0.6}N$ and did not have the $In_{0.85}Ga_{0.15}N$ disks. The absence of the disks eliminated the possibility of absorption of the 850 nm excitation light.

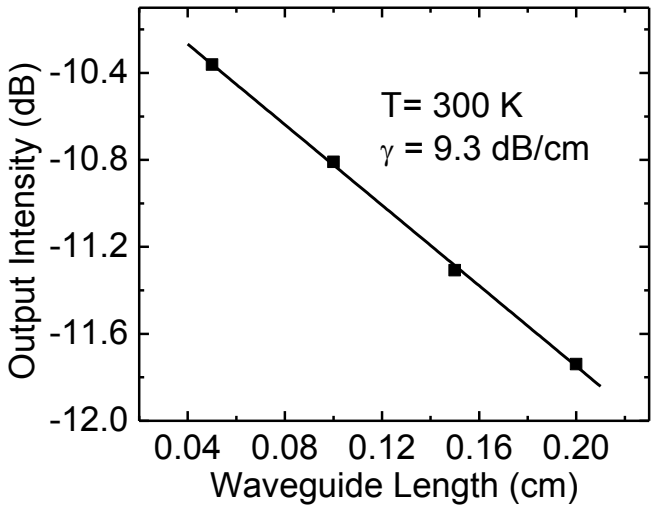

Figure 4.10 Output intensity of nanowire heterostructure ridge waveguides as a function of waveguide length.

Waveguide fabrication was carried out using similar steps as that for the laser fabrication. High-reflectivity DBRs were replaced by the formation of dielectric anti-reflection (AR) coating on the facets. Waveguides were defined to be 50 μm in width and varying lengths. These were end-fired with 850nm light, and the transmitted light intensity was measured using an infrared detector. The measured data is shown in Fig. 4.10. The data was analyzed to derive a waveguide (cavity) loss of 9.3dB/cm. This value is comparable to that measured in InGaN/GaN quantum dot lasers with planar waveguide and cladding layers [112], [113]. The low transverse optical mode confinement factor is

the primary cause of this loss, and such loss can further contribute to an increase in the threshold current.

4.3.3 DC laser characteristics

50 μm × 1 mm lasers were measured to determine the light-current-voltage (L-I-V) characteristics using pulsed (5% duty cycle) bias conditions to avoid device heating. Apart from this, no other specialized heat sinking or device mounting techniques were used. Figure 4.11 shows the output characteristics measured at room temperature below and above the threshold.

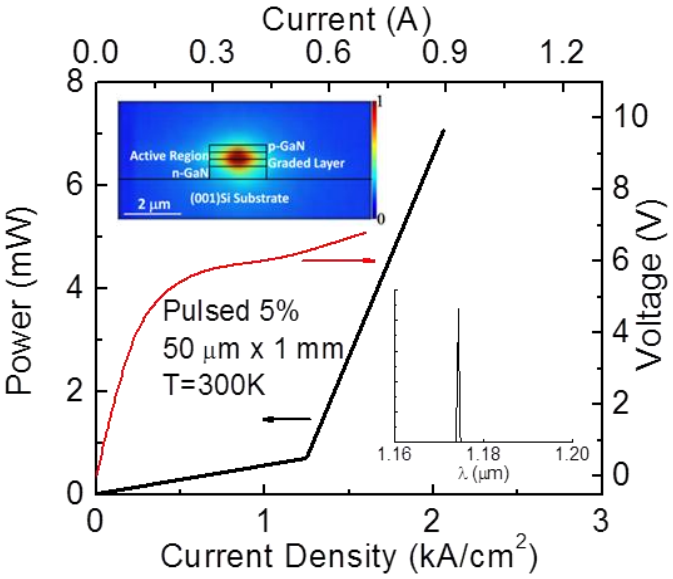

Figure 4.11 Light-current characteristics of a broad area laser. Top inset shows a near-field image of the laser mode superimposed with the laser heterostructure schematic, and the bottom inset shows electroluminescence spectrum above the threshold.

A fill factor of 0.85 of the nanowire ensemble was derived from the nanowire area density and diameter. The fill factor and nanowire density were used to measure the threshold current density (J_{th}) to be 1.24 kA/cm^2. A differential efficiency η_d = 0.13 W/A (12.8%), and a wall-plug efficiency of 0.07% were also derived from the measured L-I-V data. The measured value of J_{th} is amongst the lowest for lasers that use nitride-based

quantum wells and quantum dots [57], [113]. The laser output was fiber coupled to an optical spectrum analyzer to measure the spectral characteristics of the electroluminescence at different biases. Inset of Fig. 4.11 shows the spectral output at room temperature at an injection current of 600 mA ($1.13J_{th}$). The emission peak is measured to be at 1.17 μm. Such spectral data show a blueshift between the peak seen in the laser output and the peak obtained from the photoluminescence measurements, which is at 1.46 μm. This blueshift is due to the quantum confined Stark effect (QCSE) which is a result of the polarization field in the $In_{0.85}Ga_{0.15}N$ disks. The smallest recorded linewidth is calculated to be 6Å which was measured from the variation of the spectral linewidth (full-width-at-half-maximum) with injection current density. The variation of the threshold current density with temperature was also measured to determine the temperature stability of these lasers. These measurements were done under pulsed bias (5% duty cycle) conditions with the help of a Peltier cooler. The measured variation is shown in Fig. 4.12. This data was analyzed with the relation: $J_{th}(T) = J_{th0}.\exp(T/T_0)$ which results in a characteristics temperature (T_0) value of 242K. Such characteristic temperature values have also been measured for GaAs-based ~ 1.0 μm quantum well lasers [114]. The value obtained here is significantly higher than the GaAs-based devices. The T_0 values are also comparable to visible III-nitride nanowire lasers already reported [42], [115] indicating that the nanowire lasers are promising regarding temperature stability. It is highly likely that the high value of T_0 is a result of the large band offsets in the quantum disk heterostructure which reduces carrier leakage.

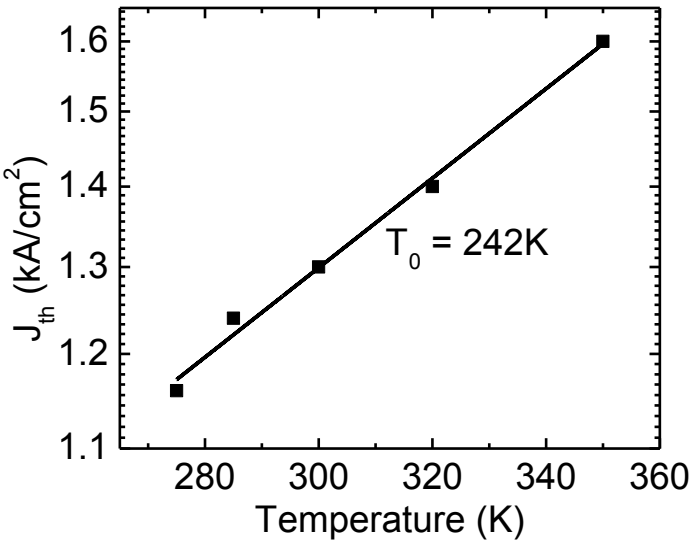

Figure 4.12 Temperature dependence of the threshold current density.

The laser output characteristics were also measured for varying cavity lengths (L) at room temperature. The variation of η_d^{-1} versus L and J_{th} vs. 1/L are shown in Figs. 4.13(a) and (b), respectively. The cavity length dependent data has been analyzed using the following equations:

$$\frac{1}{\eta_d} = \alpha_i L ln \frac{1}{\sqrt{R_1 R_2}} + \frac{1}{\eta_i} \tag{4.1}$$

$$J_{th} = J_{th}^0 + \frac{qd}{\Gamma \eta_i \tau_r \frac{dg}{dn}} [\alpha_i + \frac{1}{2L} \ln(\frac{1}{R_1 R_2})] \tag{4.2}$$

where η_d is the differential efficiency, R_1 and R_2 are the mirror reflectivities, L is the cavity length, α_i is the cavity loss, J_{th} is the threshold current density, J_{th}^0 is the transparency current density, dg/dn is the differential gain, d is the active region thickness, Γ is the product of the transverse optical confinement factor and the nanowire fill factor, and τ_r is the radiative lifetime. For equation 4.1, α_i and η_i are the analysis parameters and for equation 4.2, J_{th}^0, and dg/dn are the analysis parameters.

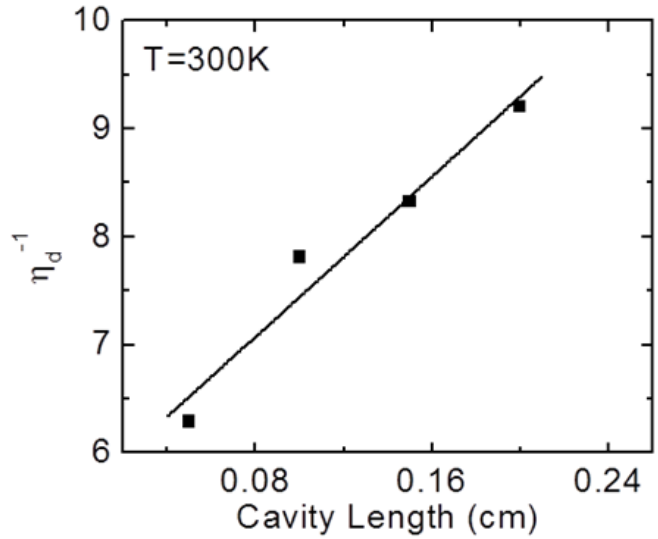

(a)

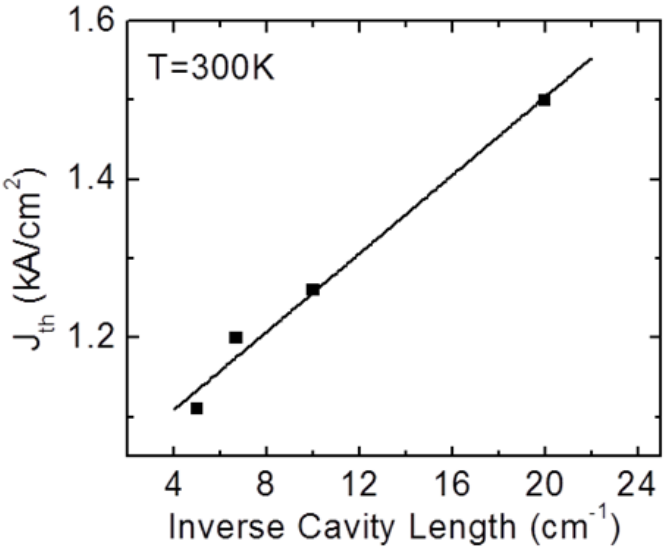

(b)

Figure 4.13 (a) Measured variation of inverse differential quantum efficiency as a function of cavity length, and (b) measured variation of threshold current density as a function of inverse cavity length.

The analysis resulted in an IQE value of 0.18 assuming 100% injection efficiency. The data was further analyzed to determine a differential gain (dg/dn) of ~5.6×10^{-17} cm^2. This calculation was done assuming a value of the radiative carrier lifetime (τ_r) to be 1.84 ns which was derived from TRPL measurements mentioned earlier. This value was compared to the dg/dn values of already reported InGaAs/GaAs pseudomorphic quantum

well and quantum dot lasers. The value from the demonstrated InGaN nanowire lasers is approximately an order of magnitude smaller [116], [117]. The J_{th} value measured for these nanowire lasers are relatively large compared to typical values of ~200 A/cm^2 for GaAs-based quantum well devices [114]. Such high J_{th} values are probably due to the smaller differential gain and a lower gain coefficient which is a result of polarization field induced reduction of the electron-hole overlap in the disks (~0.3-0.4) [118], [119]. The low quantum efficiency is also responsible for the large threshold current density.

Light-current characteristics of the InN/$In_{0.4}Ga_{0.6}N$ lasers of 50 μm × 1 mm dimensions were also measured under pulsed (5% duty cycle) bias conditions to avoid device heating. The measured output data at room temperature below and above threshold are shown in Fig. 4.14(a). The threshold current is I_{th} = 673 mA. A differential efficiency η_d = 0.01 W/A (1.07%), and a wall-plug efficiency of 0.15% were derived from these characteristics. The spectral characteristics of the laser electroluminescence at different biases were recorded by fiber-coupling the output to an optical spectrum analyzer. These characteristics are shown in Fig. 4.14(b). Injection currents of 800mA ($1.2I_{th}$) for above threshold and 200mA ($0.15I_{th}$) for below threshold were used for this measurement. The measurement was carried out at room temperature (300K). The emission peak is measured to be at 1.32 μm above threshold. From the measured variation of the spectral linewidth (full-width-at-half-maximum) with injection current density, the smallest recorded linewidth is calculated to be 9Å. The blueshift of this peak is again due to the quantum confined Stark effect (QCSE) arising from the polarization field in the InN disks. The blue shift is measured to be 114meV.

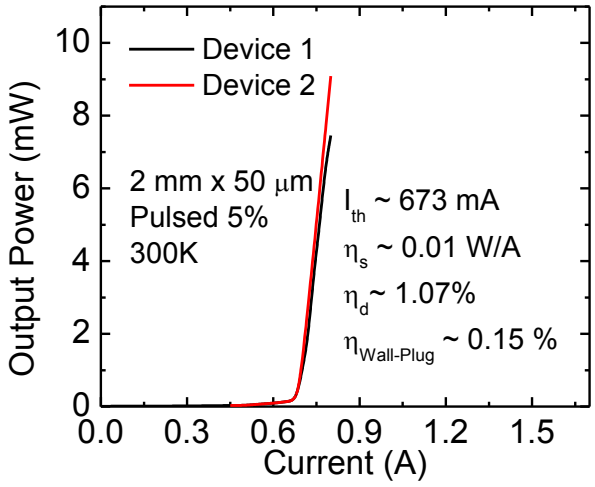

(a)

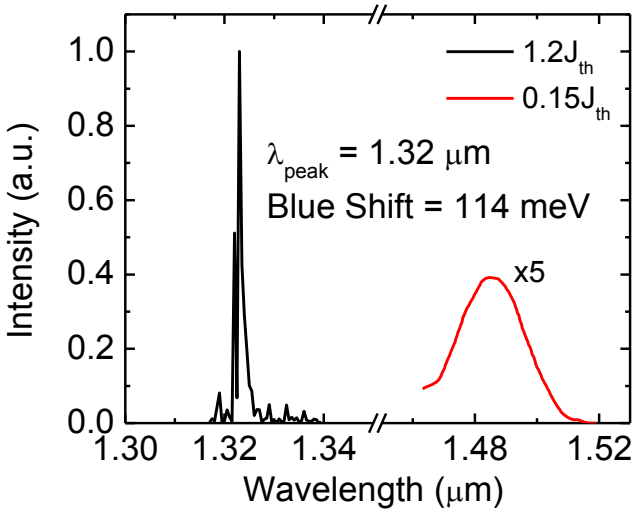

(b)

Figure 4.14 (a) Light-current characteristics of a broad area laser and (b) electroluminescence spectra below and above the threshold.

There is a variation of the emission wavelengths from nanowire array sample to sample probably because the exact value of the polarization field is immensely sensitive to the growth conditions. Such a variation can be seen in Fig. 4.15. Here the emission wavelength is at 1.38μm unlike the previous case (1.32μm). Nonetheless, all the emission wavelengths measured were around 1.3μm.

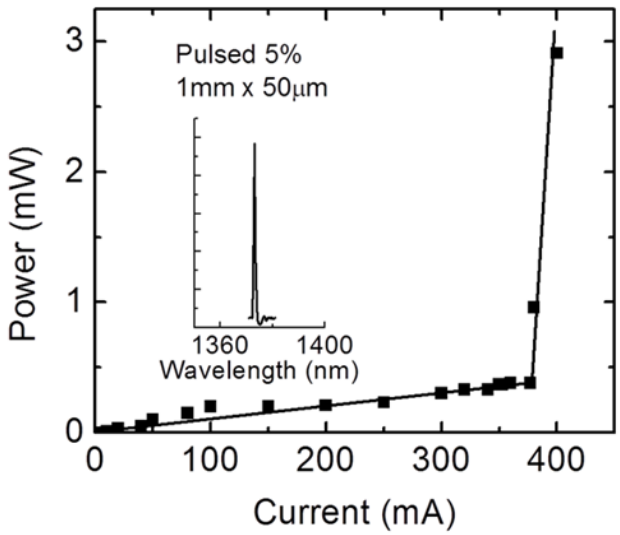

Figure 4.15 L-I characteristics of another nanowire laser with the electroluminescence spectrum above the threshold shown in the inset.

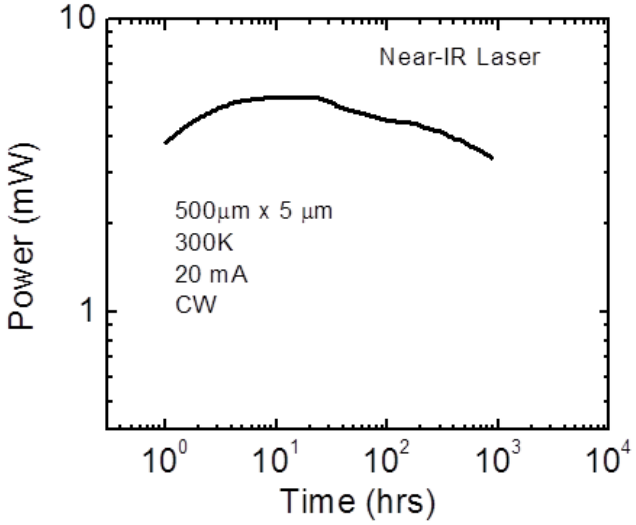

Figure 4.16 Reliability measurements on the 1.3μm near-IR laser.

Lasers with smaller dimensions were biased slightly above their threshold currents, and the output of the laser was measured over extended periods of time to determine the lifetime of these lasers as seen in Fig. 4.16. Under CW bias conditions it has been determined that the lasers have a lifetime of about ~1000 hours. With active cooling and better heat sinking, this lifetime value can be significantly improved. More

advanced heterostructures can also improve the lifetime of the lasers which has already been observed in visible nanowire lasers. Previous reports have demonstrated a lifetime value close to ~7000 hours [42] for green light emitting nanowires.

4.3.4 Small signal modulation

The small-signal modulation response of 500 μm long and 5 μm wide ridge waveguide lasers was measured under pulsed bias conditions (5 μs pulses; 0.5 % duty cycle) using a sweep oscillator with a bias T, low-noise amplifier, a high-speed silicon detector and a spectrum analyzer. The measured response was calibrated taking into account the losses due to cable, connectors, bias network and dc-blocking capacitor.

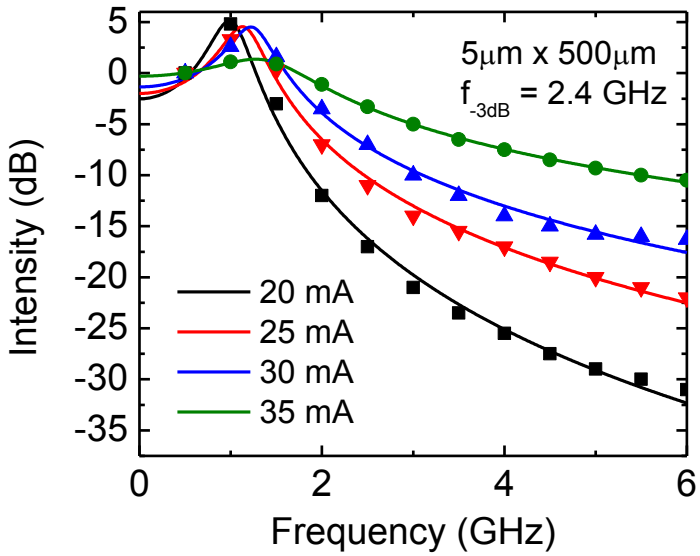

Figure 4.17 The small signal modulation response of a 500 μm long ridge waveguide InN/$In_{0.4}Ga_{0.6}N$ nanowire laser.

The modulation response is shown in Fig. 4.17. The measured data have been analyzed with the small-signal response function:

$$|M(f)|^2 \propto \frac{1}{\left(f-f_r^2\right)^2+\left(\frac{\gamma_d}{2\pi}\right)^2 f^2} \tag{4.3}$$

where γ_d is the damping factor, and f_r is the resonance frequency of the modulation response.

A -3 dB modulation bandwidth of 2.4 GHz was measured at an injection current of 35 mA, and the resonance frequency at this injection level is 1.46 GHz. A higher -3 dB modulation bandwidth can be measured with higher injection currents, but this was not possible due to device and facet heating. The differential gain dg/dn can be derived from the small-signal modulation data using the relation:

$$f_r = \frac{1}{2\pi}\left[\frac{v_g \Gamma (I - I_{th})\frac{dg}{dn}\eta_i}{L w d_{act} q}\right]^{\frac{1}{2}} \tag{4.4}$$

where v_g is the photon group velocity, Γ is the confinement factor, η_i is the internal quantum efficiency, L is the cavity length, and d_{act} is the thickness of the active region. A value of η_i = 30% was used in the calculation. Taking the fill factor into account and a 24 nm active region, the confinement factor is 0.015 for the laser heterostructure. The plot of f_r vs. $(I\text{-}I_{th})^{1/2}$, obtained from the data of Fig. 4.17, is shown in Fig. 4.18. The slope of the plot is 0.103 GHz/$mA^{1/2}$, from which a differential gain dg/dn = 5.7×10^{-17} cm^2 is derived. The value is comparable to that of shorter wavelength (λ = 430 nm) strained and strain compensated InGaN/GaN quantum well lasers [120], [121]. However, it is considerably smaller than In(Ga)As/GaAs quantum dot lasers [122] possibly due to the large carrier effective masses in these materials. The differential gain value also matched well with the value calculated from length dependent measurements described in the previous section. The lasers do have some difference, and that explains why the determined differential gain values are not exactly same. The next chapter details further research that has been performed to enhance the values of the differential gain.

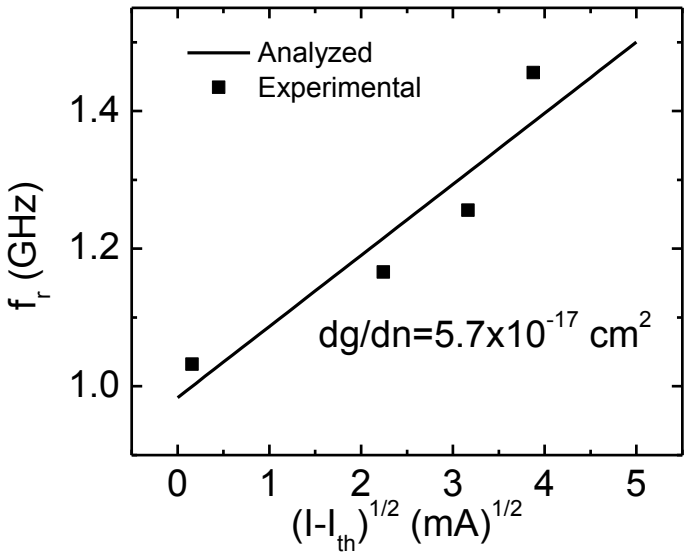

Figure 4.18 Plot of resonance frequency f_r versus square root of the injection current.

It is known that hole injection is non-uniform in InGaN/GaN multi-quantum well light-emitting diodes (LEDs) and lasers and a similar situation exist in multi-quantum dot devices. Most of the injected holes pile up in the first couple of wells or dots from the injecting p-layer, leading to increased carrier density, and hot-carrier effects, including gain compression. Our group has demonstrated tunnel injection of holes in InGaN/GaN QD LEDs [123] as a means to alleviate this problem to some extent. It is believed that such a tunnel injection design of the active region may lead to higher differential gain, lower threshold current density and higher modulation bandwidth in the InN/$In_{0.4}Ga_{0.6}N$ disk-in-nanowire array lasers. Under gain compression limited modulation response in the above-mentioned devices, the damping factor γ_d is related to f_r by the approximate relationship: $\gamma_d = Kf_r^2$. The proportionality constant is the K-factor which is a measure of the damping limited bandwidth. A plot of γ_d versus f_r^2, obtained from the analysis of the data of Fig. 4.17 using the equation mentioned above, is illustrated in Fig. 4.19.

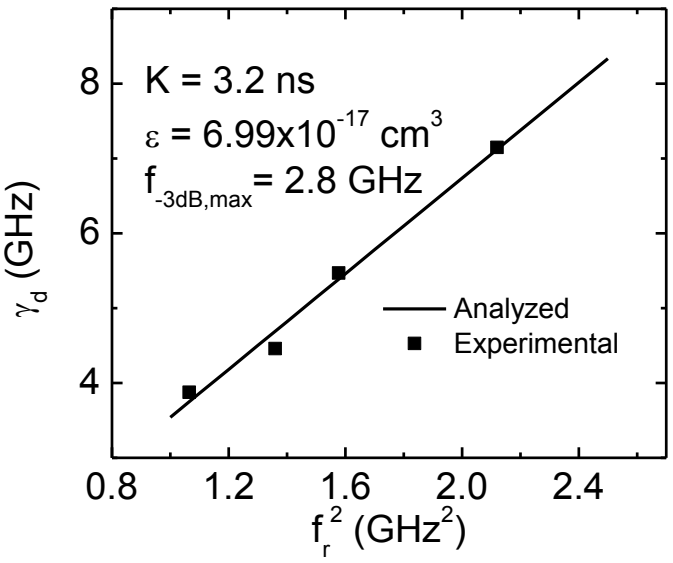

Figure 4.19 Plot of damping factor γ_d versus f_r^2.

A value of K = 3.2 ns is derived from the slope of this plot. A gain compression factor (ε) of 6.99×10^{-17} cm^3 is then derived from the approximate relationship:

$$K \cong 4\pi^2 \left(\frac{\epsilon}{v_g \frac{dg}{dn}} + \tau_p \right) \tag{4.5}$$

where τ_p is the cavity photon lifetime. This value of ε is comparable to those measured for In(Ga)As/GaAs quantum dot lasers [124].

Overall, the lasers show a significant advantage over existing lasers with higher temperature stability, lower threshold current density, and high differential gain. The lasers also have a high bandwidth which is ideal for communication-related purposes making them ideal for use in a variety of applications including photonics at extreme environmental conditions, silicon photonics, biomedical applications, and on-chip communication. The bandwidth of the lasers can be increased with better designs and fabrication processes. Overall the laser output characteristics can also be improved with better packaging and heat dissipation techniques.

4.4 Summary

This chapter describes and discusses the characteristics of monolithic III-nitride nanowire LEDs, and lasers directly grown on (001) silicon. Mainly two types of lasers with active regions as $In_{0.85}Ga_{0.15}N$ and InN disks are explored. LEDs with such high In disks have been demonstrated. These LEDs have favorable characteristics and can emit light at 1.3μm suitable for silicon photonics applications. These diodes have low series resistance making them ideal for high current applications. Edge-emitting lasers have also been made with the same laser heterostructure. Due to the high polarization fields in these materials, the $In_{0.85}Ga_{0.15}N/In_{0.4}Ga_{0.6}N$ laser emission wavelength is measured at 1.2μm. To further extend the emission wavelength InN disks have been incorporated. The lasers that use InN emit at a wavelength of 1.3μm which again is favorable for silicon photonics applications. The laser fabrication has been discussed in detail. Both steady state and dynamic measurements have been performed. The lasers have been modulated at high frequencies (few GHz) to demonstrate their usability for modulated signal based communication. Overall the lasers have sufficient optical power, acceptable slope efficiency, high characteristic temperature, appreciable bandwidth, promising differential gain, and low gain compression factor. The infrared output spectrum also makes these laser operations eye-safe. The favorable attributes of these lasers will make them ideal for a variety of applications, including, communication automobile, and biomedical applications.

Chapter V

III-Nitride Nanowire based Photonic Integrated Circuits and Infrared Detectors on Silicon Substrate

5.1 Introduction

This chapter describes a complete monolithic photonic integrated circuit on (001) silicon and mid-IR to long wavelength IR absorption of the disk-in-nanowires. The photonic circuit is based on disk(dot)-in-nanowire arrays which are directly grown on the silicon substrate using plasma enhanced molecular beam epitaxy. The device described here is first of its kind. The device employs InN/$In_{0.4}Ga_{0.6}N$/GaN based lasers and detectors with externally deposited dielectrics (SiO_2/Si_3N_4) as waveguides.

Such a monolithic photonic circuit can operate as a practical optical interconnect on a silicon based complementary metal-oxide-semiconductor (CMOS) chip. Both the diode laser and optical detector are monolithically integrated with guided wave components on a (001)Si wafer which is also useful as all the devices operate in the wavelength range of 1.3 – 1.55 μm at room temperature. Other advantages include relatively straightforward and reproducible fabrication technique.

Different methods have been used before to demonstrate photonic circuits, e.g., optically- and electrically-pumped GaAs- and InP-based lasers on silicon, integration of

the laser on silicon using wafer bonding, selective area epitaxy, epitaxy on tilted substrates, and using quantum dot or planar buffer layers to grow direct bandgap materials on Si. In the present study, all the active devices are realized with the same nanowire heterostructure which has been grown using a one-step epitaxy. The laser, emitting at the desired wavelength of 1.3 μm, with threshold current ~ 350 mA for a device of dimension 50μm×2mm, has been characterized in detail. The detector exhibits a responsivity of ~0.11 A/W at 1.3 μm. Operation of the entire optical interconnect via the dielectric waveguide has also been demonstrated.

The second part of the chapter discusses intersubband absorption of these disks-in-nanowire arrays. Such absorption characteristics have been determined from FTIR measurements at room temperature. The measured room temperature long wavelength absorption characteristics can be extremely favorable for next generation IR detectors. Strong absorption between ~1.6μm to ~20μm have been measured and described.

5.2 Photonic Integrated Circuit on (001) Silicon

5.2.1 Background

The biggest inhibitor in silicon photonics is the inability of silicon to work as an efficient optoelectronic emitter due to the indirect bandgap of Si. Therefore researchers have used various other methods to incorporate direct bandgap materials in silicon based circuits. There are two most common techniques of incorporating an electrically-pumped laser on a silicon platform. In both methods, the direct bandgap based device is integrated on the silicon either by direct epitaxy [25], [26], [125] or by wafer bonding [28], [126], [127]. There are three major challenges in the direct epitaxial growth of III-V materials

and heterostructures on silicon. There is a significant lattice mismatch between Si and the direct bandgap material which leads to a high density of threading dislocations. Also, there is a thermal mismatch between the two types of materials due to unequal thermal expansion coefficients. Finally, antiphase domains (APDs) are formed by the epitaxy of polar III-V materials such as GaAs on non-polar Si. The most common way to circumvent this problem is to grow the III-V heterostructure on a (001)Si substrate offcut by 4° toward the [011] plane [25], [26], [125]. Such tilted platforms are incompatible to the existing CMOS industry which significantly reduces the applicability of such photonic technology. So far, selective area epitaxy [128] and growth on special buffer layers [26], [129]–[132] have led to some success.

A monolithic optical interconnect consisting of a diode laser, a passive waveguide or other guided-wave elements, and a photodiode would be extremely useful. The lasers should have reasonable modulation characteristics so that they can constitute an optical communication system. Most importantly, the desired operating wavelength for such a system is ~1.3 μm, which results in zero dispersion in silica-based fibers and being eye-safe at the same time.

The unique properties of III-nitride nanowires and their heterostructures discussed in chapter I and the ability to epitaxially grow the nanowires directly on (001)Si discussed in chapter II, make them ideal for the realization of nanowire-based photonic integrated circuits with active devices on a (001)Si platform. The discussed optical interconnect has been realized by one-step epitaxy of III-nitride based nanowire heterostructure arrays on (001)Si, dielectric deposition, and standard device processing

steps. The optical interconnect also operates at ~1.3μm fitting very well to the above-mentioned requirements.

5.2.2 Epitaxy and fabrication

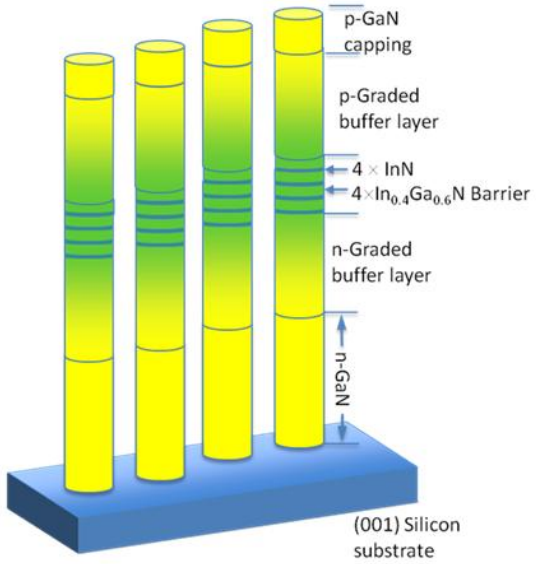

Figure 5.1 Schematic of $InN/In_{0.4}Ga_{0.6}N/GaN$ nanowire array laser heterostructure monolithically grown on (001)Si by plasma-assisted molecular beam epitaxy.

Figure 5.1 shows a graded refractive index separate confinement heterostructure (GRIN-SCH) nanowire array grown by plasma-assisted molecular beam epitaxy (PAMBE) on (001)Si substrates in a Veeco GEN II system. Epitaxial growth of similar heterostructures has been discussed in the previous chapter. Here, the epitaxial growth of the nanowire heterostructure array, used for the optical interconnect, is briefly discussed. Nitrogen plasma flows during the growth of the nanowire heterostructure was kept constant at a flow rate of 1sccm. The bottom n-GaN sections in the heterostructure were grown at a substrate temperature of 820°C and the top p^+-GaN region was grown at 800°C. Graded $In_xGa_{1-x}N$ cladding layers ($0 \leq x \leq 0.4$) were placed on both sides of the active region to improve the strain characteristics and the optical confinement. The

graded layer is formed with 10 equal steps of 15nm on both sides. The gain region consists of 4 InN disks of 6nm thickness surrounded by 12nm $In_{0.4}Ga_{0.6}N$ barriers grown at 489°C. The surrounding graded region was grown at substrate temperatures varying from 631°C ($In_{0.4}Ga_{0.6}N$) to 819°C (GaN). The Ga and In fluxes were varied in the range of 1.1×10^{-8}-1.2×10^{-7} Torr and 2×10^{-8}-1×10^{-7} Torr, respectively, depending on the composition of the material being grown. The heterostructure was designed without an electron blocking layer (EBL). Results from previous fabrications were used to infer that the electrical characteristics of the fabricated laser diodes, having 15 nm $Al_{0.15}Ga_{0.85}N$ EBL, were substantially inferior to those without the EBL. The height, diameter, and density of the nanowires were estimated to be ~700 nm, ~60 nm, and ~3.2×10^{10} cm^{-2}, respectively, from scanning electron microscope (SEM) images. The values of nanowire diameter and nanowire array density were then used to determine the fill factor of the nanowire array to be about 0.91. There is evidence of a quantum dot formation inside the active (disk) region of the nanowires which is shown in chapter I in Fig. 1.17. Such TEM data can be seen in [45] and are courtesy of Lifan Yan under the supervision of Professor Joanna Millunchick at the University of Michigan.

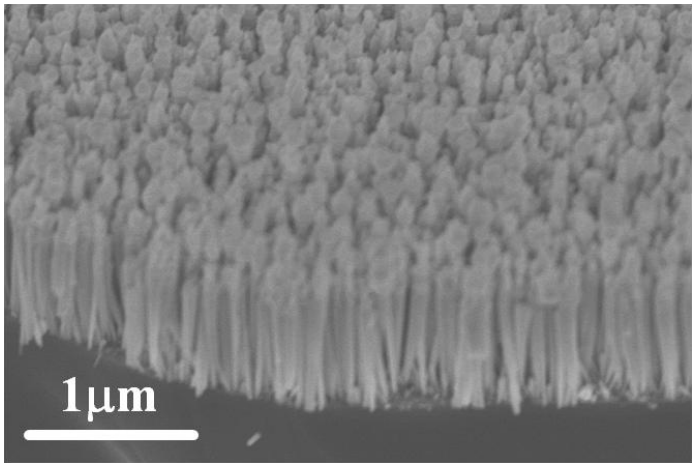

Figure 5.2 SEM image of heterostructure nanowire array.

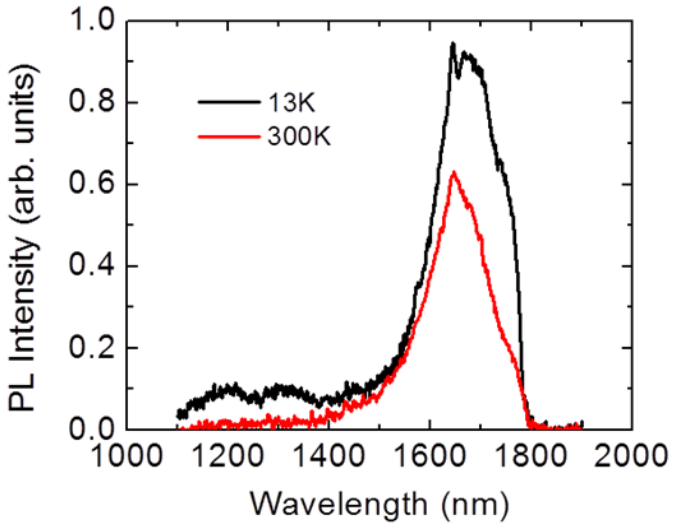

Figure 5.3 Measured room temperature and low temperature photoluminescence spectra of a nanowire array sample in which epitaxial growth was terminated after four $InN/In_{0.4}Ga_{0.6}N$ disk/barrier periods.

Low temperature (13K) and room temperature (300K) photoluminescence (PL) measurements were made on the half laser heterostructure. In these half laser heterostructures, growth was terminated after four periods of InN disks and $In_{0.4}Ga_{0.6}N$ barriers and the heterostructures were grown with the optimized parameters described earlier. The spectra recorded at 13K and 300K are illustrated in Fig. 5.3. An approximate value of the radiative efficiency (η_r) of 67% is estimated from the integrated PL peak intensities at 300K and 13K, assuming that non-radiative recombination channels are frozen at the latter cryogenic temperature [69].

To fabricate the laser diodes, the nanowire array was first planarized with parylene, which was deposited by physical vapor deposition (PVD) at room temperature. It has been reported that parylene is transparent at 1.3 μm [47] and thus the use of parylene does not reduce the efficiency of the laser. Furthermore, it is also known that parylene helps to passivate the nanowire surfaces and enhances the internal quantum

efficiency by 10-12% [111]. The PVD deposits the lowest thickness of about 2μm of parylene which is much thicker than the nanowires. The excess parylene is dry etched using a Cl_2 plasma to expose the nanowire tips, which are treated with ammonium sulfide to reduce the p-contact resistance [133], [134]. Ridge waveguide devices were fabricated in clean room environment by a combination of reactive ion etching, photolithography, and contact metal deposition. Al was used as the n-ohmic contact which was formed on the Si substrate top surface, and the Ni/Au p-ohmic contact was formed on the top to the exposed p^+-GaN nanowire tips. Ridge widths of 5 to 50 μm were defined by photolithography and etching which was followed by planarization with SiO_2 and interconnects and contact pad deposition. Cavity lengths of 0.5 to 2 mm were defined by dicing the substrate perpendicular to the cavity. The diced end facets on both sides were further polished by focused ion beam (FIB) etching using a Ga source. Finally, 3 pairs of MgF_2/ZnSe (237 nm/132 nm) distributed Bragg reflectors (DBR) were deposited on both end facets enabling the facets to attain a reflectivity of 88%. The contact geometry was arranged in a ground-signal-ground configuration to facilitate high-frequency probing. The laser diodes are characterized by a forward turn-on voltage of ~3V, a series resistance of 10 to 25Ω, and reverse breakdown voltage of 8 to 12V. The detector fabrication was also fabricated in similar steps, but instead of enhancing the facet reflectivity, the facet was engineered to be anti-reflective by depositing 223nm of SiO_2 on one facet. As discussed before, a facet reflectivity value of only 5% at 1.3μm was determined from simulations for such thickness of SiO_2.

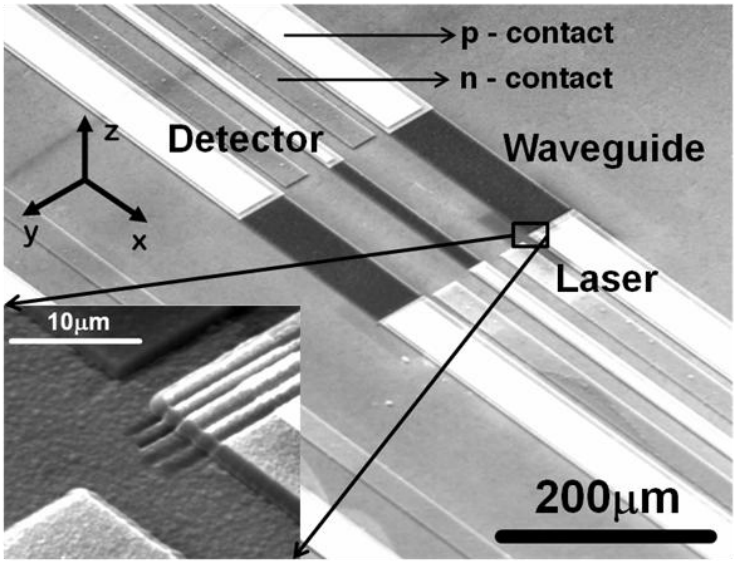

Figure 5.4 SEM image of the fabricated nanowire array photonic integrated circuit consisting of nanowire diode laser, guided wave photodiode and SiO_2/Si_3N_4 dielectric waveguide in between. The inset shows a magnified image of the air/nanowire DBR mirror formed by FIB etching.

The fabrication of the photonic integrated circuit follows near-identical steps enabling us to fabricate both the laser and the detector on the same chip, forming the photonic integrated circuit. The dielectric waveguide in between the nanowire laser and detector is formed by selective etching of the nanowires and deposition of 400 nm SiO_2 followed by 400 nm of Si_3N_4. This multilayer waveguide has reduced waveguide loss significantly. For the laser, the facet away from the waveguide was made reflective by FIB etching, and subsequent deposition of $MgF_2/ZnSe$ DBR layers and the facet coupled to the waveguide was made reflective with 4 pairs of air/nanowire-parylene DBR layers. These air/semiconductor DBR layers were formed by FIB etching (shown in the inset of Fig. 5.4). For the detector, ~220 nm of anti-reflective SiO_2 was deposited on the facet away from the waveguide. The coupling grooves between the waveguide and the two active devices are ~5μm.

We have also fabricated discrete nanowire lasers, detectors and dielectric waveguides in addition to fabricating the entire monolithic photonic integrated circuit. The discrete devices enabled detail performance characterizations which are reported in this work. A SEM image of the whole photonic circuit is shown in Fig. 5.4 wherein the laser, waveguide, detector and the p- and n-contacts for current injection are indicated.

Control devices were also made to measure the propagation loss of the SiO_2/Si_3N_4 dielectric waveguide. Waveguides were fabricated by the deposition of 400 nm SiO_2 followed by 400 nm of Si_3N_4 directly on (001)Si substrates and subsequent photolithography and etching. Waveguides of lengths varying from 100 μm to 200 μm and width of 5 μm to 50 μm were defined by the photolithography and etching process. The waveguides were end-fired with focused light from an 850 nm laser, and the output intensity was measured with an infrared detector. The measured output as a function of waveguide length is plotted in Fig. 5.5, from which a propagation loss of 12.4 dB/cm is derived.

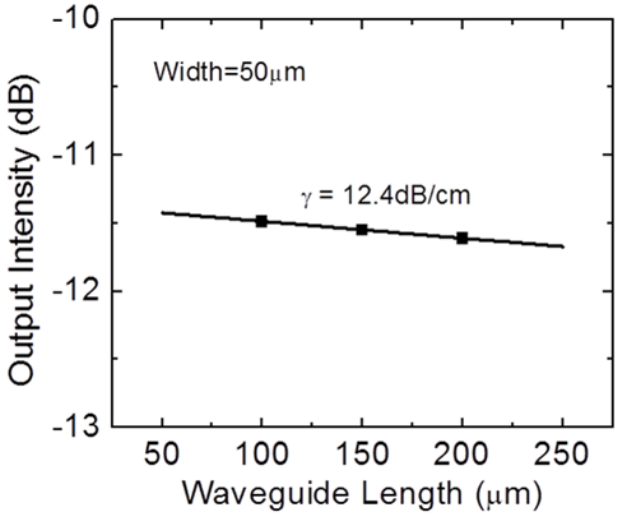

Figure 5.5 Measured variation of transmitted light intensity with dielectric waveguide length. The waveguides were end-fired with a constant 850 nm input excitation.

The low loss waveguide adds only 0.2dB loss of the laser light throughout the entire length of the 200μm waveguide. The waveguide loss can even be further reduced by increasing the bottom SiO_2 thickness. However, the light is coupled using the Si_3N_4 layer. Accordingly, the nanowire height has to be changed. There are reports of waveguides with minimal loss using this multilayer technique [135], [136]. The light from the laser does encounter a significant loss which will be depicted later in this chapter. The waveguide loss measurement proves that the majority of the laser light loss is from the scattering loss at various facets and junctions, for example, waveguide to detector junction, laser to waveguide junction and the FIB based mirror facets.

Different aspects of the nanowire heterostructure have been characterized in detail in a collaborative manner between multiple research groups. The electric field distribution, strain distribution and their significance in light propagation, and photoluminescence have been discussed in depth in [45].

5.2.3 Nanowire array laser and guided wave detector

5.2.3.1 Laser

This section describes measurements performed on the discrete nanowire lasers and guided wave detectors. The section described both steady state and dynamic measurements performed on the optoelectronic device.

First, steady state measurements were made on the discrete nanowire lasers. These lasers were mounted on a copper block without any additional heat sinking. The laser temperature was maintained at the ambient temperature (~300K) with active biasing using a Peltier cooler.

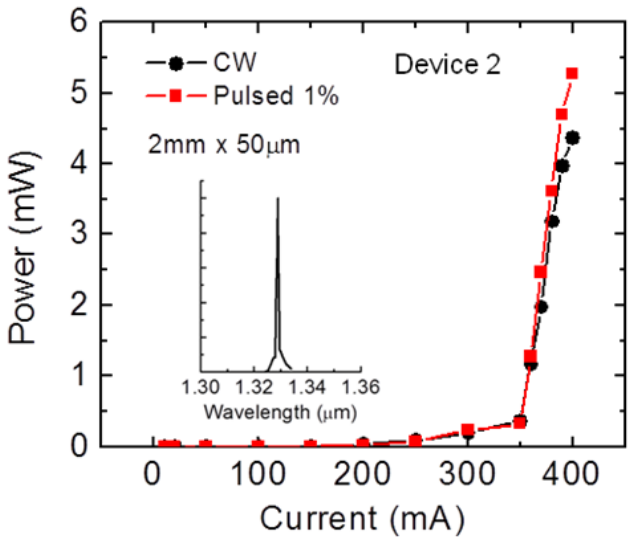

Figure 5.6 Measured output light-current characteristics of discrete edge-emitting heterostructure InN/InGaN/GaN dot-in-nanowire diode laser. The laser end mirrors are created by FIB etching followed by deposition of MgF_2/ZnSe DBR. The output power is from one facet. The inset shows the spectral output for an injection $I = 1.2I_{th}$, where I_{th} is ~ 350 mA.

Figure 5.6 shows the light-current (L-I) characteristics of a broad area (50 μm × 1.5 mm) laser measured in both continuous wave (CW) and pulsed bias mode (20 μs pulses, 1% duty cycle). A Keithley power source and a Newport IR detector were used to measure the L-I characteristics. The slope efficiency has improved for the pulsed biasing mode compared to the CW mode and calculated to be 0.12 W/A. Detailed spectral measurements of the lasing spectrum were also performed, and a peak emission wavelength at a bias of $I_{inj}=1.2I_{th}$ has been shown in the inset of Fig. 5.6. The peak wavelength has been measured to be at ~1.3 μm. There is a strong blueshift of this EL emission peak compared to the PL emission peak which was measured at ~1.6 μm, possibly due to the injection-related quantum confined Stark effect.

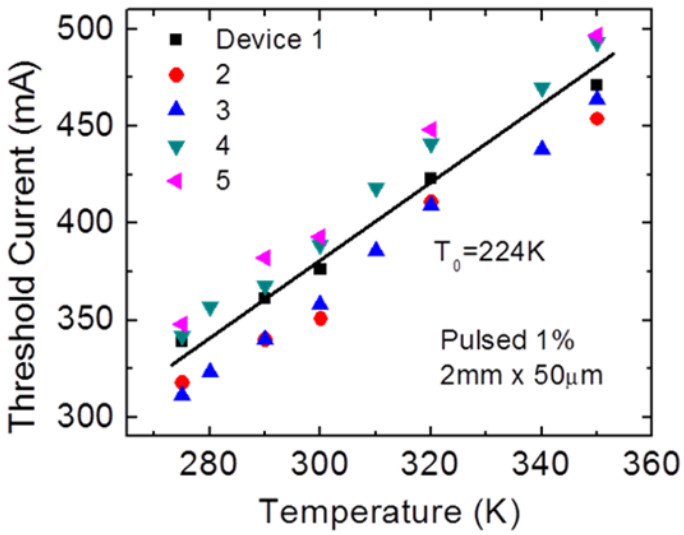

Figure 5.7 Measured variation of threshold current with temperature of multiple devices under pulsed biasing. The solid line represents the average calculated variation.

The L-I characteristics were also measured as a function of temperature to understand the temperature dependence of these lasers. The temperature dependent L-I measurements were performed by varying the laser mount temperature in the range of 275-350K. Figure 5.7 shows the measured variation of the threshold current with temperature of 5 such laser diodes. These measurements were analyzed with the following equation,

$$I_{th}(T) = I_{th}(0)\exp\left(\frac{T}{T_0}\right) \quad (5.1)$$

where $I_{th}(T)$ is the threshold current at tempearture T, $I_{th}(0)$ is the threshold current at 0K, and T_0 is the characteristic temparture.

This analysis was used to calculate a maximum temperature coefficient (T_0) value of 224K which is much higher than those measured in 1.3µm InGaAsP/InP quantum well lasers [137].

It is necessary to transmit a modulated signal for an inter- and intra-chip communication link. Therefore small-signal modulation measurements have been

performed on the discrete 5µm × 500µm ridge waveguide laser. The small-signal modulation response of these discrete lasers was measured with a Hewlett-Packard 8350B sweep oscillator, Hewlett-Packard 83599A RF plug-in, bias T, low-noise amplifier, Newport high-speed detector and Hewlett-Packard 8593A spectrum analyzer.

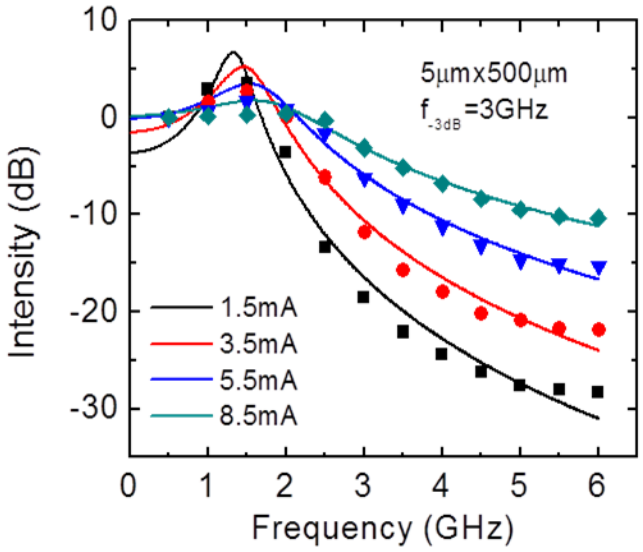

Figure 5.8 Measured response of edge-emitting 1.3µm nanowire diode laser to varying high frequencies and bias currents. The values of currents shown are above the threshold current.

Figure 5.8 shows the frequency response for varying CW injection currents ($I-I_{th}$). Each point represents the peak value of the spectral output at the corresponding frequency. The solid curves represent calculated modulation response in accordance with a response function incorporating damping limited operation. The data have been analyzed with the response function explained in equation 4.3. A -3dB modulation bandwidth of 3.0 GHz has been derived from an injection current of ($I-I_{th}$) = 8.5 mA from this measurement. Figure 5.9 shows a plot of f_r versus $(I-I_{th})^{1/2}$ from which a slope of 0.33 GHz/$(mA)^{1/2}$ is derived. This value of slope can then be used to calculate the differential gain dg/dn by the relation given in equation 4.4. Transfer-matrix-element method based simulations have been performed to determine the value of Γ. It has been determined that

Γ = 0.0137. The simulation assumes the laser as a planar device, which is evident from plane wave propagation based simulations described in chapter I. η_r value is taken to be 67% as measured from the PL measurements. These values of Γ and η_r have been used to determine the value of dg/dn which has been calculated to be 2.9×10^{-16} cm^2.

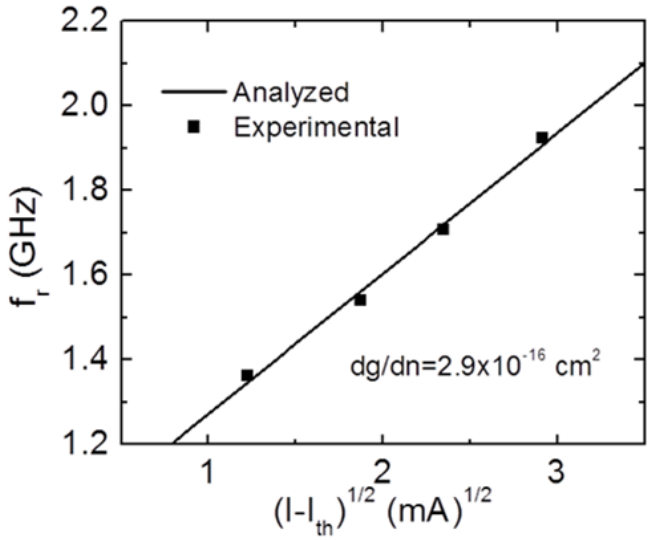

Figure 5.9 Variation of resonance frequency derived from the data in c with the square root of injection current.

The damping factor γ_d is also derived from analysis of the modulation data following similar procedure as detailed in chapter IV. Figure 5.10 shows the plot of γ_d versus f_r^2. The slope of this figure has been used to derive K = 3.75 ns and $\epsilon = 4.2\times10^{-16}$ cm^3. Here, it is assumed that the value of cavity photon lifetime τ_p = 3.2 ps.

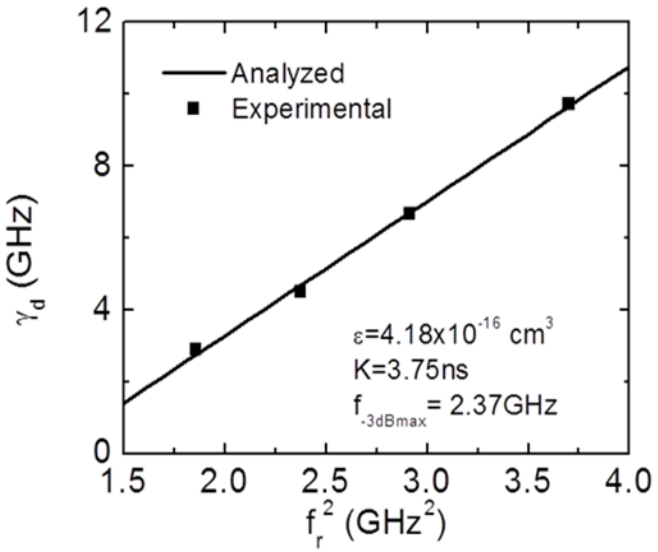

Figure 5.10 Variation of the damping factor γ_d, determined from analysis of the modulation response, with the square of the resonance frequency.

The experimental results have been used to determine the 3-dB modulation bandwidth for these monolithic lasers on silicon, which was found to be relatively low. Such low values can be a result of a variety of reasons. The bandwidth, or resonance frequency (f_r), is proportional to the photon density, or injection, and the differential gain. For these lasers, device heating has prevented the measurement of the modulation response at higher injection currents. The differential gain decreases with bandgap energy and the value measured in this study is lower than those measured in 1.3µm InGaAsP/InP quantum wells [138] and InAs/GaAs quantum dot lasers [116], [117]. With further improvement of the lasers, such as superior heat dissipation and packaging techniques, higher bandwidths can be achieved. Such methods will enable the laser operation at higher current injection levels. At such high current injection levels, the laser will be able to demonstrate a higher bandwidth.

5.2.3.2 Guided wave detector

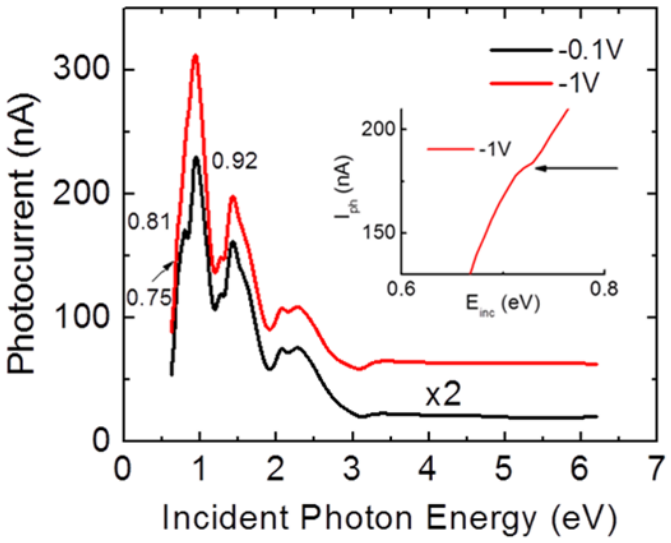

Figure 5.11 Photocurrent spectra of reverse biased nanowire photodiode. Inset shows the 0.75eV transition in the photocurrent at a bias of -1V.

Discrete guided wave dot-in-nanowire photodiodes were also measured to determine their performance characteristics. To measure the photocurrent spectra of these photodiodes, they were reverse biased and end-fired with light from a broadband source dispersed by a 0.125m CM110 monochromator with a spectral resolution of 0.2nm. The spectral measurements were performed at room temperature. The value of the reverse bias applied to the photodiode was varied to understand the evolution of the photocurrent spectra with bias. The value of the photocurrent was measured with a Keithley 6487 picoammeter having a resolution of 1 pA. Figure 5.11 shows the measured spectra. Several shoulders and peaks can be observed at energies close to the absorption edge from these figures.

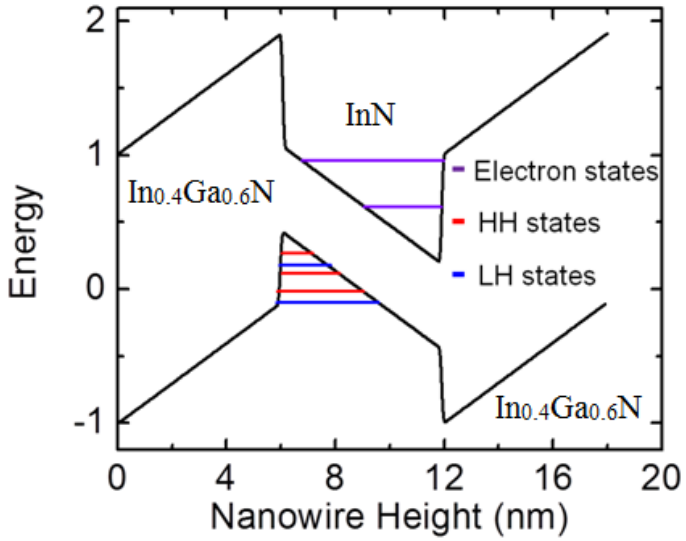

Figure 5.12 Electron and Hole subband levels in a 6nm InN disk surrounded by $In_{0.4}Ga_{0.6}N$ barrier material.

To better understand these transition energies we have performed a rudimentary simulation of the nanowire heterostructure. The simulation outputs intersubband energy levels in the disks which can be seen in Fig. 5.12. A polarization field value of 3MV/cm is used as one of the input parameters of the simulation. The value of the polarization field has been determined from the difference between the measured PL emission peak and the above-threshold EL emission peak. The simulations and the experimental data can be used to infer that the shoulders at ~0.75 and ~0.81 eV and a peak at approximately ~0.92 eV correspond to the transition energy values for E_1-H_1, E_2-H_2, and E_3-H_3 transitions, respectively. Here $E_{1,2,3}$ is defined as the electron ground state and first and second excited states in the conduction band. Similarly, $H_{1,2,3}$ is defined for the hole states. The simulation has also been performed as a function of bias to ensure these electron and hole subband levels do not significantly change due to the variation of the reverse bias which is shown in Fig. 5.13. It can be observed from the Fig. 5.13 that the

band bending due to the change in reverse bias is negligible as large polarization field already exists in the nanowire heterostructure.

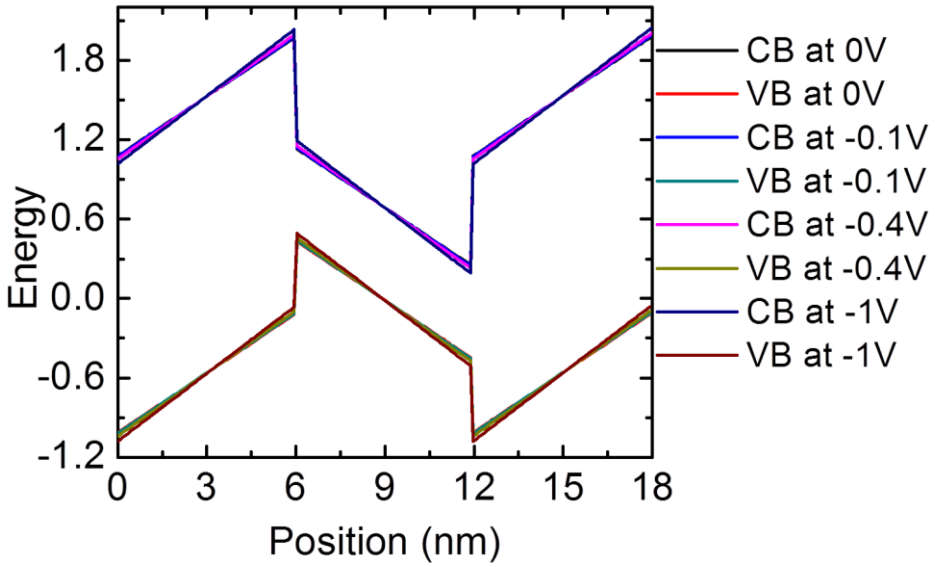

Figure 5.13 Variation of the band bending as a function of applied reverse bias.

Initial simulations also show there is a good degree of band mixing in the hole states which makes it difficult to ascertain whether the hole states originate from heavy or light holes. There are more peaks and shoulders observed at higher energies in the photocurrent spectra. These are probably originating from the graded and other regions of the nanowire heterostructure. There is a slight shift in the peaks between the spectra recorded with -0.1 and -1.0 V bias explained from the simulation shown in Fig. 5.13. Since the laser emits at 1.3 μm, it is important to understand the responsivity of the photodiode at this wavelength. The responsivity value is determined to be 0.11 A/W at 1.3 μm from the spectrum recorded at -1.0 V. This value is determined by taking into account the incident power of 923 μW, a facet coupling of 0.33% and a nanowire fill factor of 0.91. The coupling factor is much smaller than that shown in the previous

chapter due to the different detector geometry, and the difference in the fiber used for the light coupling.

5.2.4 Characterization of photonic integrated circuit

This section describes the characteristics of a monolithic photonic integrated circuit on (001)Si. For this measurement, the laser has been excited with a dc pulsed injection bias (20 μs pulses, 1% duty cycle). The photocurrent response of the detector to the light emitted by the laser and coupled to the waveguide between the two devices has been recorded. Figure 5.14 shows the evolution of the reverse photocurrent of the photodiode as a function of laser injection current while the photodiode was reverse biased at -1.0V. The measurement can also be done at other reverse biases. If the reverse bias is too much, the dark current may be too high. Therefore, a low value of -1V is chosen. For this measurement, both the laser and detector fabricated have a width of 50 μm, and they have a length of 2 mm and 1 mm, respectively. There is a SiO_2/Si_3N_4 waveguide in between which is 200 μm long and 50 μm wide. The results demonstrate that the photodiode reverse saturation current follows the laser light-current characteristics quite well. A 10-fold increase (0.2μA to 2μA) in the reverse saturation current of the photodiode has been measured. It is estimated that only ~ 20 μW of optical power is received by the photodiode from the laser when the laser is biased at 400mA. This calculation has been done considering the measured detector responsivity of 0.11 A/W at 1.3 μm. The waveguide has a minimal loss as measured from the waveguide loss measurements. Hence, it is highly likely that the factors that contribute to the loss of power emitted by the laser and ultimately coupled to the photodiode are scattering losses at the air/semiconductor DBR mirror, coupling into and out of the waveguide and

reflection losses at the input facet of the photodiode. It is expected that improved design and fabrication can substantially increase the light coupled into the photodiode. Better FIB techniques and facet coating can also improve the amount of light coupling.

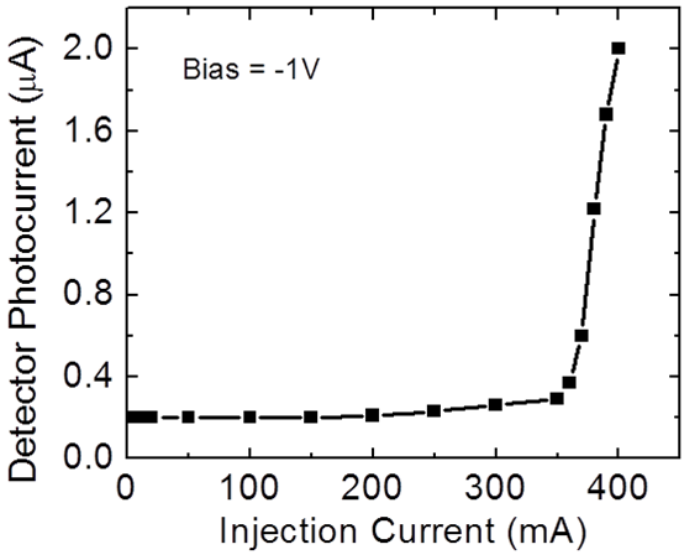

Figure 5.14 Steady-state photocurrent of reverse biased nanowire photodiode in the photonic integrated circuit in response to pulsed injection current applied to nanowire laser. The light is coupled to and guided by the dielectric waveguide to the detector.

5.3 Intersubband Absorption in Disk-in-nanowire Arrays

5.3.1 Introduction

So far the discussion has been limited to light emitted and absorbed at near-infrared using III-nitride nanowires. It is possible to further extend the wavelength of operation of III-nitride nanowire heterostructures to mid- to long-wave infrared which is the main topic of discussion of this section. Simulations of various nanowire heterostructures were used to conclude that $In_{0.34}Ga_{0.66}N$/GaN nanowire heterostructures have more available electron and hole subbands compared to InN/$In_{0.4}Ga_{0.6}N$ nanowire heterostructures. The simulated band diagram of $In_{0.34}Ga_{0.66}N$/GaN nanowire heterostructure can be seen in Fig. 5.15. In the previous section (Fig. 5.12) the simulated

band diagram of InN/$In_{0.4}Ga_{0.6}N$ nanowire heterostructures is shown. Hence in this section, the focus will be on the epitaxial growth and characteristics of green emitting $In_{0.34}Ga_{0.66}N$/GaN disks-in-nanowire heterostructure arrays.

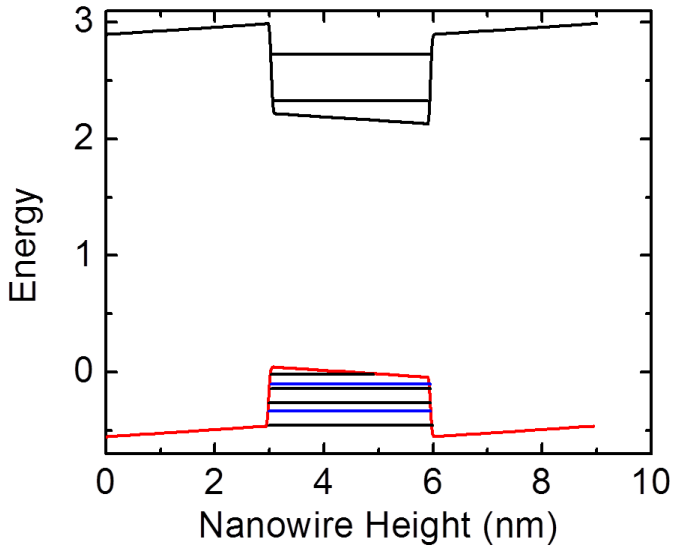

Figure 5.15 Electron and Hole subband levels in a 3nm $In_{0.34}Ga_{0.66}N$ disk surrounded by GaN.

Mid- and long wave-infrared (MIR and LWIR) detectors are being utilized in a wide variety of applications, including chemical spectroscopy, terrestrial and extra-terrestrial communication and imaging [9], [10]. These are also extremely useful as the absorption lines of many gas molecules, such as ozone, water, carbon monoxide, carbon dioxide, and nitrous oxide occur in the wavelength region from 3 to 18 μm. Hence, MIR and LWIR regions (3–18 μm) are also useful in imaging systems. These imaging systems are required in many space applications such as monitoring the global atmospheric temperature profiles, relative humidity profiles, cloud characteristics, and the distribution of minor constituents in the atmosphere which are being planned for NASA's earth observing systems. Usually, semiconductor IR detectors are categorized into interband detectors with small-bandgap semiconductors, intersubband detectors utilizing bound-

state transitions in quantum confined heterostructures and antimonide-based superlattice detectors [139]. InSb [140] and HgCdTe-based devices [141] are examples of the first type. Some examples of the second category of detectors are Quantum Well Intersubband Photodetectors (QWIPs) [142], [143] and Quantum Dot Intersubband Photodetectors (QDIPs) [144], [145]. These IR detectors are mostly based on homoepitaxial growth on relatively more expensive and often difficult to acquire III-V substrates compared to economically viable Si substrates. So far, a monolithic silicon-based IR detection technology has not been demonstrated mostly because of the difficulty in the growth of suitable defect-free light absorbing semiconductor heterostructures that have high quantum efficiency on silicon. Hence, a viable silicon-based infrared detector array technology represents a breakthrough in the field of MIR and LWIR detectors. Such a revolutionary device would be able to eliminate In-bump bonding of the detector arrays onto silicon readout integrated circuits (ROICs). The elimination of In-bump bonding will be a major advantage over existing devices which suffer from performance degradation due to the hybridization process associated with In-bump bonding. The traditional detector arrays and ROICs also suffer from thermal mismatch which can also be circumvented with the use of such ground-breaking Si-based detectors.

Overall, this section mainly focuses on the growth of the $In_{0.34}Ga_{0.66}N$/GaN disk-in-nanowire arrays on (001)Si substrates by molecular beam epitaxy and their infrared absorbance which have been measured at room temperature. The average diameter of the nanowires and area density of the nanowire arrays were determined to be 60nm and $2\times10^{10}cm^{-2}$, respectively from SEM measurements. The nanowires have a peak emission wavelength of 540nm at room temperature as measured by photoluminescence

measurements. The absorbance has been measured with a Fourier Transform Infrared Spectrometer both in transmission and reflection modes shown in Figs. 5.20 and 5.21. Multiple absorption peaks ranging from ~1.6 to ~20μm have been observed in these Figs. The peak energies measured from the absorbance have been compared with the intersubband transitions calculated with the simulations previously described. It is observed that some of the peaks do agree well with the simulated values.

5.3.2 Epitaxial growth of the $In_{0.34}Ga_{0.66}N$/GaN disk-in-nanowire arrays

This section specifically discusses the epitaxial growth of MIR and LWIR absorbing nanowire arrays. Chapter II was dedicated for the discussion of the epitaxial growth of the nanowires.

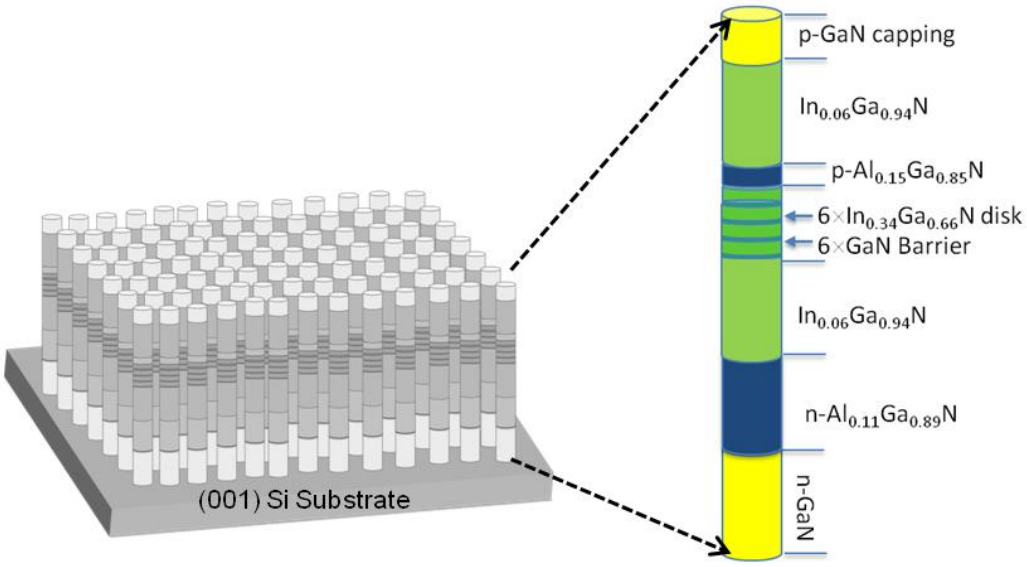

Figure 5.16 Schematic of InGaN/GaN disk-in-nanowire heterostructure array grown directly on (001)Si substrate by plasma assisted molecular beam epitaxy. Inset shows the different regions incorporated in the heterostructure.

Figure 5.16 illustrates the schematic of a III-nitride disk-in-nanowire array grown by plasma-assisted molecular beam epitaxy (PA-MBE). The nanowires were grown on both undoped and n-type (n ~$5\times10^{19}cm^{-3}$) doped (001)Si substrates. The active absorbing

region of the heterostructure consists of 6 pairs of 3nm $In_{0.34}Ga_{0.66}N$ and 12nm GaN barrier surrounded by 250nm $In_{0.06}Ga_{0.94}N$ regions on both sides. The nanowire epitaxial growth is initiated with 150nm n-type ($n = 0.5\times1.0\times10^{19}cm^{-3}$) GaN, followed by a 600nm n-type ($n = 5\times10^{18}cm^{-3}$) $Al_{0.11}Ga_{0.89}N$ region. The top $In_{0.06}Ga_{0.94}N$ region is followed by 540nm of p-type GaN with a doping level of around $5\times10^{18}cm^{-3}$. There is a thin 15nm p-type $Al_{0.15}Ga_{0.85}N$ region which is inserted on top of the $In_{0.06}Ga_{0.94}N$ region. The heterostructure is ideal to make photodiodes for future guided-wave photodetector measurements. Hence absorbance data from such a heterostructure will be straightforward to correlate with any future photocurrent data. The ternary alloy compositions were measured by X-ray diffraction (XRD) measurements performed on control bulk nanowire samples as XRD signal from such thin disk layers can be very weak and erroneous.

Detailed growth conditions have been described next. All the heterostructures are epitaxially grown under nitrogen rich conditions with a nitrogen flow rate of 1sccm. First, a n-type GaN region was grown at a substrate temperature of 819°C and a Ga flux of 1.17×10^{-7} Torr. Then the $Al_{0.11}Ga_{0.89}N$ layer was grown. The growth temperature was kept same, but Ga flux was changed to 1.1×10^{-7} Torr and Al flux was kept at 2×10^{-9} Torr. Next, the $In_{0.06}Ga_{0.94}N$ regions were grown at 717°C. In this layer, the Ga flux was kept at 1×10^{-7} Torr and the In flux of 4×10^{-8} Torr. The active region, 6 $In_{0.34}Ga_{0.66}N$ disks and GaN barriers, was grown at 639°C. For the disks, the In flux was kept at 2×10^{-8} Torr and the Ga flux was kept at 6.2×10^{-8} Torr. Then the $Al_{0.15}Ga_{0.85}N$ region was grown at a growth temperature of 781°C with an Al flux of 2.2×10^{-9} Torr and Ga flux of 9.2×10^{-8}

Torr. Finally, the top p-GaN region was grown at 781°C with a Ga flux of 9.8×10^{-8} Torr. Si and Mg were used as the n-dopant, and p-dopant, respectively. The average length and diameter of the nanowires were determined to be ~2μm and 60nm, respectively from scanning electron microscope (SEM) images. Such a SEM image is shown in Fig. 5.17. From these SEM images nanowire area density and fill factor were estimated to be ~$2x10^{10}cm^{-2}$ and 0.47, respectively. Similar to the previous measurements, the SEM tool used here also was a Hitachi SU8000. More details of the SEM tool can be obtained in the previous chapters.

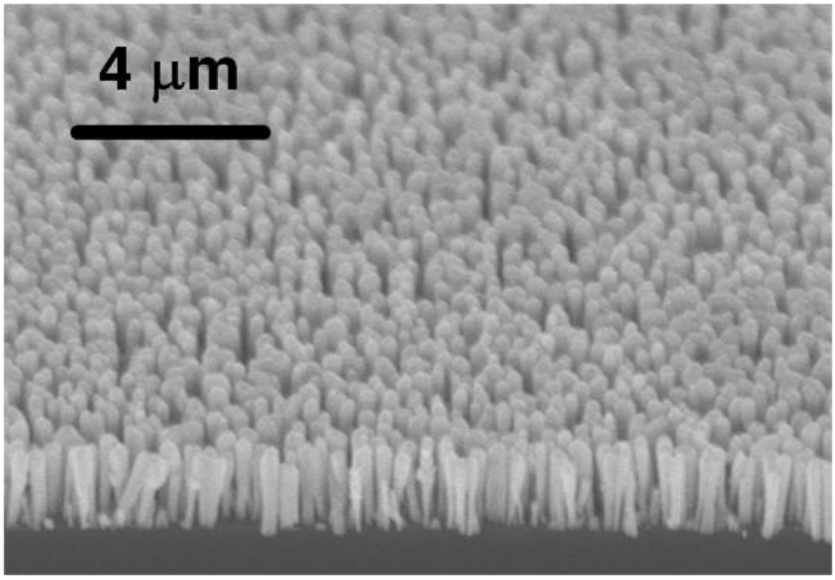

Figure 5.17 Scanning electron microscope image of an $In_{0.34}Ga_{0.66}N$/GaN disk-in-nanowire array.

5.3.3 Optical characterization

A variable temperature cryostat has been used to perform temperature dependent photoluminescence (PL) measurements on the nanowire samples. A He-Cd laser (λ = 325nm) or a diode laser (λ = 405nm) was used to excite the nanowire array. A 0.75m Princeton Instruments monochromator was used to analyze the luminescence, and a

Hamamatsu photomultiplier tube (PMT) was used to detect the luminescence of the nanowire array. The PMT can detect light from 185 to 900nm. The incident intensity of the focused light on the samples was estimated to be ~30kW/cm^2 from measuring the light power incident on the sample and from the knowledge of the objective lens employed in this measurement. The closed loop He cryostat has been used to vary the temperature of the samples in the range of 8K to 300K (room temperature).

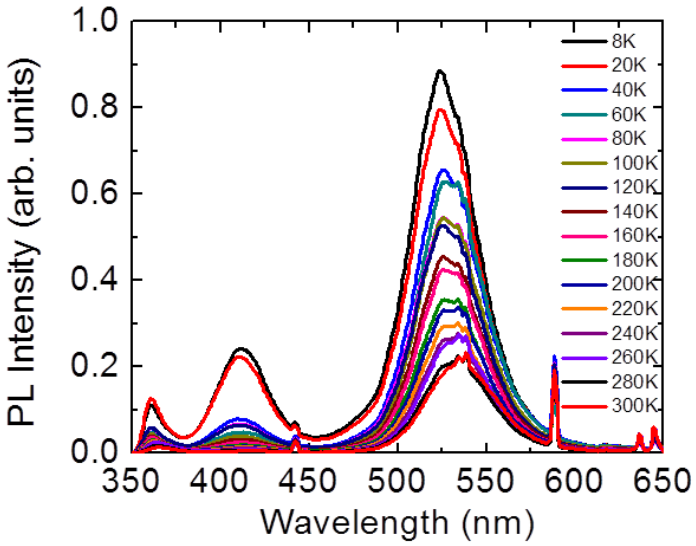

Figure 5.18 Temperature dependent photoluminescence on the $In_{0.34}Ga_{0.66}N$/GaN disk-in-nanowire samples.

The variation of the PL spectra with temperature is shown in Fig. 5.18. The GaN peak can be seen at 367nm, and there is another weak peak around 420nm most possibly due to alloys formed in between the GaN barriers and the $In_{0.34}Ga_{0.66}N$ disks. Other sharp peaks are from spurious emissions from the He-Cd laser. The main peak is seen at ~540nm. It is evident from this image that the peak position varies with temperature as predicted by Varshni's equation [62].

Figure 5.19 shows the variation of PL peak energy with temperature for a sample grown on undoped (001)Si substrate. The inset shows the PL spectrum recorded at 300K,

with peak emission wavelength at 540nm (green). The ultraviolet diode laser has been used to measure this PL. This diode laser does not have any spurious emissions which is apparent from the plotted PL data. As the sample temperature is varied from 300K to 8K, a blue shift of ~40meV has been calculated from the PL peak emission.

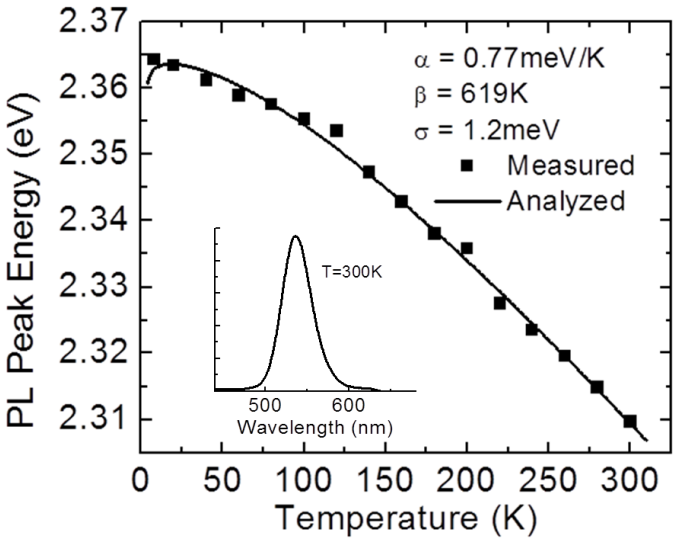

Figure 5.19 Variation of photoluminescence peak energy with temperature for an $In_{0.34}Ga_{0.66}N$/GaN disk-in-nanowire array grown on undoped (001)Si substrate. The solid line represents an analysis of the measured data. Inset shows the measured photoluminescence spectrum recorded at 300K.

This shift in the PL peak emission has been analyzed with the Varshni equation, wherein localization effects are also included [146], [147]. The localization factor is added to the Varshni equation by addition of the third term on the right-hand side of the following equation,

$$E_g(T) = E_g(0) - \frac{\alpha T^2}{\beta + T} - \frac{\sigma^2}{k_B T} \qquad (5.2)$$

where $E_g(T)$ is the bandgap of the material at temperature T, $E_g(0)$ is the bandgap of the material at 0K, k_B is the Boltzmann constant, and α, β and σ are analysis parameters. The localization factor is given by σ.

The solid curve represents the analyzed variation of the peak energy with temperature in accordance with the values of α, β and σ shown in the figure. The α and β values are in good agreement with previously published ones [63]. The small value of σ (1.2meV) and the absence of any significant S-type behavior [148], [149] suggest that phase separation, clustering, and related localization effects, if present, are minimal.

5.3.4 Infrared absorption in $In_{0.34}Ga_{0.66}N$/GaN disk-in-nanowires

The measurement and the results detailed in this section have been performed by Dr. Alexander Soibel in Dr. Sarath D. Gunapala's research group at Jet Propulsion Laboratory (JPL), California. A Nicolet Fourier Transform Infrared spectrometer (FTIR) equipped with deuterated triglycine sulfate (DTGS) detector and IR source, operating in the fast scan mode, was used to measure the transmission and reflection spectra of the InGaN/GaN disk-in-nanowire arrays. The absorption of the nanowires has been calculated from the measurement of such transmission and reflection spectra from bare Si substrates and substrates with epitaxially grown nanowire arrays. The measurements were performed at room temperature. First, the absorbance data measured from transmission measurements will be described. The data has been shown in Fig. 5.20.

In all transmission measurements, the nanowire samples were grown on undoped Si as doped Si absorbed the entire incident IR light. The transmission measurements are performed by normal incidence. Two samples were measured for each growth run. The first sample was the nanowire array on the undoped Si substrate, and in the second sample the nanowire array was completely etched away by plasma assisted reactive ion etching. The second sample enabled the transmission through the substrate alone to be measured providing an estimate of the Si substrate absorption when compared to the

incident signal. The difference of the transmissions measured for these two samples is the absorption in the disk-in-nanowire array. The absorbance is shown in Fig. 5.20 normalized with respect to the background signal.

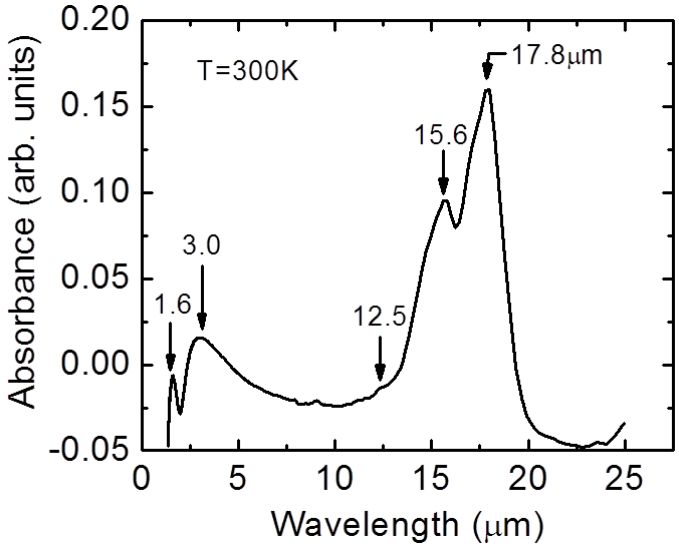

Figure 5.20 Room temperature absorbance determined from transmission measurements on $In_{0.34}Ga_{0.66}N$/GaN disk-in-nanowire arrays on undoped Si substrate. (Courtesy of Dr. Alexander Soibel in Dr. Sarath D. Gunapala's research group at Jet Propulsion Laboratory (JPL), California.)

In contrast, reflection measurements were done on nanowire samples that were grown on n-type doped (001)Si to ensure all the light is reflected rather than transmitted. Similar to the transmission measurements, reflection measurements were performed from both the bare n-type Si substrate and the nanowire array on the substrate. The measurements were conducted at an angle of 8 degrees to the normal. The differences between these two types of samples' reflection spectra provide estimations for the nanowire array absorption features seen as sharp peaks in the absorbance plot of Fig. 5.21.

It can be observed that both spectra in Figs. 5.20 and 5.21 display negative values of absorbance which can be due to multiple reasons. Changes in the surface morphology

of the Si substrate caused by etching and epitaxial overgrowth of the nanowires are the most likely cause of such negative values.

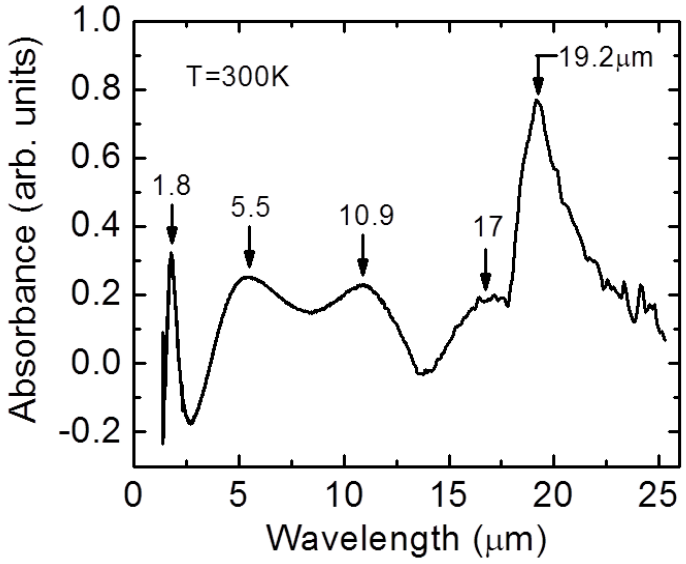

Figure 5.21 Room temperature absorbance determined from reflectance measurements on $In_{0.34}Ga_{0.66}N$/GaN disk-in-nanowire arrays on n-type Si substrate. (Courtesy of Dr. Alexander Soibel in Dr. Sarath D. Gunapala's research group at Jet Propulsion Laboratory (JPL), California.)

The spectra in Figs. 5.20 and 5.21 show clear infrared absorption peaks. The spectrum in Fig. 5.20 obtained from transmission measurements shows absorption peaks at 1.6, 3.0, 15.6 and 17.8μm. There is also a weak shoulder observed at ~12.5μm. Similarly, clear peaks are observed at 1.8, 5.5, 10.9, 17, and 19.2μm in the absorbance plot of Fig. 5.21 obtained from reflectance measurements. It is quite evident that the peaks from the two measurements are at different spectral positions even though the samples used in the transmission and reflectance measurements have nominally identical compositions and thicknesses in the nanowire and disk regions. Such differences are most possibly because they were grown at different times which can cause slight differences in InGaN disk compositions, strain and polarization field. Such small changes in material parameters can cause small variations in the energy position of the bound states. It is

indeed seen from the measured data that the differences between the peak energy in Figs. 5.20 and 5.21 are quite small. For example, the difference in energy between 1.6 and 1.8μm is 86.1meV, while that between 17 and 17.8μm is only 3.3meV.

The bound electron and hole state energies in the $In_{0.34}Ga_{0.66}N$/GaN disks were calculated by iteratively solving the Poisson and Schrödinger equations and the data has been shown in Fig. 5.15. In this calculation, the 3nm disks were assumed to be quantum wells. The bandgap energy of the quantum wells is taken to be 2.18eV. Following previously reported data [63], 760meV is taken to be the value of the conduction band offset (ΔE_c), and 510meV is taken to be the value of the valence band offset (ΔE_v). A polarization field of 618kV/cm [42] was also included in the calculations. The calculated values of the bound state transitions have been compared with the absorption peaks measured in the absorbance shown in Figs. 5.20 and 5.21. The E_1-E_2 transition energy in the conduction band matches well with the peak at 3.0μm. Also, the peaks measured at 5.5μm and 19.2μm are in good agreement with the HH_2-LH_2 transition wavelength (5.65μm) and HH_1-LH_1 transition wavelength (20μm). Shorter wavelength peaks are also seen in Figs. 5.25 and 5.26 at 1.6 and 1.8μm, respectively. These may correspond to intersubband transitions from the electron state E_1 to the continuum in the conduction band since the transition energy is close to the offset ΔE_c. There is some bandmixing in the valence band, which may result in IR transitions that do not match the values obtained from the simple model used here for the calculations of the bound states. Furthermore, the calculation assumes the disks to be planar quantum wells, but there is evidence that a quantum dot is formed in the disk region [46] adding some additional degree of quantum confinement which will change the bound state energies.

5.4 Summary

A photonic integrated circuit directly on (001)Si will be extremely useful in silicon photonics and will be compatible to CMOS technology. Ideally, the wavelength of operation must also be in the eye-safe region of the spectrum. Hence a monolithic Si-based electrically-pumped laser, preferably emitting light at ~1.3 μm is the ideal light source in silicon photonics. There are reports of quantum dot lasers emitting light at this wavelength which have been grown on silicon wafers [25]. However, the substrates have to be tilted from the (001) plane to reduce defects making such technology incompatible with CMOS technology. In contrast, highly mismatched GaN-based nanowires can be grown on (001)Si with relative ease. These nanowires are grown relatively free of extended defects. The photonic integrated circuit described in this chapter utilizes InN disks as the gain media grown in between InGaN barriers. The use of such InN disks has not been successfully achieved before this study.

The work here is a successful demonstration of the coupling of the edge emitting laser emission into a monolithic dielectric waveguide and a subsequent coupling of the guided light into an in-plane guided wave photodiode. Passive waveguides or other guided wave components will form parts of an optical interconnect on a silicon chip. This work demonstrates an optical interconnect employing such a passive waveguide. The optical interconnect is fabricated using a bottom-up monolithic approach which will allow optoelectronic integration. In future developments, it will also be possible for Si-based electronic circuits to be incorporated for laser biasing and modulation. As the nanowires are grown at comparably lower temperatures, the process will be easier to integrate with CMOS processing of the electronics.

In the study of the photonic integrated circuits, the laser and detector are realized with a random array of dot-in-nanowire heterostructures. Parylene is used to enhance the internal quantum efficiency of the nanowires by reduction of surface states which further reduces recombination via these surface states. Core-shell nanowires can be grown to improve the effectiveness of the nanowires further. In future development, an ordered array of nanowires can also be used where the nanowires are grown on suitably patterned substrates.

The in-plane photodiode of the photonic integrated circuit is realized with the same nanowire array identical to the one used to fabricate the laser. Such symmetry enables one-step epitaxy and further simplifies the entire fabrication process of the photonic integrated circuit. The detector demonstrates a reasonably good value of responsivity of 0.11A/W at 1.3 μm. Sharp peaks were present in the measured spectral output which are believed to be due to interband transitions also discussed in the previous chapter. Such transitions occur between discrete quasi-bound electron and hole states in the InN disks. These features are usually observed in the absorption spectra of quantum dots [150], which further prove the formation of quantum-dot like nanostructure in the InN disk active region. Such observation from the measured data has led to the second part of the chapter where intersubband transitions are investigated. This work has the potential for applications in infrared (IR) long wavelength detectors. Additionally, such a silicon based detector will be of high technological value.

In this chapter, the infrared absorbance of $In_{0.34}Ga_{0.66}N$/GaN disk-in-nanowire arrays have also been measured at room temperature from both transmission and reflection measurements. Similar to the nanowires used for the photonic integrated circuit

the nanowire arrays for the absorbance study were also grown on (001)Si substrates by plasma assisted MBE system. A simple model has been used to calculate the intersubband electron and hole transition energies for these materials. Some of these transition energies match well with the absorption peaks measured from the transmission and reflection measurements. Such promising results suggest that a breakthrough silicon-based monolithic nanowire IR detector technology is indeed possible.

Chapter VI

Dilute III-Nitride-Antimonide Alloy Nanowires

6.1 Introduction

The work presented in this thesis focuses on III-nitride nanowires emitting in the near-infrared. One of the major drawbacks of nanowires in the near-IR is the high polarization field, resulting from the high In composition required to attain near-IR light emission [151]–[153]. Addition of antimony (Sb) is expected to cause a red-shift [154]–[156] in the III-nitride alloys' light emission wavelengths, creating a possibility of reaching near-IR emissions without adding a significant amount of In. Circumventing the need of incorporating high amounts of In can substantially reduce strain in the nanowires, resulting in better structural and optical characteristics, and achieving long wavelengths that would have been impossible to achieve with just the III-nitrides [140]. Dilute-antimonide III-nitride alloys demand a higher degree of investigation than what has been explored so far [154]–[159].

This chapter focuses on preliminary results from the growth of the dilute-antimonide III-nitride (III-N-Sb) compound. For this growth, the PA-MBE described in Chapter II has been used with a Sb cracker cell (Sb_2). The cracker cell uses bulk, conduction, and

cracking zones, along with a precise opening (Jog) to produce accurate and controlled flux values.

The results discussed below are from the first batch of growths. Different approaches have been taken to include Sb in the nitride crystals. Sb has almost 8 times more volume than N [160], making it challenging to incorporate in the crystal without causing significant crystal deterioration. Additionally, this chapter describes the drawbacks from the first batch of Sb growths using the Sb cracker. Detailed photoluminescence (PL), X-ray diffraction (XRD), and scanning electron microscopy (SEM) measurements were performed to characterize these new crystals, and several reasons for possible crystal quality deterioration have been explained. The chapter also discusses how different techniques were used to solve those drawbacks.

6.2 Growth and Characteristics of InGaNSb Nanowire Arrays

6.2.1 Growth of InGaNSb alloys

In the first approach, Sb was incorporated in the InGaN disks. These disks are the active region of the InGaN/GaN disks-in-nanowire arrays. Half-laser heterostructures (Fig. 6.1), similar to that described in chapter II, were grown to perform optical and structural characterization.

In the absence of Sb, typical InGaN disks-in-nanowire arrays were epitaxially grown on (001)Si substrates in nitrogen-rich environments. Nitrogen flow was kept at 1sccm throughout the entire growth of the nanowires. 100nm of GaN was grown first on the (001)Si sample at a growth temperature of 820°C. Next, six InGaN disks were grown on top of the GaN layer at 640°C. Each disk was expected to be about 3nm thick. The

disks were separated by 12nm of GaN barrier material. In composition in the disks was estimated to be about 34%. The Ga flux was kept at 1.1×10^{-7} Torr for all the layers, and the In flux was maintained at 4×10^{-8} Torr during the growth of the disks. These growths resulted in high-density nanowires.

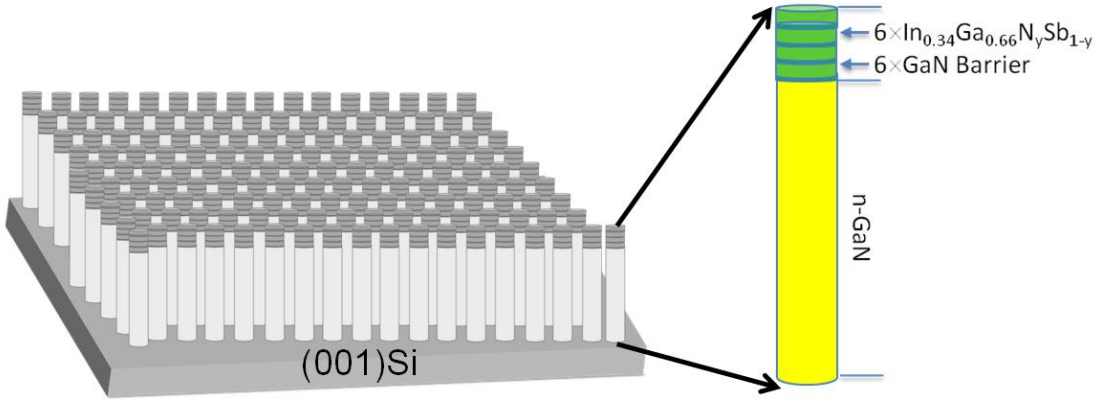

Figure 6.1 Schematic of the grown disks-in-nanowire heterostructure arrays on (001)Si. Inset shows one such nanowire heterostructure in detail.

The area density and diameter of the nanowires were measured to be $3\times10^{10}cm^{-2}$ and 60nm, respectively. Similar InGaNSb disks-in-nanowires samples were then grown with antimony (Sb) incorporated in the disk regions. The Sb flux was kept between 1×10^{-10} to 3×10^{-9} Torr to ensure minimal amounts of Sb addition. The addition of Sb resulted in enhanced lateral growth and reduced uniformity of the nanowires, seen in the SEM images taken before and after Sb incorporation (Fig. 6.2).

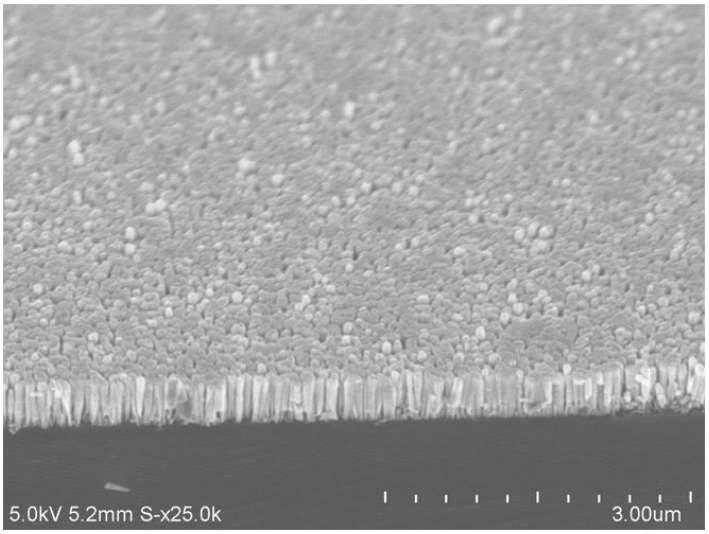

(a)

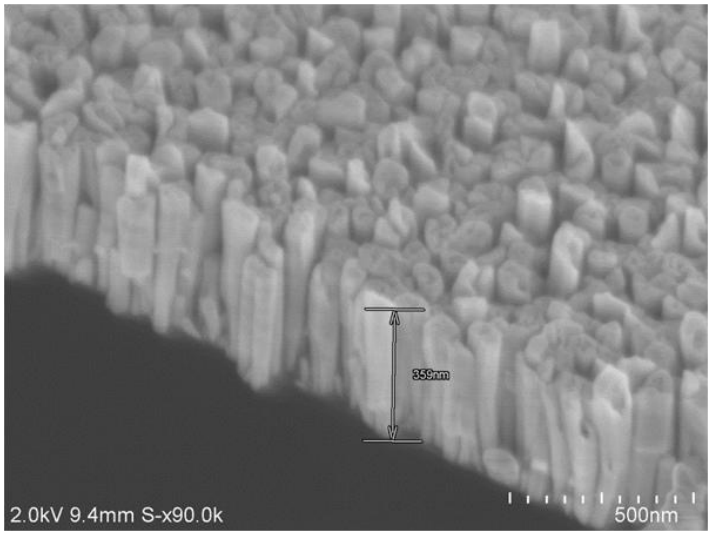

(b)

Figure 6.2 Scanning electron microscope (SEM) images of (a) $In_{0.34}Ga_{0.66}N$/GaN disks-in-nanowire arrays and (b) $In_{0.34}Ga_{0.66}N_xSb_{1-x}$/GaN disks-in-nanowire arrays.

6.2.2 Structural characteristics of GaNSb nanowires determined from X-ray diffraction

Due to the small thickness of the disks, X-ray diffraction (XRD) could not be performed on the individual disks in the disks-in-nanowire samples using our experimental set-up. Hence, control bulk GaN_ySb_{1-y} nanowire arrays were grown for the XRD measurements. Control samples of bulk GaN_ySb_{1-y} nanowire arrays, with and

without Sb (y = 1), were grown. The GaN_ySb_{1-y} nanowires were grown at a considerably lower temperature of 747°C to ensure incorporation of Sb. To reduce the coalescence of the nanowires at such low temperatures, a low Ga flux of 4×10^{-8} Torr was used. For the samples with Sb, the Sb flux varied between 4×10^{-9} to 1×10^{-8} Torr. As with the other nanowire growths, the nitrogen flow rate was kept at 1sccm to ensure a nitrogen-rich environment. The control GaN_ySb_{1-y} samples proved to be non-uniform due to their low growth temperature, but no significant coalescing of the nanowire arrays was observed from scanning electron microscope (SEM) images. One such image is shown in Fig. 6.3. The nanowires, in this case, do not indicate a strong change in structural characteristics after the incorporation of Sb probably because there is a considerable non-uniformity in GaN nanowires grown at such a low temperature. It is possible that the existing non-uniformity in low temperature GaN nanowires is comparably higher than that caused by the addition of Sb. XRD was performed using a rotating anode Rigaku XRD to determine the quality of the crystals formed using dilute-antimonide III-nitride growths. The x-rays were generated from Cu-Kα transition, which has a wavelength of 1.5406Å.

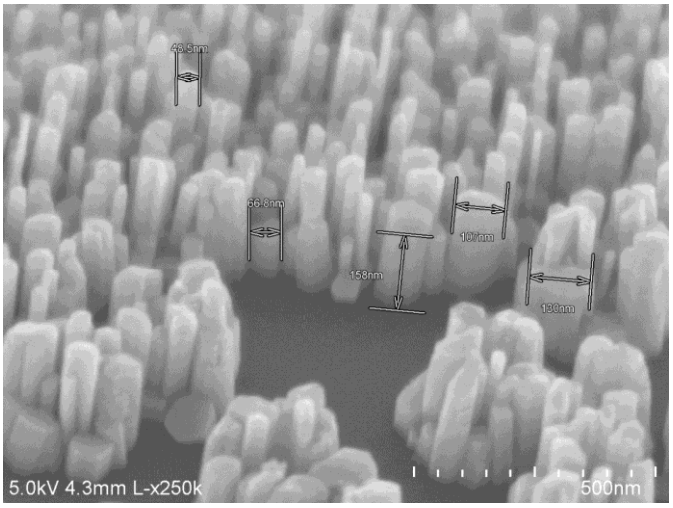

Figure 6.3 Scanning electron microscope (SEM) image of bulk GaN nanowire arrays grown at low temperature and low Ga flux.

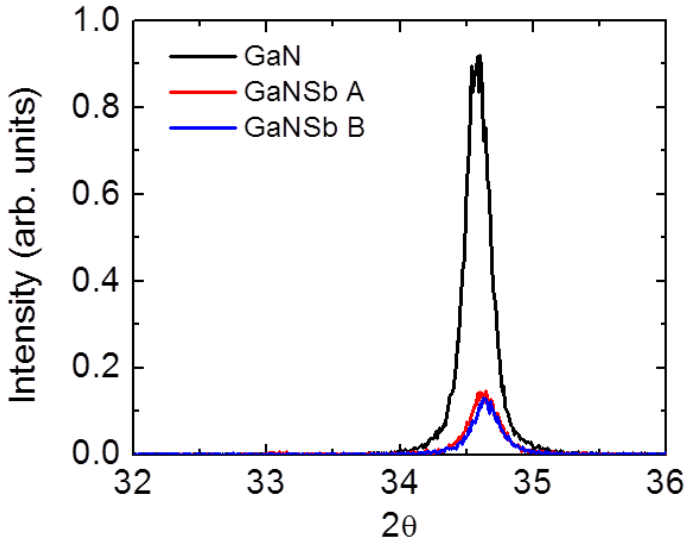

Figure 6.4 X-ray diffraction (XRD) from the GaN and GaNSb nanowires. GaNSb A sample was grown at a Sb flux of 4×10^{-9} Torr and GaNSb B sample was grown at a Sb flux of 1×10^{-8} Torr.

X-ray diffraction (XRD) measurements were made on the nanowire samples with a Rigaku rotating anode XRD machine that uses Cu-Kα radiation as the X-ray source. The XRD data are shown in Fig. 6.4. The samples with Sb have an X-ray intensity of almost one order lower compared to pure binary GaN samples. The GaN samples also show broad full-width half maxima (FWHM), probably due to the low growth temperature. The low intensity obtained from the GaNSb samples show significant degradation of the nanowires due to the incorporation of the Sb. It is apparent that the large volume of Sb (8 times higher than N) affects the overall lattice structure and also the optical properties of the GaNSb samples, which will be discussed in the next section. Indium was not included in the XRD study to ensure the simplicity of the experiment.

6.2.3 Optical characteristics

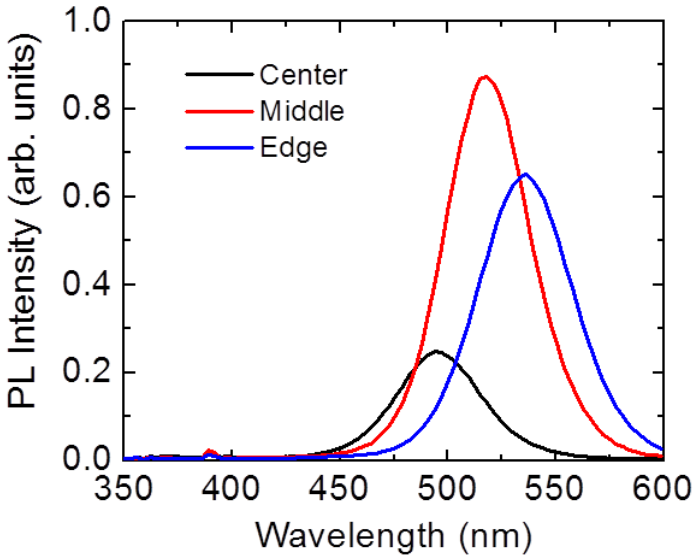

Figure 6.5 Room temperature photoluminescence spectra of the $In_{0.34}Ga_{0.66}N$/GaN disks-in-nanowire arrays. (Courtesy of Yuanpeng Wu, Professor Zetian Mi group, University of Michigan)

Due to the use of retainer plates in the MBE machine, the temperature of the substrate reached its maximum at the center of the sample and its minimum in the areas adjacent to the retainer plates. The difference between the maximum and minimum temperature points is estimated to be about 15°C. This difference can change the optical characteristics as a function of spatial location, even on the same sample. Accordingly, optical measurements were taken in the center of the sample as well as at the edges. Points in the middle of the center and the edge were also investigated. The measurements discussed here were all performed at room temperature. Preliminary optical characterization of the $In_{0.34}Ga_{0.66}N$/GaN and $In_{0.34}Ga_{0.66}N_xSb_{1-x}$/GaN disks-in-nanowire arrays were performed using a He-Cd (325nm) laser excitation source, a Princeton Instruments monochromator, and a photomultiplier tube (PMT). Photoluminescence data from the $In_{0.34}Ga_{0.66}N$/GaN disks-in-nanowire arrays are shown in Fig. 6.5.

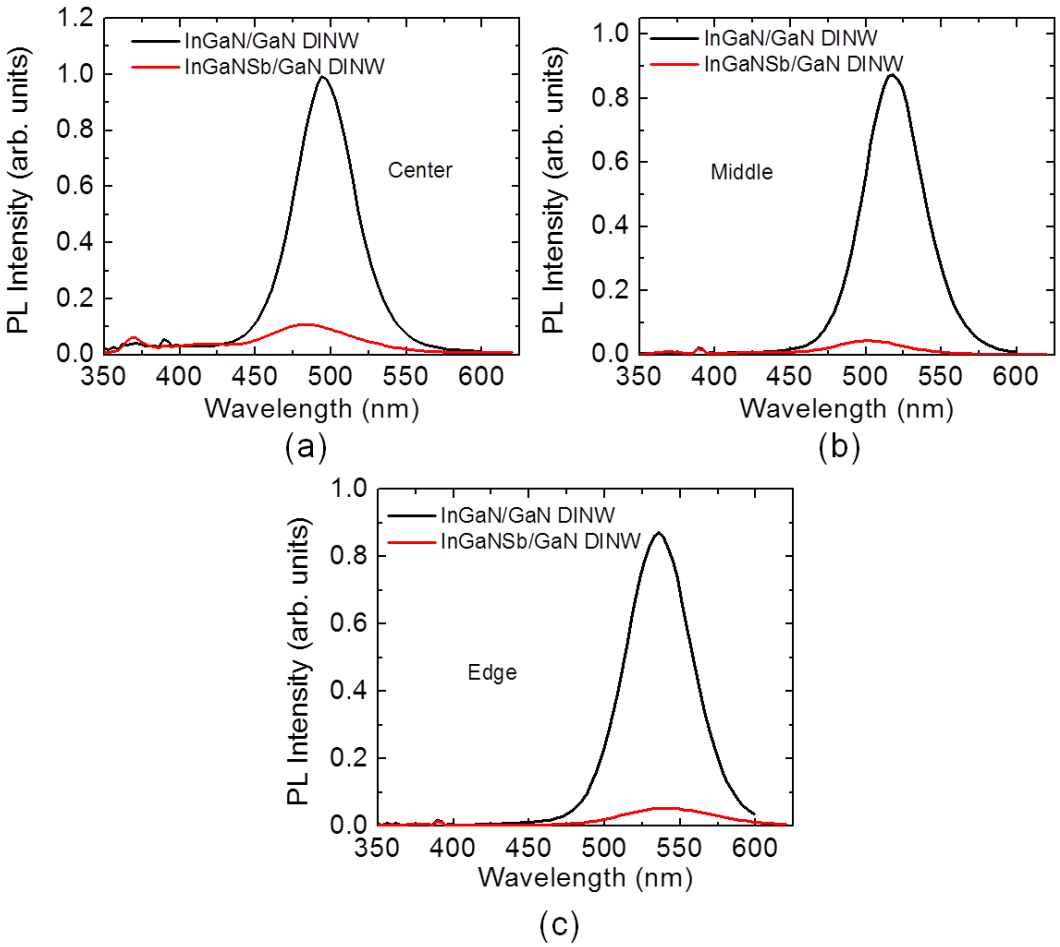

Figure 6.6 Comparison of room temperature photoluminescence spectra of the $In_{0.34}Ga_{0.66}N$/GaN disks-in-nanowire arrays to $In_{0.34}Ga_{0.66}N_xSb_{1-x}$/GaN disks-in-nanowire arrays with emission from (a) center, (b) middle, and (c) edges of the samples.

It can be observed from Fig. 6.5 that as the point, from which the PL data is extracted, moves from the center of the sample to the edge, the emission red-shifts. Such red-shifts are due to the higher In levels on the edges compared to the center of the sample originated due to lower growth temperatures at the edges. The low growth temperature caused more In to stick at the edges compared to the center. Thus, the emission wavelength is also the longest around the edges. The growth temperature also affects crystal quality: the best crystal quality corresponds to the highest intensity observed in between the center and the edge of the sample. Photoluminescence spectra from similar points in the sample were also measured from the $In_{0.34}Ga_{0.66}N_xSb_{1-x}$/GaN

disks-in-nanowire arrays. Each point of the two samples (with and without Sb) has been compared and plotted in Fig. 6.6.

The intensity of the photoluminescence from the $In_{0.34}Ga_{0.66}N_xSb_{1-x}$ /GaN disks is much weaker compared to the intensity from the $In_{0.34}Ga_{0.66}N$/GaN disks which is consistent with the XRD results. The degradation of the crystal due to the incorporation of Sb is probably the main reason for the low light emission from the Sb samples. The peak positions of the photoluminescence spectra obtained from the center and middle of the samples show blueshifts of about 12nm, instead of red shifts. A minimal red shift of 4nm was observed at the edge. The observation of the blue shift is counter-intuitive to the initial assumption that adding Sb should always result in a red shift. The reason for the blue shift is explained in Fig. 6.7 (Courtesy of Zetian Mi research group, University of Michigan) [158], [159].

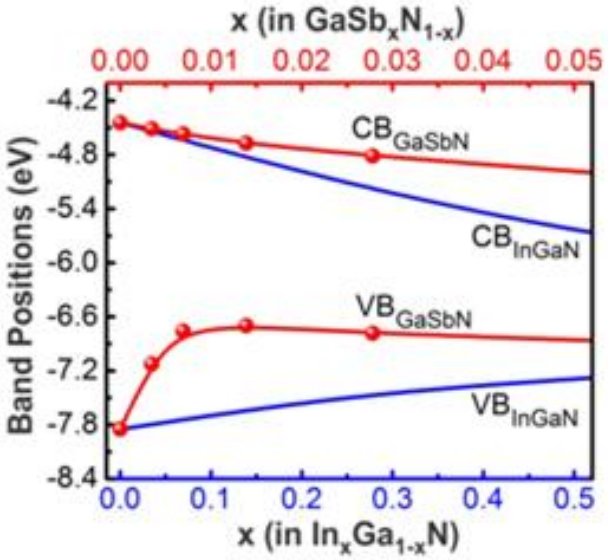

Figure 6.7 Variation of band positions in GaNSb and InGaN both as functions of In composition and Sb composition (Courtesy of Zetian Mi research group, University of Michigan) [Chowdhury et. al., Appl. Phys. Lett., **111**, 6, 061101, 2017.]

As seen in Fig. 6.7, the incorporation of Sb shifts both the valence band and the conduction band. The amount of shift in the band energies depends on the Sb composition. At low Sb compositions, the valence band energy may shift much faster than the conduction band effectively increasing the bandgap. Hence, depending on the growth window there may be a blueshift or a red shift. Further research needs to be carried out to understand the reasons behind the blueshift. These experiments highlight the major drawback of the InGaN approach. As changes in the growth window can result in a blueshift instead of a red shift, it is difficult to demonstrate a red shift in $In_xGa_{1-x}N_ySb_{1-y}$ materials. There are too many variables that need to be precisely controlled which are evident from Fig. 6.7. In this case, both group III and group V materials have individual alloying effects making the epitaxial growth complex. Therefore, a simpler method is pursued in the next section.

6.3 AlGaN/GaNSb Nanowire Heterostructure Arrays

6.3.1 Growth of AlGaN/GaN_xSb_{1-x} alloys

In the next part of this study of the dilute-antimonide III-nitrides, AlGaN/GaN_xSb_{1-x} disks-in-nanowire arrays were grown to overcome the drawbacks of the $In_yGa_{1-y}N_xSb_{1-x}$/GaN disks-in-nanowire arrays. The absence of indium in the active disk regions (GaN_xSb_{1-x}) is the main reason to explore this approach. In this study, both AlGaN/GaN and AlGaN/GaN_xSb_{1-x} disks-in-nanowire array samples were epitaxially grown and characterized. The barrier used was $Al_{0.2}Ga_{0.8}N$. These samples, similar to the previous ones, were also grown directly on (001)Si in nitrogen-rich environments. The nitrogen flow rate was kept at 1sccm.

Initially, samples without Sb were grown. First, a thin 70nm layer of GaN nanowires was first grown, followed by a thick $Al_{0.2}Ga_{0.8}N$ layer of 600nm. Then, three layers of $Al_{0.2}Ga_{0.8}N$/GaN disks-in-nanowires were grown. The thickness of the GaN disks was optimized to be 3nm, and the thickness of the $Al_{0.2}Ga_{0.8}N$ barrier was optimized to be 12nm. Due to the use of only Al and Ga, the growth temperature was kept at a high temperature of 820°C for both the GaN and the $Al_{0.2}Ga_{0.8}N$ layers before the disks. In contrast, the GaN disks were grown at a low growth temperature of 705°C because high temperatures are not suitable for Sb incorporation. The low-temperature GaN growths were separately calibrated to ensure that neighboring disks did not coalesce. These growths were performed at a low Ga flux of 4×10^{-8} Torr. Even at low flux, due to the temperature, the GaN growth rate was relatively high, estimated to be about 200nm/hour. Such a high growth rate is the result of a significantly large number of adatoms sticking at low temperatures as Ga does not desorb significantly at these low temperatures. To ensure that the Sb did not disassociate when the growth temperature was raised for the barrier growth, thin layers (3nm on both sides) of barrier material were grown on both sides of the GaN disks also at 705°C. Rest of the barrier material was grown at high temperature of 820°C.

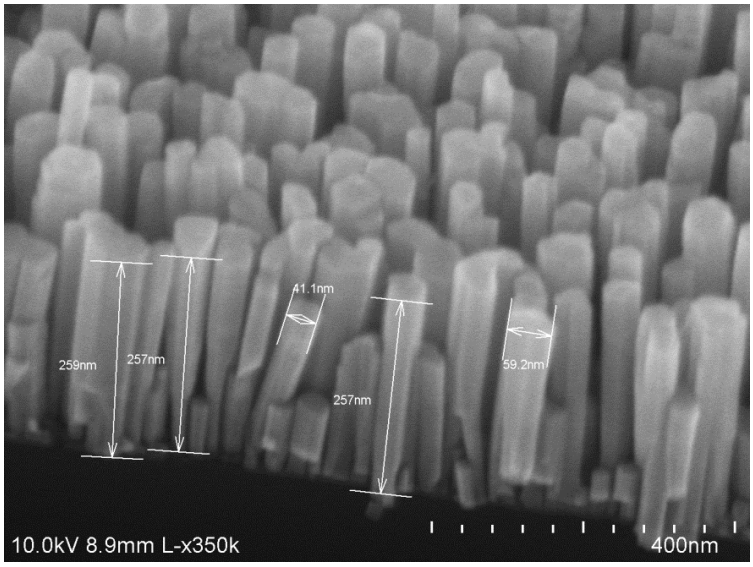

(a)

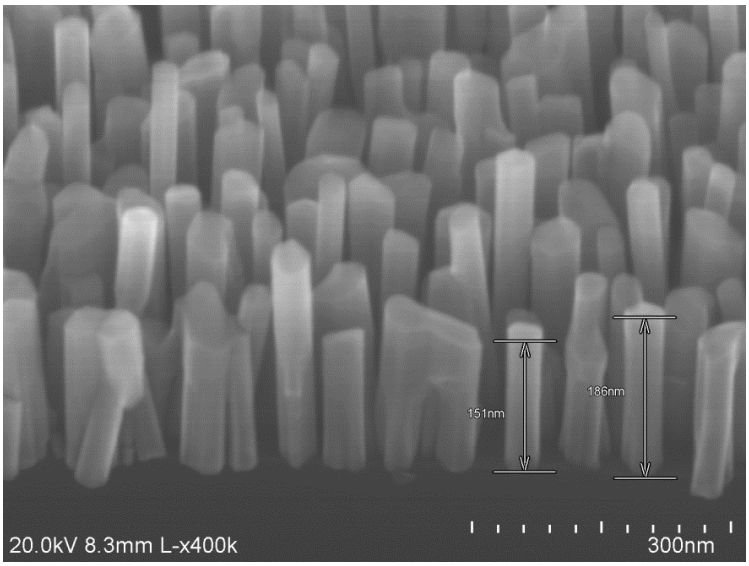

(b)

Figure 6.8 Scanning electron microscope (SEM) images of (a) $Al_{0.2}Ga_{0.8}N/GaN$ disks-in-nanowire arrays and (b) $Al_{0.2}Ga_{0.8}N/GaN_xSb_{1-x}$ disks-in-nanowire arrays.

After the optimization of the samples without Sb, samples with Sb were grown. The Sb was incorporated in the GaN disks by using Sb fluxes ranging from 1×10^{-10} Torr to 3×10^{-9} Torr. Rest of the growth parameters were kept exactly same as mentioned above. Scanning electron microscope (SEM) images of both $Al_{0.2}Ga_{0.8}N/GaN$ disks-in-

nanowire arrays and $Al_{0.2}Ga_{0.8}N/GaN_xSb_{1-x}$ disks-in-nanowire arrays are shown in Fig. 6.8. The Sb did increase non-uniformity and coalescence in the nanowires, but overall the nanowire structural characteristics did not degrade significantly.

6.3.2 Optical characteristics

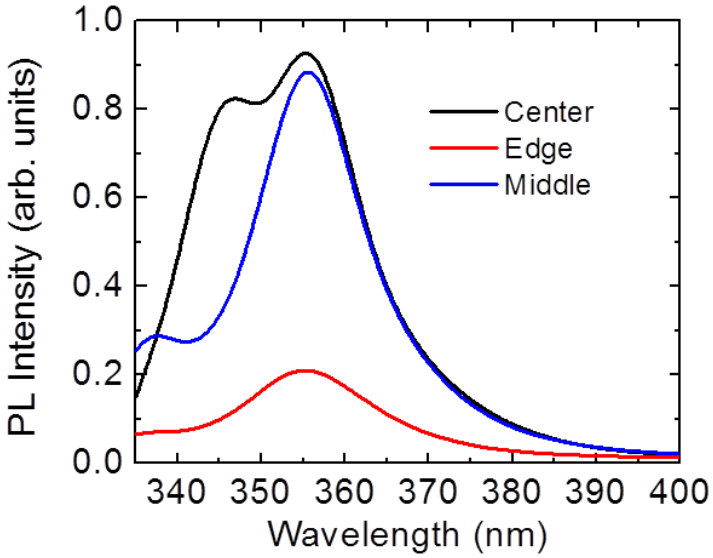

Figure 6.9 Photoluminescence (PL) data obtained from $Al_{0.2}Ga_{0.8}N/GaN$ disks-in-nanowire arrays.

Similar to the InGaNSb-based nanowire arrays, the AlGaN/GaNSb disks-in-nanowire arrays were characterized by photoluminescence (PL) measurements at room temperature (300K) using a He-Cd (325nm) laser excitation source, a Princeton Instruments monochromator, and a photomultiplier tube (PMT). PL data from the $Al_{0.2}Ga_{0.8}N/GaN$ disks-in-nanowire arrays are shown in Fig. 6.9. As stated before, there was a change of growth temperature measured from the center of the sample to the edges, due to the higher heat dissipation by the retainer plates. For this reason, PL measurements were performed at three different points (center, middle, and edge), similar to the previous measurements. The center and middle points of the measurements in Fig. 6.9

show a PL peak at 355nm instead of the 367nm bulk GaN peak. This blue shift is due to the quantum confinement associated with the disks formed using GaN. The low temperature on the edges caused a reduction in the quality of the GaN crystals which is seen from the weaker intensity of the PL data from the edges. Other secondary peaks can also be observed in the PL data, possibly from the low Al-based AlGaN alloys that formed at the interface of the barrier and the disk material [161]–[163]. The portion of the barrier that is grown at low temperatures can also increase such barrier-disk material interdiffusion and cause secondary peaks to emerge in the PL spectra.

The PL of the $Al_{0.2}Ga_{0.8}N/GaN_xSb_{1-x}$ disks-in-nanowire arrays were measured at similar points compared to the samples without Sb. A comparison of samples with and without Sb is shown in Fig. 6.10. Analogous to the InGaNSb samples, the PL signal strength from the samples with Sb were weaker compared to the signal strength from the pure GaN disks. Such weak PL signals again highlight that the incorporation of Sb in pure GaN does significantly degrade the GaN crystal quality. The PL signal also broadens with the addition of Sb, which can be attributed to the alloying effects.

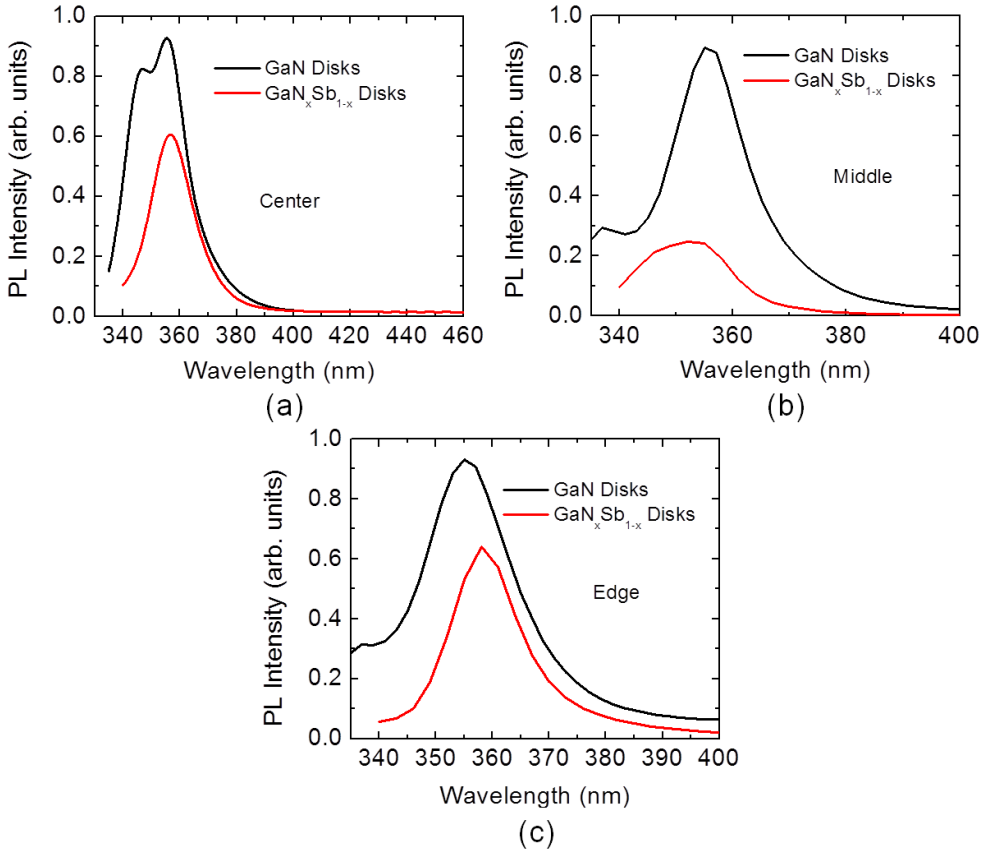

Figure 6.10 Comparison of room temperature photoluminescence spectra of the $Al_{0.2}Ga_{0.8}N/GaN$ disks-in-nanowire arrays to $Al_{0.2}Ga_{0.8}N/GaN_xSb_{1-x}$ disks-in-nanowire arrays with emission from (a) center, (b) middle, and (c) edges of the samples.

The samples with Sb again show a negligible amount of red shift, and in the case of the measurement done in the middle of the sample, there is a blue shift. Hence it can be inferred that substantial proof of red shift due to the incorporation of Sb cannot be obtained from these initial measurements. The absence of a substantial red shift can be caused due to multiple reasons. The Sb may not be correctly incorporating in the lattice. A 705°C growth temperature was chosen since further lowering of the growth temperature would significantly degrade the crystal quality of GaN and enhance coalescing of the nanowires. In contrast, a higher growth temperature would substantially

decrease the incorporation of Sb. Even so, 705°C is on the higher side for Sb incorporation which may be another reason for not observing any significant red shift.

6.4 Summary

Though the work here on dilute-antimonide III-nitride has not been able to demonstrate a substantial amount of red shift in the output emission wavelength due to the incorporation of Sb, it does present two possible approaches for future successful dilute-antimonide III-nitride growth. In the first approach, $In_{0.34}Ga_{0.66}N_xSb_{1-x}$ was used as the disk material whereas GaN was used as the barrier material. Control GaN nanowire samples were epitaxially grown on (001)Si. Structural characterization was performed by a combination of scanning electron microscopy (SEM) and X-ray diffraction (XRD). These measurements do show degradation of the nanowire crystals with the incorporation of Sb. Detailed room temperature photoluminescence (PL) measurements were also performed on these samples. The PL data does not show any significant red shift, which can be explained by the calculated variation of band positions as a function of Sb incorporation. Further research could result in the elucidation of a successful growth window where the $In_{0.34}Ga_{0.66}N_xSb_{1-x}$/GaN disks-in-nanowire arrays will demonstrate a red shift in the emission wavelength.

The second part of the study focused on $GaN_xSb_{1-x}/Al_{0.2}Ga_{0.8}N$ disks-in-nanowire arrays. The active region consisted of multiple 3nm layers of GaN_xSb_{1-x} disks and 12nm of $Al_{0.2}Ga_{0.8}N$ barriers. Here, the lattice degradation problem remained but was reduced as the binary GaN disks inherently had superior quality compared to the ternary InGaN disks. The GaN disk growth temperature has been significantly lowered to ensure Sb incorporation. Here also, detailed room-temperature PL measurements were performed,

but the PL data did not show any significant red shift which may be attributed to the growth temperature of the GaN disks. The growth temperature might still not have been low enough for successful incorporation of Sb. Future growths of similar dilute-antimonide III-nitrides should be able to identify the optimum growth window, where the effective incorporation of Sb will result in a significant red shift. Such a red shift can be used to explore wavelengths of operation beyond those currently achievable with the III-nitrides. The red shift with the addition of Sb can also be utilized to demonstrate better performance of visible or near-IR lasers with the III-nitride alloys but with less addition of indium (In). Devices with smaller amounts of In in the active region should have better characteristics due to less strain in the material.

Chapter VII

Conclusion and Future Work

7.1 Summary of Present Work

The thesis presented here focuses on self-assembled III-nitride nanowire arrays epitaxially grown directly on (001)Si. Most of the work focuses on nanowires operating at near-IR. Self-assembled nanowire growths along with optical and structural characterization of the grown nanowires were performed in great detail. The nanowires were used to fabricate different optoelectronic devices, e.g., lasers, LEDs, detectors, and photonic integrated circuits. The disks-in-nanowire arrays have shown to be promising regarding intersubband absorption which can potentially open new research areas using the III-nitrides as Mid-IR to long wavelength IR detectors. Antimony has also been employed to reduce the bandgap in the III-nitrides, and preliminary findings have been reported in this work. Successful incorporation of Sb in the III-nitrides can be utilized for long wavelength applications.

The self-assembled nanowire growth was the main topic of chapter II. First $In_{0.85}Ga_{0.15}N/In_{0.4}Ga_{0.6}N$ disks-in-nanowire arrays have been grown on (001)Si substrates which emit light at 1.4μm as measured from photoluminescence (PL) measurements. $In_{0.4}Ga_{0.6}N$ has been used instead of GaN as the barrier material to reduce strain in the

disks. The nanowire emission wavelengths have been extended by growing binary InN disks with the same $In_{0.4}Ga_{0.6}N$ barrier material. These disks emit light at around 1.6μm. Detailed optical characterization has been performed on these disks-in-nanowire arrays using temperature dependent and excitation dependent photoluminescence. Time resolved photoluminescence was also used to determine radiative and non-radiative carrier lifetimes in the nanowires. Detailed structural characterization was also performed using a combination of scanning electron microscopy (SEM), transmission electron microscopy (TEM), high angle annular dark field imaging (HAADF), and energy dispersive spectroscopy (EDS) techniques. The nanowire arrays were characterized using x-ray diffraction (XRD) to understand the lattice constants and change of lattice constants with strain and In composition. Quantum dot formation in the nanowire disk regions has been observed from TEM images. Nanowire density and diameter was properly optimized to ensure good parylene passivation of the nanowires.

Chapter III concentrated on determining optical constants of III-nitrides mainly at near-IR wavelengths. The applications of III-nitride so far have been centered in visible wavelength regime. Hence the reported optical constants also focus towards the visible spectrum and not near-IR. In this chapter optical constants at near-IR wavelengths have been measured using spectroscopic ellipsometry. Detailed optical constants have been derived from Gaussian oscillator model and Cauchy-Urbach model. The optical constants are determined within a large wavelength regime ($800nm \leq \lambda \leq 1683nm$). The ellipsometry has been carried out on planar layers instead of nanowires substantially reducing measurement errors originating from surface scattering. The planar layer growth has been explained in detail. The planar layers are also characterized using PL, SEM,

atomic force microscopy (AFM) and XRD. The background carrier density has also been determined from fabricating Schottky diodes using these InGaN alloy materials. Different laser heterostructures have been designed using these optical constants. More advanced heterostructures like GaN lattice matched $In_{0.18}Al_{0.82}N$ layers, and graded $In_xGa_{1-x}N$ layers have also been epitaxially grown and characterized using XRD.

The focus of chapter IV was optoelectronic devices fabricated using these III-nitride nanowire arrays operating at near-IR. LEDs, lasers and detectors, all operating at near-IR, were fabricated using the nanowire arrays. The epitaxial growth of the relevant nanowire heterostructure arrays along with the details of device fabrication steps have been discussed. Top emitting nanowire LEDs, which utilize $In_{0.85}Ga_{0.15}N/In_{0.4}Ga_{0.6}N$ disks-in-nanowires, have been fabricated and characterized first. The LEDs exhibited a low series resistance of ~20Ω and a good turn-on voltage of 4.1V. The peak emission wavelength of the LEDs was at ~1.3μm making these devices ideal for on-chip communication. A significant blueshift of about 860kV/cm was observed in the LEDs. Next lasers were fabricated using the same nanowire heterostructure. A stronger blueshift has been calculated in the lasers electroluminescence (EL) spectra, and the peak of the EL spectrum at relatively high injections has been measured at ~1.2μm. The lasers also exhibited promising output power of about 7mW along with excellent temperature stability determined from a high characteristics temperature (T_0) of 242K. Differential gain (dg/dn) was calculated from steady-state cavity length dependent light-current (L-I) measurements. To further extend the emission wavelength of the lasers InN was used as the disk material instead of $In_{0.85}Ga_{0.15}N$. The InN based lasers exhibited peak emission wavelength of ~1.3μm. These lasers also show significant output optical power of about

9mW. The lasers demonstrated a lifetime of ~1000 hours from steady state measurements and, a bandwidth of 2.4GHz, differential gain of ~6×10^{-17}cm^2, and gain compression factor of 7×10^{-17}cm^3 from dynamic characterizations. These long wavelength lasers on (001)Si are the first of its kind.

Chapter V detailed the photonic integrated circuit using the III-nitride nanowire arrays. This chapter also discusses intersubband absorption seen in the disks-in-nanowire heterostructure. Here also the relevant nanowire epitaxial growth has been described in detail. The nanowire arrays have been structurally and optically characterized. The optical quality of these disk-in-nanowires was determined to be quite high, and a radiative efficiency (η_r) or, internal quantum efficiency (IQE) of 67% has been determined from temperature dependent photoluminescence measurements. The demonstrated photonic integrated circuit was a complete circuit as it consisted of a laser, waveguide and a detector. All these components are individually characterized. The waveguide is a multilayer waveguide consisting of SiO_2 and Si_3N_4. The multilayer waveguide has a minimal waveguide propagation loss of 12.4dB/cm. The lasers have been characterized to have a peak emission wavelength at ~1.3μm above threshold. The lasers also emitted promising output optical power of ~5mW as measured from light-current (L-I) characteristics. Similar to previously reported nitride based lasers, these lasers also exhibited excellent temperature stability with characteristic temperature (T_0) values well beyond 200K. Average bandwidth of 3GHz has been measured from small signal modulation measurements. These dynamic measurements also enabled the calculation of differential gain and gain compression factor which were calculated to be ~3×10^{-16}cm^2 and ~4×10^{-16}cm^3, respectively. The detector responsivity was characterized

using a broadband source and 0.125m monochromator. A reasonable responsivity of 0.11A/W was calculated from the photocurrent spectra. The photonic integrated circuit overall also demonstrated good performance. A 10-fold increase in detector photocurrent was observed as a function of laser injection current. In the next section of this chapter, intersubband absorption in the III-nitride disks-in-nanowire arrays was measured. Rudimentary band diagram calculations confirmed that there are a larger number of energy states in $In_{0.34}Ga_{0.66}N$/GaN disks-in-nanowires compared to InN/$In_{0.4}Ga_{0.6}N$ disks-in-nanowires due to the low polarization field in low In based disks. Hence $In_{0.34}Ga_{0.66}N$/GaN based disks-in-nanowire arrays were epitaxially grown for intersubband absorption measurements. The growth of these nanowire heterostructure arrays has also been described in this section. Detailed optical and structural characterization was performed on these disks-in-nanowire heterostructure arrays. The absorbance was determined at room temperature from transmission and reflection measurements. Clear absorption peaks from ~1.6 to ~20μm has been observed which can potentially enable mid-IR to long wavelength IR detection using the III-nitrides.

Chapter VI discussed some preliminary growth and characterization of dilute-antimonide III-nitride (III-N-Sb) based nanowire arrays. The addition of Sb can potentially extend the emission wavelengths of the III-nitrides further in the infrared. Initially, InGaN/GaN disk-in-nanowire arrays were grown, and Sb is added in the disks. The drawbacks of these InGaNSb/GaN disks-in-nanowire arrays have been discussed. After this, GaNSb/AlGaN disks-in-nanowire arrays have been grown to circumvent these disadvantages. Sb is then added in the GaN disks. Photoluminescence data measured on the GaNSb/AlGaN disks-in-nanowire arrays have been reported. All nanowire epitaxial

growths have been described in detail. Here also, the nanowire arrays have been characterized both optically and structurally. Initial results of these dilute-antimonide III-nitride nanowire arrays have been reported in this chapter. These early measurements do not show any significant red shift. The absence of red shift can be due to different reasons which have also been detailed in this chapter. Further research needs to be carried out to demonstrate red shift using antimony.

7.2 Future Work

7.2.1 Mid-IR and long wavelength IR detectors

As discussed in chapter V, current MIR and LWIR detectors heavily depend on detector fabrication technology that uses In-bump bonding of the detector arrays onto silicon readout integrated circuits (ROICs) [164]–[166]. Such an array is shown Fig. 7.1 (Courtesy of Jet Propulsion Laboratory (JPL), National Aeronautics and Space Administration (NASA)). The use of In-bump bonding can cause significant performance degradation due to the hybridization process [167]. The intersubband absorbance, demonstrated by the InGaN/GaN disks-in-nanowire arrays discussed in chapter V, have the potential to replace these ROIC circuits with more stable detectors. The use of (001)Si and room temperature operation can be extremely useful for various applications and technologies.

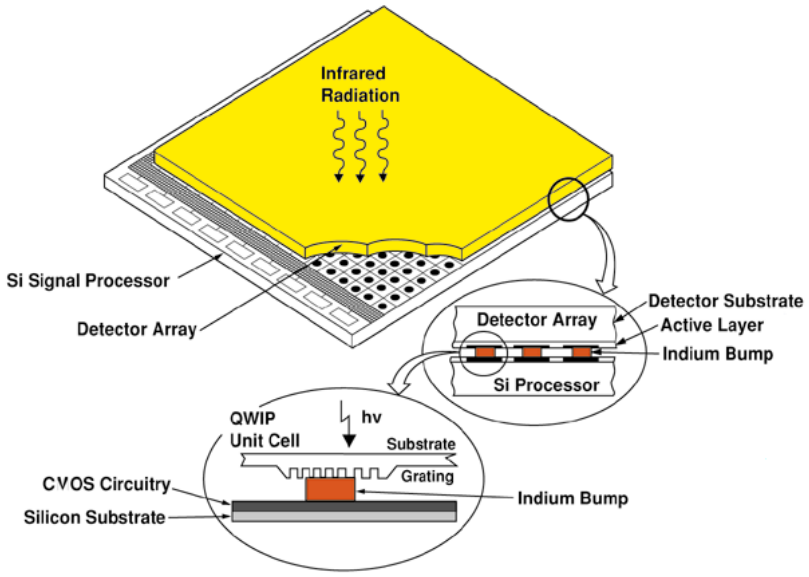

Figure 7.1 Detector array using In-bump bonding (Courtesy of Jet Propulsion Laboratory (JPL), National Aeronautics and Space Administration (NASA)).

So far the detectors fabricated using these disks-in-nanowires have not shown any photocurrent response. The two biggest challenges that need to be overcome are the design of a window through which the IR light can pass with little to no loss, and increasing the thickness of the active region without degradation of the nanowire optical quality. Since these are nanowires, a traditional ring type metal contact will not work [168]–[170]. The metal contact has to connect to all the nanowires physically. The contact metal can cause a significant loss in the IR light being incident on the devices as seen in Fig. 7.2. A thin 10nm (Ni/Au :: 5/5nm) p-contact layer absorbs almost 99.5% of the incident light. Use of transparent contact layers, e.g., indium tin oxide (ITO), is a potential solution to this problem. Novel fabrication techniques can also be developed to circumvent this disadvantage inherently present in surface absorbing nanowire detectors. The simplest way to solve this drawback is the use of guided wave detectors instead of surface absorbing detectors, but that may be incompatible with existing array fabrication techniques.

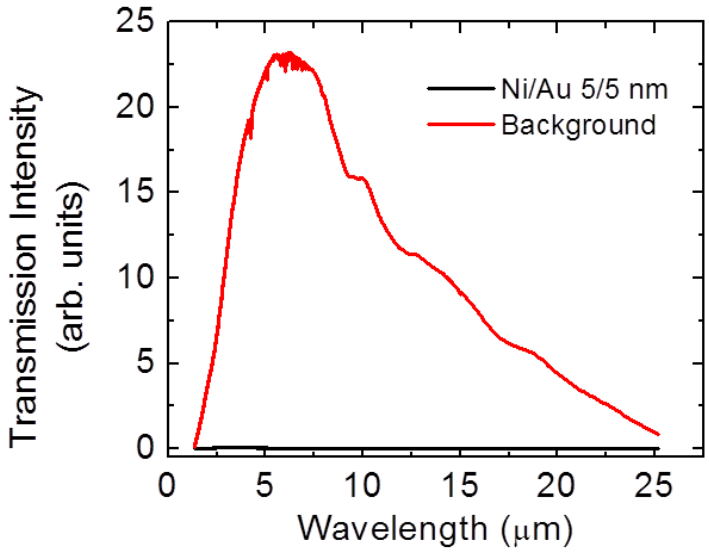

Figure 7.2 Transmission loss due to thin p-contact metal layer as compared to the incident background IR light (Courtesy of Dr. Alexander Soibel in Dr. Sarath D. Gunapala's research group at Jet Propulsion Laboratory (JPL), California.).

The other disadvantage of these detectors is the low active absorption layer. The IR light can only be absorbed in the disk regions which can have a maximum total thickness of 24nm (8 disks with each having a 3nm thickness). Larger disk thickness can cause the lower quantum confinement in the disks, consequently reducing the effect of intersubband absorption. The number of disks cannot be increased indefinitely due to strain limitations of these materials [71], [171]. Large number of disks can reduce optical quality of the disks. Hence the light absorbed by the nanowire array heterostructures, used in this thesis work, is relatively small. One possible method to solve the problem is to use resonant cavities [172]–[174] instead of traditional devices.

Nanowire heterostructures with 20 $In_{0.34}Ga_{0.66}N$ disks have already been grown and characterized. SEM image of such a nanowire array is shown in Fig. 7.3 along with the nanowire heterostructure. These 20 disk-in-nanowire heterostructure arrays can enhance the detector characteristics by improving the specific detectivity (D^*), noise

equivalent temperature difference (NEΔT), and, background limited infrared-performance (BLIP). A more quantitative analysis of the improvement of these parameters can be described by first investigating the improvement of quantum efficiency (η) of the detectors as the number of disks increase from 6 to 20. The dependence of η with the absorption coefficient of the material (α), and the thickness of the absorption region (a) is given by equation 7.1,

$$\eta \propto (1 - e^{-\alpha a}) \qquad (7.1)$$

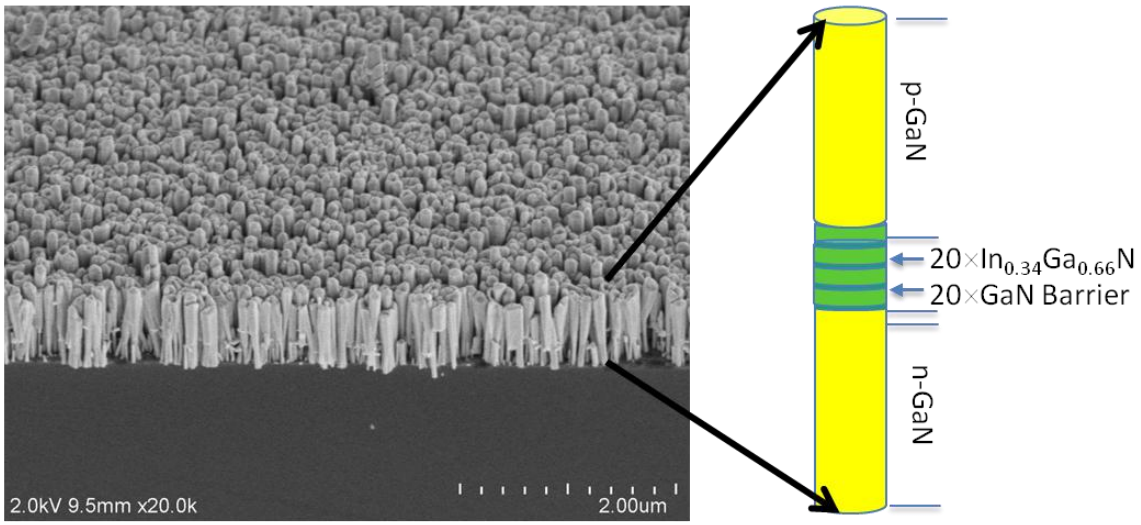

Figure 7.3 (a) Scanning electron microscopy image of a disk-in-nanowire heterostructure array with 20 disks. Inset shows the schematic of the nanowire heterostructure (Courtesy of Yuanpeng Wu, University of Michigan).

The absorption coefficient of $In_{0.34}Ga_{0.66}N$ is ~8.64×10^4 cm^{-1} [175], [176]. From TEM measurements, disk thickness of about 3nm has been measured [46]. Hence the value of a is 18nm for 6 disks and 60nm for 20 disks. Following equation 7.1, the increase of the absorption region thickness increases the quantum efficiency (η_{20}) of the samples with 20 disks by ~2.8 times compared to the quantum efficiency (η_6) of samples

with 6 disks. The calculation assumes there is no significant crystal quality degradation as the thicker active regions are epitaxially grown.

Even though the quantum efficiency increases with increasing the number of disks, the photoconductive gain (G) does reduce with increasing nanowire length. The reduction in G can be calculated from equation 7.2,

$$G = \frac{\tau_0}{\tau_t} \tag{7.2}$$

where τ_0 is the carrier lifetime and, τ_t is the transit time across the full width of the detector. As the material is same, τ_0 remains constant but with increase in disk thickness the overall nanowire length increases. The increase in nanowire length increases τ_t thereby reducing the photoconductive gain. Assuming 200nm of n-GaN and p-GaN regions on both sides the photoconductivity of 20 disk-based detectors (G_{20}) reduces by 30% compared to 6 disk-based detectors (G_6). Here the GaN barriers are 12nm and the disk thickness is 3nm. Overall, the product of η and G increases by ~2 times for the 20-disk based detectors in comparison to the 6-disk based detectors.

The increase in η.G further decreases the noise equivalent power (NEP) following equation 7.3 [177],

$$NEP = \left(\frac{hc}{\lambda}\right)\frac{1}{e\eta G} < \delta I^2 >^{\frac{1}{2}} \tag{7.3}$$

where h is the Planck's constant, c is the velocity of light in free space, λ is the incident wavelength, e is the charge of a electron, η is the quantum efficiency of the detector, G is the photoconductive gain, and $<\delta I^2>$ is the blackbody photocurrent fluctuations. Equation 7.3 describes the limit of the NEP of a detector. Following equation 7.3, the NEP will reduce by ~50% for a detector with 20 disks compared to 6 disks. Depending on the

relation between NEP and NEΔT, the latter will follow the trend of the former. As an example for a perfect blackbody NEP and NEΔT are very well defined, thus NEΔT directly scales with NEP.

The reduction of NEP will directly increase the specific detectivity (D^*) following equation 7.4,

$$D^* = \left(\frac{A^{1/2}\Delta f^{1/2}}{NEP}\right) \tag{7.4}$$

where A is the area of the photoconductor on which light is incident and, Δf is the detector bandwidth. Reference bandwidth for D^* calculations are taken to be 1 and it can be assumed the area of the detectors will remain constant even with change of the nanowire heterostructure. Then D^* becomes inversely proportional to NEP and, as NEP decreases by ~2 times, D^* will increase ~2 times as well. Thus the D^* of detectors with 20 disks will have approximately twice the specific detectivity of the detectors with 6 disks.

The limit of the BLIP (D^*_{BLIP}) is given by the equation 7.5 [177],

$$D^*_{BLIP} = \left(\frac{\lambda^3}{hc}\right)\left\{\left(\frac{\eta}{8\pi c\Delta\lambda}\right)\left[\left(\frac{\Omega}{\pi}\right) - \left(\frac{\Omega}{2\pi}\right)^2\right]^{-1}\left(e^{hc/\lambda k_B T} - 1\right)\right\}^{1/2} \tag{7.5}$$

where the spectral width of the detectors is given by Δλ, Ω is the solid angle in which the detector can absorb the light, k_B is the Boltzmann constant, and T is the temperature of the detector. It is evident that the limit of the BLIP does not depend on the photoconductive gain. D^*_{BLIP} is proportional to the square root of η as other parameters in equation 7.5 can be kept constant from 20 disks-in-nanowire based detectors to 6 disks-in-nanowire based detectors. The increase in η has already been calculated to be about ~2.8 times. Hence D^*_{BLIP} will also increase by 1.7 times for the 20 disks-in-nanowire based detectors.

To summarize, as the number of disks increases to 20 disks from 6 disks in the nanowire heterostructure, the D^* will increase by ~2 times, D^*_{BLIP} will increase by ~1.7 times, and NEΔT will reduce approximately by ~2 times. All these calculations assume the nanowire crystal quality will not significantly degrade as more $In_{0.34}Ga_{0.66}N$ disks are incorporated in the disk-in-nanowire heterostructure. The calculation also assumes that NEP and NEΔT are directly related. Hence the 20 disks-in-nanowire based IR detectors will not only be able to operate at room temperature, they will also have better performance compared to the initial 6 disk based designs.

7.2.2 1.55μm photonic devices on silicon for long-haul communication

As discussed in chapter I, infrared communication has quite a few windows where the communication is the most effective. For glass fiber based communication, 1.3μm and 1.55μm are the ideal wavelengths to operate. 1.3μm offers the zero dispersion point for glass (SiO_2) making it ideal for communication with a large number of channels [178] and 1.55μm offers the lowest attenuation of the transmitted signal in the fiber making this wavelength suitable for long-haul communication [179], [180]. Due to these advantages lasers operating at 1.3μm and 1.55μm wavelengths have been researched and developed for years. One such 1.55μm laser has been shown in Fig. 7.4 [181].

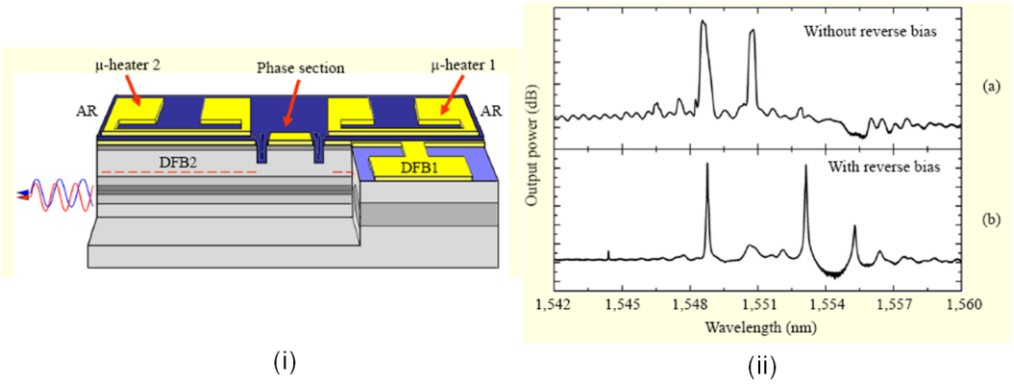

Figure 7.4 (i) Device structure of a DFB laser emitting light at 1.55μm, (ii) electroluminescence spectra of the DFB laser at different bias voltages (Kim *et. al.*, ETRI Journal 33.5 (2011): 810-813).

Though these lasers show excellent performance, they are mostly based on GaAs or InP substrates making them incompatible with CMOS technology. In this work, all the lasers are directly on (001)Si substrates thus compatible with the CMOS processing technology. This work focuses on 1.3μm wavelength which is ideal for communication in short distances with more channels [178]. The capabilities of III-nitrides can even be extended to 1.55μm which is perfect for long haul communication. InN/$In_{0.4}Ga_{0.6}N$ disks-in-nanowire arrays have been shown to emit light at ~1.6μm. The lasers fabricated from this material emit light at ~1.3μm due to the large polarization field present in the materials. Strain engineering and novel barrier materials can potentially decrease the polarization field present in the active region. Thus laser emission at 1.55μm may be possible with In-rich nitride based alloys which will open doors to new applications using the III-nitrides. The lasers designed using this method will be compatible with CMOS processing.

7.2.3 Infrared lasers and optical interconnects using AlInGaNSb

The other method to further red shift emission wavelengths of the III-nitrides is to use antimony (Sb). Chapter VI discusses some of the methods employed to demonstrate the red shift using Sb and the drawbacks associated with these methods. Further research will ensure good quality dilute-antimonide III-nitride crystal growth which will have sufficient red shift with low polarization field. Quite a few thought-provoking preliminary work has already been performed [154]–[156], [158], [159] and one such work is shown in Fig. 7.5 [155]. AlGaInNSb has the potential to reach wavelengths that would not be possible to reach with just the III-nitrides. The family of materials can also be used to design some of the lasers demonstrated in this work. Due to the use of Sb instead of high In composition, such lasers should also have superior performance. Strain related drawbacks will be significantly lower in such novel material based devices. The lower strain can enable the use of planar layers as well as nanowire arrays adding more advantages as traditional processing techniques can then be applied to the planar layers. Similar to the devices shown in this work, such devices will also be compatible with CMOS processing and will be able to operate at room temperature (300K).

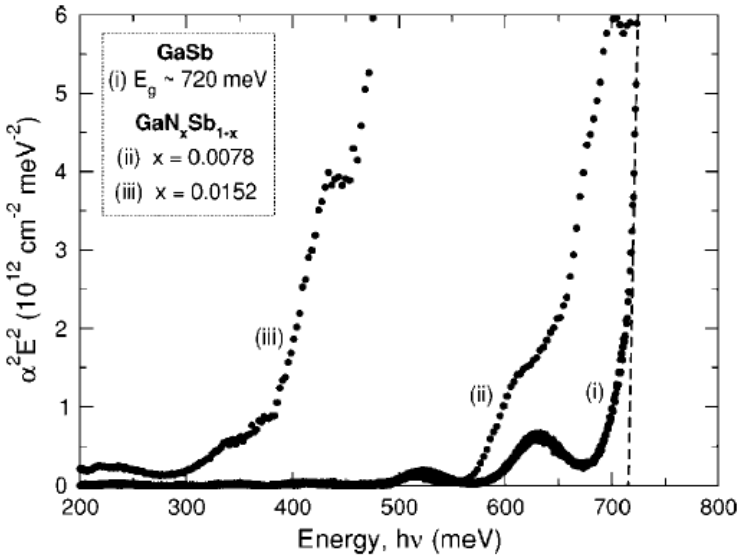

Figure 7.5 Comparison of optical absorption spectra between GaN and GaNSb (Veal *et. al.*, Appl. Phys. Lett. 87.13 (2005): 132101).

APPENDICES

APPENDIX A

Matlab Codes for the Determination of Linear and Parabolic Oxidation Rates from Wet Oxidation Measurements

The following matlab code was used to determine the linear and parabolic rates from the wet oxidation data.

```
clc
clear all;
%  f(x) = p1*x^2 + p2*x + p3 where p3 =0
% x is thickness
X=[0 80 100 120 140];
%% 800C
%% InAlN - 80
%
yIn80_800=[0 302 397 460 495];
p1 = 0.0001109; % (-0.0001783, 0.0004002)
p2 = 0.2185; % (0.09053, 0.3464)
y1= 250:0.01:680;
for i=1:length(y1)
x1(i)=p1*y1(i)*y1(i)+p2*y1(i);
```

```
end
x1=x1';
y1=y1';
X=[80 100 120 140];
Y=[302 397 460 495];
plot(x1,y1,X,Y,'*')
%}
 %% InAlN - 82
%
yIn82_800=[0 324 410 487 538];
p1 = 9.998e-005; %  (-5.31e-005, 0.0001931)
p2 = 0.2082; %  (0.1599, 0.2765)
y1= 250:0.01:680;
for i=1:length(y1)
x1(i)=p1*y1(i)*y1(i)+p2*y1(i);
end
x1=x1';
y1=y1';
X=[80 100 120 140];
Y=[324 410 487 538];
plot(x1,y1,X,Y,'*')
%}
 %% InAlN - 85
```

```
%
yIn85_800=[0 337 427 503 554];
p1 = 8.018e-005;  %(-4.518e-005, 0.0002055)
p2 = 0.2038;  %(0.1426, 0.2651)
y1= 250:0.01:680;
for i=1:length(y1)
x1(i)=p1*y1(i)*y1(i)+p2*y1(i);
end
x1=x1';
y1=y1';
X=[80 100 120 140];
Y=[337 427 503 554];
plot(x1,y1,X,Y,'*')
%}
 %% AlGaN - 85
%
yAl85_800=[0 354 435 516 574];
p1 = 8.145e-005; %  (1.317e-005, 0.0001497)
p2 = 0.1947; % (0.1603, 0.229)
y1= 250:0.01:680;
for i=1:length(y1)
x1(i)=p1*y1(i)*y1(i)+p2*y1(i);
end
```

```
x1=x1';

y1=y1';

X=[80 100 120 140];

Y=[354 435 516 574];

plot(x1,y1,X,Y,'*')

%}

 %% 860C

%% InAlN - 80

%

yIn80_860=[0 330 435 519 547];

p1 = 5.911e-005; %  (-0.0002137, 0.0003319)

p2 = 0.2121; %  (0.0779, 0.3463)

y1= 250:0.01:680;

for i=1:length(y1)

x1(i)=p1*y1(i)*y1(i)+p2*y1(i);

end

x1=x1';

y1=y1';

X=[80 100 120 140];

Y=[330 435 519 547];

plot(x1,y1,X,Y,'*')

%}

 %% InAlN - 82
```

```
%
yIn82_860=[0 361 456 546 585];
p1 = 5.465e-005; % (-9.853e-005, 0.0002478)
p2 = 0.1982;%  (0.09792, 0.2786)
y1= 250:0.01:680;
for i=1:length(y1)
x1(i)=p1*y1(i)*y1(i)+p2*y1(i);
end
x1=x1';
y1=y1';
X=[80 100 120 140];
Y=[361 456 546 585];
plot(x1,y1,X,Y,'*')
%}
 %% InAlN - 85
 %
yIn85_860=[0 374 474 568 605];
p1 = 4.968e-005; % (-0.0001075, 0.0002469)
p2 = 0.1913; % (0.08543, 0.2771)
y1= 250:0.01:680;
for i=1:length(y1)
x1(i)=p1*y1(i)*y1(i)+p2*y1(i);
end
```

```
x1=x1';

y1=y1';

X=[80 100 120 140];

Y=[374 474 568 605];

plot(x1,y1,X,Y,'*')

%}

 %% AlGaN - 85

%

yAl85_860=[0 385 501 603 637];

p1 = 4.262e-005; % (-0.0001445, 0.0002297)

p2 = 0.1834; % (0.07641, 0.2903)

y1= 250:0.01:680;

for i=1:length(y1)

x1(i)=p1*y1(i)*y1(i)+p2*y1(i);

end

x1=x1';

y1=y1';

X=[80 100 120 140];

Y=[385 501 603 637];

plot(x1,y1,X,Y,'*')

%}

 %% Model_Test

%
```

```
p1 = 4.262e-005; % (-0.0001445, 0.0002297)

p2 = 0.1834; % (0.07641, 0.2903)

y1= 0:1:10000;

for i=1:length(y1)

x1(i)=p1*y1(i)*y1(i)+p2*y1(i);

end

x1=x1';

y1=y1';

plot(x1,y1)

%}

 %% Linear and Parabolic Terms

%

xlp=[80 82 85 85];

%% 800

p1_80_800 = 0.0001109; % (-0.0001783, 0.0004002)

p2_80_800 = 0.2185; % (0.09053, 0.3464)

 p1_82_800 = 9.998e-005; %  (-5.31e-005, 0.0001931)

p2_82_800 = 0.2082; %  (0.1599, 0.2765)

p1_85_800 = 8.018e-005;  %(-4.518e-005, 0.0002055)

p2_85_800 = 0.2038;  %(0.1426, 0.2651)

 p1_Al85_800 = 8.145e-005; %  (1.317e-005, 0.0001497)

p2_Al85_800 = 0.1947; % (0.1603, 0.229)

 %% 860
```

```
 p1_80_860 = 5.911e-005; %  (-0.0002137, 0.0003319)
p2_80_860 = 0.2121; %  (0.0779, 0.3463)
 p1_82_860 = 5.465e-005; % (-9.853e-005, 0.0002478)
p2_82_860 = 0.1982;%  (0.09792, 0.2786)
 p1_85_860 = 4.968e-005; % (-0.0001075, 0.0002469)
p2_85_860 = 0.1913; % (0.08543, 0.2771)
 p1_Al85_860 = 4.262e-005; % (-0.0001445, 0.0002297)
p2_Al85_860 = 0.1834; % (0.07641, 0.2903)
 Lin800_1=[p2_80_800 p2_82_800 p2_85_800 p2_Al85_800];
Para800_1=[p1_80_800 p1_82_800 p1_85_800 p1_Al85_800];
 Lin860_1=[p2_80_860 p2_82_860 p2_85_860 p2_Al85_860];
Para860_1=[p1_80_860 p1_82_860 p1_85_860 p1_Al85_860];
 Lin800=1./Lin800_1;
Para800=1./Para800_1;
 Lin860=1./Lin860_1;
Para860=1./Para860_1;
 Lin800=Lin800';
Lin860=Lin860';
Para800=Para800';
Para860=Para860';
 subplot (2,1,1), plot(xlp,Lin800,'*',xlp,Lin860,'o')
title('linear')
%hold on
```

```
subplot (2,1,2), plot(xlp,Para800,'*',xlp,Para860,'o')
title('parabolic')
%}
```

APPENDIX B

Process Flow for the Fabrication of the Photonic Integrated Circuit

Laser and detector fabrication separately have been discussed in previous nanowire works. This section focuses on the growth and fabrication process used to fabricate the entire photonic integrated circuit. The process has been shown schematically in a relatively simplified manner. Further details on particular processes that were used can be obtained in chapter V.

Step 1: Growth of nanowire heterostructures on n-type (001)Si using plasma assisted molecular beam epitaxy (PA-MBE)

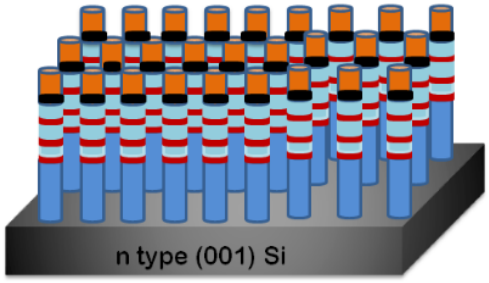

Step 2: Parylene planarization of nanowire heterostructures

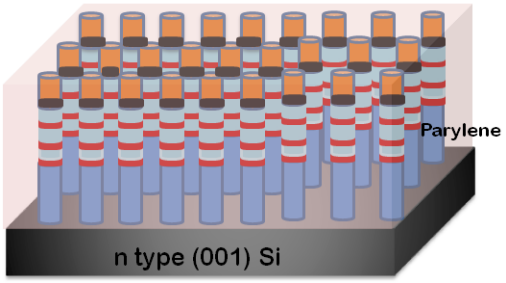

Step 3: p-metal Deposition in Selected areas of the nanowire array

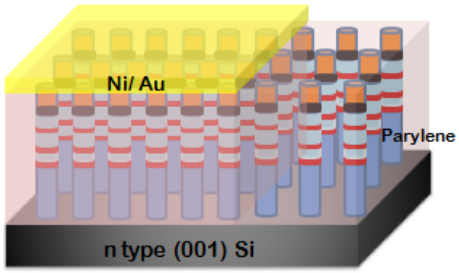

Step 4: Selective Etch of the nanowires

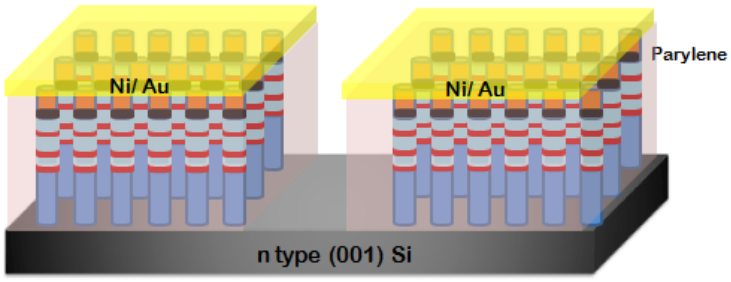

Step 5: n-metal Deposition in Selected Areas of the exposed n-Silicon

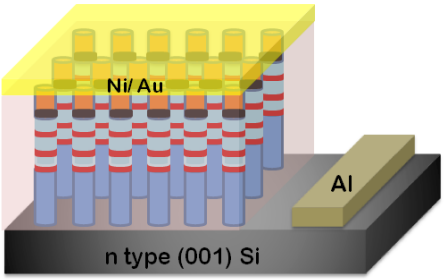

Step 6: Waveguide Layers Deposition between the Lasers and the Detectors

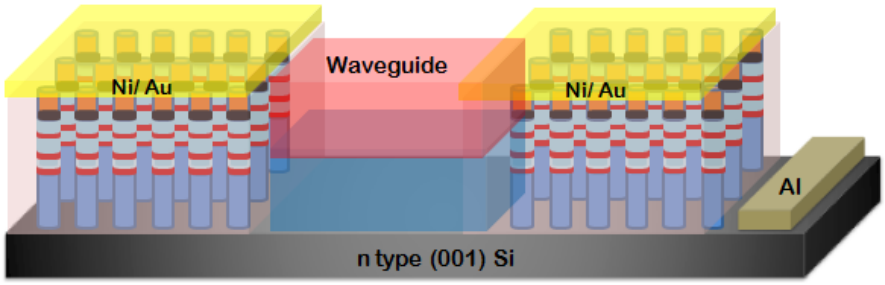

A schematic of the entire photonic integrated circuit has been shown below along with arrows indicating the direction of the guided light.

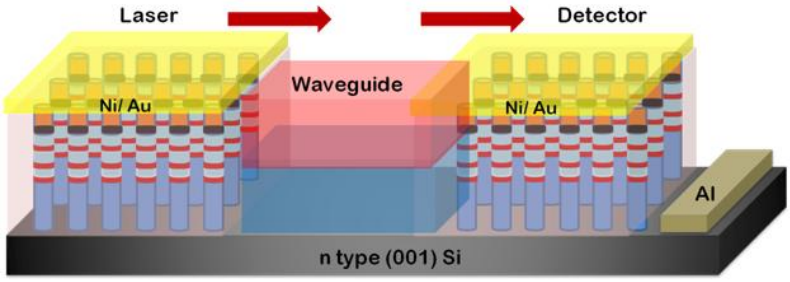

Figure B.1 Schematic of a photonic integrated circuit with arrows indicating the direction of light propagation.

APPENDIX C

Schematics of Measurement Set-ups

This section describes the set-ups required for two important measurements discussed in this thesis. The first set up-schematic discusses the photocurrent spectra measurements and the second one discusses the measurement of the photonic integrated circuit. Schematics for other measurement set ups used in this work has been detailed in previous works [182].

C.1 Photocurrent Spectra Measurement System:

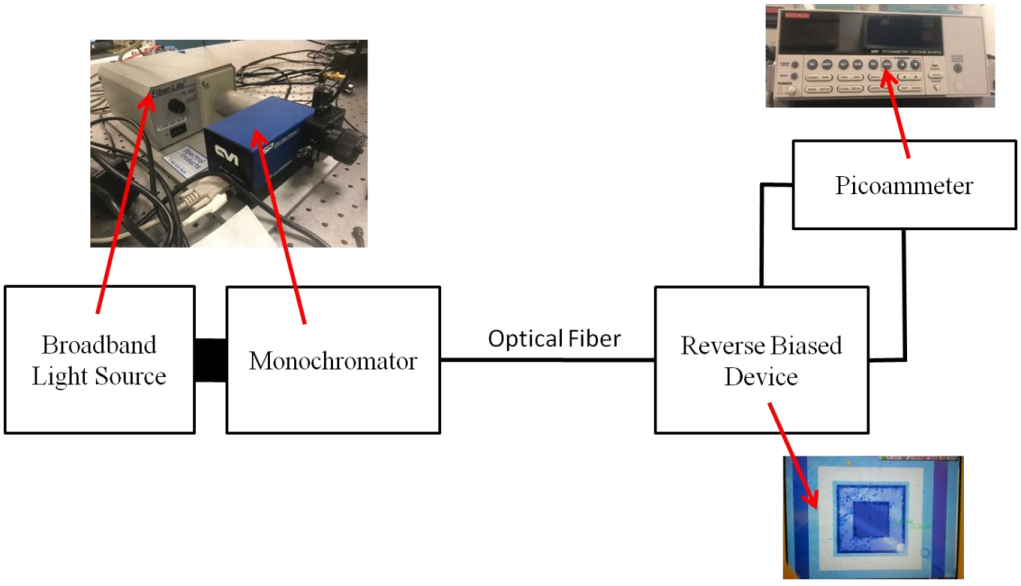

Figure C.1 Schematic of the photocurrent spectra measurement system.

The above set up schematic shows the set up required for the measurement of the photocurrent spectra. At a fixed bias voltage, the photocurrents from the reverse biased

devices were measured using the picoammeter at different incident wavelengths. The incident wavelengths were selected by the monochromator. The broadband source enabled the measurement to be carried out from 200nm to 1800nm. The reverse bias was also varied to measure the change in the photocurrent spectra as a function of both bias and incident wavelength. Such spectra in 3D can be seen in Fig. A3.2. One of the independent axes is the excitation wavelength, and the other is the reverse bias voltage. Two spectra, corresponding to two biases (-0.1 and -1V) from Fig. A3.2, have been shown in Fig. 5.16 in chapter V.

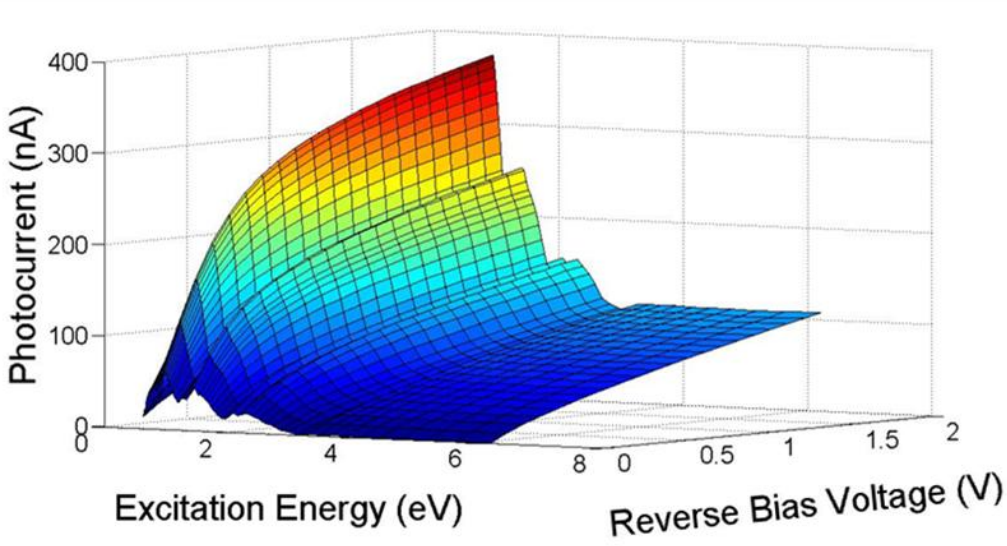

Figure C.2 Measured photocurrent (I_{ph}) spectra from a guided wave detector as a function of excitation energy and reverse bias voltage.

C.2 Photocurrent Measurement from the Photonic Integrated Circuit as a Function of the Laser Injection Current:

The two devices have to be biased separately to measure the variation of the photocurrent of the detector as a function of the laser injection current both integrated into the photonic integrated circuit. The detector is reverse biased at a fixed voltage, and the laser is forward biased. The detector bias circuit is connected in series with a

picoammeter, and the laser bias circuit is connected in series with another ammeter. The laser injection current (I_{inj}) have been varied and recorded from the ammeter. Correspondingly, the change in detector photocurrent (I_{ph}) has been recorded from the picoammeter which has been schematically shown in Fig. A3.3.

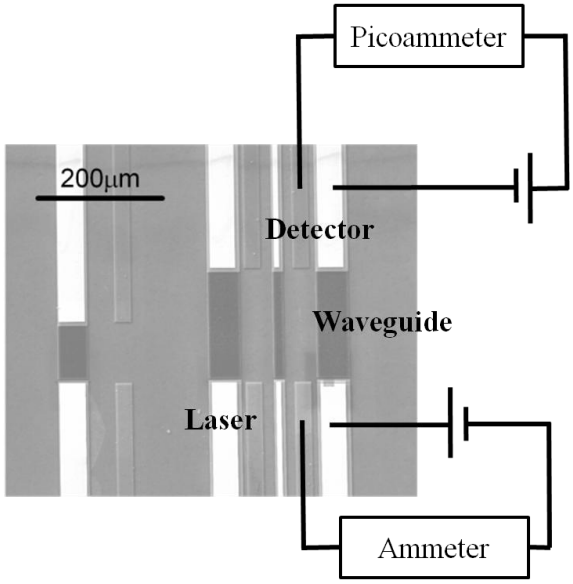

Figure C.3 Set up to required for the measurement of the variation of the detector photocurrent as a function of laser injection current. Both the detector and the laser are integrated into the photonic integrated circuit which can be seen in the scanning electron microscopy (SEM) image. The laser and the detector are coupled using the waveguide.

BIBLIOGRAPHY

BIBLIOGRAPHY

[1] "History of the Incandescent Light." [Online]. Available: http://www.edisontechcenter.org/incandescent.html.

[2] "Lighting A Revolution: Peter Cooper Hewitt." [Online]. Available: http://americanhistory.si.edu/lighting/bios/hewitt.htm.

[3] "News - First LED by the GE engineer, Nick Holonyak," *GE Lighting Europe*. [Online]. Available: http://www.gelighting.com/LightingWeb/emea/news-and-media/news/First-LED-by-the-GE-engineer-Nick-Holonyak.jsp.

[4] "Robert Hall | Lemelson-MIT Program." [Online]. Available: https://lemelson.mit.edu/resources/robert-hall.

[5] "The Story Behind Shuji Nakamura's Invention of Blue LEDs - LEDinside." [Online]. Available: http://www.ledinside.com/news/2014/10/the_story_behind_shuji_nakamuras_invention_of_blue_leds.

[6] "Light Bulb Efficiency | Center for Nanoscale Science." [Online]. Available: https://www.mrsec.psu.edu/content/light-bulb-efficiency.

[7] S. Pimputkar, J. S. Speck, S. P. DenBaars, and S. Nakamura, "Prospects for LED lighting," *Nat. Photonics*, vol. 3, no. 4, pp. 180–182, Apr. 2009.

[8] viribrightshop, "Comparing LED vs CFL vs Incandescent Light Bulbs," *Viribright® LED Light Bulbs*, 05-Apr-2017. [Online]. Available: http://www.viribright.com/lumen-output-comparing-led-vs-cfl-vs-incandescent-wattage/.

[9] A. W. Hoffman, E. Corrales, P. J. Love, J. P. Rosbeck, M. Merrill, A. Fowler, and C. McMurtry, "2Kx2K InSb for astronomy," in *Proc. SPIE 5499, Optical and Infrared Detectors for Astronomy, 59*, 2004, vol. 5499, pp. 59–67.

[10] S. Türker-Kaya and C. W. Huck, "A Review of Mid-Infrared and Near-Infrared Imaging: Principles, Concepts and Applications in Plant Tissue Analysis," *Molecules*, vol. 22, no. 1, p. 168, Jan. 2017.

[11] R. Soref, "The Past, Present, and Future of Silicon Photonics," *IEEE J. Sel. Top. Quantum Electron.*, vol. 12, no. 6, pp. 1678–1687, Nov. 2006.

[12] J. B. Carruthers, "Wireless Infrared Communications," in *Wiley Encyclopedia of Telecommunications*, John Wiley & Sons, Inc., 2003.

[13] E. M. Dianov, "Bismuth-doped optical fibers: a challenging active medium for near-IR lasers and optical amplifiers," *Light Sci. Appl.*, vol. 1, no. 5, p. e12, May 2012.

[14] C. R. Simpson, M. Kohl, M. Essenpreis, and M. Cope, "Near-infrared optical properties of ex vivo human skin and subcutaneous tissues measured using the Monte Carlo inversion technique," *Phys. Med. Biol.*, vol. 43, no. 9, p. 2465, 1998.

[15] "Moore's Law and Intel Innovation," *Intel*. [Online]. Available: http://www.intel.com/content/www/us/en/history/museum-gordon-moore-law.html.

[16] "Intel® 14 nm Technology," *Intel*. [Online]. Available: http://www.intel.com/content/www/us/en/silicon-innovations/intel-14nm-technology.html.

[17] "Element Abundance in Earth's Crust." [Online]. Available: http://hyperphysics.phy-astr.gsu.edu/hbase/Tables/elabund.html.

[18] "50 Years of Moore's Law," *Intel*. [Online]. Available: http://www.intel.com/content/www/us/en/silicon-innovations/moores-law-technology.html.

[19] G. G. Macfarlane, T. P. McLean, J. E. Quarrington, and V. Roberts, "Fine Structure in the Absorption-Edge Spectrum of Si," *Phys. Rev.*, vol. 111, no. 5, pp. 1245–1254, Sep. 1958.

[20] H. R. Philipp and E. A. Taft, "Optical Constants of Silicon in the Region 1 to 10 ev," *Phys. Rev.*, vol. 120, no. 1, pp. 37–38, Oct. 1960.

[21] A. Poruba, A. Fejfar, Z. Remeš, J. Špringer, M. Vaněček, J. Kočka, J. Meier, P. Torres, and A. Shah, "Optical absorption and light scattering in microcrystalline silicon thin films and solar cells," *J. Appl. Phys.*, vol. 88, no. 1, pp. 148–160, Jun. 2000.

[22] R. Kirchain and L. Kimerling, "A roadmap for nanophotonics," *Nat. Photonics*, vol. 1, no. 6, pp. 303–305, Jun. 2007.

[23] T. L. Koch and U. Koren, "Semiconductor photonic integrated circuits," *IEEE J. Quantum Electron.*, vol. 27, no. 3, pp. 641–653, Mar. 1991.

[24] H. Z. Chen, A. Ghaffari, H. Wang, H. Morkoc, and A. Yariv, "Continuous-wave operation of extremely low-threshold GaAs/AlGaAs broad-area injection lasers on

(100) Si substrates at room temperature," *Opt. Lett.*, vol. 12, no. 10, pp. 812–813, Jun. 1987.

[25] Z. Mi, P. Bhattacharya, J. Yang, and K. P. Pipe, "Room-temperature self-organized $In_{0.5}Ga_{0.5}As$ quantum dot laser on silicon," *Electron. Lett.*, vol. 41, no. 13, pp. 742–743, Jun. 2005.

[26] A. Y. Liu, C. Zhang, J. Norman, A. Snyder, D. Lubyshev, J. M. Fastenau, A. W. K. Liu, A. C. Gossard, and J. E. Bowers, "High performance continuous wave 1.3 μm quantum dot lasers on silicon," *Appl. Phys. Lett.*, vol. 104, no. 4, p. 041104, Jan. 2014.

[27] R. E. Camacho-Aguilera, Y. Cai, N. Patel, J. T. Bessette, M. Romagnoli, L. C. Kimerling, and J. Michel, "An electrically pumped germanium laser," *Opt. Express*, vol. 20, no. 10, pp. 11316–11320, May 2012.

[28] A. W. Fang, H. Park, O. Cohen, R. Jones, M. J. Paniccia, and J. E. Bowers, "Electrically pumped hybrid AlGaInAs-silicon evanescent laser," *Opt. Express*, vol. 14, no. 20, pp. 9203–9210, Oct. 2006.

[29] S. Wirths, R. Geiger, N. von den Driesch, G. Mussler, T. Stoica, S. Mantl, Z. Ikonic, M. Luysberg, S. Chiussi, J. M. Hartmann, H. Sigg, J. Faist, D. Buca, and D. Grützmacher, "Lasing in direct-bandgap GeSn alloy grown on Si," *Nat. Photonics*, vol. 9, no. 2, pp. 88–92, Feb. 2015.

[30] M. Nishimura, "Optical fibers and fiber dispersion compensators for high-speed optical communication," *J. Opt. Fiber Commun. Rep.*, vol. 2, no. 2, pp. 115–139, Jun. 2005.

[31] S. Nakamura, M. Senoh, and T. Mukai, "High-power InGaN/GaN double-heterostructure violet light emitting diodes," *Appl. Phys. Lett.*, vol. 62, no. 19, pp. 2390–2392, May 1993.

[32] A. T. Connie, S. Zhao, S. M. Sadaf, I. Shih, Z. Mi, X. Du, J. Lin, and H. Jiang, "Optical and electrical properties of Mg-doped AlN nanowires grown by molecular beam epitaxy," *Appl. Phys. Lett.*, vol. 106, no. 21, p. 213105, May 2015.

[33] A. Hazari, M. Zunaid Baten, L. Yan, J. M. Millunchick, and P. Bhattacharya, "An InN/InGaN/GaN nanowire array guided wave photodiode on silicon," *Appl. Phys. Lett.*, vol. 109, no. 19, p. 191102, Nov. 2016.

[34] "Daniel Feezell III-Nitrides Research Group University of New Mexico," *Daniel Feezell III-Nitrides Research Group University of New Mexico*. [Online]. Available: https://www.feezellgroup.com.

[35] W. Jia-Xing, W. Lai, H. Zhi-Biao, and L. Yi, "Efficiency Droop Effect Mechanism in an InGaN/GaN Blue MQW LED," *Chin. Phys. Lett.*, vol. 28, no. 11, p. 118105, 2011.

[36] D. F. Feezell, J. S. Speck, S. P. DenBaars, and S. Nakamura, "Semipolar (2021) InGaN/GaN Light-Emitting Diodes for High-Efficiency Solid-State Lighting," *J. Disp. Technol.*, vol. 9, no. 4, pp. 190–198, Apr. 2013.

[37] M. E. Lin, B. Sverdlov, G. L. Zhou, and H. Morkoç, "A comparative study of GaN epilayers grown on sapphire and SiC substrates by plasma-assisted molecular-beam epitaxy," *Appl. Phys. Lett.*, vol. 62, no. 26, pp. 3479–3481, Jun. 1993.

[38] C. R. Miskys, M. K. Kelly, O. Ambacher, G. Martínez-Criado, and M. Stutzmann, "GaN homoepitaxy by metalorganic chemical-vapor deposition on free-standing GaN substrates," *Appl. Phys. Lett.*, vol. 77, no. 12, pp. 1858–1860, Sep. 2000.

[39] S. D. Hersee, A. K. Rishinaramangalam, M. N. Fairchild, L. Zhang, and P. Varangis, "Threading defect elimination in GaN nanowires," *J. Mater. Res.*, vol. 26, no. 17, pp. 2293–2298, Sep. 2011.

[40] W. Guo, M. Zhang, P. Bhattacharya, and J. Heo, "Auger Recombination in III-Nitride Nanowires and Its Effect on Nanowire Light-Emitting Diode Characteristics," *Nano Lett.*, vol. 11, no. 4, pp. 1434–1438, Apr. 2011.

[41] K. A. Bertness, N. A. Sanford, and A. V. Davydov, "GaN Nanowires Grown by Molecular Beam Epitaxy," *IEEE J. Sel. Top. Quantum Electron.*, vol. 17, no. 4, pp. 847–858, Jul. 2011.

[42] T. Frost, S. Jahangir, E. Stark, S. Deshpande, A. Hazari, C. Zhao, B. S. Ooi, and P. Bhattacharya, "Monolithic electrically injected nanowire array edge-emitting laser on (001) silicon," *Nano Lett.*, vol. 14, no. 8, pp. 4535–4541, Jul. 2014.

[43] S. Jahangir, T. Schimpke, M. Strassburg, K. A. Grossklaus, J. M. Millunchick, and P. Bhattacharya, "Red-emitting (λ = 610 nm) $In_{0.51}Ga_{0.49}N$/GaN disk-in-nanowire light emitting diodes on silicon," *IEEE J. Quantum Electron.*, vol. 50, no. 7, pp. 530–537, Jul. 2014.

[44] W. Guo, M. Zhang, A. Banerjee, and P. Bhattacharya, "Catalyst-free InGaN/GaN nanowire light emitting diodes grown on (001) silicon by molecular beam epitaxy," *Nano Lett.*, vol. 10, no. 9, pp. 3355–3359, Aug. 2010.

[45] A. Hazari, F. C. Hsiao, L. Yan, J. Heo, J. M. Millunchick, J. M. Dallesasse, and P. Bhattacharya, "1.3 μm Optical Interconnect on Silicon: A Monolithic III-Nitride Nanowire Photonic Integrated Circuit," *IEEE J. Quantum Electron.*, vol. 53, no. 4, May 2017.

[46] S. Deshpande, T. Frost, L. Yan, S. Jahangir, A. Hazari, X. Liu, J. Mirecki-Millunchick, Z. Mi, and P. Bhattacharya, "Formation and nature of InGaN quantum dots in GaN nanowires," *Nano Lett.*, vol. 15, no. 3, pp. 1647–1653, Feb. 2015.

[47] Y. S. Jeong, B. Ratier, A. Moliton, and L. Guyard, “UV–visible and infrared characterization of poly(p-xylylene) films for waveguide applications and OLED encapsulation,” *Synth. Met.*, vol. 127, no. 1, pp. 189–193, Mar. 2002.

[48] X. Wang, S.-B. Che, Y. Ishitani, and A. Yoshikawa, “Step-Flow Growth of In-Polar InN by Molecular Beam Epitaxy,” *Jpn. J. Appl. Phys.*, vol. 45, no. 7L, p. L730, Jul. 2006.

[49] E. H. C. Parker, Ed., *The Technology and Physics of Molecular Beam Epitaxy*, 1 edition. New York: Springer, 1985.

[50] E. Calleja, J. Ristić, S. Fernández-Garrido, L. Cerutti, M. A. Sánchez-García, J. Grandal, A. Trampert, U. Jahn, G. Sánchez, A. Griol, and B. Sánchez, “Growth, morphology, and structural properties of group-III-nitride nanocolumns and nanodisks,” *Phys. Status Solidi B*, vol. 244, no. 8, pp. 2816–2837, Aug. 2007.

[51] K. Merrill, K. Yalavarthi, and S. Ahmed, “Giant growth-plane optical anisotropy in wurtzite InN/GaN disk-in-wire structures,” *Superlattices Microstruct.*, vol. 52, no. 5, pp. 949–961, Apr. 2012.

[52] J. S. Major, J. S. Osinski, and D. F. Welch, “8.5 W CW 2.0 μm InGaAsP laser diodes,” *Electron. Lett.*, vol. 29, no. 24, pp. 2112–2113, Nov. 1993.

[53] Y. F. Chen, “Compact efficient all-solid-state eye-safe laser with self-frequency Raman conversion in a Nd:YVO_4 crystal,” *Opt. Lett.*, vol. 29, no. 18, pp. 2172–2174, Sep. 2004.

[54] K. Hotate and T. Okugawa, “Optical information processing by synthesis of the coherence function,” *J. Light. Technol.*, vol. 12, no. 7, pp. 1247–1255, Jul. 1994.

[55] K. Kuriki, Y. Koike, and Y. Okamoto, “Plastic Optical Fiber Lasers and Amplifiers Containing Lanthanide Complexes,” *Chem. Rev.*, vol. 102, no. 6, pp. 2347–2356, Jun. 2002.

[56] G. P. Agrawal, *Fiber-Optic Communication Systems*, 4 edition. New York: Wiley, 2010.

[57] S. Nakamura, M. Senoh, S. Nagahama, N. Iwasa, T. Yamada, T. Matsushita, H. Kiyoku, and Y. Sugimoto, “InGaN-Based Multi-Quantum-Well-Structure Laser Diodes,” *Jpn. J. Appl. Phys.*, vol. 35, no. 1B, pp. L74–L76, Jan. 1996.

[58] T. Takeuchi, H. Amano, and I. Akasaki, “Theoretical Study of Orientation Dependence of Piezoelectric Effects in Wurtzite Strained GaInN/GaN Heterostructures and Quantum Wells,” *Jpn. J. Appl. Phys.*, vol. 39, no. 2R, p. 413, Feb. 2000.

[59] S. Ino, “Some New Techniques in Reflection High Energy Electron Diffraction (RHEED) Application to Surface Structure Studies,” *Jpn. J. Appl. Phys.*, vol. 16, no. 6, p. 891, Jun. 1977.

[60] H. Hibino, T. Fukuda, M. Suzuki, Y. Homma, T. Sato, M. Iwatsuki, K. Miki, and H. Tokumoto, “High-temperature scanning-tunneling-microscopy observation of phase transitions and reconstruction on a vicinal Si(111) surface,” *Phys. Rev. B*, vol. 47, no. 19, pp. 13027–13030, May 1993.

[61] S. Jahangir, “III-Nitride self-assembled nanowire light emitting diodes and lasers on (001) silicon,” *Dr. Diss. Univ. Mich.*, 2015.

[62] Y. P. Varshni, “Temperature dependence of the energy gap in semiconductors,” *Physica*, vol. 34, pp. 149–154, 1967.

[63] S. L. Chuang, *Physics of Photonic Devices*, vol. 80. John Wiley & Sons, 2012.

[64] S.-W. Feng, Y.-C. Cheng, Y.-Y. Chung, C. C. Yang, Y.-S. Lin, C. Hsu, K.-J. Ma, and J.-I. Chyi, “Impact of localized states on the recombination dynamics in InGaN/GaN quantum well structures,” *J. Appl. Phys.*, vol. 92, no. 8, pp. 4441–4448, Jul. 2002.

[65] K. S. Ramaiah, Y. K. Su, S. J. Chang, B. Kerr, H. P. Liu, and I. G. Chen, “Characterization of InGaN/GaN multi-quantum-well blue-light-emitting diodes grown by metal organic chemical vapor deposition,” *Appl. Phys. Lett.*, vol. 84, no. 17, pp. 3307–3309, Mar. 2004.

[66] J. Krustok, H. Collan, and K. Hjelt, “Does the low-temperature Arrhenius plot of the photoluminescence intensity in CdTe point towards an erroneous activation energy?,” *J. Appl. Phys.*, vol. 81, no. 3, pp. 1442–1445, Feb. 1997.

[67] B. J. Skromme, J. Jayapalan, R. P. Vaudo, and V. M. Phanse, “Low-temperature luminescence of exciton and defect states in heteroepitaxial GaN grown by hydride vapor phase epitaxy,” *Appl. Phys. Lett.*, vol. 74, no. 16, pp. 2358–2360, Feb. 1999.

[68] C. Adelmann, J. Simon, G. Feuillet, N. T. Pelekanos, B. Daudin, and G. Fishman, “Self-assembled InGaN quantum dots grown by molecular-beam epitaxy,” *Appl. Phys. Lett.*, vol. 76, no. 12, pp. 1570–1572, Jan. 2000.

[69] Ž. Gačević, A. Das, J. Teubert, Y. Kotsar, P. K. Kandaswamy, T. Kehagias, T. Koukoula, P. Komninou, and E. Monroy, “Internal quantum efficiency of III-nitride quantum dot superlattices grown by plasma-assisted molecular-beam epitaxy,” *J. Appl. Phys.*, vol. 109, no. 10, p. 103501, May 2011.

[70] B. Damilano, N. Grandjean, S. Dalmasso, and J. Massies, “Room-temperature blue-green emission from InGaN/GaN quantum dots made by straininduced islanding growth,” *Appl. Phys. Lett.*, vol. 75, no. 24, pp. 3751–3753, Oct. 1999.

[71] K. A. Grossklaus, A. Banerjee, S. Jahangir, P. Bhattacharya, and J. M. Millunchick, "Misorientation defects in coalesced self-catalyzed GaN nanowires," *J. Cryst. Growth*, vol. 371, pp. 142–147, Feb. 2013.

[72] S. F. Chichibu, A. Uedono, T. Onuma, B. A. Haskell, A. Chakraborty, T. Koyama, P. T. Fini, S. Keller, S. P. DenBaars, J. S. Speck, U. K. Mishra, S. Nakamura, S. Yamaguchi, S. Kamiyama, H. Amano, I. Akasaki, J. Han, and T. Sota, "Origin of defect-insensitive emission probability in In-containing (Al,In,Ga)N alloy semiconductors," *Nat. Mater. Lond.*, vol. 5, no. 10, pp. 810–6, Oct. 2006.

[73] W. Walukiewicz, J. W. A. III, K. M. Yu, Z. Liliental-Weber, J. Wu, S. X. Li, R. E. Jones, and J. D. Denlinger, "Structure and electronic properties of InN and In-rich group III-nitride alloys," *J. Phys. Appl. Phys.*, vol. 39, no. 5, p. R83, 2006.

[74] T. Stoica, R. J. Meijers, R. Calarco, T. Richter, E. Sutter, and H. Lüth, "Photoluminescence and Intrinsic Properties of MBE-Grown InN Nanowires," *Nano Lett.*, vol. 6, no. 7, pp. 1541–1547, Jul. 2006.

[75] P. W. Fry, I. E. Itskevich, S. R. Parnell, J. J. Finley, L. R. Wilson, K. L. Schumacher, D. J. Mowbray, M. S. Skolnick, M. Al-Khafaji, A. G. Cullis, M. Hopkinson, J. C. Clark, and G. Hill, "Photocurrent spectroscopy of InAs/GaAs self-assembled quantum dots," *Phys. Rev. B*, vol. 62, no. 24, pp. 16784–16791, Dec. 2000.

[76] A. V. Latyshev, A. B. Krasilnikov, A. L. Aseev, L. V. Sokolov, and S. I. Stenin, "Reflection electron microscopy study of clean Si(111) surface reconstruction during the (7 × 7) ς (1 × 1) phase transition," *Surf. Sci.*, vol. 254, no. 1, pp. 90–96, Aug. 1991.

[77] T. Hoshino, K. Kumamoto, K. Kokubun, T. Ishimaru, and I. Ohdomari, "Evidence for the leading role of the stacking-fault triangle in the Si(111) 1x1 -> 7x7 phase transition," *Phys. Rev. B*, vol. 51, no. 20, pp. 14594–14597, May 1995.

[78] G. Cheng, E. Stern, D. Turner-Evans, and M. A. Reed, "Electronic properties of InN nanowires," *Appl. Phys. Lett.*, vol. 87, no. 25, p. 253103, Dec. 2005.

[79] L. Yan, S. Jahangir, S. A. Wight, B. Nikoobakht, P. Bhattacharya, and J. M. Millunchick, "Structural and Optical Properties of Disc-in-Wire InGaN/GaN LEDs," *Nano Lett.*, vol. 15, no. 3, pp. 1535–1539, Mar. 2015.

[80] T. Peng and J. Piprek, "Refractive index of AlGaInN alloys," *Electron. Lett.*, vol. 32, no. 24, p. 2285, Nov. 1996.

[81] D. V. P. McLaughlin and J. M. Pearce, "Analytical model for the optical functions of indium gallium nitride with application to thin film solar photovoltaic cells," *Mater. Sci. Eng. B*, vol. 177, pp. 239–244, Dec. 2011.

[82] S. Zhao, H. P. T. Nguyen, M. G. Kibria, and Z. Mi, "III-Nitride nanowire optoelectronics," *Prog. Quantum Electron.*, vol. 44, pp. 14–68, Nov. 2015.

[83] H. Okumura, S. Misawa, and S. Yoshida, "Epitaxial growth of cubic and hexagonal GaN on GaAs by gas-source molecularbeam epitaxy," *Appl. Phys. Lett.*, vol. 59, no. 9, pp. 1058–1060, Jun. 1991.

[84] J. Wu, H. Yaguchi, K. Onabe, R. Ito, and Y. Shiraki, "Photoluminescence properties of cubic GaN grown on GaAs(100) substrates by metalorganic vapor phase epitaxy," *Appl. Phys. Lett.*, vol. 71, no. 15, pp. 2067–2069, Aug. 1997.

[85] H. Fujiwara, *Spectroscopic Ellipsometry*. Wiley, 2007.

[86] G. M. Laws, E. C. Larkins, I. Harrison, C. Molloy, and D. Somerford, "Improved refractive index formulas for the $Al_xGa_{1-x}N$ and $In_yGa_{1-y}N$ alloys," *J. Appl. Phys.*, vol. 89, no. 2, pp. 1108–1115, Aug. 2000.

[87] A. Hazari, A. Bhattacharya, T. Frost, S. Zhao, M. Z. Baten, Z. Mi, and P. Bhattacharya, "Optical constants of $In_xGa_{1-x}N$ ($0 \leq x \leq 0.73$) in the visible and near-infrared wavelength regimes," *Opt. Lett.*, vol. 40, no. 14, pp. 3304–3307, Jul. 2015.

[88] A. T. Cheng, Y. K. Su, and W. C. Lai, "Improved Light Output of Nitride-Based Light-Emitting Diodes by Lattice-Matched AlInN Cladding Structure," *IEEE Photonics Technol. Lett.*, vol. 20, no. 12, pp. 970–972, Jun. 2008.

[89] R. Butté, J.-F. Carlin, E. Feltin, M. Gonschorek, S. Nicolay, G. Christmann, D. Simeonov, A. Castiglia, J. Dorsaz, H. J. Buehlmann, S. Christopoulos, G. B. H. von Högersthal, A. J. D. Grundy, M. Mosca, C. Pinquier, M. A. Py, F. Demangeot, J. Frandon, P. G. Lagoudakis, *et al.*, "Current status of AlInN layers lattice-matched to GaN for photonics and electronics," *J. Phys. Appl. Phys.*, vol. 40, no. 20, p. 6328, 2007.

[90] S. Dasgupta, Nidhi, S. Choi, F. Wu, J. S. Speck, and U. K. Mishra, "Growth, Structural, and Electrical Characterizations of N-Polar InAlN by Plasma-Assisted Molecular Beam Epitaxy," *Appl. Phys. Express*, vol. 4, no. 4, p. 045502, Mar. 2011.

[91] E. Luder, "Polycrystalline Silicon-Based Sensors," *Sens. Actuators*, vol. 10, no. 1–2, pp. 9–23, Jun. 1986.

[92] G. B. Levy, W. Evans, J. Ebner, P. Farrell, M. Hufford, B. H. Allison, D. Wheeler, H. Lin, O. Prache, and E. Naviasky, "An 852 600 Pixel OLED-on-Silicon Color Microdisplay Using CMOS Subthreshold-Voltage-Scaling Current Drivers," *IEEE J. Solid-State Circuits*, vol. 37, no. 12, pp. 1879–1889, Dec. 2002.

[93] J. Sanchez-Paramo, J. M. Calleja, M. A. Sanchez-Garcia, E. Calleja, and U. Jahn, "Structural and optical characterization of intrinsic GaN nanocolumns," *Phys. E*, vol. 13, no. 2, pp. 1070–1073, Mar. 2002.

[94] T. Kouno, K. Kishino, K. Yamano, and A. Kikuchi, "Two-dimensional light confinement in periodic InGaN/GaN nanocolumn arrays and optically pumped blue stimulated emission," *Opt. Express*, vol. 17, no. 22, pp. 20440–20447, Oct. 2009.

[95] Q. Li, J. B. Wright, W. W. Chow, T. S. Luk, I. Brener, L. F. Lester, and G. T. Wang, "Single-mode GaN nanowire lasers," *Opt. Express*, vol. 20, no. 16, pp. 17873–17879, Jul. 2012.

[96] Q. Wang, A. T. Connie, H. P. T. Nguyen, M. G. Kibria, S. Zhao, S. Sharif, I. Shih, and Z. Mi, "Highly efficient, spectrally pure 340 nm ultraviolet emission from $Al_xGa_{1-x}N$ nanowire based light emitting diodes," *Nanotechnology*, vol. 24, no. 34, p. 345201, Jul. 2013.

[97] S. Arafin, X. Liu, and Z. Mi, "Review of recent progress of III-nitride nanowire lasers," *J. Nanophotonics*, vol. 7, no. 074599, pp. 1–27, Jan. 2013.

[98] A. Hazari, A. Aiello, T.-K. Ng, B. S. Ooi, and P. Bhattacharya, "III-nitride disk-in-nanowire 1.2 μm monolithic diode laser on (001)silicon," *Appl. Phys. Lett.*, vol. 107, no. 19, p. 191107, Nov. 2015.

[99] J. Wang, M. S. Gudiksen, X. Duan, Y. Cui, and C. M. Lieber, "Highly Polarized Photoluminescence and Photodetection from Single Indium Phosphide Nanowires," *Science*, vol. 293, no. 5534, pp. 1455–1457, Aug. 2001.

[100] C. Soci, A. Zhang, B. Xiang, S. A. Dayeh, D. P. R. Aplin, J. Park, X. Y. Bao, Y. H. Lo, and D. Wang, "ZnO Nanowire UV Photodetectors with High Internal Gain," *Nano Lett.*, vol. 7, no. 4, pp. 1003–1009, Feb. 2007.

[101] L. Rigutti, M. Tchernycheva, A. D. L. Bugallo, G. Jacopin, F. H. Julien, L. F. Zagonel, K. March, O. Stephan, M. Kociak, and R. Songmuang, "Ultraviolet Photodetector Based on GaN/AlN Quantum Disks in a Single Nanowire," *Nano Lett.*, vol. 10, no. 8, pp. 2939–2943, Jul. 2010.

[102] C.-L. Hsu, S.-J. Chang, Y.-R. Lin, P.-C. Li, T.-S. Lin, S.-Y. Tsai, T.-H. Lu, and I.-C. Chen, "Ultraviolet photodetectors with low temperature synthesized vertical ZnO nanowires," *Chem. Phys. Lett.*, vol. 416, no. 1, pp. 75–78, Oct. 2005.

[103] A. D. L. Bugallo, M. Tchernycheva, G. Jacopin, L. Rigutti, F. H. Julien, S.-T. Chou, Y.-T. Lin, P.-H. Tseng, and L.-W. Tu, "Visible-blind photodetector based on p–i–n junction GaN nanowire ensembles," *Nanotechnology*, vol. 21, no. 31, pp. 315201-1-315201–5, Jul. 2010.

[104] S. Han, W. Jin, D. Zhang, T. Tang, C. Li, X. Liu, Z. Liu, B. Lei, and C. Zhou, "Photoconduction studies on GaN nanowire transistors under UV and polarized UV illumination," *Chem. Phys. Lett.*, vol. 389, no. 1, pp. 176–180, Feb. 2004.

[105] W. Y. Weng, S. J. Chang, C. L. Hsu, and T. J. Hsueh, "A ZnO-Nanowire Phototransistor Prepared on Glass Substrates," *ACS Appl. Mater. Interfaces*, vol. 3, no. 2, pp. 162–166, Jan. 2011.

[106] R. Songmuang, O. Landré, and B. Daudin, "From nucleation to growth of catalyst-free GaN nanowires on thin AlN buffer layer," *Appl. Phys. Lett.*, vol. 91, no. 25, p. 251902, Dec. 2007.

[107] J. Ristic, E. Calleja, S. Fernandez-Garrido, L. Cerutti, A. Trampert, U. Jahn, and K. H. Ploog, "On the mechanisms of spontaneous growth of III-nitride nanocolumns by plasma-assisted molecular beam epitaxy," *J. Cryst. Growth*, vol. 310, no. 8, pp. 4035–4045, Jun. 2008.

[108] Y.-L. Chang, F. Li, A. Fatehi, and Z. Mi, "Molecular beam epitaxial growth and characterization of non-tapered InN nanowires on Si(111)," *Nanotechnology*, vol. 20, no. 345203, pp. 1–6, Jul. 2009.

[109] C. Cheze, L. Geelhaar, O. Brandt, W. M. Weber, H. Riechert, S. Munch, R. Rothemund, S. Reitzenstein, A. Forchel, T. Kehagias, P. Komninou, G. P. Dimitrakopulos, and T. Karakostas, "Direct Comparison of Catalyst-Free and Catalyst-Induced GaN Nanowires," *Nano Res.*, vol. 3, no. 7, pp. 528–536, Jul. 2010.

[110] J. Wu, "When group-III nitrides go infrared: New properties and perspectives," *J. Appl. Phys.*, vol. 106, no. 1, p. 011101, Jul. 2009.

[111] S. Jahangir, M. Mandl, M. Strassburg, and P. Bhattacharya, "Molecular beam epitaxial growth and optical properties of red-emitting ($\lambda = 650$ nm) InGaN/GaN disks-in-nanowires on silicon," *Appl. Phys. Lett.*, vol. 102, no. 7, p. 071101, Feb. 2013.

[112] A. Banerjee, T. Frost, E. Stark, and P. Bhattacharya, "Continuous-wave operation and differential gain of InGaN/GaN quantum dot ridge waveguide lasers (λ = 420 nm) on c-plane GaN substrate," *Appl. Phys. Lett.*, vol. 101, no. 041108, Jul. 2012.

[113] T. Frost, A. Banerjee, K. Sun, S. L. Chuang, and P. Bhattacharya, "InGaN/GaN Quantum Dot Red (λ = 630 nm) Laser," *IEEE J. Quantum Electron.*, vol. 49, no. 11, pp. 923–931, Nov. 2013.

[114] D. L. Huffaker, G. Park, Z. Zou, O. B. Shchekin, and D. G. Deppe, "1.3 μm room-temperature GaAs-based quantum-dot laser," *Appl. Phys. Lett.*, vol. 73, no. 18, pp. 2564–2566, Sep. 1998.

[115] S. Jahangir, T. Frost, A. Hazari, L. Yan, E. Stark, T. LaMountain, J. Mirecki-Millunchick, B. S. Ooi, and P. Bhattacharya, "Small signal modulation characteristics of red-emitting (λ = 610 nm) III-nitride nanowire array lasers on (001) silicon," *Appl. Phys. Lett.*, vol. 106, no. 071108, Feb. 2015.

[116] D. Bimberg, N. Kirstaedter, N. N. Ledentsov, Z. I. Alferov, P. S. Kop'ev, and V. M. Ustinov, "InGaAs–GaAs quantum-dot lasers," *IEEE J. Sel. Top. Quantum Electron.*, vol. 3, no. 2, pp. 196–205, Dec. 1996.

[117] P. Bhattacharya, S. Ghosh, S. Pradhan, J. Singh, Z.-K. Wu, J. Urayama, K. Kim, and T. B. Norris, "Carrier dynamics and high-speed modulation properties of tunnel injection InGaAs–GaAs quantum-dot lasers," *IEEE J. Quantum Electron.*, vol. 39, no. 8, pp. 952–962, Aug. 2003.

[118] Y.-R. Wu, Y.-Y. Lin, H.-H. Huang, and J. Singh, "Electronic and optical properties of InGaN quantum dot based light emitters for solid state lighting," *J. Appl. Phys.*, vol. 105, no. 1, p. 013117, Jan. 2009.

[119] G.-L. Su, T. Frost, P. Bhattacharya, and J. M. Dallesasse, "Physical model for high indium content InGaN/GaN self-assembled quantum dot ridge-waveguide lasers emitting at red wavelengths ($\lambda \sim 630$ nm)," *Opt. Express*, vol. 23, no. 10, pp. 12850–12865, May 2015.

[120] H. Zhao, R. A. Arif, Y.-K. Ee, and N. Tansu, "Optical gain analysis of strain-compensated InGaN–AlGaN quantum well active regions for lasers emitting at 420–500nm," *Opt. Quantum Electron.*, vol. 40, pp. 301–306, Jan. 2008.

[121] W. G. Scheibenzuber, U. T. Schwarz, L. Sulmoni, J. Dorsaz, J.-F. Carlin, and N. Grandjean, "Recombination coefficients of GaN-based laser diodes," *J. Appl. Phys.*, vol. 109, no. 9, p. 093106, May 2011.

[122] N. Kirstaedter, O. G. Schmidt, N. N. Ledentsov, D. Bimberg, V. M. Ustinov, A. Y. Egorov, A. E. Zhukov, M. V. Maximov, P. S. Kop'ev, and Z. I. Alferov, "Gain and differential gain of single layer InAs/GaAs quantum dot injection lasers," *Appl. Phys. Lett.*, vol. 69, no. 9, pp. 1226–1228, Jun. 1996.

[123] P. Bhattacharya, M. Zhang, and J. Hinckley, "Tunnel injection $In_{0.25}Ga_{0.75}N$/GaN quantum dot light-emitting diodes," *Appl. Phys. Lett.*, vol. 97, no. 25, p. 251107, Dec. 2010.

[124] P. Bhattacharya and S. Ghosh, "Tunnel injection $In_{0.4}Ga_{0.6}As$/GaAs quantum dot lasers with 15 GHz modulation bandwidth at room temperature," *Appl. Phys. Lett.*, vol. 80, no. 19, pp. 3482–3484, Mar. 2002.

[125] H. Z. Chen, A. Ghaffari, H. Wang, H. Morkoc, and A. Yariv, "Low-threshold (~600 A/cm^2 at room temperature) GaAs/AlGaAs lasers on Si (100)," *Appl. Phys. Lett.*, vol. 51, no. 17, pp. 1320–1321, Aug. 1987.

[126] D. Liang and J. E. Bowers, "Recent progress in lasers on silicon," *Nat. Photonics*, vol. 4, no. 8, pp. 511–517, Jul. 2010.

[127] S. Tanaka, S.-H. Jeong, S. Sekiguchi, T. Kurahashi, Y. Tanaka, and K. Morito, "High-output-power, single-wavelength silicon hybrid laser using precise flip-chip bonding technology," *Opt. Express*, vol. 20, no. 27, pp. 28057–28069, Dec. 2012.

[128] S. Lourdudoss, "Heteroepitaxy and selective area heteroepitaxy for silicon photonics," *Curr. Opin. Solid State Mater. Sci.*, vol. 16, no. 2, pp. 91–99, Mar. 2012.

[129] M. E. Groenert, C. W. Leitz, A. J. Pitera, V. Yang, H. Lee, R. J. Ram, and E. A. Fitzgerald, "Monolithic integration of room-temperature cw GaAs/AlGaAs lasers on Si substrates via relaxed graded GeSi buffer layers," *J. Appl. Phys.*, vol. 93, no. 1, pp. 362–367, Jan. 2003.

[130] A. Jallipalli, M. N. Kutty, G. Balakrishnan, J. Tatebayashi, N. Nuntawong, S. H. Huang, L. R. Dawson, D. L. Huffaker, Z. Mi, and P. Bhattacharya, "1.54 μm GaSb/AlGaSb multi-quantum-well monolithic laser at 77 K grown on miscut Si substrate using interfacial misfit arrays," *Electron. Lett.*, vol. 43, no. 22, Oct. 2007.

[131] B. Kunert, S. Zinnkann, K. Volz, and W. Stolz, "Monolithic integration of Ga(NAsP)/(BGa)P multi-quantum well structures on (0 0 1) silicon substrate by MOVPE," *J. Cryst. Growth*, vol. 310, no. 23, pp. 4776–4779, Nov. 2008.

[132] L. Cerutti, J. B. Rodriguez, and E. Tournie, "GaSb-based laser, monolithically grown on silicon substrate, emitting at 1.55 μm at room temperature," *IEEE Photonics Technol. Lett.*, vol. 22, no. 8, pp. 553–555, Apr. 2010.

[133] D. Mistele, T. Rotter, A. Horn, O. Katz, Z. Bougrioua, J. Aderhold, J. Graul, G. Bahir, and J. Salzman, "Incorporation of dielectric layers into the processing of III-nitride-based heterostructure field-effect transistors," *J. Electron. Mater.*, vol. 32, no. 5, pp. 355–363, May 2003.

[134] W. Guo, A. Banerjee, M. Zhang, and P. Bhattacharya, "Barrier height of Pt–$In_xGa_{1-x}N$ ($0 \leq x \leq 0.5$) nanowire Schottky diodes," *Appl. Phys. Lett.*, vol. 98, no. 18, p. 183116, May 2011.

[135] C. S. Lee, T. Frost, W. Guo, and P. Bhattacharya, "High Temperature Stable Operation of 1.3-μm Quantum-Dot Laser Integrated With Single-Mode Tapered Si_3N_4 Waveguide," *IEEE Photonics Technol. Lett.*, vol. 24, no. 11, pp. 918–920, Jun. 2012.

[136] C. S. Lee, T. Frost, W. Guo, and P. Bhattacharya, "Integration of 1.3-μm Quantum-Dot Lasers With Si_3N_4 Waveguides for Single Mode Optical Interconnects," *IEEE J. Quantum Electron.*, vol. 48, no. 10, pp. 1346–1351, Oct. 2012.

[137] P. J. A. Thijs, T. van Dongen, L. F. Tiemeijer, and J. J. M. Binsma, "High-performance $\lambda = 1.3$ μm InGaAsP-InP strained-layer quantum well lasers," *J. Light. Technol.*, vol. 12, no. 1, pp. 28–37, Jan. 1994.

[138] H. Zhao, R. A. Arif, and N. Tansu, "Self-consistent gain analysis of type-II 'W' InGaN–GaNAs quantum well lasers," *J. Appl. Phys.*, vol. 104, no. 4, p. 043104, Aug. 2008.

[139] J. B. Rodriguez, E. Plis, G. Bishop, Y. D. Sharma, H. Kim, L. R. Dawson, and S. Krishna, "nBn structure based on InAs/GaSb type-II strained layer superlattices," *Appl. Phys. Lett.*, vol. 91, no. 4, p. 043514, Jul. 2007.

[140] B. R. Bennett, R. Magno, J. B. Boos, W. Kruppa, and M. G. Ancona, "Antimonide-based compound semiconductors for electronic devices: A review," *Solid-State Electron.*, vol. 49, no. 12, pp. 1875–1895, Dec. 2005.

[141] M. Kopytko and A. Rogalski, "HgCdTe barrier infrared detectors," *Prog. Quantum Electron.*, vol. 47, pp. 1–18, Mar. 2016.

[142] B. F. Levine, S. D. Gunapala, J. M. Kuo, S. S. Pei, and S. Hui, "Normal incidence hole intersubband absorption long wavelength GaAs/$Al_xGa_{1-x}As$ quantum well infrared photodetectors," *Appl. Phys. Lett.*, vol. 59, no. 15, pp. 1864–1866, Oct. 1991.

[143] B. F. Levine, "Quantum-well infrared photodetectors," *J. Appl. Phys.*, vol. 74, no. 8, pp. R1–R81, Oct. 1993.

[144] A. D. Stiff, S. Krishna, P. Bhattacharya, and S. W. Kennerly, "Normal-incidence, high-temperature, mid-infrared, InAs-GaAs vertical quantum-dot infrared photodetector," *IEEE J. Quantum Electron.*, vol. 37, no. 11, pp. 1412–1419, Nov. 2001.

[145] S. Krishna, "Quantum dots-in-a-well infrared photodetectors," *J. Phys. Appl. Phys.*, vol. 38, no. 13, p. 2142, 2005.

[146] T. Wang, J. Bai, S. Sakai, and J. K. Ho, "Investigation of the emission mechanism in InGaN/GaN-based light-emitting diodes," *Appl. Phys. Lett.*, vol. 78, no. 18, pp. 2617–2619, Apr. 2001.

[147] G. Sun, G. Xu, Y. J. Ding, H. Zhao, G. Liu, J. Zhang, and N. Tansu, "Investigation of fast and slow decays in InGaN/GaN quantum wells," *Appl. Phys. Lett.*, vol. 99, no. 8, p. 081104, Aug. 2011.

[148] Y.-H. Cho, G. H. Gainer, A. J. Fischer, J. J. Song, S. Keller, U. K. Mishra, and S. P. DenBaars, "'S-shaped' temperature-dependent emission shift and carrier dynamics in InGaN/GaN multiple quantum wells," *Appl. Phys. Lett.*, vol. 73, no. 10, pp. 1370–1372, Sep. 1998.

[149] F. B. Naranjo, M. A. Sánchez-García, F. Calle, E. Calleja, B. Jenichen, and K. H. Ploog, "Strong localization in InGaN layers with high In content grown by molecular-beam epitaxy," *Appl. Phys. Lett.*, vol. 80, no. 2, pp. 231–233, Jan. 2002.

[150] J. Phillips, K. Kamath, and P. Bhattacharya, "Far-infrared photoconductivity in self-organized InAs quantum dots," *Appl. Phys. Lett.*, vol. 72, no. 16, pp. 2020–2022, Apr. 1998.

[151] F. Bernardini and V. Fiorentini, "Macroscopic polarization and band offsets at nitride heterojunctions," *Phys. Rev. B*, vol. 57, no. 16, pp. R9427–R9430, Apr. 1998.

[152] F. Della Sala, A. Di Carlo, P. Lugli, F. Bernardini, V. Fiorentini, R. Scholz, and J.-M. Jancu, "Free-carrier screening of polarization fields in wurtzite GaN/InGaN laser structures," *Appl. Phys. Lett.*, vol. 74, no. 14, pp. 2002–2004, Apr. 1999.

[153] J. Piprek, "Efficiency droop in nitride-based light-emitting diodes," *Phys. Status Solidi A*, vol. 207, no. 10, pp. 2217–2225, Oct. 2010.

[154] L. Buckle, B. R. Bennett, S. Jollands, T. D. Veal, N. R. Wilson, B. N. Murdin, C. F. McConville, and T. Ashley, "Growth of dilute GaNSb by plasma-assisted MBE," *J. Cryst. Growth*, vol. 278, no. 1, pp. 188–192, May 2005.

[155] T. D. Veal, L. F. J. Piper, S. Jollands, B. R. Bennett, P. H. Jefferson, P. A. Thomas, C. F. McConville, B. N. Murdin, L. Buckle, G. W. Smith, and T. Ashley, "Band gap reduction in GaNSb alloys due to the anion mismatch," *Appl. Phys. Lett.*, vol. 87, no. 13, p. 132101, Sep. 2005.

[156] D. Wang, S. P. Svensson, L. Shterengas, G. Belenky, C. S. Kim, I. Vurgaftman, and J. R. Meyer, "Band edge optical transitions in dilute-nitride GaNSb," *J. Appl. Phys.*, vol. 105, no. 1, p. 014904, Jan. 2009.

[157] J. Ito, T. Chiyo, N. Shibata, H. Watanabe, S. Asami, and S. Asami, "Group III nitride compound semiconductor device," US6426512 B1, 30-Jul-2002.

[158] Q. Shi, Y.-C. Chen, F. A. Chowdhury, Z. Mi, V. Michaud-Rioux, and H. Guo, "Band engineering of GaSbN alloy for solar fuel applications," *Phys. Rev. Mater.*, vol. 1, no. 3, p. 034602, Aug. 2017.

[159] F. A. Chowdhury, S. M. Sadaf, Q. Shi, Y.-C. Chen, H. Guo, and Z. Mi, "Optically active dilute-antimonide III-nitride nanostructures for optoelectronic devices," *Appl. Phys. Lett.*, vol. 111, no. 6, p. 061101, Aug. 2017.

[160] "Periodic Table of Elements: Sorted by Atomic Radius (EnvironmentalChemistry.com)." [Online]. Available: https://environmentalchemistry.com/yogi/periodic/atomicradius.html.

[161] M. J. Holmes, S. Kako, K. Choi, P. Podemski, M. Arita, and Y. Arakawa, "Temperature Dependent Photoluminescence Excitation Spectroscopy of GaN Quantum Dots in Site Controlled GaN/AlGaN Nanowires," *Jpn. J. Appl. Phys.*, vol. 52, no. 8S, p. 08JL02, May 2013.

[162] S. Zhao, S. Y. Woo, M. Bugnet, X. Liu, J. Kang, G. A. Botton, and Z. Mi, "Three-Dimensional Quantum Confinement of Charge Carriers in Self-Organized AlGaN Nanowires: A Viable Route to Electrically Injected Deep Ultraviolet Lasers," *Nano Lett.*, vol. 15, no. 12, pp. 7801–7807, Dec. 2015.

[163] M. Belloeil, B. Gayral, and B. Daudin, "Quantum Dot-Like Behavior of Compositional Fluctuations in AlGaN Nanowires," *Nano Lett.*, vol. 16, no. 2, pp. 960–966, Feb. 2016.

[164] J. D. Brown, Z. Yu, J. Matthews, S. Harney, J. Boney, J. F. Schetzina, J. D. Benson, K. W. Dang, C. Terrill, T. Nohava, W. Yang, and S. Krishnankutty, "Visible-Blind UV Digital Camera Based On a 32 × 32 Array of GaN/AlGaN p-i-n Photodiodes," *Mater. Res. Soc. Internet J. Nitride Semicond. Res.*, vol. 4, no. 1, Jan. 1999.

[165] J. D. Brown, J. Boney, J. Matthews, P. Srinivasan, J. F. Schetzina, T. Nohava, W. Yang, and S. Krishnankutty, "UV-Specific (320-365 nm) Digital Camera Based On a 128×128 Focal Plane Array of GaN/AlGaN p-i-n Photodiodes," *Mater. Res. Soc. Internet J. Nitride Semicond. Res.*, vol. 5, no. 1, Jan. 2000.

[166] S. Verghese, J. P. Donnelly, E. K. Duerr, K. A. McIntosh, D. C. Chapman, C. J. Vineis, G. M. Smith, J. E. Funk, K. E. Jensen, P. I. Hopman, D. C. Shaver, B. F. Aull, J. C. Aversa, J. P. Frechette, J. B. Glettler, Z. L. Liau, J. M. Mahan, L. J. Mahoney, K. M. Molvar, *et al.*, "Arrays of InP-based Avalanche Photodiodes for Photon Counting," *IEEE J. Sel. Top. Quantum Electron.*, vol. 13, no. 4, pp. 870–886, Jul. 2007.

[167] B. J. Rauscher, C. Stahle, R. J. Hill, M. Greenhouse, J. Beletic, S. Babu, P. Blake, K. Cleveland, E. Cofie, B. Eegholm, C. W. Engelbracht, D. N. B. Hall, A. Hoffman, B. Jeffers, C. Jhabvala, R. A. Kimble, S. Kohn, R. Kopp, D. Lee, *et al.*, "Commentary: JWST near-infrared detector degradation— finding the problem, fixing the problem, and moving forward," *AIP Adv.*, vol. 2, no. 2, p. 021901, Jun. 2012.

[168] F. J. Effenberger and A. M. Joshi, "Ultrafast, dual-depletion region, InGaAs/InP p-i-n detector," *J. Light. Technol.*, vol. 14, no. 8, pp. 1859–1864, Aug. 1996.

[169] A. Rogalski, "Infrared detectors: status and trends," *Prog. Quantum Electron.*, vol. 27, no. 2, pp. 59–210, Jan. 2003.

[170] O. G. Memis, J. Kohoutek, D. Dey, W. Wu, and H. Mohseni, "Resonant tunneling injection detectors and imagers," in *2009 IEEE LEOS Annual Meeting Conference Proceedings*, 2009, pp. 363–364.

[171] G. Tourbot, C. Bougerol, F. Glas, L. F. Zagonel, Z. Mahfoud, S. Meuret, P. Gilet, M. Kociak, B. Gayral, and B. Daudin, "Growth mechanism and properties of InGaN insertions in GaN nanowires," *Nanotechnology*, vol. 23, no. 13, p. 135703, 2012.

[172] K. Kishino, M. S. Unlu, J. I. Chyi, J. Reed, L. Arsenault, and H. Morkoc, "Resonant cavity-enhanced (RCE) photodetectors," *IEEE J. Quantum Electron.*, vol. 27, no. 8, pp. 2025–2034, Aug. 1991.

[173] F. Sugihwo and J. S. H. Jr, "Wavelength tunable narrow linewidth resonant cavity light detectors," US6380531 B1, 30-Apr-2002.

[174] O. I. Dosunmu, D. D. Cannon, M. K. Emsley, L. C. Kimerling, and M. S. Unlu, "High-speed resonant cavity enhanced Ge photodetectors on reflecting Si substrates for 1550-nm operation," *IEEE Photonics Technol. Lett.*, vol. 17, no. 1, pp. 175–177, Jan. 2005.

[175] J. W. Trainor and K. Rose, "Some properties of inn films prepared by reactive evaporation," *J. Electron. Mater.*, vol. 3, no. 4, pp. 821–828, Nov. 1974.

[176] J. F. Muth, J. H. Lee, I. K. Shmagin, R. M. Kolbas, H. C. Casey, B. P. Keller, U. K. Mishra, and S. P. DenBaars, "Absorption coefficient, energy gap, exciton binding energy, and recombination lifetime of GaN obtained from transmission measurements," *Appl. Phys. Lett.*, vol. 71, no. 18, pp. 2572–2574, Nov. 1997.

[177] R. Westervelt, H. Abarbanel, R. Garwin, R. Jeanioz, and J. Kimbel, "Imaging Infrared Detectors II," MITRE CORP MCLEAN VA JASON PROGRAM OFFICE, MITRE CORP MCLEAN VA JASON PROGRAM OFFICE, JSR-97-500, Oct. 2000.

[178] T. L. Koch, *Optical Fiber Telecommunications IIIB: v. 3, Pt. B*, 1 edition. Academic Press, 2012.

[179] M. Nakazawa, K. Washio, Y. Asahara, and M. Tokuda, "130-km-long fault location for single-mode optical fiber using 1.55-μm Q-switched Er^{3+}:glass laser," *Opt. Lett.*, vol. 9, no. 7, pp. 312–314, Jul. 1984.

[180] T. L. Koch, T. J. Bridges, E. G. Burkhardt, P. J. Corvini, L. A. Coldren, R. A. Linke, W. T. Tsang, R. A. Logan, L. F. Johnson, R. F. Kazarinov, R. Yen, and D. P. Wilt, "1.55-μm InGaAsP distributed feedback vapor phase transported buried heterostructure lasers," *Appl. Phys. Lett.*, vol. 47, no. 1, pp. 12–14, Jul. 1985.

[181] N. Kim, Y. A. Leem, H. Ko, M. Y. Jeon, C. W. Lee, S.-P. Han, D. Lee, and K. H. Park, "Widely Tunable 1.55-um Detuned Dual-Mode Laser Diode for Compact Continuous-Wave THz Emitter," *ETRI J.*, vol. 33, no. 5, pp. 810–813, Oct. 2011.

[182] T. A. Frost, "Red-Emitting III-Nitride Self-Assembled Quantum Dot Lasers.," *Dr. Diss. Univ. Mich.*, 2016.